Journal of Nanomaterials

Synthesis, Characterization, and Applications of Polymer Nanocomposites

Lead Guest Editor: Emad M. Masoud
Guest Editors: Laijun Liu and Biaolin Peng

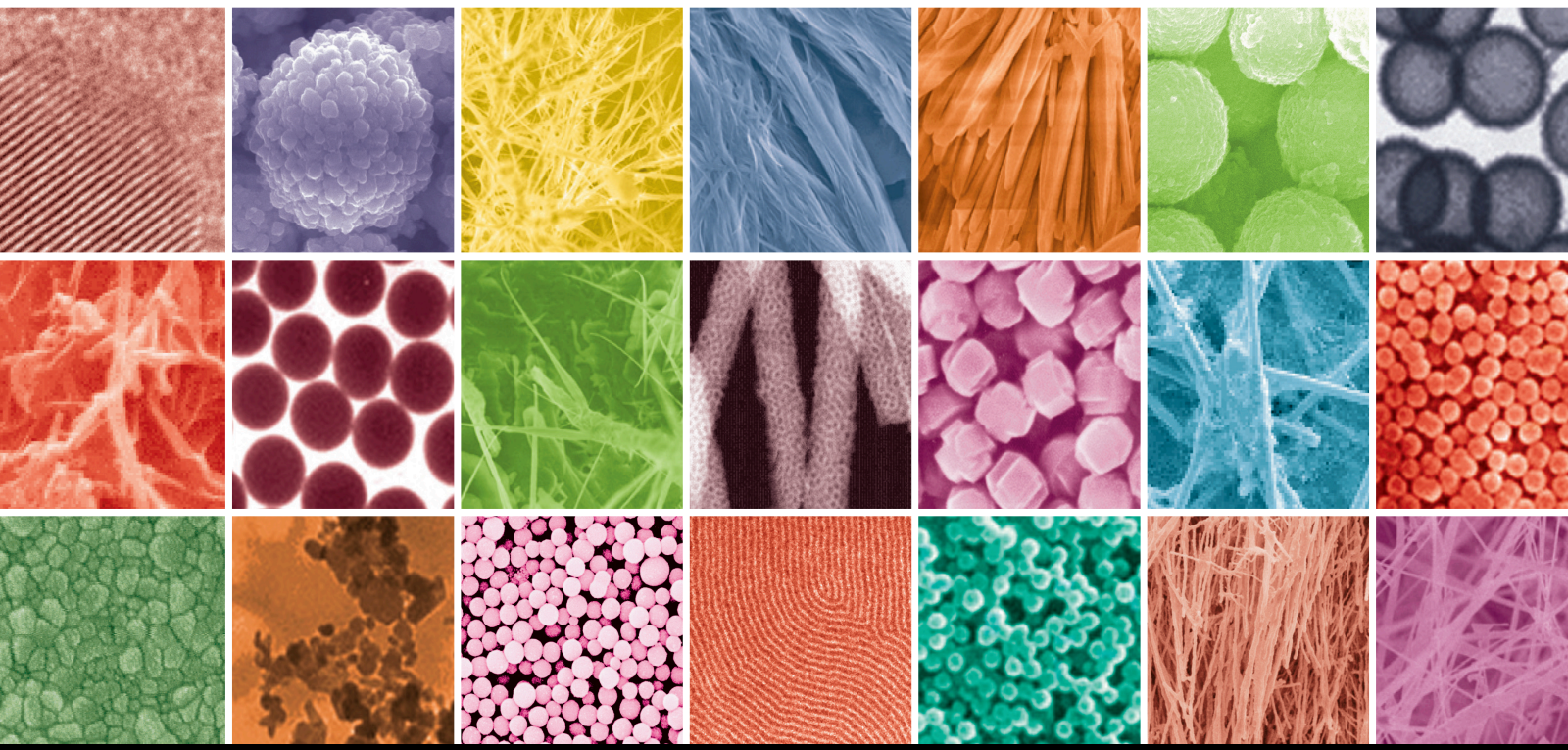

Synthesis, Characterization, and Applications of Polymer Nanocomposites

Journal of Nanomaterials

Synthesis, Characterization, and Applications of Polymer Nanocomposites

Lead Guest Editor: Emad M. Masoud
Guest Editors: Laijun Liu and Biaolin Peng

Editorial Board

Contents

Hindawi
Journal of Nanomaterials
Volume 2020, Article ID 5439136, 2 pages
https://doi.org/10.1155/2020/5439136

Editorial

Synthesis, Characterization, and Applications of Polymer Nanocomposites

Emad M. Masoud,[1,2] **Laijun Liu**,[3] **and Biaolin Peng**[4]

[1]*Chemistry Department, Faculty of Science, Islamic University of Madinah, 20012 Madinah, Saudi Arabia*
[2]*Chemistry Department, Faculty of Science, Benha University, 13518 Benha, Egypt*
[3]*College of Materials Science and Engineering, Guilin University of Technology, Guilin 541004, China*
[4]*Guangxi Key Laboratory for Relativistic Astrophysics, School of Physical Science & Technology, Guangxi University, Nanning 530004, China*

Correspondence should be addressed to Emad M. Masoud; emad.youssef@fsc.bu.edu.eg, Laijun Liu; ljliu2@163.com, and Biaolin Peng; pengbl8@126.com

Received 28 November 2019; Accepted 29 November 2019; Published 6 January 2020

Polymer nanocomposites can be defined as materials in which nanoscopic inorganic particles, in at least one dimension, are dispersed in an organic polymer matrix to improve its performance properties. Polymer nanocomposites represent a new alternative to conventional filled polymers. Because of their size, the filler dispersion that nanocomposites exhibit markedly improves their properties when compared to pure polymers [1–7] or their traditional composites. These properties include increased tensile strength, conductivity and thermal stability as well as decreased flammability.

This special issue focuses on the synthesis, characterization, electrical properties, and applications of polymer nanocomposites such as sun protection, resistive switching device, wastewater treatment, and biosensors.

For the topics of synthesis and characterization of polymer nanocomposites, hybrid composites can be used as effective protective materials against ultraviolet rays since they have a low transmission and high reflection. Also, the result proves that hybrid composites, Nia/ZnO, are an excellent material for ultraviolet ray protection.

For the topics of the structure and electrical properties of polymer nanocomposites, WORM/volatile static random access memory (SRAM) conversion was triggered by the composite of the oxadiazole small molecule. FTO/PMMA/Ag device possesses nonvolatile WORM memory behavior, while the FTO/PMMA+oxadiazole/Ag device shows vastly different volatile SRAM feature. The FTO/PMMA/Ag and FTO/PMMA+oxadiazole/Ag memory devices both exhibit high ON/OFF ratio nearly 10^4. The results manifest the significance of oxadiazole small molecule to the memory effects and will arouse the interest of a scholar to research small molecule composite for the expecting memory devices. Broadband dielectric spectra of epoxy resin composites are filled with WS_2 nanotubes in wide temperature range and demonstrate for the first time influence of WS_2 nanotubes on the electrical properties of composites. Electrical and thermal behavior of high-density polyethylene (HDPE) polymer with alumina nanofillers was reported in this issue. This is significant because studies related to environment pollution have shown that these nonbiodegradable materials cause global warming in all over the world. A novel method to control the localization of APP and CNTs in blends was proposed. Excellent flame retardancy was exhibited only in blends with localization of APP in the PA6 phase and CNTs in the LLDPE phase. A kind of nanocomposite paper was obtained by evaporation-induced self-assembly of a mixture of sisal cellulose nanofibers (CNF) and polyethylene glycol (PEG) as the matrix and citric acid (CA) as the crosslinking agent. The CNF/PEG/CA paper exhibited good water swelling

resistance which could be controlled by changing the concentration of CA. In addition, this nanocomposite paper exhibited good mechanical properties and water-induced shape memory performance.

For the topics of application of polymer nanocomposites in water treatments and biosensors, magnetite-alginate nanoparticles (M-AlgNPs) were synthesized via the coprecipitation method. The M-AlgNPs were applied as a green adsorbent for removing Ni^{2+} and Co^{2+} from wastewater. Nanocomposites IL-RGO/ZIF-8 (ionic liquid functionalized reduced graphene oxide/zeolitic imidazolate framework-8) were prepared by in situ growth of ZIF-8 on a small quantity of IL-RGO temple. The prepared composites were coated on a glass carbon electrode (GCE) as a sensor for detecting dopamine (DA). The electrochemical performance for DA detection is enhanced owing to the synergistic effect of ZIF-8 with a large surface area and order porous structure and IL-RGO with high electron conductivity. A high-sensitivity sensor for DA can be obtained. The IL-RGO/ZIF-8-modified electrode exhibits good electrocatalytic activity and electroconductive properties towards dopamine (DA) which were investigated by cyclic voltammetry and differential pulse voltammetry (DPV). The sensor was shown to provide satisfactory stability for the determination of DA. Rituximab/MTX-PEG-PLL-PLGA nanoparticles were designed and further crosslinked transferrin-receptor-monoantibody (TfRmAb). It had excellent physical properties and long-termed sustained drug release efficiency. The nanoparticle-loaded system can precisely and efficiently transport the rituximab and methotrexate (MTX) drug into SU-DHL-4 cells, a typical kind of B lymphocytes, resulting in the significant increase of the cell apoptosis in the SU-DHL-4 cells. The novel multifunctional drug-loaded nanoparticles are persistently and precisely targeted to SU-DHL-4 cells, which enhanced the anticancer efficiency in B lymphocytes.

Conflicts of Interest

The authors declare that there is no conflict of interest regarding the publication of this article.

Acknowledgments

We would like to thank the editorial board who provided us with the chance to manage this special issue. The professional support team and user-friendly system make our editorial work with ease. Special thanks should be given to all authors who contributed their papers including those that have not been published in this special issue. All the participants have made it possible to have a very stimulating interchange of ideas. The acceptance rate of this special issue (11 out of 23) is less than 50%, implying that all the submitted works are in high quality. We wish you all enjoy this quality-controlled special issue.

Emad M. Masoud
Laijun Liu
Biaolin Peng

References

[1] A. A. ElBellihi, W. A. Bayoumy, E. M. Masoud, and M. A. Mousa, "Preparation, characterizations and conductivity of composite polymer electrolytes based on PEO-$LiClO_4$ and Nano ZnO filler," *Bulletin of the Korean Chemical Society*, vol. 33, no. 9, pp. 2949–2954, 2012.

[2] E. M. Masoud, A.-A. El-Bellihi, W. A. Bayoumy, and M. A. Mousa, "Organic–inorganic composite polymer electrolyte based on PEO–$LiClO_4$ and nano-Al_2O_3 filler for lithium polymer batteries: dielectric and transport properties," *Journal of Alloys and Compounds*, vol. 575, pp. 223–228, 2013.

[3] E. M. Masoud, A.-A. El-Bellihi, W. A. Bayoumy, and M. A. Mousa, "Effect of $LiAlO_2$ nanoparticle filler concentration on the electrical properties of PEO–$LiClO_4$ composite," *Materials Research Bulletin*, vol. 48, no. 3, pp. 1148–1154, 2013.

[4] E. M. Masoud, "Nano lithium aluminate filler incorporating gel lithium triflate polymer composite: Preparation, characterization and application as an electrolyte in lithium ion batteries," *Polymer Testing*, vol. 56, pp. 65–73, 2016.

[5] E. M. Masoud, M. E. Hassan, S. E. Wahdaan, S. R. Elsayed, and S. A. Elsayed, "Gel P (VdF/HFP)/PVAc/lithium hexafluorophosphate composite electrolyte containing nano ZnO filler for lithium ion batteries application: effect of nano filler concentration on structure, thermal stability and transport properties," *Polymer Testing*, vol. 56, pp. 277–286, 2016.

[6] E. M. Masoud, A.-A. El-Bellihi, W. A. Bayoumy, and E. A. Mohamed, "Polymer composite containing nano magnesium oxide filler and lithiumtriflate salt: an efficient polymer electrolyte for lithium ion batteries application," *Journal of Molecular Liquids*, vol. 260, pp. 237–244, 2018.

[7] E. M. Masoud, "Montmorillonite incorporated polymethylmethacrylate matrix containing lithium trifluoromethanesulphonate (LTF) salt: thermally stable polymer nanocomposite electrolyte for lithium-ion batteries application," *Ionics*, vol. 25, no. 6, pp. 2645–2656, 2019.

Hindawi
Journal of Nanomaterials
Volume 2019, Article ID 5957606, 9 pages
https://doi.org/10.1155/2019/5957606

Research Article

Development of a Hybrid Chitosan- and Niacinamide-Coupled ZnO Nanoparticle Composite for Sun Protection Application

Hyun-jun Jo,[1] Sang-Myoung Joo,[2] Jeong Yup Kim,[2] Kook-Hyun Yu,[2] and Sang Wook Kim [1]

[1]*Department of Advanced Materials Chemistry, College of Science and Technology, Dongguk University-Gyeongju, Gyeongbuk 38066, Republic of Korea*
[2]*Department of Chemistry, College of Natural Sciences, Dongguk University-Seoul, Seoul 04620, Republic of Korea*

Correspondence should be addressed to Sang Wook Kim; swkim@dongguk.ac.kr

Received 2 May 2019; Accepted 8 October 2019; Published 16 November 2019

Guest Editor: Biaolin Peng

Zinc oxide nanoparticles (ZnO) have long been utilized as UV-protective sunscreen components due to their high durability and lower skin irritation while maintaining capability for blocking UV rays. However, the dispersal and transparency properties of ZnO need to be enhanced in order to improve the capacity for creating effective sunscreen through control of the physiochemical properties of ZnO. In this study, chitosan or niacinamide, which are suitable functional cosmetic compounds and effective skin lightening agents, are combined with ZnO for the development of better UV-protective products. Each biocompatible coating material is individually attached on its surface after the synthesis of ZnO. The size is 70 nm using the sol-gel method. Their morphology and chemical structure are characterized by FT-IR, XRD, SEM, TEM, TGA, and zeta potential. The results indicate that approximately 50% of chitosan and 5% niacinamide were coated on the ZnO. To confirm the capacity of each surface-coated ZnO with chitosan and niacinamide as a sunscreen, we measured their transmission, reflectance, and sun protection factor (SPF) using a UV spectrophotometer and SPF. As a result, the niacinamide-coated ZnO shows remarkably lower transmission and high reflectance against UV rays than that of bare ZnO and chitosan-coated ZnO. Furthermore, niacinamide-coated ZnO exhibits great lightening effects. Consequently, these results demonstrate that niacinamide coating is highly effective for the production of sunscreen emulsions.

1. Introduction

Ultraviolet (UV) rays are categorized into 3 different types: UV-A (320-400 nm), UV-B (280-320 nm), and UV-C (200-290 nm). When UV rays are exposed to a 200-400 nm wavelength area of sunlight, they can cause skin diseases such as skin cancer and premature aging. Sunscreen emulsion is defined as a skin protectant against UV rays. Exposure to UV-A radiation leads to damage to the elastic and collagenic fibers of connective tissue of skin, which leads to premature aging (photoaging). Furthermore, UV-B radiation causes acute inflammation (sunburn) and intensification of photoaging [1–5]. Organic sunscreen absorbs UV rays and then transfers either infrared rays or heat energy. For example, benzoic acid ester types and benzophenone types such as cinnamate and p-aminobenzoic are often present in organic sunscreen. Although these organic materials have excellent sunscreen attributes, there are some disadvantages. For example, the UV wavelength protection is narrow, skin irritation is common, and effective sunburn resistance is poor [6, 7].

When used in sunscreen emulsion, inorganic materials such as zinc oxide (ZnO) have several attributes. Inorganic sunscreen scatters UV rays with components that have a wide protective area. It has higher durability and lower skin irritation than organic materials. Due to ZnO's low refractive index compared to that of titanium dioxide (TiO_2), it can reduce the appearance of a white cast. As TiO_2 generates oxygen free radicals, it causes damage to skin cells and neuron cells which are harmful to the body. Furthermore, ZnO is nontoxic, has optically active attribution, and is both physically and chemically secure. It is also used in fabric, photocatalysis, and electronic industries as well as in the manufacturing of medical supplies. ZnO has a high exciton binding energy (60 meV). Also, because it has the band gap

energy of 3.22 eV, ZnO can protect against the range of UV-A (320~400 nm) [2, 5, 8–10].

Typically, in the case of metal oxide nanoparticles, the attribution is known to be size dependent. Smaller ZnO nanoparticles are more efficient at protecting against harmful UV rays. The optimal size of ZnO nanoparticles is 40-70 nm, which results in effective absorbance and high band gap energy. When the particles' sizes are smaller than 40 nm, the protective absorbance decreases and the band gap energy increases. Therefore, the particles have to be at least 40 nm in size [11–19].

Although ZnO has an excellent protective effect in its nanoparticles status, there are some disadvantages. For example, it is difficult for ZnO nanoparticles to disperse, the particles are aggregative, and also the white cast the produce would be visible due to reflection of radiation. To compensate aggregation and white cast, chitosan and niacinamide (natural organic materials) are utilized to synthesize chitosan (CS)/ZnO and niacinamide (Nia)/ZnO composites.

Chitosan resulted from processing chitin with alkali, a glucosamine polymer. Chitosan is comprised of glucosamine binding, and the molecule structure of chitosan is very similar to that which is found in the human body. Furthermore, it is friendly to the body and nontoxic. It has high moisturization and dispersibility capacity, which are suitable for functional cosmetic compounds [20–23].

Niacinamide is a functional natural organic material. In the body, niacinamide is a component of nicotinamide adenine dinucleotide (NAD) (also known as coenzyme I) and nicotinamide adenine dinucleotide phosphate (NADP) (also recognized as coenzyme II). These coenzymes are involved in many intracellular oxidation-reduction reactions. As a result, niacinamide is used as an antioxidant. Niacinamide has been effective on the treatment of cutaneous hyperpigmentation. In clinical trials, the niacinamide moisturizer provides inhibition of melanosome shift from melanocytes to keratinocytes, proving to be an effective skin lightening agent [23–25].

In this study, ZnO is synthesized to 70 nm using the sol-gel method in order to provide nontoxicity, boost up dispersion, and reduce a white cast. Synthesized ZnO nanoparticles were coupled with natural organic chitosan and niacinamide by modifying the surface to achieve CS/ZnO and Nia/ZnO.

The prepared chitosan- and niacinamide-associated ZnO nanoparticle compounds gave excellent UV protection activity.

2. Method

As a precursor, zinc oxide nanoparticles were prepared using zinc acetate. The surface of synthesized ZnO NPs was modified using either chitosan or niacinamide. Reagents for synthesis were used without a refining process. Zinc acetate dihydrate, oxalic acid dihydrate (99.5%), niacinamide, and medium molecular weight chitosan were purchased from Sigma-Aldrich, USA. The second group (acetic acid glacial (99.5%), ethyl alcohol anhydrous (99.9%), and sodium hydroxide) was purchased from Daejung Chemical, Korea.

Table 1: Formula for W/O emulsion.

Material name	Content (%)	Phase
Liquid paraffin	34	Oil phase
Olivem 900	5	
ZnO, CS/ZnO, Nia/ZnO	5	
Sodium chloride	2	Water phase
Water	To 100	

Structural analysis of synthesized materials verified functional groups using the following analysis methods: Fourier transform infrared spectroscopy (Tendo 30 of the company, Bruker, USA), X-ray diffraction (Ultima IV X-ray diffractometer, Rigaku Corporation, USA), field-emission scanning electron microscopy energy-dispersive spectroscopy (SU-8010, Hitachi, Japan), biotransmission electron microscopy (HT 7700, Hitachi, Japan), thermogravimetric analysis (STA 6000, PerkinElmer, USA), and dynamic light scattering-zeta potential (Zetasizer Nano ZS90, USA). Transmission ratio and reflectance of synthesized materials are confirmed by ultraviolet-visible spectroscopy (Carry 4000, Varian Corporation). Sun protection factor was measured using a UV Sunscreen Analyzer (UV-2000S, Labsphere, USA).

2.1. Synthesis of Materials

2.1.1. The Synthesis of ZnO. Zinc acetate (5.01 mmol) and 300 mL ethyl alcohol are stirred at 50°C for an hour using a reflux system. Typically, the oxalic acid (14 mmol) was dissolved in 200 mL ethyl alcohol, followed by the dissolved addition of zinc acetate to the above mixture (5.01 mmol, ethyl alcohol 300 mL). The mixture was stirred at 50°C in a reflux system for 1 h. The gel of ZnO was cooled down to room temperature, and it was dried at 70°C in the oven for 20 min. Afterwards, it was sintered at 650°C for 4 h using an electric furnace [26].

2.1.2. The Synthesis of Chitosan-Integrated ZnO. The surface of ZnO was modified into CS/ZnO by the following steps. Initially, ZnO (0.1 g) was stirred in 100 mL of 1% acetic acid solution. Later, 0.1 g of chitosan was transferred into the dissolved ZnO solution, and the combination of chitosan (0.1 g) and the dissolved ZnO was sonicated for 30 min. Next, 1 M of sodium hydroxide was added into the above mixture (pH 10). It was kept at 60°C and stirred for 3 h. Later, the gel was washed with distilled water several times and dried at 50°C for 3 hours [23].

2.1.3. The Synthesis of Niacinamide-Integrated ZnO. ZnO (0.1 g) was added to ethyl alcohol (3.17 mL) and stirred at 700 rpm at 25°C for 20 min. The mixture of sodium hydroxide (0.01 g) and ethyl alcohol (0.25 mL) was added to the above solution and stirred for 20 min. It was dispersed using sonication for 30 min. The dispersed ZnO was stirred at 700 rpm at 75°C for 30 min. The mixture of niacinamide (0.25 g) and ethyl alcohol (0.32 mL) was added to the dispersed ZnO solution, and it was stirred at 700 rpm at 75°C for 3 h. The resultant solid was washed with ethyl alcohol several times and dried in a vacuum.

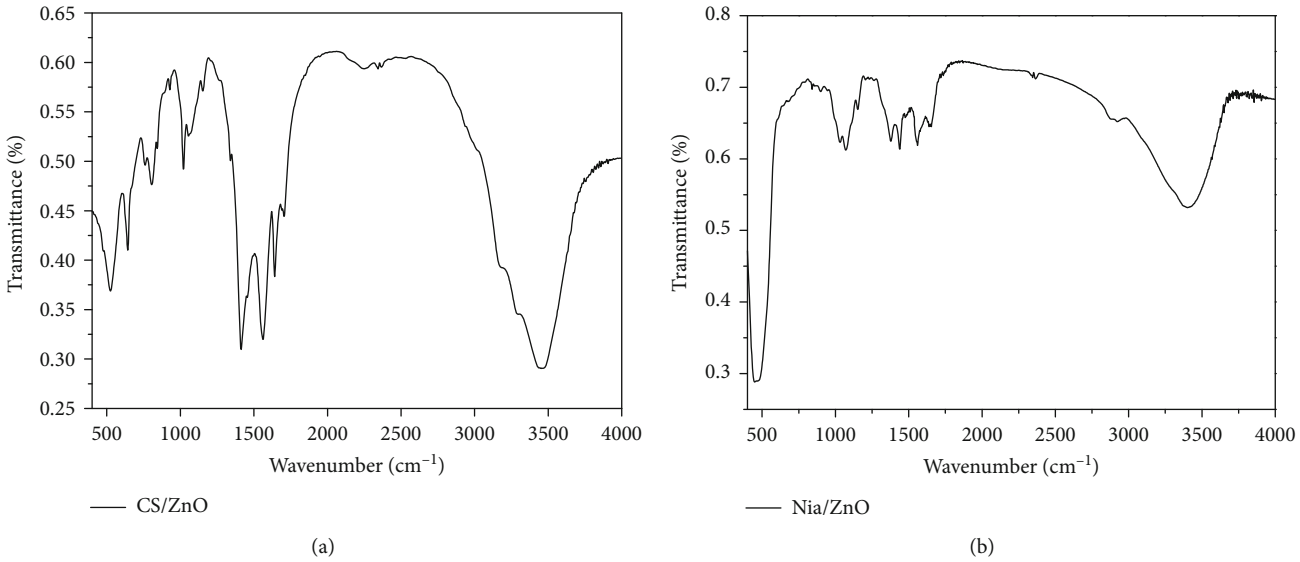

Figure 1: FT-IR spectra of CS/ZnO (a) and Nia/ZnO (b).

2.2. Evaluation of Sunscreen Emulsion Formulation. W/O emulsion was formulated based on the ratio shown in Table 1 so as to confirm the sun protection factor (SPF) of ZnO, CS/ZnO, and Nia/ZnO. The water phases consist of dissolved sodium chloride into water at 80°C. Next, the oil phase is formulated. Olivem 900 and liquid paraffin are mixed at 80°C. This mixture is divided into three parts, with each part added to the synthesized ZnO, CS/ZnO, and Nia/ZnO, respectively, at 80°C. The water phase and oil phase were mixed, and the mixture was dispersed for 30 minutes [27].

2.3. Tyrosinase Inhibition Assay. A variety of concentrated samples of 20 μL and 0.1 M phosphate buffer (100 μL) were mixed and reacted for 5 minutes at room temperature. 1 k unit/mℓ of tyrosinase (in 0.1 M phosphate buffer) (30 μL) and 1.5 mM tyrosine (30 μL) were mixed for 10 min at 37°C, and the enzyme reaction was proceeded.

The absorbance was measured at 490 nm of wavelength after the completion of reaction. Based on the standard of the inhibition assay, 0.1 M phosphate buffer was added instead of the samples. For comparative analysis, arbutin was used as a positive control.

2.4. Cell Viability. The culture medium consists of 10% heat-inactivated fetal bovine serum, 100 units/mL penicillin, and 100 μg/mL streptomycin. The melamine cell (SK-MEL-28) was incubated with the formulated culture medium in the cell plate, then incubated at 5% of CO_2 at 37°C. The culture medium mixture and melamine cell (SK-MEL-28) were moved to the three different well plates. ZnO, CS/ZnO, and Nia/ZnO were added into each well plate. When this procedure was completed, incubated cells were moved to each well plate. After 24 hours, the culture medium was removed. Then, 100 μL of MTT (5 mg/mL in PBS) was added into the well plate at 5% of CO_2 at 37°C for 2-3 hours. This caused some of the MTT to react, thereby transforming it into a burgundy-colored formazan. Next, the excess MTT that did not react was removed. Later, DMSO was added to the formazan/SK-MEL-28 well plate, and the mixture was shaken for 15-20 min. 540 nm of the absorbance was measured upon analysis [28, 29].

3. Results and Discussion

3.1. Characterization of CS/ZnO and Nia/ZnO

3.1.1. Fourier Transform Infrared Spectroscopy. The IR spectra of CS/ZnO were confirmed that the -OH and -NH groups displayed a stretching vibration of its bands from 3400 to 3250 cm^{-1}. The band at 2876 cm^{-1} is assigned to the asymmetric stretching vibration of the -CH group. 1650 cm^{-1} shows a stretching vibration of N-H while 1424 cm^{-1} demonstrates C-N and 1047 cm^{-1} indicates C-O-C of the band. As the result of the spectra, the synthesis of CS/ZnO is validated by the results (Figure 1(a)).

The IR spectra of Nia/ZnO display both an OH peak and NH peak of the stretching vibration at 3600~3100 cm^{-1} band. The C-H peak of the stretching vibration reads 2850~3000 cm^{-1}, and the peak of C=O of the stretching vibration is displayed at 1650~1700 cm^{-1}. The NH peak of the stretching vibration is indicated at 1600~1650 cm^{-1}, and C-N of the stretching vibration reads 1335~1250 cm^{-1}. Therefore, the synthesis of Nia/ZnO was confirmed by FTIR analysis (Figure 1(b)).

3.1.2. X-Ray Diffraction Analysis. The XRD pattern of ZnO (ICDD card 01-075-0576) is verified, and the crystal face is confirmed as a hexagonal structure. The crystal faces of CS/ZnO and Nia/ZnO, which result from the synthesis of CS and Nia with ZnO, respectively, confirm the identical crystal face of ZnO, as shown in Figure 2.

3.1.3. Scanning Electron Microscope (SEM). Figure 3(a) shows that the particle size of ZnO is 65~80 nm. The ZnO's particle shape displays the characteristics of a hexagonal structure. The ZnO analysis results using the EDS confirm the ingredients of both zinc and oxygen as shown in Table 2.

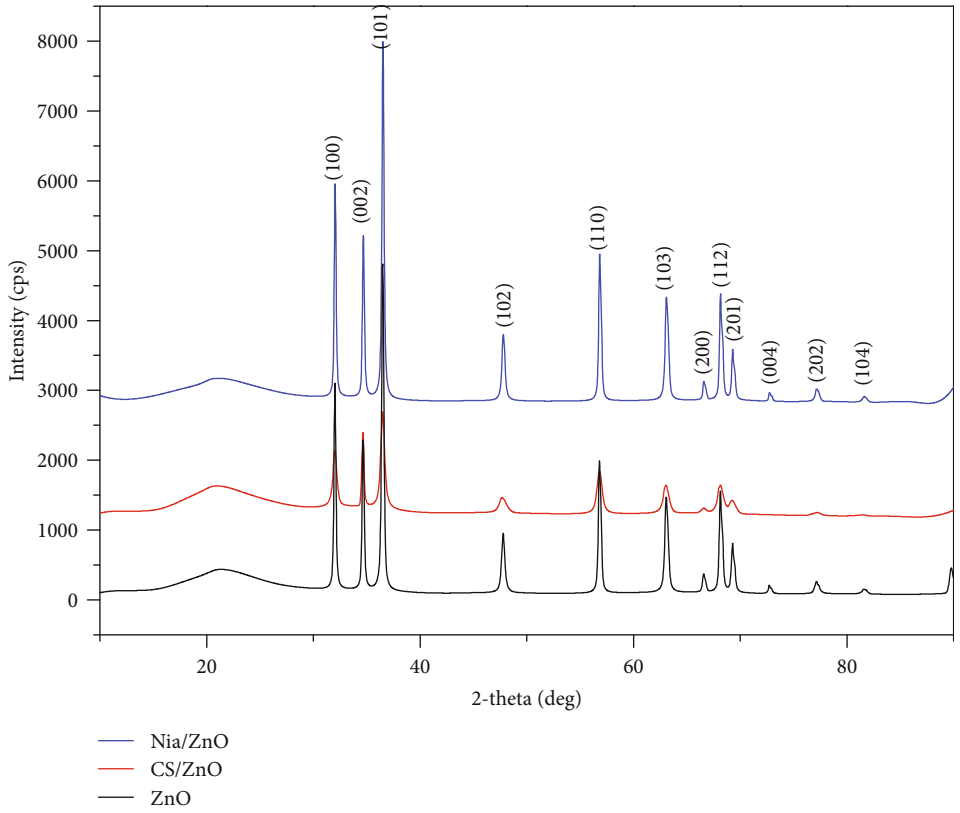

Figure 2: X-ray diffraction pattern of ZnO, CS/ZnO, and Nia/ZnO. This shows the results of X-ray diffraction analysis. The bottom line in black shows the pattern of ZnO, the middle one in red illustrates the pattern of CS/ZnO, and the top one in blue displays the pattern of Nia/ZnO.

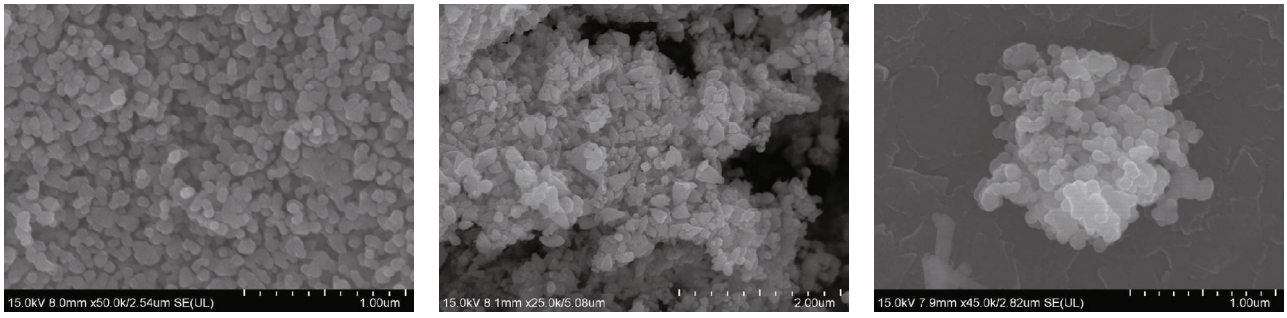

(a) (b) (c)

Figure 3: SEM images of ZnO (a), CS/ZnO (b), and Nia/ZnO (c). The measurements were processed with a platinum pretreatment of ZnO (a), CS/ZnO (b), and Nia/ZnO (c).

The particle size of CS/ZnO is between 150 and 180 nm as indicated in Figure 3(b). The SEM image of CS/ZnO has a rough surface as compared to that of ZnO. EDS results confirm the binding of chitosan with ZnO nanoparticles.

The SEM image proves the size of Nia/ZnO between 90 and 100 nm, as indicated in Figure 3(c). As mentioned previously, the EDS analysis confirms that zinc and oxygen combine to form ZnO. Furthermore, it was found that Nia/ZnO was coated with niacinamide, as shown in Table 2. The results exhibited that chitosan and niacinamide are associated with ZnO.

Table 2: The composites were analyzed by energy-dispersive spectroscopy.

	Wt (%)		
	ZnO	CS/ZnO	Nia/ZnO
Zinc	80.17	58.50	17.82
O	13.34	18.37	49.53
C	—	17.14	27.12
N	—	2.48	2.32
Pt	6.49	3.51	3.21
Total	100.00	100.00	100.00

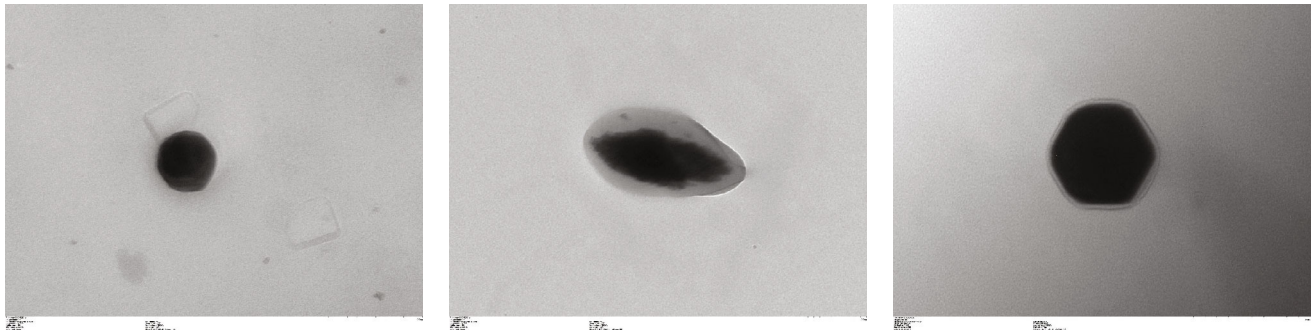

(a) (b) (c)

Figure 4: TEM images of ZnO (a), CS/ZnO (b), and Nia/ZnO (c). The measurements are processed with a chloroform pretreatment of ZnO (a), CS/ZnO (b), and Nia/ZnO (c).

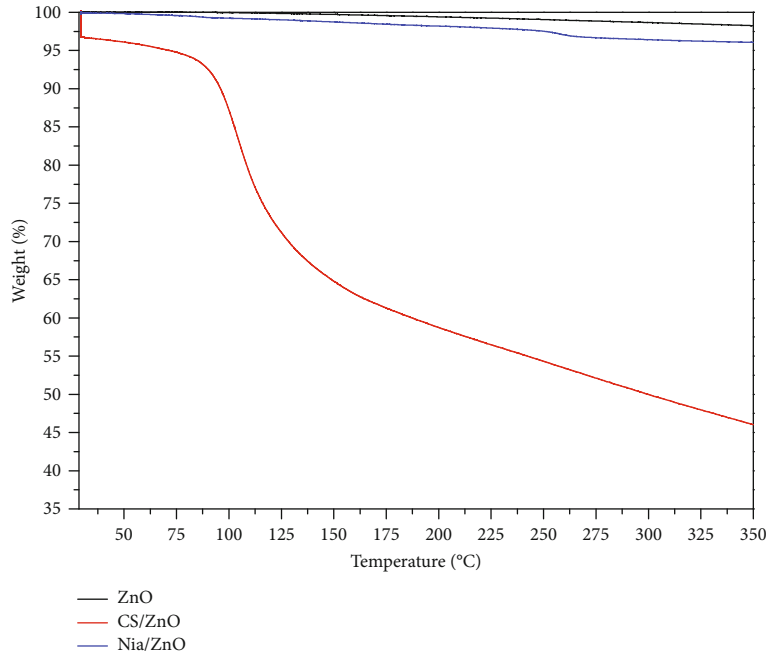

Figure 5: Thermogravimetric analysis of ZnO, CS/ZnO, and Nia/ZnO. These three samples, 50 mg each, are subjected to heat, specifically 10°C per minute. The thermogravimetric analysis was completed when each sample was subjected to a temperature of 350°C. The numbers on the left of the graph show the percentage of weight loss. The black line shows the weight loss of pure ZnO (to be referred to as ZnO from this point forward), the red line illustrates the Nia/ZnO weight loss, and the blue line displays the CS/ZnO weight loss.

3.1.4. Transmission Electron Microscope (TEM). The TEM images show the dispersal of each sample in chloroform on a nickel grid. The samples are dissolved in chloroform through sonication for 30 minutes. After this is completed, the three grids are absorbed and dried for an additional 30 minutes. ZnO nanoparticles are shown in Figure 4(a). On the other hand, when the TEM images are confirmed as to whether or not the organic material is introduced, they show that chitosan and niacinamide are sufficiently covered with organic materials in Figures 4(b) and 4(c). When the organic layers of chitosan are observed, many organic layers are confirmed by the TEM images, which means that the organic layers of chitosan are largely covered. In comparison, niacinamide is found to be coated as thin as the composite ratio of 5% niacinamide/95% ZnO.

Table 3: Dynamic light scattering-zeta potential.

	DLS (nm)	Zeta potential (mV)
ZnO	95.07	-2.81
CS/ZnO	86.60	10.4
Nia/ZnO	95.07	-32.3

3.1.5. Thermogravimetric Analysis. The differences between ZnO, CS/ZnO, and Nia/ZnO confirm the organic layers as seen in Figure 4. The purpose of conducting thermogravimetric analysis is to determine the composite ratio of organic weight loss with respect to these three materials. When the temperature of ZnO increased in thermogravimetric analysis, the weight loss was not considerable. This means that ZnO is highly stable under extreme heat, up to 1975°C. However,

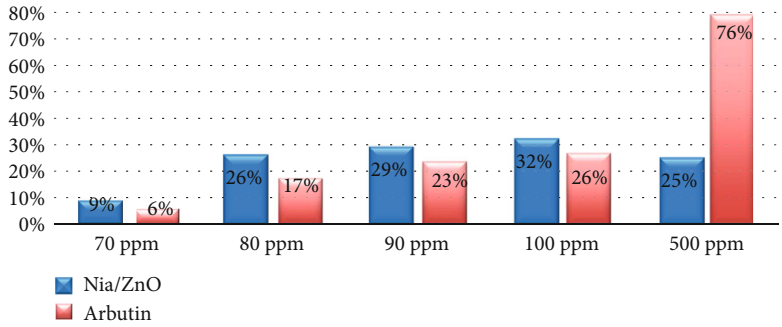

Figure 6: Concentrations of tyrosinase inhibitory activity of Nia/ZnO and arbutin. Arbutin was used as the positive control of Nia/ZnO. When concentration increased, the samples were not dissolved, which led to the measurement value being significantly lower than that of the positive control.

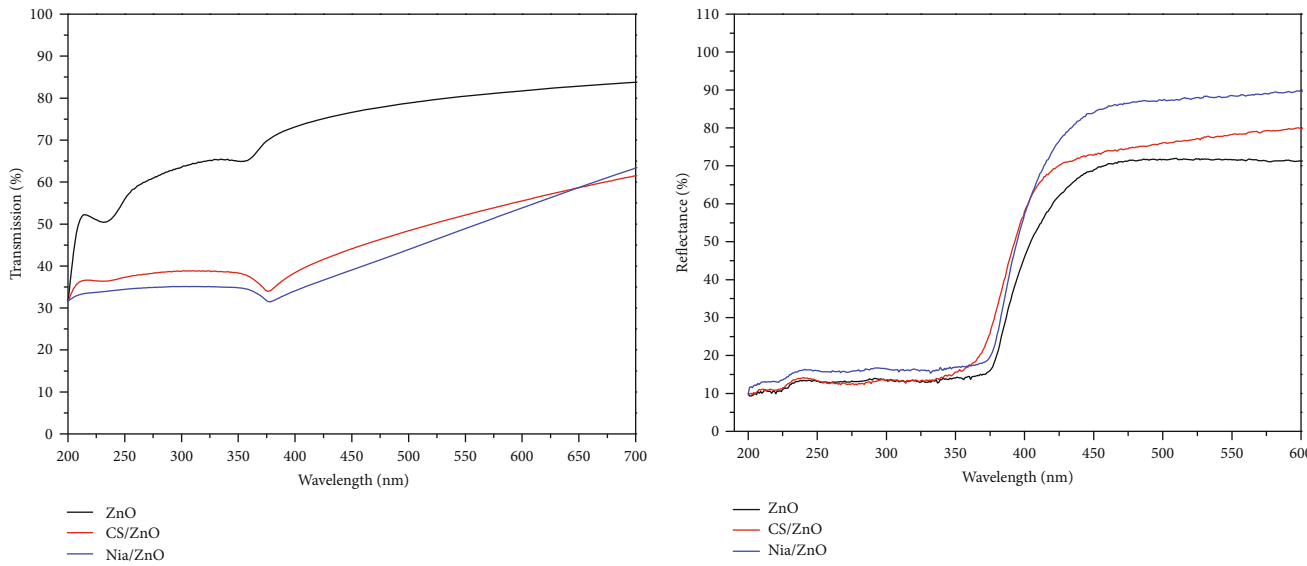

(a) (b)

Figure 7: UV-visible transmission (a) of and reflectance (b) spectra of ZnO, CS/ZnO, and Nia/ZnO. After the three samples were dissolved into the 0.01% distilled water, they were scanned at 200~800 nm by ultraviolet-visible spectroscopy.

because of the water molecules present in chitosan, the CS/ZnO polymer displayed a two-phase weight loss. The first phase resulted in a weight loss of water at under 100°C. The final decline of polymer occurred at the point between 110 and 325°C. The composite ratio of chitosan and ZnO is 50/50, meaning that 50% of each sample was used. In order to confirm the ratio, the weight loss of chitosan was monitored. As a result, all of the chitosan evaporated during this process. The remaining ratio of the CS/ZnO (now just ZnO is remaining) was 50%, which confirms that the ratio was accurate. In the case of Nia/ZnO, the composite ratio of 5% Nia and 95% ZnO was used. The 5% decrease refers to the niacinamide coating which was a result of the synthesis experiment in Section 2.3. Based on the results, a small thermal change at 250°C occurred and the weight loss was observed at the end. Niacinamide was stable until it reached 235°C, but decreased in weight by 5% at 276°C. The remaining 95% consists entirely of ZnO.

The results in Figure 5 display clear comparisons between ZnO, CS/ZnO, and Nia/ZnO with regard to their weight loss under thermogravimetric analysis. Thermogravimetric analysis of ZnO shows that the weight loss of ZnO only slightly occurs at high temperatures. Furthermore, CS/ZnO exhibits significant weight loss at around 100°C until the chitosan completely disappears at 350°C. Lastly, Nia/ZnO lost all of the niacinamide, but not until it reached a heat of 276°C. Therefore, Nia/ZnO, with its lower composite ratio and higher stability under heat, is far more effective than CS/ZnO, which has a higher composite ratio and lower stability under heat. Further studies involving UV and SPF are discussed in Sections 3.1.8 and 3.1.9.

3.1.6. Dynamic Light Scattering- (DLS-) Zeta Potential Study. Table 3 indicates that the dispersed particle sizes of Zn, CS/ZnO, and Nia/ZnO are 95.07 nm, 86.60 nm, and 95.07 nm based on the DLS measurement result, respectively.

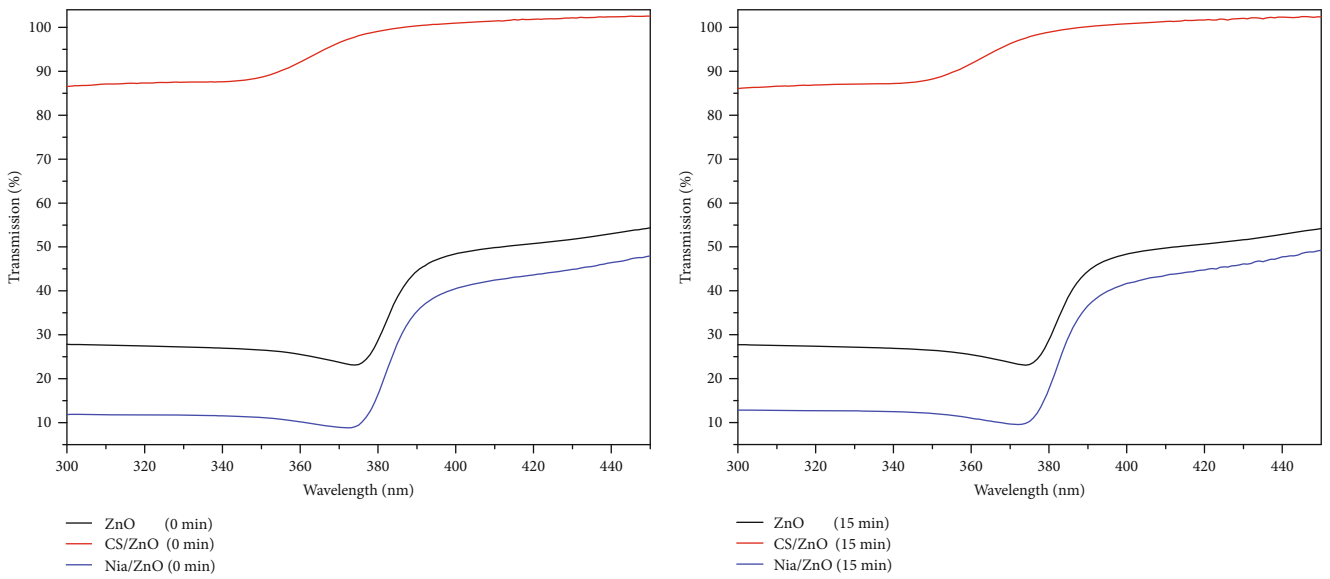

Figure 8: SPF activity of ZnO, CS/ZnO, and Nia/ZnO with time. The emulsions which was prepared for the experiment method of the previous part (Section 2.2) were applied on the cell plates and measured at UV-2000 300 mg/cm^3.

As a result, the zeta potential of CS/ZnO (10.4 mV) and Nia/ZnO (-32.3 mV) was higher than that of the pure ZnO nanoparticle (-2.81 mV).

3.1.7. Tyrosinase Assay Ratio. Tyrosinase stimulates the significant process of generating melanin in the skin cell. When melanin is excessively pigmented, it causes skin aging. The tyrosinase experiment that prohibits tyrosinase reaction is usually used for studies on the effects of skin lightening.

Under the tyrosinase experiment, tyrosinase inhibitory activity is not measured from ZnO and CS/ZnO materials while tyrosinase inhibitory activity is accomplished from the Nia/ZnO composite and has a lightening effect. The tyrosinase inhibitory activity of Nia/ZnO is measured at different concentrations (Figure 6). The higher concentration of Nia/ZnO produced more inhibitory activity increases. When the sample over 500 ppm concentration is dispersed, the dispersion of the nanoparticles did not occur. Therefore, the experiment was performed at a lower concentration than the inhibitory activity of the positive control. The positive control of tyrosinase inhibitory activity is confirmed by using arbutin. The results of the measurement demonstrate that upon increment of amount of the tyrosinase assay of Nia/ZnO, the tyrosinase inhibitory activity increases. Therefore, the lightening effects of Nia/ZnO are confirmed [30–33].

3.1.8. Ultraviolet-Visible Spectroscopy. In order to measure transmission, 0.001% of each ZnO, CS/ZnO, and Nia/ZnO sample was dispersed in distilled water. The result of this experiment shows that transmission of the synthesized materials, CS/ZnO and Nia/ZnO, is lower than the transmission of ZnO (Figure 7(a)). The difference of transmission between the pure ZnO and CS/ZnO is 34.7%, and the difference of transmission between the pure ZnO and Nia/ZnO was 39% in the UV ray range (200-400 nm). The transmission difference between CS/ZnO and Nia/ZnO was 4.3% in the same UV ray range. On the other hand, the reflectance differences between the pure ZnO, CS/ZnO, and Nia/ZnO were not significant, as shown in Figure 7(b). The reflectance difference between ZnO and CS/ZnO is 3%, and the reflectance difference between ZnO and Nia/ZnO is 15.1% in the visible ray region. However, CS/ZnO and Nia/ZnO have 2.8% and 3% reflectance with respect to ZnO, which is lower in the UV ray region.

Table 4: SPF timed mean study of ZnO, CS/ZnO, and Nia/ZnO.

	SPF mean	T (UVA)	T (UVB)	Lambda critical
ZnO 0 min	4.06	0.3023	0.2769	383.2
ZnO 15 min	4.11	0.3019	0.2762	383.1
CS/ZnO 0 min	1.15	0.9325	0.8869	355.3
CS/ZnO 15 min	1.18	0.9293	0.8823	356
Nia/ZnO 0 min	8.83	0.1653	0.1184	380.3
Nia/ZnO 15 min	9.96	0.1658	0.1187	380.2

3.1.9. Sun Protection Factor (SPF). The sunscreen emulsions were formulated as previously described in Section 2.2. The SPF mean of each sunscreen emulsion in UV-2000 was studied as shown in Figure 8 and Table 4. The measurement was carried out at 0 min and 15 min. As a result, the CS/ZnO and Nia/ZnO emulsions show remarkable UV ray protection efficiency compared to the ZnO emulsion. However, CS/ZnO was proven as not being able to function as an effective sunscreen emulsion for two reasons. (i) The transmission of CS/ZnO was significantly higher than that of ZnO, which means that CS/ZnO transmitted more than 90% of UV rays. (ii) Also, the SPF mean for CS/ZnO showed to be 1.18

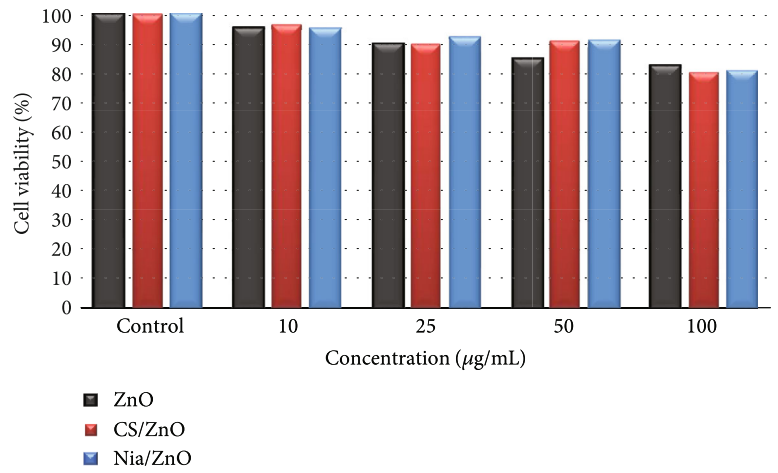

Figure 9: Cell viability of ZnO, CS/ZnO, and Nia/ZnO. The graph shows the result of the MTT experiment which in the three samples was carried out by using the skin cell (SK-Mel-28). The concentration shown in the graph is generally used for the nanoparticles.

(15 min), which was the lowest among the three materials. Nia/ZnO, on the other hand, measured an SPF mean of 9.96 at 15 min and has a UV ray transmission of 16%, which is more efficient than that of pure ZnO.

3.1.10. Cell Viability. As ZnO, CS/ZnO, and Nia/ZnO can be used as sunscreen emulsions, it was concluded that their nanoparticles were cytotoxic to the skin using the cell viability. The cell viability of ZnO, CS/ZnO, and Nia/ZnO was tested using a specific skin cell (SK-Mel-28) [34–36]. When the concentration of nanoparticles was exposed at 100 μg/mL, more than 80% of cells survived (Figure 9). This concentration (100 μg/mL) is used for the nanoparticle MTT assay. The high survival rate was displayed at the highest concentration. The poison did not show a significant difference in this concentration.

4. Conclusion

In the present study, chitosan and niacinamide, natural organic materials, play an important role as components of functional cosmetics. They each have a skin dispersible capacity, provide high levels of moisture, and are mild to the skin. With these benefits, chitosan and niacinamide should be synthesized with ZnO nanoparticles for maximum effectiveness. Remarkably, 0.18 g of ZnO was yielded through the sol-gel method while 0.17 g of CS/ZnO and 0.08 g of Nia/ZnO were yielded in our experiments. The formation of three synthesized materials (ZnO, CS/ZnO, and Nia/ZnO) was characterized through the use of IR, XRD, FE-SEM-EDS, Bio-TEM, TGA, DLS, and zeta potential technics.

Nia/ZnO was determined to have a lightening effect as a result of the tyrosinase experiment. Also, as the concentrations of ZnO, CS/ZnO, and Nia/ZnO were high under the cell viability, the cell extinction did not display a significant difference. In terms of reflectance properties, pure ZnO did not show a significant difference compared to the UV reflectance properties of CS/ZnO and Nia/ZnO. Due to CS/ZnO and Nia/ZnO showing lower levels of UV transmission than pure ZnO, they are more efficient against UV rays. In the SPF mean study, more than 90% of CS/ZnO was transmitted through UV rays, which indicates that CS/ZnO is not as efficient as ZnO. However, the transmission of Nia/ZnO was lower than that of pure ZnO while maintaining a higher SPF mean than that of pure ZnO, resulting in Nia/ZnO being the most effective compound for sunscreen lotion. Furthermore, UV transmission and SPF experiments suggested that Nia/ZnO outperformed both ZnO and CS/ZnO. Furthermore, Nia/ZnO was the only compound to produce a lightening effect.

Data Availability

The data used to support the findings of this study are included within the article.

Conflicts of Interest

The authors declare that they have no conflicts of interest.

Acknowledgments

This study was supported by the National Research Foundation Grant funded by the Korean Government (2017R1D1A1B03035589) and Dongguk University-Gyeongju Research Fund 2019.

References

[1] M. R. Serafini, C. B. Detoni, P. D. P. Menezes et al., "UVA-UVB Photoprotective Activity of Topical Formulations Containing *Morinda citrifolia* Extract," *BioMed Research International*, vol. 2014, Article ID 587819, 10 pages, 2014.

[2] T. G. Smijs and S. Pavel, "Titanium dioxide and zinc oxide nanoparticles in sunscreens: focus on their safety and effectiveness," *Nanotechnology, Science and Applications*, vol. 4, 2011.

[3] A. Nasu and Y. Otsubo, "Effects of polymeric dispersants on the rheology and UV-protecting properties of complex suspensions of titanium dioxides and zinc oxides," *Colloids and Surfaces A: Physicochemical and Engineering Aspects*, vol. 326, no. 1-2, pp. 92–97, 2008.

[4] V. C. Seixas and O. A. Serra, *Molecules*, vol. 19, no. 7, pp. 9907–9925, 2014.

[5] A. Nasu and Y. Otsubo, "Rheology and UV-protecting properties of complex suspensions of titanium dioxides and zinc oxides," *Journal of Colloid and Interface Science*, vol. 310, no. 2, pp. 617–623, 2007.

[6] C. R. Srinivas and R. Rai, "Photoprotection," *Indian Journal of Dermatology, Venereology, and Leprology*, vol. 73, no. 2, p. 73, 2007.

[7] S. Kale, A. Sonawane, A. Ansari, P. Ghoge, and A. Waje, "Formulation and in-vitro determination of sun protection factor of Ocimum basilicum, Linn. leaf oils sunscreen cream," *International Journal of Pharmacy and Pharmaceutical Sciences*, vol. 2, 2010.

[8] R. Yoshida, "Novel multifunctional zinc oxide for improving makeup cosmetics," *Fragrance Journal Korea*, vol. 1, 2016.

[9] A. Kołodziejczak-Radzimska and T. Jesionowski, "Zinc oxide—from synthesis to application: a review," *Materials.*, vol. 7, no. 4, pp. 2833–2881, 2014.

[10] Z. L. Wang, "Zinc oxide nanostructures: growth, properties and applications," *Journal of Physics: Condensed Matter*, vol. 16, 2004.

[11] H. S. Kil, Y. H. Kim, M. Park, and S. W. Rhee, "Synthesis and Characterization of Mica Coated with Zinc Oxide Nanoparticles," *Applied Chemistry for Engineering*, vol. 23, no. 3, pp. 271–278, 2012.

[12] E. G. Goh, X. Xu, and P. G. McCormick, "Effect of particle size on the UV absorbance of zinc oxide nanoparticles," *Scripta Materialia*, vol. 78, pp. 49–52, 2014.

[13] N. A. Monteiro-Riviere, K. Wiench, R. Landsiedel, S. Schulte, A. O. Inman, and J. E. Riviere, "Safety evaluation of sunscreen formulations containing titanium dioxide and zinc oxide nanoparticles in UVB sunburned skin: an in vitro and in vivo study," *Toxicological Sciences*, vol. 123, no. 1, pp. 264–280, 2011.

[14] R. Vandebriel and W. De Jong, "A review of mammalian toxicity of ZnO nanoparticles," *Nanotechnology, Science and Applications*, vol. 5, 2012.

[15] Z. Cao, Z. Zhang, F. Wang, and G. Wang, "Synthesis and UV shielding properties of zinc oxide ultrafine particles modified with silica and trimethyl siloxane," *Colloids and surfaces A: physicochemical and engineering aspects*, vol. 340, no. 1-3, pp. 161–167, 2009.

[16] H. M. Cheng, H. C. Hsu, S. L. Chen et al., "Efficient UV photoluminescence from monodispersed secondary ZnO colloidal spheres synthesized by sol-gel method," *Journal of Crystal Growth*, vol. 277, no. 1-4, pp. 192–199, 2005.

[17] L. Qin, C. Shing, S. Sawyer, and P. S. Dutta, *Optical Materials*, vol. 33, no. 3, pp. 359–362, 2011.

[18] M. S. Latja, *The Journal of Clinical and Aesthetic Dermatology*, vol. 6, pp. 16–26, 2013.

[19] M. A. Suva, "Evaluation of sun protection factor of Zingiber officinale Roscoe extract by ultraviolet spectroscopy method," *Journal of Pharmaceutical Sciences*, vol. 3, pp. 95–97, 2014.

[20] J. Kumirska, M. X. Weinhold, J. Thöming, and P. Stepnowski, "Biomedical activity of chitin/chitosan based materials—influence of physicochemical properties apart from molecular weight and degree of N-acetylation," *Polymers*, vol. 3, no. 4, pp. 1875–1901, 2011.

[21] M. M. AbdElhady, "Preparation and characterization of chitosan/zinc oxide nanoparticles for imparting antimicrobial and UV protection to cotton fabric," *International Journal of Carbohydrate Chemistry*, vol. 2012, Article ID 840591, 6 pages, 2012.

[22] M. Thirumavalavan, K. L. Huang, and J. F. Lee, "Preparation and morphology studies of nano zinc oxide obtained using native and modified chitosans," *Materials*, vol. 6, no. 9, pp. 4198–4212, 2013.

[23] Y. Haldorai and J. J. Shim, "Chitosan-zinc oxide hybrid composite for enhanced dye degradation and antibacterial activity," *Composite Interfaces*, vol. 20, no. 5, pp. 365–377, 2013.

[24] *Alternative Mediecine Review*, vol. 7, p. 525, 2002.

[25] F. Lin, W. Xu, C. Guan et al., "Niacin protects against UVB radiation-induced apoptosis in cultured human skin keratinocytes," *International Journal of Molecular Medicine*, vol. 29, no. 4, pp. 593–600, 2012.

[26] H. Benhelbal, "IFC - Editorial Board," *Alexandria Engineering Journal.*, vol. 52, 2013.

[27] C. K. Zhoh, H. J. Kwon, and S. R. Ahn, "The Optical Characteristics of Titanium Dioxide and UV-block Effect," *Korean Journal of Aesthetics and Cosmetics Society*, vol. 9, no. 2, 2011.

[28] S. Tao, S. L. Park, M. R. De La Vega, D. D. Zhang, and G. T. Wondrak, "Systemic administration of the apocarotenoid bixin protects skin against solar UV-induced damage through activation of NRF2," *Free Radical Biology and Medicine*, vol. 89, pp. 690–700, 2015.

[29] M. Ramani, M. C. Mudge, R. T. Morris et al., "Zinc Oxide Nanoparticle–Poly I:C RNA Complexes: Implication as Therapeutics against Experimental Melanoma," *Molecular Pharmaceutics*, vol. 14, no. 3, pp. 614–625, 2017.

[30] B. X. Gu, C. X. Xu, G. P. Zhu, S. Q. Liu, L. Y. Chen, and X. S. Li, "Tyrosinase Immobilization on ZnO Nanorods for Phenol Detection," *The Journal of Physical Chemistry B*, vol. 113, no. 1, pp. 377–381, 2009.

[31] D. Y. Im and K. I. Lee, "Antioxidative activity and tyrosinase inhibitory activity of the extract and fractions from Arctium lappa roots and analysis of phenolic compounds," *Korean Journal of Pharmacognosy*, vol. 45, pp. 141–146, 2014.

[32] V. del Marmol and F. Beermann, *FEBS Letters*, vol. 381, no. 3, pp. 165–168, 1996.

[33] S. W. Jung, N. K. Lee, S. J. Kim, and D. S. Han, "Screening of tyrosinase inhibitor from plants," *Korean Journal of Food Science and Technology*, vol. 27, pp. 891–896, 1995.

[34] R. Jiang, H.-Y. Zhu, H.-H. Chen et al., "Effect of calcination temperature on physical parameters and photocatalytic activity of mesoporous titania spheres using chitosan/poly(vinyl alcohol) hydrogel beads as a template," *Applied Surface Science*, vol. 319, pp. 189–196, 2014.

[35] H. S. Joung, "Antimelanogenic effect of taurine in murine melanoma B16F10 cells," *The Pharmaceutical Society of Korea*, vol. 51, pp. 350–354, 2007.

[36] M. Orazizadeh, A. Khodadadi, V. Bayati, S. Saremy, M. Farasat, and L. Khorsandi, "*In Vitro* Toxic Effects of Zinc Oxide Nanoparticles on Rat Adipose Tissue-Derived Mesenchymal Stem Cells," *Cell Journal*, vol. 17, no. 3, pp. 412–421, 2015.

Hindawi
Journal of Nanomaterials
Volume 2019, Article ID 9490602, 6 pages
https://doi.org/10.1155/2019/9490602

Research Article

Effects of AKD Sizing on the Morphology and Pore Distribution Properties of OCC Fibers

Hua Chen,[1,2,3] **Jing Yang**,[4] **Zhijun Hu**,[1] **Bingbing Zheng**,[3] **Jun Sun**,[3,5] **Qizhong Wo**,[6] **Xiangzhi Zeng**,[7] **Xufeng Qiu**,[8] **Chenying Song**,[1] **and Ruifeng Zhu**[1]

[1]*Zhejiang Provincial Key Lab for Chem & Bio Processing Technology of Farm Product, Key Laboratory of Recycling and Eco-Treatment of Waste Biomass of Zhejiang Province, Zhejiang University of Science and Technology, 310023 Hangzhou, China*
[2]*State Key Lab of Pulp and Paper Engineering, South China University of Technology, 510640 Guangzhou, China*
[3]*Hangzhou NanQi Technology Co. Ltd., 310023 Hangzhou, China*
[4]*Greentown Technology Industry Service Limited Company, 310012 Hefei, China*
[5]*Hangzhou Fulun Ecological Technology Co. Ltd., 311418 Hangzhou, China*
[6]*Zhejiang Paper Products Quality Test Center, 311400 Hangzhou, China*
[7]*Hunan Xiangfeng Special Paper Co. Ltd., 422211 Longhui, China*
[8]*Zhejiang Hengchuan New Material Co. Ltd., 324400 Longyou, China*

Correspondence should be addressed to Jing Yang; 513414453@qq.com

Received 22 February 2019; Revised 3 April 2019; Accepted 26 June 2019; Published 9 October 2019

Guest Editor: Laijun Liu

Changes of the morphology and pore structure of old corrugated container (OCC) fibers during an alkyl ketene dimer (AKD) sizing process were studied. The resulting samples were characterized by scanning electron microscopy (SEM), atomic force microscopy (AFM), contact angle, and BET surface area analysis. The length of fibers had obvious influence on the AKD sizing effect, and the length of fibers ranged from 100 to 200 meshes showed the best sizing performance. The surface roughness of 0.3% AKD sizing OCC fibers decreased from 27.949 nm to 12.811 nm. Compared with the control sample, the pore volume of fibers sized with 0.1% AKD decreased 4.3% when the average pore diameter was fixed at 2.4~3.0 nm. And when the usage of AKD increased to 0.3% and 0.5%, the pore volume decreased 1.4% and 6.3% accordingly. The decrease in the pore volume of AKD-sized fiber indicated the penetration and deposition of dispersed particles of AKD in the fiber lumens.

1. Introduction

In recent years, papermaking industry has made rapid progress along with the development of China's economy, and recycled fiber has become an extremely important raw material because of its low pulping cost, energy saving, environment protection, circulating use, and other advantages [1].

Old corrugated container (OCC), as an environmental friendly packaging material, is one of the main sources of recycled fibers, with a high degree of recycling for many years. OCC is mainly composed of used unbleached kraft pulp, bleached kraft pulp, hardwood semichemical pulp, and grass pulp. The fibers irreversibly change their structure; both the tensile strength and the water retention value of fibers decreased upon recycling [2].

Many researches have been studying on recycling of fibers from different points; it was found that fibrils and other bonding sites are not fully rehydrated when the dried fiber is repulped, which reduces their ability of the fiber, which is consistent with the decreased ability of the fiber to hold water; this is called hornification [3]. Several authors considered the different fiber structure changes affecting the amount of water that fibers hold within the walls and the tendency to be stiffer, including irreversible pore closure [4], microfibril aggregation or coalescence [5], combination of rearrangement of cellulose [6], crosslinking between cellulose

and hemicelluloses [7], crystallization [8], and hemicellulose removal [9]. However, the mechanism for hornification has still not been completely understood.

Internal sizing is a widely used process in papermaking to reduce the rate of liquid penetration into a paper. The traditional method of sizing is using acid sizing (rosin sizes and aluminium sulfate) as sizing agents. However, with the wide application of calcium carbonate (ground calcium carbonate (GCC) and precipitated calcium carbonate (PCC)) used in papermaking, neutral or alkaline sizing has been a widespread use and highly regarded owing to economic reasons and paper storage durability and avoided the corrosive action to approaching system or paper machine caused by aluminium ion [10].

Alkyl ketene dimer (AKD) is a common commercial chemical that is classified as nonhazardous (under OSHA regulations); the chemical structure of AKD is shown in Figure 1 [11]. In a drying process, AKD particles form β-ketoester bonds with cellulose. As a result, the hydrophobic groups become aligned and the surface free energy is reduced. A reduction in hydrogen-bonding potential implies a reduction in the hydrophilicity of the fiber, which is consistent with the decreased ability of fiber to hold water.

Therefore, it can be concluded that AKD might play an important role in the swelling properties or hornification of fiber. In recent years, many research results about the hydrophobic interaction of AKD on original fibers have been published [12, 13]. In general, it is believed that AKD reacts with cellulose fiber and forms a β-keto ester bond, hence making paper hydrophobic [14]. But there was little attention given to the influences on recycled fiber swelling properties, hornification, and morphology of AKD. In fact, original and recycled fibers had been significantly different in sizing and swelling ability, zeta potential, filler distribution, chemical agent content, and other aspects; further research is needed to inhibit hornification and improve the recycling performance of recycled fiber.

In this study, we observe the effect of AKD sizing on the morphology of OCC fiber. The factors influencing this study such as the surface contact angle and BET analysis of AKD-sized OCC fiber were also investigated.

2. Experimental

2.1. Materials

2.1.1. Raw Materials. AKD sizing emulsion was supplied by Tianma Specialty Chemicals (1865, China), the solid content was 13.2%, and its mean diameter was determined to be 0.5 μm using a Laser Diffraction Particle Size Analyzer (MS2000MU, Malvern, Worcestershire, UK).

OCC fiber made in China was torn into pieces of about 25 × 25 mm in size and soaked in water for 12 h at room temperature, then slurried with a slusher (N-197VT, Adirondack Machine Corporation, USA) at a beating degree of 38°SR.

2.1.2. Classification of OCC Fibers. OCC fibers were classified by the Bauer-McNett Classifier according to the Tappi T 233 cm-06 standard: mesh of sieves: 30, 50, 100, and 200.

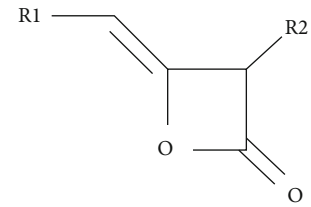

Figure 1: Chemical structure of AKD. R1 and R2 represent straight chains of lengths varying between 16 and 18 atoms.

2.1.3. Preparation of Handsheets. From a beaten pulp, a fiber suspension with a fiber consistency of 0.15% was prepared, and 0.1%, 0.2%, 0.3%, 0.4%, or 0.5% of AKD (based on dry weight of pulp) was added to the pulp suspensions with continuous stirring at 6,000 revolutions. The samples were identified as A1, A2, A3, A4, and A5 according to the AKD level employed in preparation. The control sample (no AKD added) was designated as Sample C. Then, the mixture was subjected to the preparation of handsheets with a basis weight of 80 g/m^2 on a handsheet machine (RK3-KWTjul, Vorchdorf, Austria) with the Rapid-Köthen method according to the GB/T 24214-2009 standard.

2.1.4. Scanning Electron Microscopy (SEM) Analysis. Morphologies of the handsheet surfaces were examined with a scanning electron microscope (SEM S3700, Hitachi, Japan) operating at an accelerating voltage of 15 kV. Before observation, the samples were coated with gold using a vacuum sputter coater.

2.1.5. Atomic Force Microscopy (AFM) Analysis. AFM images were recorded at room temperature on a MultiMode NanoScope IIIA (Digital Instruments, Santa Barbara, CA) operating in a tapping model.

2.1.6. Determination of Pore Distribution. A pore size distribution detector ASAP2010M (Micromeritics, USA) was used for the structural analyses of the fiber pores. High-purity N_2 was used as an adsorbate, and the adsorption-desorption of high-purity N_2 was determined at 77 K in a liquid nitrogen trap using a static volumetric method.

2.1.7. Contact Angle Measurements. Contact angles with distilled water on the paper were measured with an OCA Data Physics Instruments GmbH equipment.

2.1.8. Water Absorption Measurements. Water absorption of handsheets was measured according to the GB/T 1540-2002 standard.

All experiments were run in triplicate with the relative standard deviations (RSD) of about 5%.

3. Results and Discussion

3.1. SEM Imaging of Sized and Unsized Handsheets. Figure 2 presents the images of the surface morphology of unsized and sized handsheets. It was found that unsized fiber shows smooth image contours and crisp edges. As a result of AKD sizing, white membrane materials cover most of the surface

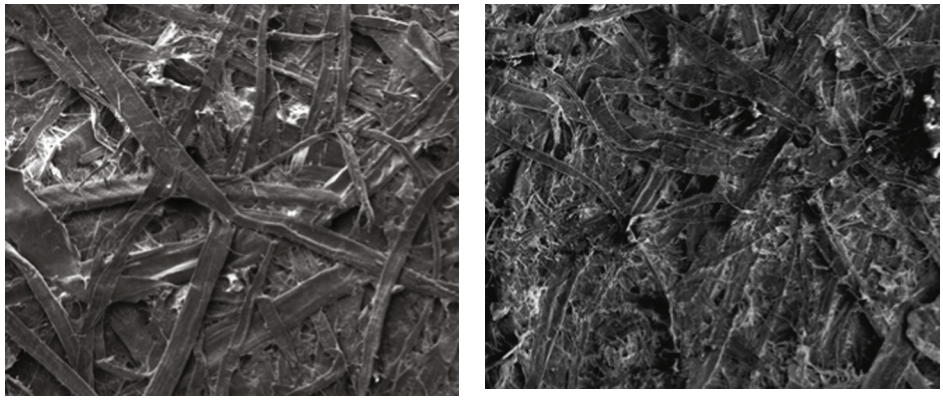

(a) (b)

Figure 2: SEM images of unsized and sized handsheets: (a) unsized handsheet and (b) sized handsheet (the dosage of AKD was 0.3%).

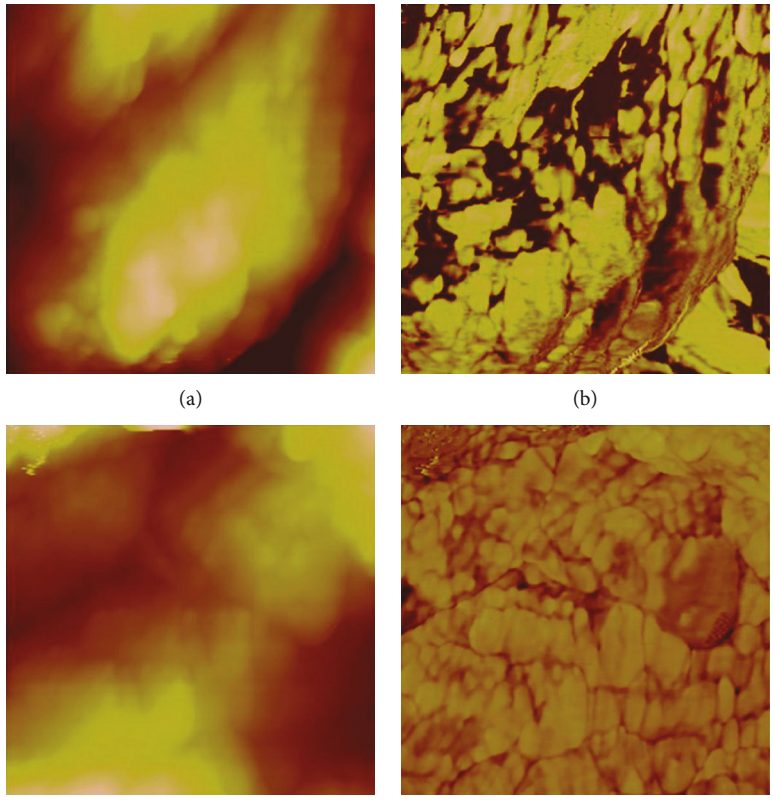

(a) (b)

(c) (d)

Figure 3: AFM images of unsized and sized handsheet: (a, c) unsized handsheet, (b, d) sized handsheet (the dosage of AKD was 0.3%), (a, b) height image, and (c, d) phase image.

and of gaps of fibers; the hydrophobic polymer film on the surface of the handsheet was formed [15].

3.2. AFM Imaging of Sized and Unsized Handsheets. Figure 3 shows the different AFM images of unsized and sized handsheet (scan range $1\,\mu m \times 1\,\mu m$). In Figure 3(a), many folds and grooves were found on the surface of the unsized handsheet, resulting in an increase in surface roughness (Rq = 27.949 nm). Compared with Figure 3(a), the surface roughness of the sized handsheet decreased because of the form of the AKD film on the surface of the handsheet, and the Rq has fallen by a shocking 54% down to 12.811 nm. Generally, the white and black areas in the phase image varied with the surface properties of samples reflecting all sorts of things, including soft and hard degree, elasticity, hydrophily, and adhesion. In a previous study, it was found that a dark area has a higher hydrophily; on the contrary, a bright area reflects strong hydrophobicity [16]. The dark area in Figure 3(d) indicated the existence of hydrophilic cellulose, and there are two reasons for the bright area in Figure 3(d): the hydrophobic film formed by AKD emulsion and amorphous lignin exist in OCC fibers.

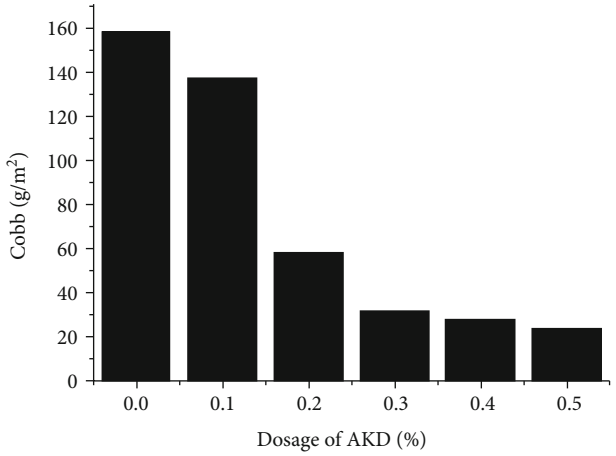

Figure 4: Changes of Cobb with different dosages of AKD.

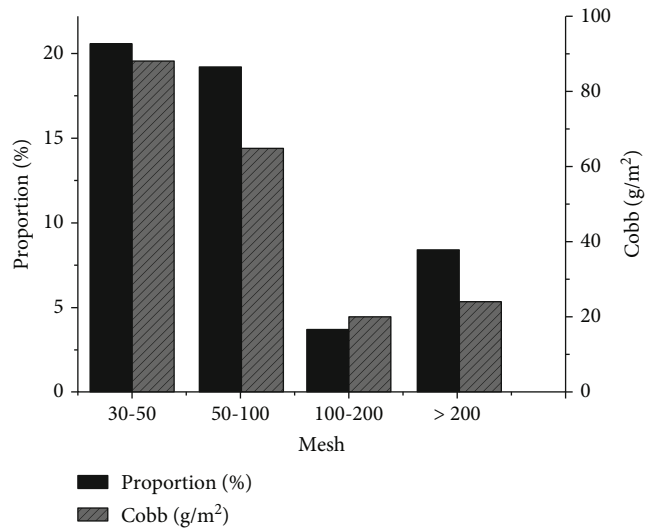

Figure 5: Effects of fiber length on sizing degree (the dosage of AKD was 0.3%).

3.3. Sizing Degree of Handsheets. The changes of Cobb with different dosages of AKD are shown in Figure 4. With AKD added, the hydrophobicity of the handsheets was dramatically increased. However, when the dosage of AKD reached to 0.3%, the hydrophobicity of handsheets cannot obviously be improved; the result prompts us that it is important to investigate the best dosage of AKD in a certain system. In engineering applications, excessive high dosage of AKD can lead to a high cost of production and slip phenomenon because of the lower friction coefficient of paper. More seriously, AKD particles in white water may be hydrolyzed to produce double alkyl ketone which can cause precipitation of the suspension and make a deposition problem on the net, blanket, dryer, and calendar rolls. This process ultimately results in papersheet breaks and holes or spots on the surface of papersheet. Therefore, an urgent problem faced by the researchers in papermaking is how to avoid excessive use of AKD emulsion.

3.4. Effects of Fiber Length on Sizing Degree. An interesting thing can be found in Figure 5 that the sizing degrees of OCC fibers have a significant relationship with their length; the length of fibers ranged from 100 to 200 meshes showing the best sizing performance. The main reason given for this is that uniform handsheets get higher a retention ratio of AKD particles. Though short fibers are helpful for AKD retention, AKD holds on fines' lose easily with the fines losing on wire section, but longer fiber length could be related to the reduction in the AKD particle retention ratio because of the cracks between long fibers. In a word, a suitable length is an important factor of improving the hydrophobic property of AKD sizing OCC fibers [17].

3.5. Effects of AKD Sizing on Contact Angles. Sharma et al. established the well-regarded Young's equation which defines the balances of forces caused by a wet drop on a dry surface [18]. Young's equation gives the following relation:

$$\cos\theta = \frac{\gamma_{sg} - \gamma_{sl}}{\gamma_{gl}} \quad (1)$$

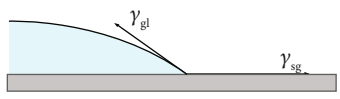

where γ_{sl}, γ_{gl}, and γ_{sg} are the interfacial tensions between the solid and liquid, the gas and liquid, and the solid and gas, respectively. The equilibrium contact angle is denoted by θ.

Figure 6 shows the comparison of Samples C and A2 at the time of contact (5 s). As can be seen in Figure 6(a), on the surface of unsized handsheet, the water contact angle approached zero, which indicated that unsized OCC fibers had good surface wettability. However, the fibers sized by 0.2% AKD (Sample A2) showed a good hydrophobic property at the time of contact (5 s). The contact angle is related to the contact time of aqueous solutions with paper during printing and other applications (contact time in milliseconds). Therefore, it is very important to study the relationship the contact angle and contact time [19].

Table 1 shows that with the increasing time, the contact angle of different samples showed a decreasing trend. Besides that, there is an obvious decrease in that of the group with lower sizing degree (Sample A1). In other words, a bigger contact angle shows better sizing stability.

3.6. Effects of AKD Sizing on Porous Structure of OCC Fiber. As shown in Figure 7, the effects of AKD sizing on the porous structure of OCC fibers were evaluated. The dosage of AKD used in the sizing procedure significantly influenced the pore characteristic of OCC fibers. It was found that the pore volume of fibers decreased with the increase in the dosage of AKD. The corresponding pore volume was at maximum when the average pore diameter was 2.4~3.0 nm. Compared with the control sample, the pore volume of fibers sized with 0.1% AKD decreased 4.3% when the average pore diameter was fixed at 2.4~3.0 nm. And when the usage of AKD increased to 0.3% and 0.5%, the pore volume decreased to 1.4% and 6.3% accordingly. The decrease in the pore volume of AKD-sized fiber indicated the penetration and deposition of dispersed particles of AKD in the fiber lumens.

Figure 6: Contact angle of unsized and AKD-sized papers (contact time = 5 s): (a) Sample C, no AKD added; (b) Sample A2, 0.2% AKD added.

Table 1: Contact angle behavior of different papers at different contact times.

Sample	5 s	10 s	20 s	30 s	40 s
A1	88.4°	86.2°	80.9°	76.5°	65.8°
A3	116.2°	115.3°	113.0°	112.5°	111.4°
A5	125.7°	120.8°	119.3°	118.2°	116.5°

A1: 0.1% AKD added; A3: 0.3% AKD added; A5: 0.5% AKD added.

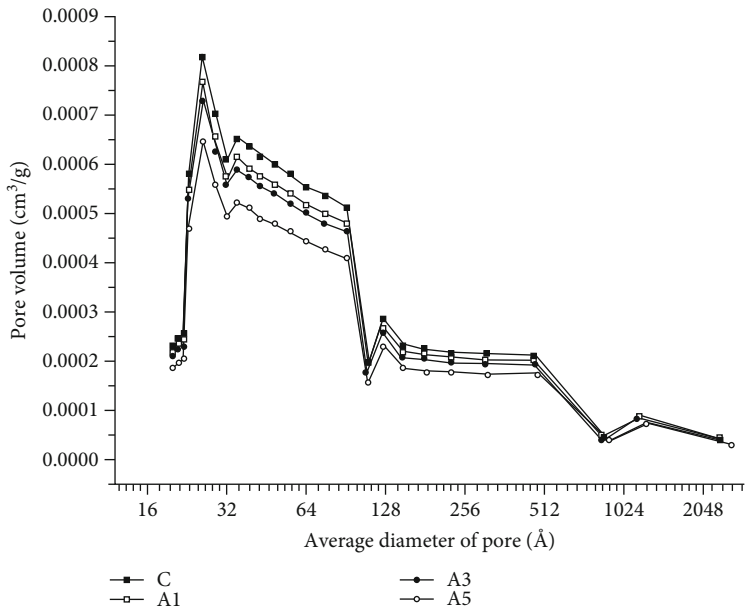

Figure 7: Pore size distribution of unsized and AKD-sized OCC fibers: C—no AKD added; A1—0.1% AKD added; A3—0.3% AKD added; A5—0.5% AKD added.

4. Conclusions

AKD is widely used as an internal sizing agent in papermaking to increase paper hydrophobicity. The smoothness of fiber further increased after AKD sizing. The length of fibers had obvious influence on the AKD sizing effect. In this paper, the length of fibers ranged from 100 to 200 meshes showing the best sizing performance. The surface morphology of OCC fibers is drastically changed after AKD sizing. The surface roughness of 0.3% AKD sizing OCC fibers decreased from 27.949 nm to 12.811 nm compared with the control sample. The pore volume of AKD-sized fiber decreased with the increase in the AKD emulsion additional level indicating the penetration and deposition of dispersed particles of AKD in the fiber lumens. The evidence suggests that AKD sizing will have important influence on not only the hydrophobic property but also the great factors of the hornification or swelling ability of OCC fibers during recycling.

Data Availability

The data used to support the findings of this study are included within the article.

Conflicts of Interest

The authors declare that they have no conflicts of interest.

Acknowledgments

The authors would like to acknowledge the support from the Key Research & Development Project of Zhejiang Province (Grant Nos. 2017C03045 and 2019C02042), State Key Laboratory of Pulp and Paper Engineering (Grant No. 201744), Zhejiang Provincial Collaborative Innovation Center of Agricultural Biological Resources Biochemical Manufacturing, Zhejiang Provincial Key Lab for Chem. & Bio. Processing Technology of Farm Products (Grant Nos. 2016KF0016 and 2016KF0201), Key Laboratory of Recycling and Eco-Treatment of Waste Biomass of Zhejiang Province (Grant Nos. 2016REWB12 and 2016REWB24), and Zhejiang Provincial Public Welfare Technology Research Project (Grant No. LGG19C160001).

References

[1] Y. Man, Y. Han, J. Li, M. Hong, and W. Zheng, "Life cycle energy consumption analysis and green manufacture evolution for the papermaking industry in China," *Green Chemistry*, vol. 21, no. 5, pp. 1011–1020, 2019.

[2] J. Q. Wan, J. Yang, Y. W. Ma, and Y. Wang, "Effects of the pulp preparation and papermaking processes on the properties of OCC fibers," *BioResource*, vol. 6, no. 2, pp. 1615–1630, 2011.

[3] D. E. Giacomozzi and O. Joutsimo, "Drying temperature and hornification of industrial never-dried pinus radiata pulps. 1. Strength, optical, and water holding properties," *BioResources*, vol. 10, no. 3, pp. 5791–5808, 2015.

[4] Y. Chen, Y. Wang, J. Wan, and Y. Ma, "Crystal and pore structure of wheat straw cellulose fiber during recycling," *Cellulose*, vol. 17, no. 2, pp. 329–338, 2010.

[5] R. Pönni, T. Vuorinen, and E. Kontturi, "Proposed nano-scale coalescence of cellulose in chemical pulp fibers during technical treatments," *BioResources*, vol. 7, no. 4, pp. 6077–6108, 2012.

[6] M. A. Hubbe, R. A. Venditti, and O. J. Rojas, "What happens to cellulosic fibers during papermaking and recycling? A review," *BioResources*, vol. 2, no. 4, pp. 739–788, 2007.

[7] A. Pantze, O. Karlsson, and U. Westermark, "Esterification of carboxylic acids on cellulosic material: solid state reactions," *Holzforschung*, vol. 62, no. 2, pp. 136–141, 2008.

[8] A. Idström, H. Brelid, M. Nydén, and L. Nordstierna, "CP/MAS ^{13}C NMR study of pulp hornification using nanocrystalline cellulose as a model system," *Carbohydrate Polymers*, vol. 92, no. 1, pp. 881–884, 2013.

[9] J. Q. Wan, Y. Wang, and Q. Xiao, "Effects of hemicellulose removal on cellulose fiber structure and recycling characteristics of eucalyptus pulp," *Bioresource Technology*, vol. 101, no. 12, pp. 4577–4583, 2010.

[10] Q. Miao, L. Huang, and L. Chen, "Advances in the control of dissolved and colloidal substances present in papermaking processes: a brief review," *BioResources*, vol. 8, no. 1, pp. 1431–1455, 2013.

[11] C. Quan, O. Werner, L. Wågberg, and C. Turner, "Generation of superhydrophobic paper surfaces by a rapidly expanding supercritical carbon dioxide–alkyl ketene dimer solution," *The Journal of Supercritical Fluids*, vol. 49, no. 1, pp. 117–124, 2009.

[12] M. Liang, B. He, and L. Zhao, "Hydrophobicity of lime sludge filled paper assisted by a cationic starch/CPAM/bentonite retention aids system," *BioResources*, vol. 9, no. 4, pp. 6440–6452, 2014.

[13] Y. Peng, B. He, L. Zhao, and G. Zhao, "Effect of preflocculation of lime mud $CaCO_3$ filler on AKD sizing efficiency," *BioResources*, vol. 9, no. 4, pp. 5976–5987, 2014.

[14] S. Kumar, V. S. Chauhan, and S. K. Chakrabarti, "Separation and analysis techniques for bound and unbound alkyl ketene dimer (AKD) in paper: a review," *Arabian Journal of Chemistry*, vol. 9, Supplement 2, pp. S1636–S1642, 2016.

[15] M. A. Hubbe, "Puzzling aspects of the hydrophobic sizing of paper and its inter-fiber bonding ability," *BioResources*, vol. 9, no. 4, pp. 5782-5783, 2014.

[16] L. M. Davies and P. J. Harris, "Atomic force microscopy of microfibrils in primary cell walls," *Planta*, vol. 217, no. 2, pp. 283–289, 2003.

[17] B. T. Yen, B. Yen, W. Shen, and I. Parker, "Effect of primary fines and surface charge of hardwood pulps on AKD sizing," *IPPTA Journal*, vol. 56, no. 1, pp. 30–34, 2003.

[18] A. Sharma, V. S. Chauhan, S. K. Chakrabarti, and R. Varadhan, "Control of degree of sizing through measurement of contact angle and surface energy," *IPPTA Journal*, vol. 22, no. 2, pp. 143–147, 2010.

[19] M. A. Hubbe, D. J. Gardner, and W. Shen, "Contact angles and wettability of cellulosic surfaces: a review of proposed mechanisms and test strategies," *BioResources*, vol. 10, no. 4, pp. 8657–8749, 2015.

Hindawi
Journal of Nanomaterials
Volume 2019, Article ID 6597494, 13 pages
https://doi.org/10.1155/2019/6597494

Research Article

Tailoring the Localization of Carbon Nanotubes and Ammonium Polyphosphate in Linear Low-Density Polyethylene/Nylon-6 Blends for Optimizing Their Flame Retardancy

Shuai Zhang, Chang Lu, Xi-ping Gao, Da-hu Yao, and Yu-xin He

Chemical Engineering & Pharmaceutics School, Henan University of Science and Technology, Luoyang 471003, China

Correspondence should be addressed to Chang Lu; luchang139@126.com

Received 27 February 2019; Accepted 18 August 2019; Published 30 September 2019

Guest Editor: Laijun Liu

Carbon nanotubes (CNTs) and ammonium polyphosphate (APP) was used to improve the flame retardancy of linear low-density polyethylene/nylon-6 (LLDPE/PA6) blends. It was observed that APP or CNTs tended to be dispersed in the PA6 phase of the blends when all components were melt-blended together. CNTs dispersed in the PA6 phase caused the decrease of flame retardancy. Different processing methods were used to tailor the localization of APP and CNTs in the blends. The results showed that the localization of CNTs or APP strongly influenced the flame retardancy of blends. APP-incorporated CNTs had antagonism in blends with APP localized in the LLDPE phase and CNTs in the PA6 or LLDPE phases. A synergism between APP and CNTs was exhibited only in blend with the localization of APP in the PA6 phase and CNTs in the LLDPE phase. SEM observation showed that the residual char layer in blends with poor flame retardancy was either discontinuous or continuous but porous. A continuous and compact-residue char layer was observed in blends with excellent flame retardancy. Different morphologies of the residual char layer could be attributed to the difference of residual char mass and network structure.

1. Introduction

The application of carbon nanotubes (CNTs) in flame-retarded polymers was first reported by Kashiwagi et al. in 2002, attracting significant recent research interest because it affords the enhancement of thermal stability and reduction in heat release rate in a polymer matrix through the use of low loadings [1–6]. The use of CNTs as a flame retardant is also possible, primarily through the formation of a solid, jammed network structure consisting of CNTs and tangled polymer chains. Such a network can form a continuous protective layer during combustion to hinder the diffusion of oxygen and heat and slow the release of combustion products [7, 8].

The addition of CNTs into polymers primarily decreases their peak heat release rate (PHRR), which is a flame-retardant property obtained from a typical cone calorimeter test. CNTs did not exhibit consistent enhancement of flame retardancy when the limiting oxygen index (LOI) and standard UL 94 tests were used to evaluate the flame retardancy [9, 10]. Therefore, CNTs were always employed as a synergist of flame retardants to improve the flame retardancy of polymers or polymer blends.

Intumescent flame-retardant additives (IFR), with characters of nonhalogen and low poison, have become a hot point in a flame retardant area [11–14]. During combustion, IFR can form a foamy, charred layer on the surface of the polymer matrix to improve its flame retardancy [15–17]. One of the drawbacks of IFR is relatively low flame-retardant efficiency. The synergistic effects of CNTs with IFR are expected to optimize the flame-retardant efficiency of IFR because both function according to a condensed flame-retardant mechanism. Although synergistic effects between IFRs and CNTs were reported [18–21], Du and Fang found that the introduction of CNTs deteriorated flame retardancy [9]. The conflicting results indicate that the combined effect of IFR and CNTs on flame retardancy deserved further research.

Polymer blends are typically comprised of a two-phase structure. CNTs or IFR may localize in one of the two phases

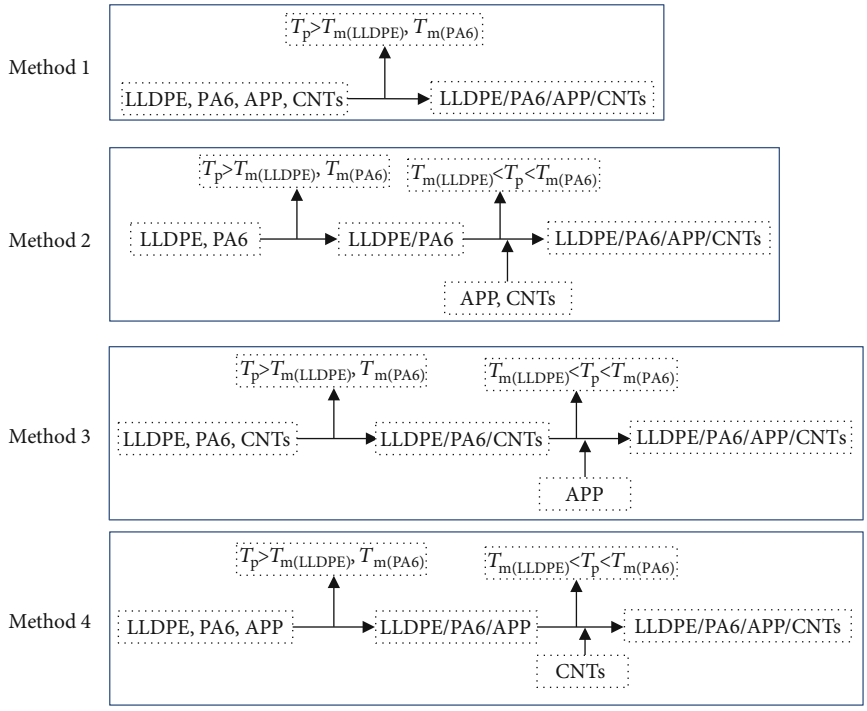

Figure 1: Four processing methods for controlling APP and CNT distribution in LLDPE/PA6 blends. Method 1: all the components were melt-blended at 230°C. The processing temperature was higher than the melt temperature of LLDPE and PA6. Method 2: the blends were prepared through two steps. LLDPE/PA6 blend was prepared at 230°C firstly, and then LLDPE/PA6 blend was blended with APP and CNTs at 160°C. In the second step, the processing temperature was lower than the melt temperature of PA6. Method 3: the blends were prepared through two steps. LLDPE/PA6/CNT blend was prepared at 230°C firstly, and then LLDPE/PA6/CNT blend was blended with APP at 160°C. In the second step, the processing temperature was lower than the melt temperature of PA6. Method 4: the blends were prepared through two steps. LLDPE/PA6/APP blend was prepared at 230°C firstly, and then LLDPE/PA6/APP blend was blended with CNTs at 160°C. In the second step, the processing temperature was lower than the melt temperature of PA6.

in polymer blends. Although the effect of IFR and CNT localization on blend flame retardancy has not been reported, some of the studies found that clay or IFR localization in polymer blends is critical in improving flame retardancy. Lu et al. [22, 23] and Pack et al. [24] found that clay tended to segregate into one of the phases and the blend morphology affected the flame retardancy greatly. Pack et al. [25, 26] found that the synergistic effects between flame retardant and clay in the blends with clay localization at the interface were more efficient than in the polymers. Moreover, it was reported that tailoring the localization of clay or IFR was used for optimizing the flame retardancy of polymer blends [27–30]. Lu et al. [27, 28] tailored clay localization from the PA6 phase to the interface and improved the flame retardancy of PS/PA6. In LLDPE/PA6 blends, tailoring the localization of clay from the PA6 phase to the LLDPE phase caused a remarkable improvement of flame retardancy. Jin et al. [29] found the selective dispersion of IFR in polypropylene blends and compatibilizer can be applied to adjust the dispersion of IFR in the blends, causing the improvement of flame retardancy.

The results that suitable localization of clay or IFR in polymer blends can improve their synergistic effects indicated that tailoring the localization of CNTs and IFR may be also used for optimizing their flame retardancy in polymer blends. Therefore, CNTs and ammonium polyphosphate (APP) were employed to improve the flame retardancy of LLDPE/PA6. The method [28] that we had used to tailor IFR and clay dispersion in polymer blends was also employed to prepare blends with different APP and CNT localization. The flame retardancy of the blends with different APP and CNT localization was investigated.

2. Experimental

2.1. Materials. Linear low-density polyethylene (LL6201XR) was supplied by ExxonMobil Corp. Polyamide-6 (PA6) (33500) was supplied by Xinhui Meida-DSM Nylon Chips Co., Ltd. Ammonium polyphosphate ($(NH_4PO_3)_n$, $n = 1500$, purity level > 90%) was supplied by Zhejiang Longyou Gede Chemical Factory (China). The CNTs were obtained from Chengdu Organic Chemical Co., Ltd. They were multiwalled with hydroxyl groups providing surface functionality.

2.2. Preparation of Composites. A corotating twin-screw extruder was used to melt-blend the blends, and an injection-molding machine was employed to shape the blends. Before processing, the components and blends were dried at 80°C for 24 h to remove any moisture. We followed the methods [28] to control the localization of APP and CNTs in LLDPE/PA6 blends, as shown in Figure 1. The formula and code of the blends are shown in Table 1.

Table 1: Formulation of blends.

Sample code	LLDPE	PA6	APP	CNTs	Preparing method
Blends	80	20	0	0	
Blends/CNTs	80	20	0	0.5	
D1	60	15	25	0	Method 1
M1	60	15	25	0.5	Method 1
M2	60	15	25	0.5	Method 2
M3	60	15	25	0.5	Method 3
M4	60	15	25	0.5	Method 4

2.3. Measurement and Characterization. The values of the LOI were tested in accordance with the standard oxygen index test (ASTM D2863-77). The vertical burning grade was evaluated in accordance with the UL 94 test (ASTM D635-77).

A cone calorimeter (Fire Testing Technology Ltd, United Kingdom) was employed to test the flammability of samples ($100 \times 100 \times 3$ mm). The external heat flux was 35 kW/m^2.

The blend of LLDPE/PA6/CNTs (80/20/0.5) was cryogenically cut at -120°C to obtain the slice with the thickness of 70 nm. The slice was examined by TEM (FEI TECNAI-G20) to observe the dispersion of CNTs at an acceleration voltage of 300 kV.

The thermal degradation of the samples was characterized by thermogravimetric analysis (NETZSCH, STA409PC). The test was implemented using a heating rate of 20°C/min in nitrogen.

The morphology of the fractured specimen surface and char residue was observed by SEM (JEOL 6301F). The samples were immersed in liquid nitrogen for 2 h and then broken quickly to obtain the fractured specimen. Char residue was obtained from the samples after vertical flammability tests. The samples were coated with a gold layer before examination. The elemental compositions of fractured specimen surface were measured using an energy-dispersive spectrometry (EDS) analyzer.

The rheological performance of the samples was measured using an ARES rheometer (AR 1500ex) in dynamic mode, on a parallel-plate geometry with a diameter of 25 mm and a gap of ~1 mm. The measurement temperature was 225°C and frequencies ranged from 100 to 0.01 rad/s.

3. Results and Discussion

3.1. Localization of APP and CNTs in LLDPE/PA6 Blends. The blend of LLDPE/PA6/CNTs (80/20/0.5) was melt-blended at 230°C, and the localization of CNTs in the blend was investigated by TEM (Figure 2). From Figure 2(a), the CNTs were observed in the dispersed PA6 phase with no CNTs in the LLDPE matrix. The enlarged view of Figure 2(b) shows that the aggregation of CNTs occurred due to their large specific surface energy. In the blends, it has been known that CNTs tended to disperse in the phase with low viscosity [31]. As long as the viscosities of two polymers are comparable, affinity of CNTs for each component is the main factor determining uneven distribution of CNTs in polymer blends. The CNTs used in this research were multi-walled with hydroxyl groups providing surface functionality, indicating higher affinity of CNTs for PA6 than for LLDPE. Moreover, lower viscosity of PA6 than LLDPE was also benefited for the localization of CNTs in the PA6 phase. Therefore, the combined factors caused that CNTs were dispersed in the PA6 phase rather than in the LLDPE phase.

Samples of LLDPE/PA6/APP (60/15/25) were prepared by two processing methods, in which LLDPE/PA6 blends were melt-blended with CNTs at 230°C or 160°C, respectively. The samples were characterized by SEM-EDS to investigate the dispersion of APP in the blends. The SEM-EDS results are shown in Figure 3. For the blends prepared at 160°C, the dispersed phase consisted of irregular particles and spherical voids (Figure 3(a)). The P content in the irregular particles was 20.36 wt%, indicating that the irregular particles were APP. For the blends prepared at 230°C, the spherical particles were observed, as shown in Figure 3(b). The EDS results of Figure 3(b) showed that the P content in the spherical particles or continuous phase was 2.27 wt% or 1.27 wt%, respectively. The results indicated that irregular APP particles were coated by the PA6 phase, causing the spherical particles observed and low P contents detected at the surface of spherical particles.

The melt temperature of PA6 is about 220°C. Therefore, the PA6 phase was melted when APP was processed with LLDPE/PA6 at 230°C. Correspondingly, the PA6 phase did not melt when APP was processed with LLDPE/PA6 at 160°C. Therefore, SEM-EDS results indicated that APP was coated by the melted PA6 phase when APP were melt-blended with LLDPE/PA6 at 230°C. While APP were melt-blended with LLDPE/PA6 at 160°C, APP was obligated to localize at the LLDPE phase due to that the PA6 phase was not melted.

The spontaneous dispersion of APP or CNTs in the PA6 phase of the LLDPE/PA6 blends prepared at 230°C indicated that the localization of APP and CNTs in the blends can be tailored by the methods employed in this paper. The blends with the localization of APP and CNTs in the PA6 phase can be obtained when all the components were melt-blended at 230°C (method 1). For method 2, when LLDPE/PA6 blend was blended with APP and CNTs at 160°C, APP and CNTs were obligated to localize at the LLDPE phase due to that the PA6 phase was not melted. For method 3, CNTs were localized in the PA6 phase due to that CNTs were melt-blended with LLDPE and PA6 at 230°C in the first step. Meanwhile, APP was obligated to localize in the LLDPE phase because APP was melt-blended with LLDPE/PA6/CNTs at 160°C in the second step. In the method 4, LLDPE/PA6/APP blend was prepared at 230°C firstly, and then LLDPE/PA6/APP blend was blended with CNTs at 160°C. Therefore, the blends with the dispersion of APP in the PA6 phase and CNTs in the LLDPE phase can be prepared.

3.2. Flame Retardancy of LLDPE/PA6/APP/CNTs. The flame retardancy of the blends was investigated by LOI and horizontal burning rating (UL 94) tests, as shown in Table 2. The results showed that addition of CNTs, LOI value

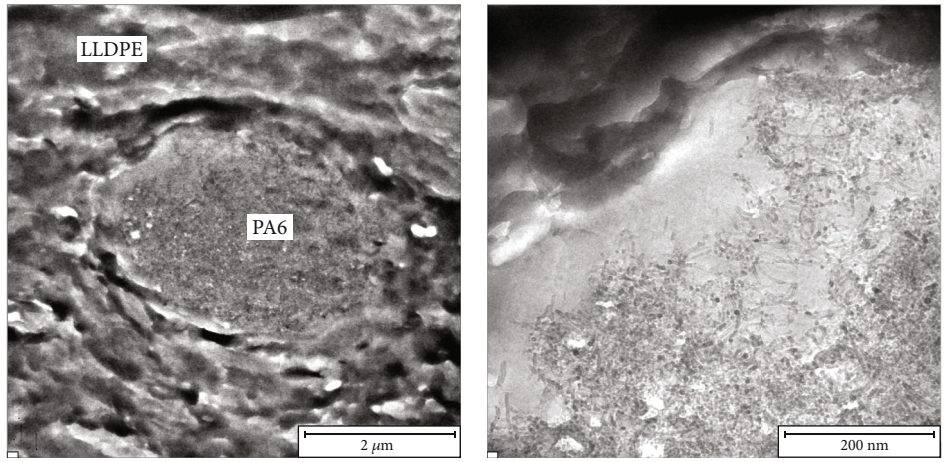

(a) (b)

Figure 2: TEM of (a) LLDPE/PA6/CNTs prepared above the melt temperature of LLDPE and PA6 and (b) enlarged view.

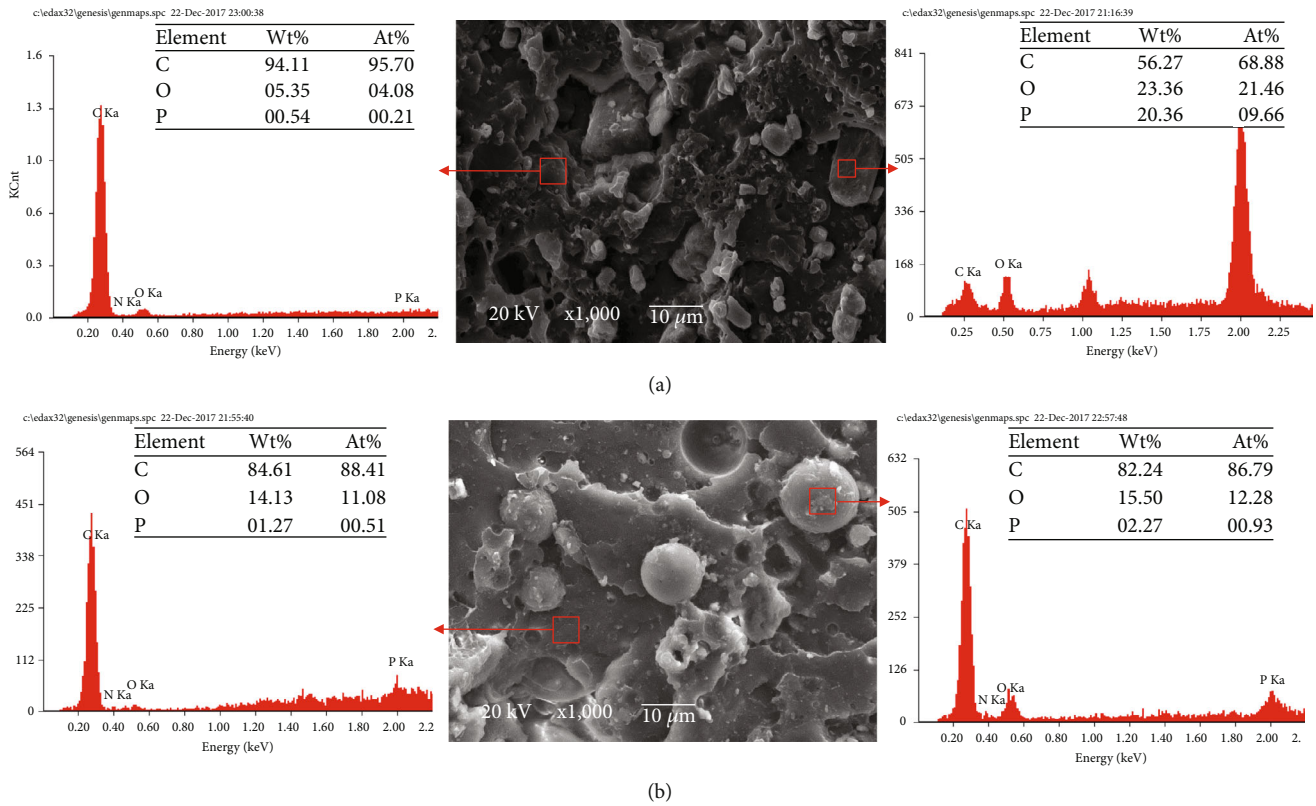

Figure 3: SEM-EDS of LLDPE/PA6/APP prepared by different methods. (a) APP blended with LLDPE/PA6 at 160°C, (b) APP blended with LLDPE/PA6 at 230°C.

increased slightly, indicating that CNTs were not an effective flame retardant towards LLDPE/PA6. The presence of APP increased the LOI value of LLDPE/PA6 sharply, as the value was raised from 19.8 to 25.5.

The flame retardancy of blends with different CNTs and APP localization is also shown in Table 2. The LOI value of D1 was slightly higher than that of M1~3, and all of the samples failed the vertical UL 94 test by burning completely. The highest LOI value (LOI = 28.3) was observed in M4, and the samples reached the UL 94 V-1 grade. The results show that the localization of CNTs and APP in the LLDPE/PA6/APP/CNT blends significantly affects flame retardancy. The localization of CNTs and APP in the PA6 phase, CNTs and APP in the LLDPE phase, or CNTs in the PA6 phase and APP in the LLDPE phase was unfavorable to improve flame retardancy. The localization of CNTs in the LLDPE phase and APP in the PA6 phase favorably improved flame retardancy.

Table 2: Flammability characteristics of blends.

Samples	Flammability		ΔLOI
	LOI (%)	UL 94 rating	
Blends	19.8	No rating	
Blends/CNTs	20.4	No rating	
D1	25.5	No rating	
M1	24.8	No rating	-1.3
M2	25.5	No rating	-0.6
M3	24.8	No rating	-1.3
M4	28.3	V-1	2.2

The comparison of L_{AB} and L_{A+B} can be employed to judge the synergism of two kinds of flame retardant according to the formula of $L_{A+B} = L_A + L_B\text{-}L_P$. L_{AB} is the LOI value of the composites containing two kinds of flame retardant. L_A or L_B is the LOI value of the composites with flame retardant used alone, L_P is the LOI value of polymer matrix. Two kinds of flame retardant have synergism only when the result of $L_{AB} > L_{A+B}$ is exhibited. The result of $L_{AB} < L_{A+B}$ indicates the antagonism of two kinds of flame retardant [29].

The ΔLOI ($\Delta\text{LOI} = L_{AB}\text{-}L_{A+B}$) values of LLDPE/-PA6/APP/CNT blends with different APP and CNT localization are also listed in Table 2. The results showed that ΔLOI > 0 in M4 and ΔLOI < 0 in M1~3, respectively. Therefore, APP-incorporated CNTs had synergism in blends with the localization of APP in the PA6 phase and CNTs in the LLDPE phase. An antagonism between APP and CNTs was exhibited in blends with other localizations of APP and CNTs.

3.3. Morphology of Residual Char. An intumescent flame-retardant primarily plays a role in the condensed phase by forming porous carbonaceous char, which helps to provide effective fire retardation [13, 32]. The characterization of the morphologies of residue char enables an understanding of the relationship between APP and CNT localization and flame retardancy. Photographs of the residual char after cone calorimeter tests are shown in Figure 4. APP localization in the blends exhibits a remarkable influence on the appearance of the residual char. In the samples where APP was localized in the PA6 phase (D1, M1, and M4), the sample holders were covered by a continuous residual char layer. In samples where APP was localized in the LLDPE phases (M2, M3), aluminum foil covering the sample holder was exposed, and residual char accumulated around its inner wall, indicating that discontinuous residual char formed in these samples. Discontinuous residual char provided poor protection on the substrate, causing poor flame retardancy shown for M2 and M3.

For blends with continuous residual char, the flame-retardant properties of M1 and D1 were lower than that of M4. In order to understand this, SEM was used to investigate the microstructure of the residual char, as shown in Figure 5. The morphologies of the residual chars in D1, M1, and M4 are entirely different. A continuous residual char with abundant voids is observed in D1. Residual chars in M1 were made of spherical cokes and contained abundant voids. Meanwhile, a tight and compact intumescent char was observed in M4. Compared with a char residue with many voids, a compact residue char was more effective in heat insulation and impeding the release of flammable volatiles, which were benefited for the improvement of flame retardancy. Therefore, good flame retardancy in M4 can be attributed to the formation of compact residue char.

3.4. Residual Char Mass. TGA and cone calorimetry were used to investigate the residual char mass of LLDPE/-PA6/APP/CNT blends. The residual char mass curves from TGA and cone calorimetry are corresponding to oxygen-free thermal degradation and oxygen combustion, respectively. The curves of residual char mass obtained from the cone calorimeter test are shown in Figure 6. The residual char mass of LLDPE/PA6/APP/CNT blends with APP localized in the PA6 phase (M1 and M4) was higher than that when APP was localized in the LLDPE phase (M2 and M3), indicating that localization of APP in PA6 was favored for improving the residual char mass. For blends with the same APP localization, residual char mass in blends with CNTs localized in the LLDPE phase was higher than that of CNTs in the PA6 phase. For example, the residual char mass of M4 was higher than that of M1, and M2 higher than M3. The results obtained from cone calorimetry show that the localization of APP in the PA6 phase and CNTs in the LLDPE phase can promote charring during combustion, resulting in a high residue char mass.

The TGA curves for LLDPE/PA6/APP and LLDPE/-PA6/APP/CNTs are shown in Figure 7. They show two significant slope changes, proving a two-step process of the degradation. The degradation occurred within the temperature range of 280–360°C was APP thermal degradation and its reaction with PA6 [33, 34]. In this step, the reaction of APP and PA6 produced the intumescent char. It was observed that the degradation rate of LLDPE/PA6/APP/CNT was higher than that of LLDPE/PA6/APP. The results suggested that the intumescent char of LLDPE/PA6/APP was more conductive to delay thermal degradation, resulting in improved thermal stability.

The second step began at approximately 360°C, and degradation curves of different blends were overlapped, indicating similar thermal degradation process. As above, the thermal stability shows that the APP and CNT dispersion in blends had a little influence on the degradation of the LLDPE and PA6 at this step. However, APP and CNT dispersion in blends did have a major impact on char residue mass. The char residue mass in blends with APP dispersed in the PA6 phase (M1, M4) was higher than the blends with APP dispersed in the LLDPE phase (M2, M3). The comparison between M1 and M3 or between M2 and M4 shows that the CNT localization in the LLDPE phase is more advantageous to increasing residual char mass than in the PA6 phase.

The results of TGA and cone calorimetry show that APP localization in the PA6 phase or CNTs in the LLDPE phase are both beneficial in promoting charring. Compared to blends with APP dispersed in the PA6 phase, a lower residual

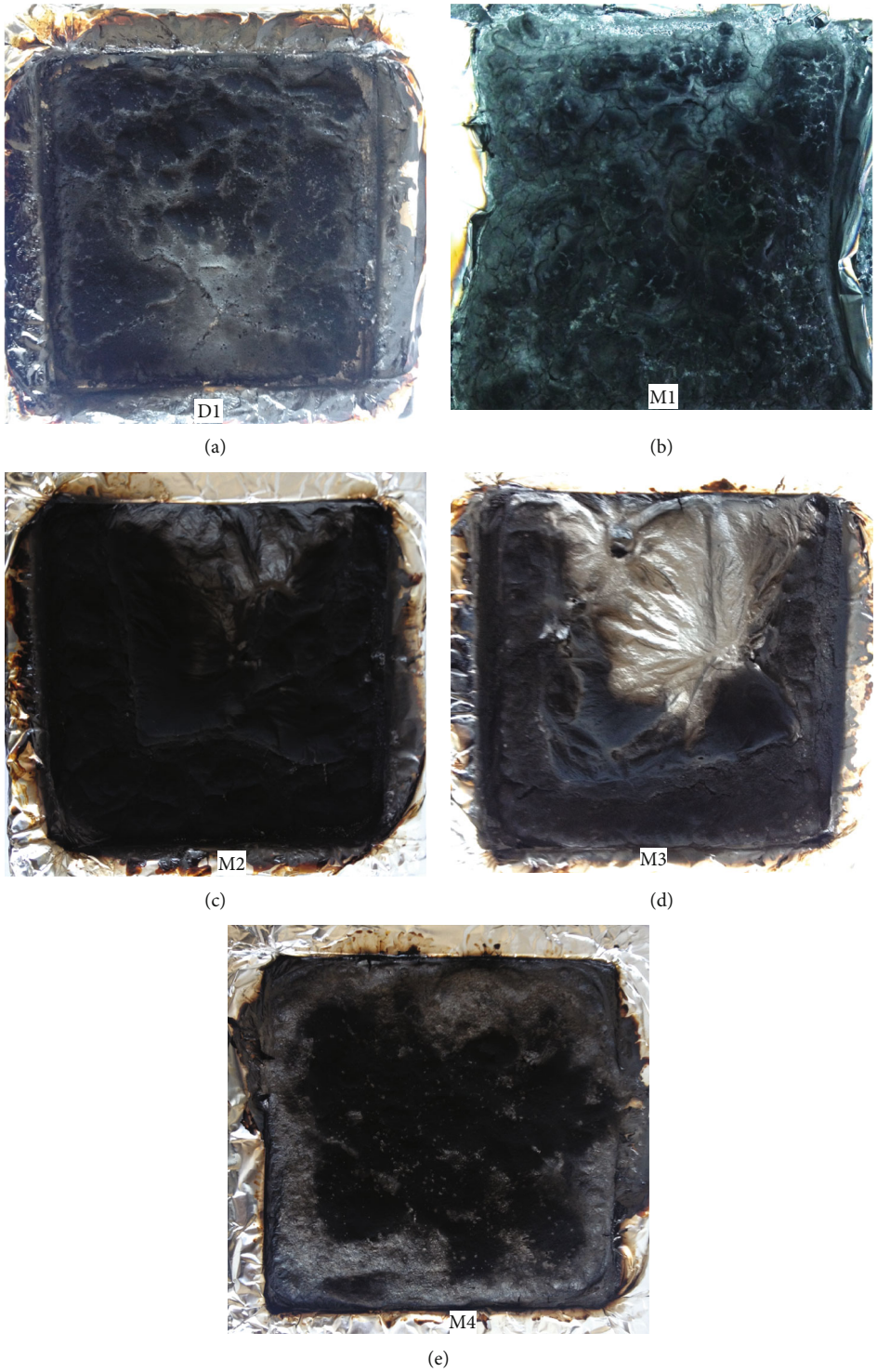

Figure 4: The photos of the aspect of the crust of blends after a cone calorimeter test.

char mass was exhibited in blends with APP dispersed in the LLDPE phase regardless of where the CNTs were localized. These results indicate that APP localization in the PA6 phase was more conductive to improve residual char mass than the localization of CNTs in the LLDPE phase. The reaction of APP and PA6 produced the intumescent char. For blends with APP localized in the PA6 phase, APP and PA6 can contact each other, benefitting their reaction and causing the improvement of char residue mass. For blends with APP dispersed in the LLDPE phase, APP and PA6 were insulated from contact by the LLDPE. The isolation between APP and PA6 in blends prevented their interaction, causing a low char residue mass.

3.5. Rheological Behavior. CNTs can form a network structure to enhance the thermal stability of polymer matrix,

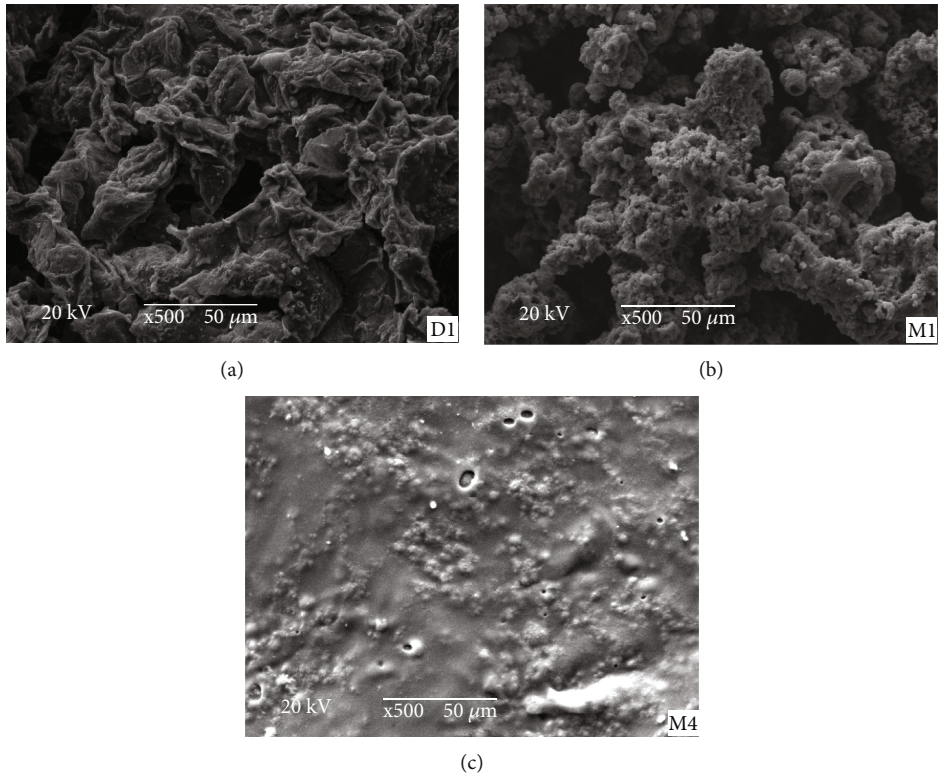

Figure 5: SEM of intumescent char residue for LLDPE/PA6/APP and LLDPE/PA6/APP/CNTs after vertical flammability tests.

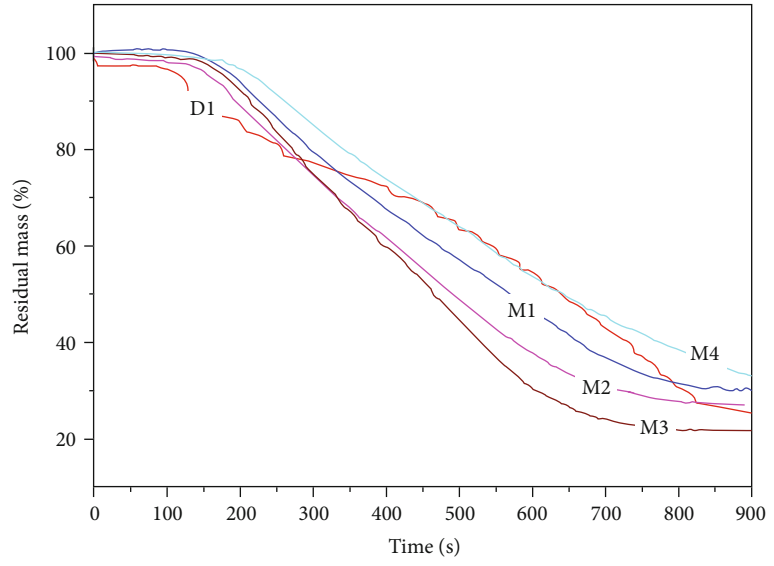

Figure 6: Residual mass curves of LLDPE/PA6/APP and LLDPE/PA6/APP/CNTs prepared by different processing methods.

causing the reduction of heat release rate and the improvement of flame retardancy [5, 7, 8]. A high residual char mass in blends with CNTs dispersed in LLDPE rather than in PA6 may be related to a CNT network structure, and so a rheological test was used to investigate it.

The relationship between storage modulus (G') and frequency (ω) in LLDPE/PA6/APP/CNTs with different APP and CNT localization is shown in Figure 8. For the blends with CNTs localized in the PA6 phase (M1, M3), G' was decreased as the reduction of ω at low frequencies. The results indicated that the blends exhibited Newtonian liquid behavior at low frequencies, suggesting that CNTs cannot form networks. However, in blends with CNT localization in the LLDPE phase (M2, M3), an ideal Hookean solid was

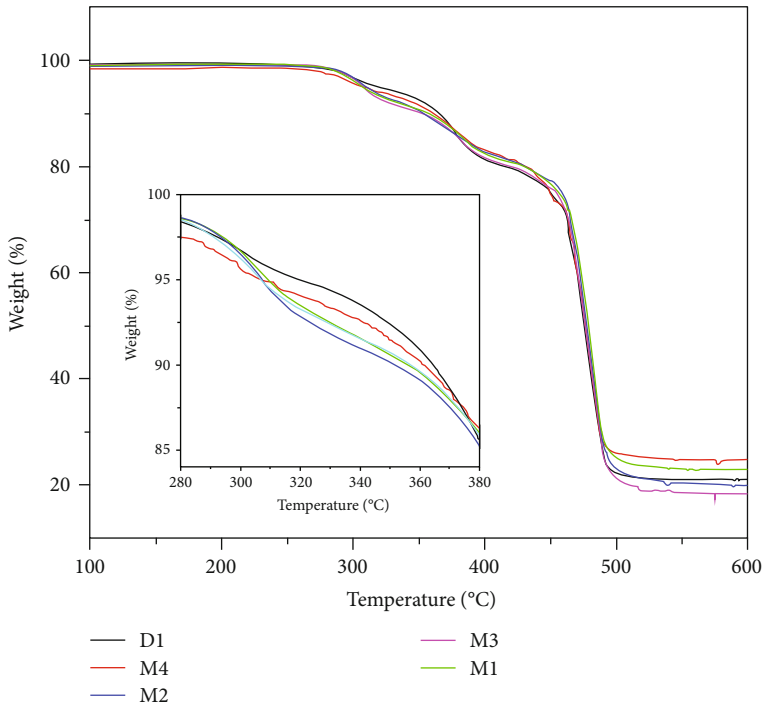

Figure 7: TGA curves of LLDPE/PA6/APP and LLDPE/PA6/APP/CNTs prepared by different processing methods.

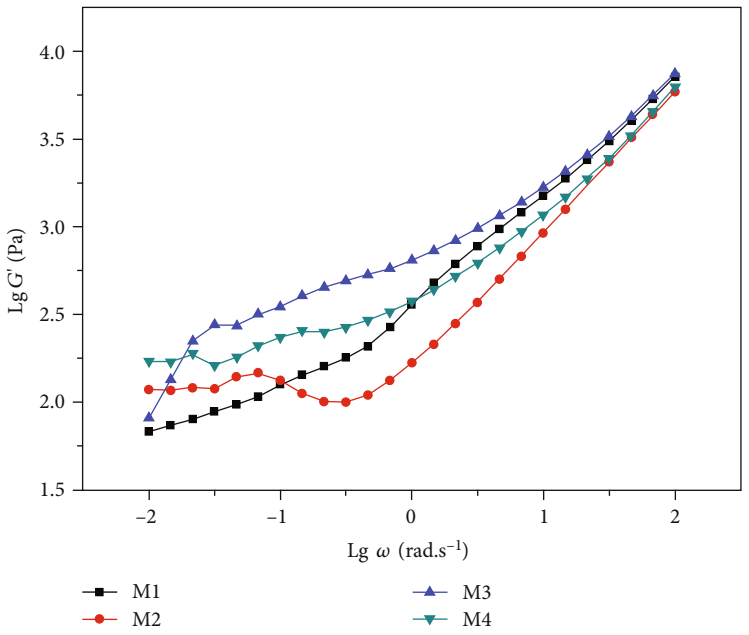

Figure 8: Storage modulus (G') of LLDPE/PA6/APP/CNTs prepared by different processing methods versus frequency (ω).

observed due to that G' became nearly constant as the reduction of ω at low frequencies, indicating the network structure of CNTs formed in these blends.

The results of Figure 8 indicate that localization of CNTs in LLDPE was more favorable to the forming network structure than that in the PA6 phase. SEM results showed that the PA6 phase was the dispersed phase and the LLDPE phase was the continuous phase. The heterogeneous dispersion of CNTs in blends caused CNTs to form a network structure only in the PA6 or the LLDPE phase, respectively. For blends with CNTs dispersed in LLDPE, CNTs can form networks in the continuous LLDPE phase, causing a network structure itself to be continuous and therefore allow it to be detected in blends. For blends with CNTs dispersed in the PA6 phase, the network structure was continuous in the PA6 phase but discontinuous in whole samples. As a result, the network

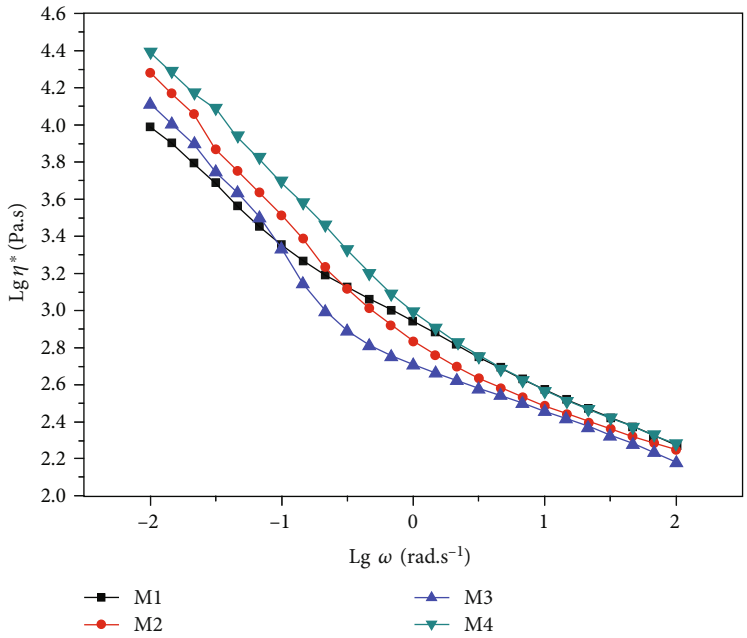

Figure 9: Complex viscosity (η^*) of LLDPE/PA6/APP/CNTs prepared by different processing methods versus frequency (ω).

structure in the matrix could not be detected. It can be observed that the residual char mass in continuous blends was higher than in blends with discontinuous network structure. Therefore, it can be concluded that continuous network structure benefitted from improved residual char mass.

The effect of CNT and APP localization in the LLDPE/-PA6/APP/CNT blends on complex viscosities (η^*) is shown in Figure 9. The increase of ω caused the decrease of η^*, indicating shear thinning behaviors. Although the components' proportion in blends was kept consistent, the η^* at low frequencies was quite different. High complex viscosities were observed in blends with CNTs localized in the continuous LLDPE phase (M2, M4). In general, the formation of a CNT network structure can increase melt viscosity. Therefore, high complex viscosity in blends of M2 and M4 could be attributed to a continuous network structure. In the blends with CNTs localized instead in the PA6 phase (M1, M3), the network structure was discontinuous in the matrix even though the CNTs also formed a network structure in the dispersed PA6 phase, with the CNTs' network structure showing a weak influence on melt viscosity.

High viscosity of blends can hinder the penetration of O_2 and combustible gas [16], enhances the antidripping property, causing the improvement of flame retardancy. Therefore, the synergistic effect between CNTs and APP in blends with APP localization in the PA6 phase may be related to its high melt viscosity.

3.6. Cone Calorimeter. The cone calorimeter was employed to investigate the combustion process of LLDPE/PA6/APP and LLDPE/PA6/APP/CNTs, as shown in Figure 10 and Table 3. Compared with LLDPE/PA6 composites, the time to ignition (TTi) increases after CNTs were added. This is due to that the good thermal conductivity of carbon nanotubes can effectively transfer heat to the interior of the composites, causing the increase of TTi. The lowest values of peak HHR and maximum of the average rate of heat emission (MAHRE) were exhibited in M4, compared with D1, M1, M2, and M3. The difference of the THR values between D1 and M4 was small and lower than that of M1, M2, and M3. The results indicated the best flame retardancy was exhibited in M4, which was in accordance with the results of LOI and UL 94.

In Figure 10, the HRR curves show a double PHRR and double peaks are also exhibited in the smoke production rate (SPR) curves, indicating two processes of combustion. According to other studies [12, 32, 35], the first peak or the second peak is ascribed to the ignition and the formation of an intumescent shield and is assigned to the destruction of the intumescent shield and the formation of a carbonaceous residue. It was observed that the first PHRR value of LLDPE/-PA6/APP was lower than that of LLDPE/PA6/APP/CNT blends prepared by different methods. TG results also showed that the expanded protective shield of LLDPE/-PA6/APP/CNTs provided weaker protection on matrix than that of LLDPE/PA6/APP in the initial degradation period. The results indicated that CNTs went against the formation of expanded protective shield. High HHR in LLDPE/-PA6/APP/CNTs suggested that the samples burned more violently, causing high SPR. The second PHHR value of D1 was lower than that of M2 and M3 and higher than that of M1 and M4. Meanwhile, the SPR values of M1 and M4 were lower than that of D1 after 600 s. The char residue of M1 and M4 was higher than that of D1, as shown in Figures 6 and 7. Therefore, the results indicated that CNTs can improve the carbonaceous residue only when APP is localized in the PA6 phase of blends, causing lower PHHR and SPR.

For the LLDPE/PA6/APP blend (D1), dispersed PA6 particles acted as "flame-retardant particles" because of the

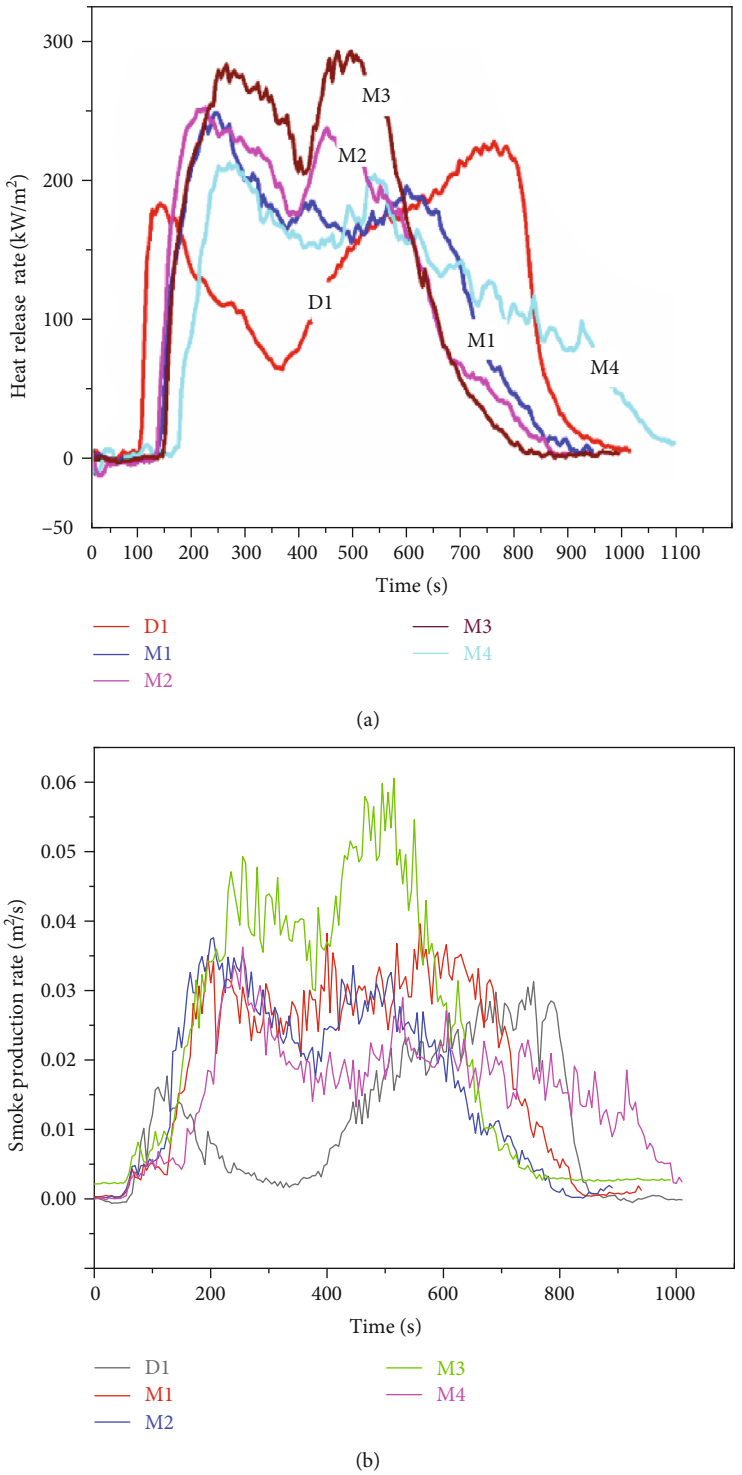

Figure 10: Heat release rate curves (a) and smoke production rate curves (b) of LLDPE/PA6/APP and LLDPE/PA6/APP/CNTs prepared by different processing methods.

flame-retardant properties of dispersed APP in the PA6 phase. In the first combustion process, the decomposition of APP and interaction of APP and PA6 transformed "flame-retardant particles" into charred particles. NH_3 produced by the decomposition of APP expanded charred particles until they joined each other to form a continuous residual char. With the development of the combustion process (the second process), the accumulation of pyrolysis gas in the interior of the material caused the rupture of the superficial intumescent char, resulting in the formation of residual char with abundant voids, as shown in Figure 5(a).

When APP and CNTs were both localized in the PA6 phase (M1), the first or second PHRR and SPR values were higher or lower than that of LLDPE/PA6/APP, respectively.

Table 3: Cone calorimeter data of blends.

Sample code	Peak HRR (kW/m^2)	THR (MJ/m^2)	MAHRE (kW/m^2)	Time to ignition (s)
D1	222.15	114.78	132.37	84
M1	242.00	110.92	144.65	116
M2	245.29	111.99	160.15	117
M3	284.77	122.70	182.32	128
M4	206.80	116.26	123.97	158

In this blend, dispersed PA6 particles also acted as "flame-retardant particles" due to their localization. CNTs sharply increased the melt viscosity of the PA6 particles due to the formation of a network structure in the PA6 phase. In the first combustion process, "flame-retardant particles" were transformed into charred particles. However, high melt viscosity of the PA6 phase restrained the coalescence of intumescent charred particles to form a continuous char layer, resulting in a high PHRR value in the first combustion process. The morphology of spherical cokes formed in the residual char also indicates the inhibition of CNTs in aggregating into charred particles. Spherical cokes cannot provide effective protection for the matrix during the combustion, resulting in poor flame retardancy exhibited in this blend.

Good flame retardancy was exhibited in the blend with APP localized in the PA6 phase and with CNTs in the LLDPE phase (M4). The results attributed the network structure of CNTs formed in the continuous LLDPE phase and the localization of APP in the PA6 phase. In the initial combustion process, interaction of APP and PA6 formed charred particles. Network structure increased the melt viscosity of the LLDPE and delayed the aggregation of charred particles, resulting in its initial PHRR values being higher than that of LLDPE/PA6/APP in its initial stage. As combustion developed, CNTs would perform three beneficial roles. The localization of the CNTs in LLDPE improved the residual char mass, causing a thick char layer. Meanwhile, the network structure of the CNTs reinforced that char layer. The high strength of the intumescent char layer was difficult to rupture during combustion, causing the formation of a tight and compact intumescent char layer. Moreover, CNTs can enhance the antidripping property due to that CNTs improved melt viscosity. As a result, the synergistic effect between CNTs and APP was exhibited.

For blends where APP was dispersed in the LLDPE phase (M2 and M3), the first or second PHRR values were both higher than that of LLDPE/PA6/APP, indicating an antagonistic effect between the CNTs and APP with regard to flame retardancy. The results of TGA and the cone calorimeter tests both indicate that the localization of APP in blends played a key role in the continuity of the residual char layer. The separation of APP and PA6 did not benefit their interaction, causing low residual char and the formation of a discontinuous char layer. Clearly, this kind of char layer provided poor protection for the substrate, causing poor flame retardancy.

4. Conclusion

The influence of localization of CNTs and APP in LLDPE/-PA6/APP/CNT blends on flame retardancy was investigated. The different localization of CNTs and APP in blends formed different morphologies of a residual char layer, causing remarkable differences in flame retardancy. For blends where APP was localized in the LLDPE phase and CNTs were localized in the PA6 or LLDPE phases, APP localization in the LLDPE phase contributed to a decrease in the interaction of APP and PA6, causing a low residual char mass and a discontinuous char layer to appear, resulting in poor flame retardancy. For blends with APP and CNT localization in the PA6 phase, even though the APP localization in the PA6 phase promoted the formation of a continuous residual char layer, the CNT network structure in the PA6 phase restrained the swell and coalescence of the char layer, causing a continuous residual char layer to appear that consisted of microscopic spherical cokes. As a result, poor flame retardancy was exhibited in this blend. For blends where APP and CNTs were localized in the LLDPE phase, the localization of APP in the PA6 phase benefitted the formation and appearance of a continuous char layer. In addition to reinforcing the residual char layer, the CNT network structure in the LLDPE phase showed poor influence on the swell and coalescence of the char layer. As a result, a tight and compact intumescent char layer was formed, causing good flame retardancy.

Data Availability

The data used to support the findings of this study are available from the corresponding author upon request.

Conflicts of Interest

The authors declare that there is no conflict of interest regarding the publication of this paper.

Acknowledgments

The authors gratefully acknowledge the financial support of this work by the National Natural Science Foundation of China (Contract Number: 51673059), the Natural Science Foundation of Education Department of Henan Province (Contract Number: 17A150009), the Natural Science Foundation of Henan Province (Contract Number: 112300410208), and the Project National United Engineering Laboratory for Advanced Bearing Tribology of Henan University of Science and Technology (Contract Number: 201813).

References

[1] S. Bourbigot, F. Samyn, T. Turf, and S. Duquesne, "Nanomorphology and reaction to fire of polyurethane and polyamide nanocomposites containing flame retardants," *Polymer Degradation and Stability*, vol. 95, no. 3, pp. 320–326, 2010.

[2] J. B. Dahiya, S. Rathi, H. Bockhorn, M. Haußmann, and B. K. Kandola, "The combined effect of organic phoshphinate/ammonium polyphosphate and pentaerythritol on thermal and

fire properties of polyamide 6-clay nanocomposites," *Polymer Degradation and Stability*, vol. 97, no. 8, pp. 1458–1465, 2012.

[3] J. Alongi, M. Poskovic, P. M. Visakh, A. Frache, and G. Malucelli, "Cyclodextrin nanosponges as novel green flame retardants for PP, LLDPE and PA6," *Carbohydrate Polymers*, vol. 88, no. 4, pp. 1387–1394, 2012.

[4] T. Kashiwagi, E. Grulke, J. Hilding, R. Harris, W. Awad, and J. Douglas, "Thermal degradation and flammability properties of poly(propylene)/carbon nanotube composites," *Macromolecular Rapid Communications*, vol. 23, no. 13, pp. 761–765, 2002.

[5] S. Peeterbroeck, F. Laoutid, B. Swoboda et al., "How carbon nanotube crushing can improve flame retardant behaviour in polymer nanocomposites?," *Macromolecular Rapid Communications*, vol. 28, no. 3, pp. 260–264, 2007.

[6] H. Y. Ma, P. A. Song, and Z. P. Fang, "Flame retarded polymer nanocomposites: development, trend and future perspective," *Science China Chemistry*, vol. 54, no. 2, pp. 302–313, 2011.

[7] B. Schartel, P. Potschke, U. Knoll, and M. Abdel-Goad, "Fire behaviour of polyamide 6/multiwall carbon nanotube nanocomposites," *European Polymer Journal*, vol. 41, no. 5, pp. 1061–1070, 2005.

[8] T. Kashiwagi, E. Grulke, J. Hilding et al., "Thermal and flammability properties of polypropylene/carbon nanotube nanocomposites," *Polymer*, vol. 45, no. 12, pp. 4227–4239, 2004.

[9] B. Du and Z. Fang, "Effects of carbon nanotubes on the thermal stability and flame retardancy of intumescent flame-retarded polypropylene," *Polymer Degradation and Stability*, vol. 96, no. 10, pp. 1725–1731, 2011.

[10] S. Bourbigot, S. Duquesne, G. Fontaine, S. Bellayer, T. Turf, and F. Samyn, "Characterization and reaction to fire of polymer nanocomposites with and without conventional flame retardants," *Molecular Crystals and Liquid Crystals*, vol. 486, no. 1, pp. 325/[1367]–339/[1381], 2008.

[11] M. Chen, Y. Xu, X. Chen et al., "Thermal stability and combustion behavior of flame-retardant polypropylene with thermoplastic polyurethane-microencapsulated ammonium polyphosphate," *High Performance Polymers*, vol. 26, no. 4, pp. 445–454, 2014.

[12] S. Bourbigot, B. M. Le, C. I. Siat, and M. Lewin, *Recent advances in flame retardancy of polymeric materials*, BCC Pub, Norwalk, 1997.

[13] X. Wang, Y. Li, W. Liao, J. Gu, and D. Li, "A new intumescent flame-retardant: preparation, surface modification, and its application in polypropylene," *Polymers for Advanced Technologies*, vol. 19, no. 8, pp. 1055–1061, 2008.

[14] R. Delobel, M. L. Bras, N. Ouassou, and F. Alistiqsa, "Thermal behaviours of ammonium polyphosphate-pentaerythritol and ammonium pyrophosphate-pentaerythritol intumescent additives in polypropylene formulations," *Journal of Fire Sciences*, vol. 8, no. 2, pp. 85–108, 1990.

[15] K. S. Lim, S. T. Bee, L. T. Sin et al., "A review of application of ammonium polyphosphate as intumescent flame retardant in thermoplastic composites," *Composites Part B: Engineering*, vol. 84, pp. 155–174, 2016.

[16] S. H. Chiu and W. K. Wang, "Dynamic flame retardancy of polypropylene filled with ammonium polyphosphate, pentaerythritol and melamine additives," *Polymer*, vol. 39, no. 10, pp. 1951–1955, 1998.

[17] X. Almeras, M. Le Bras, P. Hornsby et al., "Effect of fillers on the fire retardancy of intumescent polypropylene compounds," *Polymer Degradation and Stability*, vol. 82, no. 2, pp. 325–331, 2003.

[18] Y. Ma, P. Ma, Y. Ma, D. Xu, P. Wang, and R. Yang, "Synergistic effect of multiwalled carbon nanotubes and an intumescent flame retardant: toward an ideal electromagnetic interference shielding material with excellent flame retardancy," *Journal of Applied Polymer Science*, vol. 134, no. 31, 2017.

[19] Q. Zhao, Y. Hu, and X. Wang, "Mechanical performance and flame retardancy of polypropylene composites containing zeolite and multiwalled carbon nanotubes," *Journal of Applied Polymer Science*, vol. 133, no. 3, article 42875, 2016.

[20] G. Huang, S. Wang, P.'. Song, C. Wu, S. Chen, and X. Wang, "Combination effect of carbon nanotubes with graphene on intumescent flame-retardant polypropylene nanocomposites," *Composites Part A: Applied Science and Manufacturing*, vol. 59, pp. 18–25, 2014.

[21] H. Y. Ma, L. F. Tong, Z. B. Xu, and Z. P. Fang, "Functionalizing carbon nanotubes by grafting on intumescent flame retardant: nanocomposite synthesis, morphology, rheology, and flammability," *Advanced Functional Materials*, vol. 18, no. 3, pp. 414–421, 2008.

[22] C. Lu, D. Yang, Q. Q. Cao, X. H. Huang, J. C. Liu, and Y. Q. Zhang, "Influence of morphology on the flame retardancy of polystyrene/nylon-6/ammonium polyphosphate/clay blends," *High Performance Polymers*, vol. 26, no. 5, pp. 507–516, 2014.

[23] C. Lu, Q. Q. Cao, X. N. Hu, C. Y. Liu, X. H. Huang, and Y. Q. Zhang, "Influence of morphology and ammonium polyphosphate dispersion on the flame retardancy of polystyrene/nylon-6 blends," *Fire and Materials*, vol. 38, no. 8, pp. 765–776, 2014.

[24] M. Entezam, H. A. Khonakdar, and A. A. Yousefi, "On the flame resistance behavior of PP/PET blends in the presence of nanoclay and a halogen-free flame retardant," *Macromolecular Materials and Engineering*, vol. 298, no. 10, pp. 1074–1084, 2013.

[25] S. Pack, M. Si, J. Koo et al., "Mode-of-action of self-extinguishing polymer blends containing organoclays," *Polymer Degradation and Stability*, vol. 94, no. 3, pp. 306–326, 2009.

[26] S. Pack, T. Kashiwagi, D. Stemp et al., "Segregation of carbon nanotubes/organoclays rendering polymer blends self-extinguishing," *Macromolecules*, vol. 42, no. 17, pp. 6698–6709, 2009.

[27] C. Lu, X. P. Gao, D. Yang et al., "Flame retardancy of polystyrene/nylon-6 blends with dispersion of clay at the interface," *Polymer Degradation and Stability*, vol. 107, pp. 10–20, 2014.

[28] C. Lu, X. P. Gao, D. H. Yao, C. L. Cao, and Y. J. Luo, "Improving flame retardancy of linear low-density polyethylene/nylon 6 blends via controlling localization of clay and intumescent flame-retardant," *Polymer Degradation and Stability*, vol. 153, pp. 75–87, 2018.

[29] J. Jin, H. Wang, Z. Shu, and L. Lu, "Impact of selective dispersion of intumescent flame retardant on properties of polypropylene blends," *Journal of Materials Science*, vol. 52, no. 6, pp. 3269–3280, 2017.

[30] Y. Chen, Z. Guo, and Z. Fang, "Relationship between the distribution of organo-montmorillonite and the flammability of flame retardant polypropylene," *Polymer Engineering & Science*, vol. 52, no. 2, pp. 390–398, 2012.

[31] R. A. Khare, A. R. Bhattacharyya, A. R. Kulkarni, M. Saroop, and A. Biswas, "Influence of multiwall carbon nanotubes on morphology and electrical conductivity of PP/ABS blends,"

Journal of Polymer Science Part B: Polymer Physics, vol. 46, no. 21, pp. 2286–2295, 2008.

[32] S. Bourbigot, M. Le Bras, and R. Delobel, "Fire degradation of an intumescent flame retardant polypropylene using the cone calorimeter," *Journal of Fire Sciences*, vol. 13, no. 1, pp. 3–22, 1995.

[33] S. V. Levchik, L. Costa, and G. Camino, "Effect of the fire-retardant, ammonium polyphosphate, on the thermal decomposition of aliphatic polyamides: part II—polyamide 6," *Polymer Degradation and Stability*, vol. 36, no. 3, pp. 229–237, 1992.

[34] S. V. Levchik, G. F. Levchik, A. I. Balabanovich, G. Camino, and L. Costa, "Mechanistic study of combustion performance and thermal decomposition behaviour of nylon 6 with added halogen-free fire retardants," *Polymer Degradation and Stability*, vol. 54, no. 2-3, pp. 217–222, 1996.

[35] S. Bourbigot, M. Le Bras, R. Delobel, P. Bréant, and J. M. Tremillon, "4A zeolite synergistic agent in new flame retardant intumescent formulations of polyethylenic polymers — Study of the effect of the constituent monomers," *Polymer Degradation and Stability*, vol. 54, no. 2-3, pp. 275–287, 1996.

Hindawi
Journal of Nanomaterials
Volume 2019, Article ID 6326012, 8 pages
https://doi.org/10.1155/2019/6326012

Research Article

Synthesis and Characterization of Magnetite-Alginate Nanoparticles for Enhancement of Nickel and Cobalt Ion Adsorption from Wastewater

Omnia A. A. El-Shamy,[1] **Ragaa E. El-Azabawy**,[2,3] **and Olfat. E. El-Azabawy**[1]

[1]*Egyptian Petroleum Research Institute, Nasr City, Cairo 11727, Egypt*
[2]*Chemistry Department, Faculty of Science, Al-Azhar University (Girls), Nasr City, Cairo, Egypt*
[3]*Chemistry Department, Faculty of Science and Art-Al Mandaq (Girls), Al-Baha University, Saudi Arabia*

Correspondence should be addressed to Omnia A. A. El-Shamy; omniaelshamy@yahoo.com

Received 1 May 2019; Revised 29 June 2019; Accepted 18 July 2019; Published 16 September 2019

Guest Editor: Emad M. Masoud

Superparamagnetic magnetite-alginate nanoparticles (M-AlgNPs) were synthesized utilizing a coprecipitation method. Then, the prepared M-AlgNPs were characterized via Fourier transform infrared spectroscopy (FTIR) and X-ray diffraction spectroscopy (XRD) to affirm the formation and the crystallinity of this composite. In addition, the surface morphology of the prepared nanoparticles was inspected by transmission electron microscopy (TEM) which revealed well-dispersed nanoparticles of Fe_3O_4 into alginate. The adsorption characteristics of the synthesized nanoparticles for removing Ni^{+2} and Co^{+2} from wastewater were evaluated via atomic absorption measurements (AAS). The elimination efficiency of the M-AlgNPs was detected at $pH = 7$ in 100 ppm (initial concentration) of Ni^{+2} and Co^{+2}, separately. The M-AlgNPs provided the maximum equilibrium uptake percentage for Ni^{+2} and Co^{+2} of 97.88 and 95.01%, respectively. The adsorption of Ni^{+2} and Co^{+2} onto the M-AlgNP surface was found to fit the Langmuir model with R^2 values higher than that obtained from the Freundlich model for both metal ions. Moreover, R_L "separating factor" for the adsorption process was assessed and found to be less than unity; this expresses the higher ability of the investigated metal ions to be adsorbed onto the M-AlgNP surface. The adsorption method was discovered to be pH-dependent and well-suited to the isothermal equations of Langmuir and Freundlich. For regeneration studies, M-AlgNPs have been investigated and results confirmed that it could be reused with effective sorption capacity over three cycles.

1. Introduction

Water pollution with metal ions is an enormous ecological problem, as they damage even at small levels. Metal ions, for instance, nickel, cobalt, lead, and iron, are toxic and have nonbiodegradable characteristics that cause difficulty for both the earth and life. Removing these metal ions from the sewage stream is an important demand for a healthy setting. Several techniques have been used to eliminate metal ions from wastewater such as exchange of ions, extraction of solvents, flotation, oxidation, and adsorption [1–3]. Adsorption has gradually gained a lot of attention since late in perspective of the fact that this technique is essential and it generally has minimal effort and energy in expelling important metal particles from water.

Numerous sorts of adsorbents for treatment have been produced, for example, activated carbon, natural bentonite, tobacco stem ash, and calcium alginate beads [4–7]. As of late, with the quick advancement of nanotechnology, nanoparticles are at present concentrated. Generally, the research found that nanosorbents have great adsorption limits concerning metal ion elimination from water due to the large surface area and high reusability of these nanomaterials.

The adsorption technique combined with magnetic features for metal ion separation is utilized widely in wastewater remediation and green treatment, because of their little

size and superparamagnetic properties. Also, these particles can be efficiently regained with an outer attractive field "magnet" and have a low threat effect.

Latterly, magnetic polymer nanoparticles got developing consideration in various fields because of their higher surface area and active sites to adsorb various pollutants. The magnetic polymer composite can be prepared via different methods; the most basic one is the independent preparation for the magnetic nanoparticles and polymer materials and after that blending them physically or chemically. Another technique to get the magnetic polymer composite depends on in situ precipitation of magnetic material within the polymer, where the magnetic particles are encompassed by a hydrophilic polymer shell [8, 9].

Alginate is an unbranched polymer formed by linear block copolymerization of d-mannuronic acid and l-guluronic acid, characterized by high hydrophilicity and is considered as an ecofriendly material, biocompatible, and biodegradable [10].

In this study, magnetite-alginate nanoparticles (M-AlgNPs) were synthesized via the coprecipitation method. The structure of the prepared M-AlgNPs was expressed using FTIR and XRD. The morphology and particle size of the synthesized nanomaterial were detected using TEM. In addition, M-AlgNPs were applied as a green adsorbent for removing Ni^{+2} and Co^{+2} from wastewater. The effect of pH values and adsorbent doses was studied. Moreover, the adsorption isotherm and equilibria of Ni^{+2} and Co^{+2} adsorption onto M-AlgNPs were studied using both Langmuir and Freundlich models.

2. Materials and Experiments

2.1. Materials. $FeCl_3{\cdot}6H_2O$ (iron(III) chloride hexahydrate), $FeCl_2{\cdot}4H_2O$ (iron(II) chloride tetrahydrate), sodium hydroxide, nickel sulfate ($NiSO_4{\cdot}5H_2O$), and cobalt nitrate ($Co(NO_3)_2$) are of analytical grade and are obtained from Merck, Germany. Sodium alginate was purchased, and Pluronic PE 6400 was from Sigma.

The fresh concentration of Ni^{+2} and Co^{+2} was prepared by means of adequate dilutions for the purchased solutions.

2.2. Synthesis of M-AlgNPs. M-AlgNPs were synthesized via the coprecipitation technique, where $FeCl_3{\cdot}6H_2O$ and $FeCl_2{\cdot}4H_2O$ have been dissolved separately in the ratio of 2 : 1. Then, the two previous solutions were mixed and heated (65°C) under mild stirring using a mechanical stirrer. An aqueous solution of NaOH (3 M) is then added drop by drop until the formation of black suspended particles. The reaction continued for 30 min under the same conditions [11, 12]. Then, magnetite alginate was prepared via a ionotropic gelation method. Firstly, the previously synthesized magnetite nanoparticles were redispersed in a solution 2.5% of sodium alginate using an ultrasonic bath for 5 min. The resulting M-AlgNPs were washed several times with deionized water; then, the particles were magnetically separated.

2.3. Characterization of M-AlgNPs. FTIR was used to distinguish the functional groups of M-AlgNPs using FTIR-1615 (Perkin Elmer (USA)) using the KBr disc, in wavenumbers that ranged from 4000 to 400 cm^{-1}. The crystal structure of the synthesized M-AlgNPs was estimated via an X-ray diffraction technique (Panalytical X'Pert PRO MPD (Netherlands)). The instrument is outfitted with a copper anode (Cu-Kα) producing wavelength radiation of 1.54 Å. The diffraction pattern was registered at ambient temperature in the angular width of 4–80 (2θ) applying a scan time of 0.4 (s) and a step size of 0.02 (2θ). Zeta potential values were measured (Malvern Zetasizer ZS-HT, United Kingdom) to detect the optimum pH for the adsorption process. The morphology of the prepared M-AlgNPs was viewed utilizing the transmission electron microscope, JEM 2100 (JEOL, Japan).

2.4. Adsorption Studies. The concentration of Ni^{+2} and Co^{+2} in the aqueous solution was determined using a ZEEnit 700P atomic absorption spectrometer (Analytik Jena, Germany) equipped with an air-acetylene and a slot burner of 100 mm. The instrumental conditions were balanced by the producer's recommendations. The accuracy of measurement is accomplished through triple repetition for each concentration.

The batch experiments are used to detect the adsorption manner of the prepared M-AlgNPs for Ni^{+2} and Co^{+2} (at room temperature). In this step, M-AlgNPs were added (known weight) to the metal ion aqueous solution separately and checked well (200 rpm) for two hours (selected time). Then, the M-AlgNPs were separated by a magnet, and the remaining metal ion concentration is determined using FAAS.

The adsorption of Ni^{+2} and Co^{+2} onto the M-AlgNP surface was estimated in the pH range from 2 to 7.5 (using 0.1 M NaOH or 0.1 M HNO_3). Moreover, the effect of the different weights of the synthesized M-AlgNPs was investigated at ambient temperature.

The capacity of adsorption at equilibrium (q_e) is calculated in mg/g using the following equation:

$$q_e = \frac{(C_0 - C_e) * V}{W}, \quad (1)$$

where W is the weight of the synthesized M-AlgNPs (g), V is the volume of the sample (L), C_0 is the initial metal ion concentration (mg/L), and C_e is the concentration of the metal ions at equilibrium (mg/L).

3. Results and Discussion

The procedure of the coprecipitation reaction of formation of Fe_3O_4 can be summed up by the formation of oxygenated bridges between Fe(III) and Fe(II). Before the synthesis steps, the initial ratio of Fe(III) and Fe(II) is obtained as an acid solution to avoid the formation of hydroxide form before mixing. Then, the two ratios are mixed and dispersed well, and NaOH solution is added causing the precipitation of iron ions as hydroxide. The previously formed hydroxide

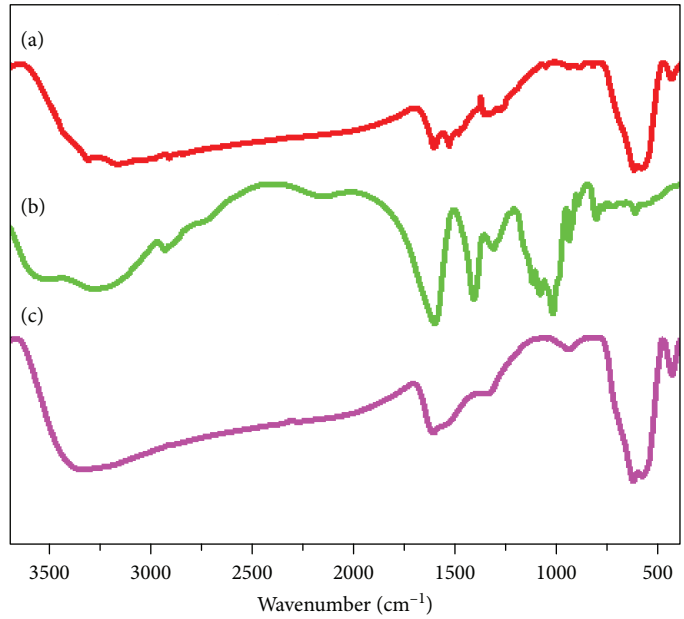

Figure 1: FTIR spectra of (a) Fe_3O_4 NPs, (b) sodium alginate, and (c) M-AlgNPs.

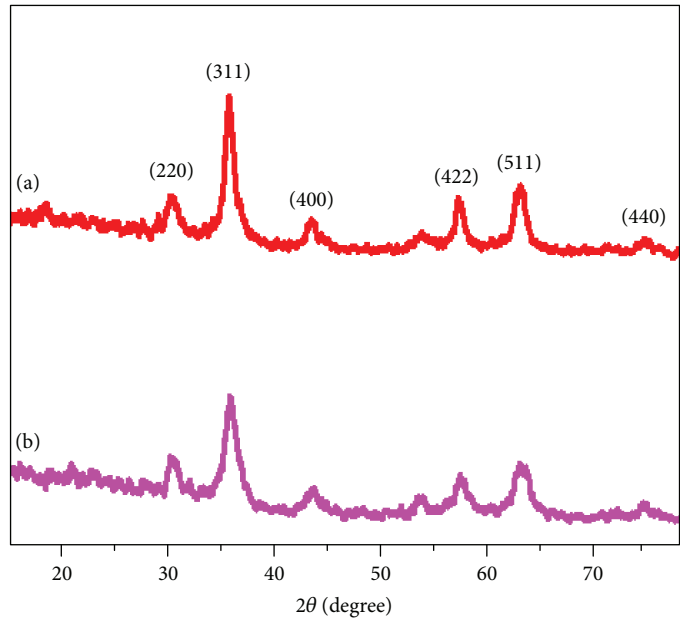

Figure 2: XRD pattern of (a) Fe_3O_4 nanoparticles and (b) M-AlgNPs.

precipitate is converted to the oxides through the formation of the oxygenated bridge [11, 13].

The reaction can be described by the following equation:

$$2Fe^{+3} + Fe^{+2} + 8OH^{-} \rightarrow Fe_3O_4 + 4H_2O \quad (2)$$

3.1. Characterization of M-AlgNPs. Figure 1 shows the FTIR spectra of M-AlgNPs, which exhibit three peaks at 635, 589, and 441 cm^{-1} caused by the vibration of FeO bond in both octahedral and tetrahedral sites of the inverse spinel cubic of Fe_3O_4, respectively [14, 15]. The peaks at 1623 and 1352 cm^{-1} were attributed to the stretching of the C=O group in the alginate. In addition, the peak that appeared at 951 cm^{-1} was caused by the C-O group. A broad band that ranged from 3200 to 3500 cm^{-1} is due to the OH group [16].

Figure 2 shows the spectrum of M-AlgNPs which is greatly matched to JCPDS file No. 19-0629. This confirms the formation of magnetite nanoparticles, as evidenced by the peaks at 2θ values of 30.33, 35.79, 43.65, 57.35, 62.99, and 74.49° that attributed to the crystal plan of magnetite at (220), (311), (400), (422), (511), and (440) (Figure 2). The presence of alginate is elucidated from the appearance of broad diffraction peaks at 2θ less than 20° [17].

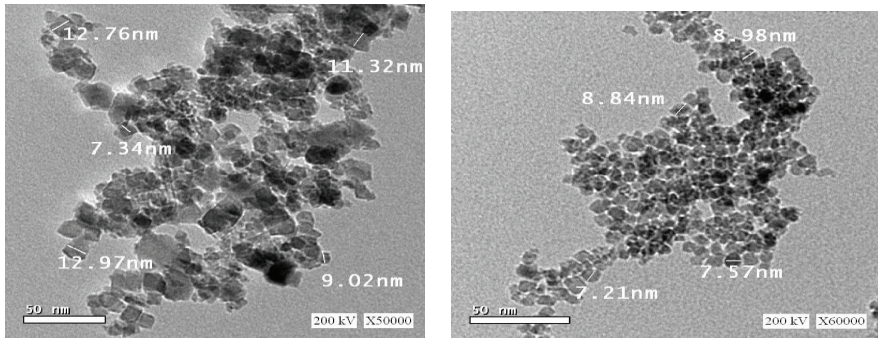

(a) (b)

Figure 3: TEM images for (a) Fe_3O_4 NPs and (b) M-AlgNPs.

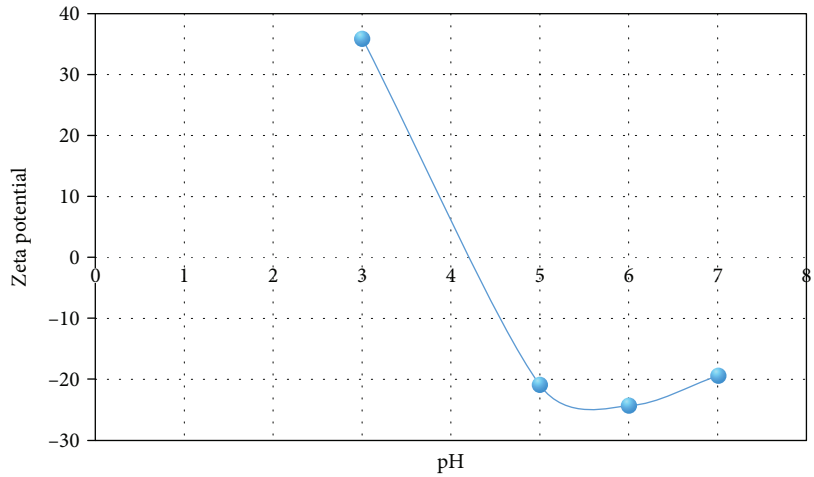

Figure 4: Zeta potential values of M-AlgNPs at different pH.

The average particle size of M-AlgNPs can be assessed utilizing the Debye-Scherrer relation [18]:

$$D = \frac{\kappa\lambda}{\beta \cos\theta}, \quad (3)$$

where D describes the mean diameter of M-AlgNPs, λ is the wavelength of the radiation source, β is FWHM (the full width at half-maximum) in radians, k is constant, and θ is the half diffraction angle—Bragg angle.

According to the Debye-Scherrer equation, particle sizes of M-AlgNPs were estimated to be 9.22 nm with respect to the most intense peak (311).

Figure 3 shows that the synthesized M-AlgNPs are present as irregular spherical shape and have uniform size distribution with average diameters of around 7-9 nm.

3.2. Adsorption Studies. It is outstanding that the pH values are a standout amongst the most essential elements that influence the manner of the adsorption process, since the pH of the metal ion solution controls the adsorption of these metals on the solid surfaces. Zeta potential measurement is determined for M-AlgNPs at different pH to detect the charge of the surface. Concerning Figure 4, the point of zero charge (isoelectric point) is found around 4.2. Above this point, the surface becomes negatively charged.

Experiments are performed to find the optimum pH on the adsorption of Ni^{+2} and Co^{+2} onto M-AlgNPs using various pH values of 2 up to 7.5; above this pH, the investigated metal ions begin to precipitate. Figure 5 shows the variation of the pH value on the adsorption behavior of Ni^{+2} and Co^{+2} onto M-AlgNPs using sorbent weight of 0.2 g/100 L at 25°C and initial metal ion concentration of 100 mg/L. The efficiency of adsorption was affected linearly by increasing the value of pH with the maximum value at pH 6.5. From zeta potential and experimental results, the removal efficiency increases above the isoelectric point reaching maximum before the neutral (pH 6.5) and higher negative value of zeta potential found around this pH. Thus, the carboxylate groups at this pH (*zeta potential* = -24.3) have more negative charges leading to more attraction to the positively charged metal ions, while at the pH value of 2, the hydroxyl groups of alginate become protonated causing a decrease in the efficiency of the adsorption of Ni^{+2} and Co^{+2} onto M-AlgNPs [19, 20].

Different sorbent doses were used that ranged from 0.1 to 0.5 g/mL for 100 mg/L metal ion concentration keeping other variables constant as shaking time, rpm, and temperature.

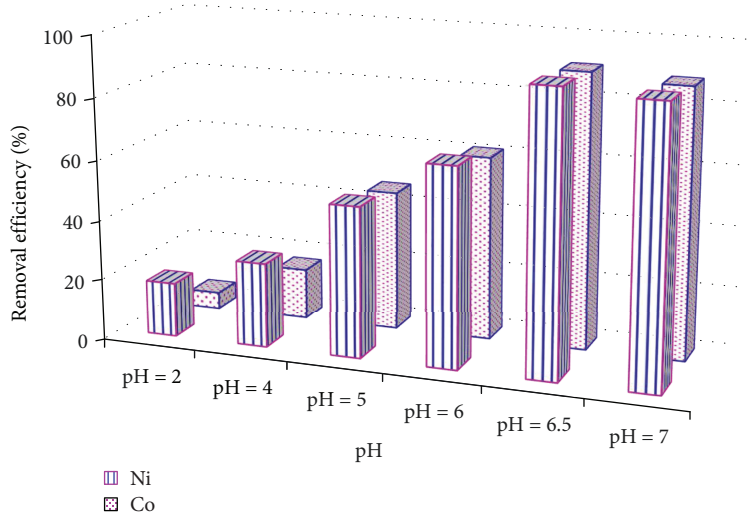

Figure 5: Effect of pH values on the removal percentage of heavy metal ions.

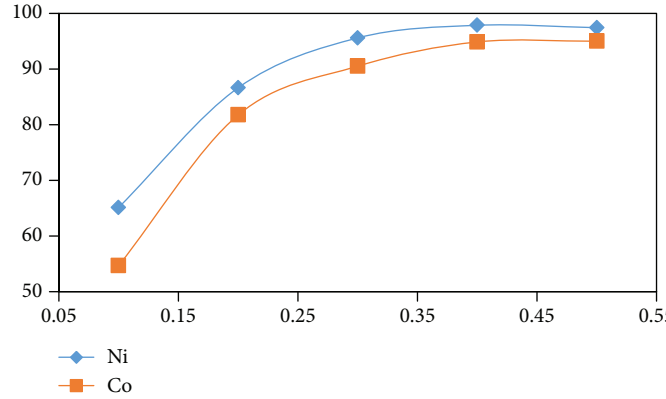

Figure 6: Effect of different weights from M-AlgNPs at pH of 6.5.

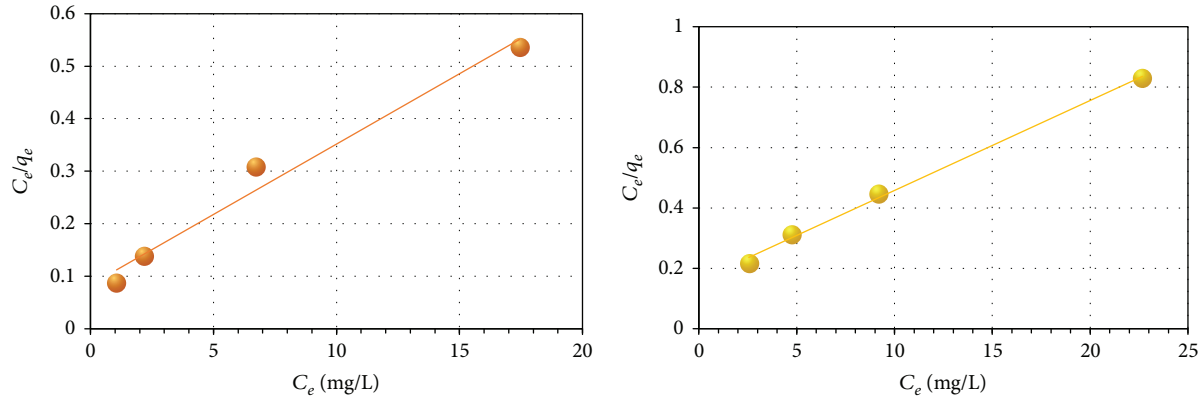

Figure 7: Langmuir isotherm for (a) Ni(II) and (b) Co(II) adsorbed at the prepared M-AlgNPs.

Figure 6 reveals that the elimination of Ni^{+2} and Co^{+2} increases with increasing the weight of M-AlgNPs. This is due to more available sites present with increasing the weight of adsorbent (M-AlgNPs) until 0.4 g/L. The decrease in the removal percentage with increasing the dose of the adsorbent surface is due to the repulsion between the large numbers of dispersed nanoparticles. So, the chance of metal ions to be attracted onto the M-AlgNP surface decreases.

3.3. Adsorption Isotherms. The Langmuir isotherm describes the adsorption as the formation of one layer that covers the

Table 1: Langmuir and Freundlich isotherm parameters for the adsorption of Ni(II) and Co(II) on the prepared M-ALgNPs.

Metal ions	Langmuir			Freundlich		
	q_{max} (mg/g)	b (L/mg)	R^2	K_f	$\frac{1}{n}$	R^2
Ni(II)	37.30	0.32	0.97	0.02	2.23	0.96
Co(II)	33.60	0.18	0.99	0.01	0.17	0.95

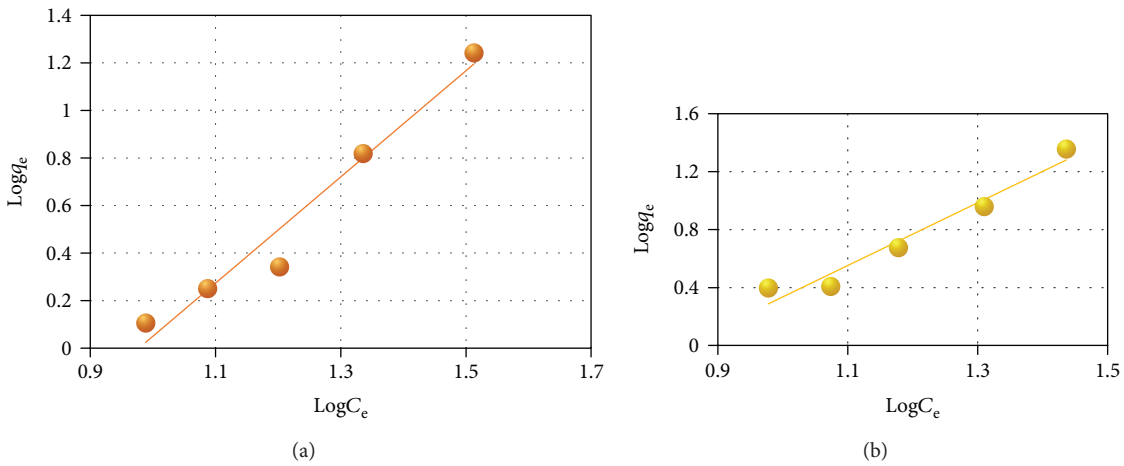

Figure 8: Freundlich isotherm for (a) Ni(II) and (b) Co(II) adsorbed at the prepared M-AlgNPs.

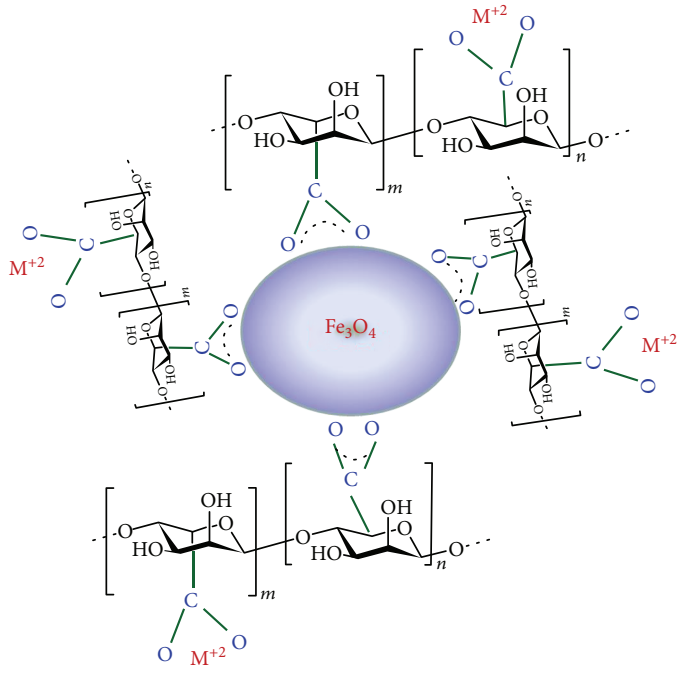

Scheme 1: The adsorption of metal ions on the M-AlgNPs.

sorbent surface and no further adsorption can occur [21], and it is represented by the following equation:

$$\frac{C_e}{q_e} = \frac{1}{bq_{max}} + \frac{C_e}{q_{max}}, \quad (4)$$

where q_{max} (mg/g) is the maximum capacity of adsorption and b (L/mg) is the Langmuir constant. Figure 7 shows the relation between C_e/q_e and C_e; the intercept and the slope facilitate the calculation of b and q_{max}, respectively. Table 1 represents the calculated adsorption parameters which confirm the obligation of the adsorption of Co^{+2} and Ni^{+2} onto the M-AlgNP surface to the Langmuir relation.

Also, the following relation is applied for the Langmuir model to announce whether Co^{+2} and Ni^{+2} have a great

affinity to be adsorbed on the M-AlgNP surface or not:

$$R_L = \frac{1}{1 + bC_0}. \quad (5)$$

where R_L is the unit less constant called "separation factor," b is the Langmuir constant, and C_0 is the initial concentration of polluted metal ions.

The values of R_L have expressed the tendency of the pollutants to be adsorbed on the adsorbent surface. When the R_L value exceeds unity, it indicates that there is no tendency for adsorption "undesirable." Meanwhile, the higher tendency of adsorption is achieved when the value of R_L becomes more than zero and less than one. The calculated R_L values for Co^{+2} and Ni^{+2} are 0.030 and 0.053, respectively, indicating their higher tendency for adsorption onto M-AlgNPs.

Also, the adsorption manner can be described by the Freundlich isotherm model using the following equation:

$$\log q_e = \log K_f + \frac{1}{n} \log C_e, \quad (6)$$

where q_e is the adsorption capacity at equilibrium (mg/g), C_e is the concentration of each metal ions in the solution at equilibrium (mg/L), K_f is the capacity of adsorption ($C_0 = 1$) (mg/g), and n describes the intensity of the adsorption and is defined as the extent of reliance of the adsorption process with the concentration at equilibrium [22].

The Freundlich model states that the sorbent surfaces are heterogeneous and possess various binding energies. Figure 8 shows Freundlich adsorption isotherm, the values of $1/n$ obtained from the slope and are observed to be more than unity, as shown in Table 1, which reveals the cooperative adsorption [8, 23]. Langmuir isotherm gives higher R^2 values for adsorption of both metals than that obtained from Freundlich isotherm as listed in Table 1 indicating that metal ions are adsorbed as monolayer on the surface of M-AlgNPs.

The previous results suggest that Co^{+2} and Ni^{+2} are adsorbed on the prepared magnetite-alginate nanoparticle surface forming monolayer through the attraction between positive metal ion and outer oxygen atom as presented in Scheme 1. The prepared M-AlgNPs and the adsorbed metals are then separated using a strong magnet. Reusability of the M-AlgNPs as adsorbents for the metal ions was examined (under the same condition) due to financial and environmental concerns [24]. After the first adsorption process, the M-AlgNPs were tested again by stirring the adsorbent for 2 hours in 5 M HNO3 [25]. M-AlgNPs were carefully cleaned, separated with powerful magnets after adsorption-desorption with deionized water, and then dried and reconditioned to the second cycle for adsorption. The findings indicate, for Ni^{+2} and Co^{+2}, respectively, that the effectiveness of M-AlgNPs was 94.1 and 92.6% after being used three times.

4. Conclusion

Magnetite-alginate nanoparticles (M-AlgNPs) are synthesized, and the structure is characterized using FTIR and XRD measurements. Also, the morphology and the particle size were determined using TEM analysis. The prepared nanoparticles were applied as a green adsorbent for removing hazard metal ions "cobalt and nickel ions" as selected pollutants from an aqueous water sample separately. The efficiency of adsorption of Co^{+2} and Ni^{+2} onto the prepared M-AlgNP surfaces were 95.01 and 97.88%, respectively. Moreover, the maximum capacity of adsorption (q_{max}) was 33.557 and 37.313 mg/g for Co^{+2} and Ni^{+2}. Both Langmuir and Freundlich isotherm models were applied, and R^2 values were obtained and showed more fitting to Langmuir models for Co^{+2} and Ni^{+2}. Additionally, the R_L "separation factor" values are calculated depending on Langmuir models and confirming the higher ability of adsorption $1 > R_L > 0$.

Data Availability

All measurements are undergone in the Egyptian Petroleum Research Institute, and the condition is inserted inside the article. The authors are ready for any question.

Conflicts of Interest

The authors declare that there is no conflict of interests.

References

[1] A. Çimen, M. Torun, and A. Bilgiç, "Immobilization of 4-amino-2-hydroxyacetophenone onto silica gel surface and sorption studies of Cu(II), Ni(II), and Co(II) ions," *Desalination and Water Treatment*, vol. 53, no. 8, pp. 2106–2116, 2013.

[2] E. A. El-Sharaky, M. R. Mishrif, and O. A. A. El-Shamy, "Synthesis and evaluation of a new trianionic surfactant for the removal of Pb (II) by flotation method," *Tenside Surfactants Detergents*, vol. 55, no. 2, pp. 148–152, 2018.

[3] M. N. Shalaby and O. A. A. El-Shamy, "Performance of some surfactants as wetting agents," *Tenside Surfactants Detergents*, vol. 42, no. 6, pp. 373–378, 2005.

[4] R. K. Ghosh and D. D. Reddy, "Tobacco stem ash as an adsorbent for removal of methylene blue from aqueous solution: equilibrium, kinetics, and mechanism of adsorption," *Water, Air, & Soil Pollution*, vol. 224, no. 6, p. 1582, 2013.

[5] M. H. Kafshgari, M. Mansouri, M. Khorram, and S. R. Kashani, "Kinetic modeling: a predictive tool for the adsorption of zinc ions onto calcium alginate beads," *International Journal of Industrial Chemistry*, vol. 4, no. 1, p. 5, 2013.

[6] A. Kassale, K. Barouni, M. Bazzaoui, and A. Albourine, "Modification of wood by grafting of carboxylic acid functions using acrylic acid," *Journal of Chemical, Biological and Physical Sciences*, vol. 5, p. 2, 2015.

[7] Ş. Kubilay, R. Gürkan, A. Savran, and T. Şahan, "Removal of Cu (II), Zn (II) and Co (II) ions from aqueous solutions by adsorption onto natural bentonite," *Adsorption*, vol. 13, no. 1, pp. 41–51, 2007.

[8] A. M. Al-Sabagh, Y. M. Moustafa, A. Hamdy, H. M. Killa, R. T. M. Ghanem, and R. E. Morsi, "Preparation and characterization of sulfonated polystyrene/magnetite nanocomposites for organic dye adsorption," *Egyptian Journal of Petroleum*, vol. 27, no. 3, pp. 403–413, 2018.

[9] N. S. Rajurkar and D. Mahajan, "Adsorption of cobalt (II) and nickel (II) ions from aqueous solution on chitosan," vol. 6, pp. 1203–1217, 2016.

[10] P. Aramwit, "Introduction to biomaterials for wound healing," in *Wound Healing Biomaterials*, pp. 3–38, Elsevier, 2016.

[11] D. Hritcu, M. I. Popa, N. POPA, V. Badescu, and V. Balan, "Preparation and characterization of magnetic chitosan nanospheres," *Turkish Journal of Chemistry*, vol. 33, pp. 785–796, 2009.

[12] N. M. Salem and A. M. Awwad, "A novel approach for synthesis magnetite nanoparticles at ambient temperature," *Nanoscience and Nanotechnology*, vol. 3, pp. 35–39, 2013.

[13] A. I. A. Sherlala, A. A. A. Raman, M. M. Bello, and A. Asghar, "A review of the applications of organo-functionalized magnetic graphene oxide nanocomposites for heavy metal adsorption," *Chemosphere*, vol. 193, pp. 1004–1017, 2018.

[14] K. Wu, S.-H. Liao, C.-H. Liu et al., "Functionalized magnetic iron oxide/alginate core-shell nanoparticles for targeting hyperthermia," *International Journal of Nanomedicine*, vol. 10, p. 3315, 2015.

[15] L. Yang, J. Tian, J. Meng et al., "Modification and characterization of Fe3O4 nanoparticles for use in adsorption of alkaloids," *Molecules*, vol. 23, no. 3, p. 562, 2018.

[16] C. Li, J. Lu, S. Li, Y. Tong, and B. Ye, "Synthesis of magnetic microspheres with sodium alginate and activated carbon for removal of methylene blue," *Materials*, vol. 10, no. 1, p. 84, 2017.

[17] J. A. Lopez, F. González, F. A. Bonilla, G. Zambrano, and M. E. Gómez, "Synthesis and characterization of Fe3O4 magnetic nanofluid," *Revista Latinoamericana de Metalurgia y Materiales*, vol. 30, pp. 60–66, 2010.

[18] M. Lee, *X-Ray Diffraction for Materials Research: From Fundamentals to Applications*, Apple Academic Press, 2016.

[19] M. R. Lasheen, I. Y. El-Sherif, M. E. Tawfik, S. T. El-Wakeel, and M. F. El-Shahat, "Preparation and adsorption properties of nano magnetite chitosan films for heavy metal ions from aqueous solution," *Materials Research Bulletin*, vol. 80, pp. 344–350, 2016.

[20] J. Shi, H. Li, H. Lu, and X. Zhao, "Use of carboxyl functional magnetite nanoparticles as potential sorbents for the removal of heavy metal ions from aqueous solution," *Journal of Chemical & Engineering Data*, vol. 60, no. 7, pp. 2035–2041, 2015.

[21] A. A. El-Feky, M. N. Shalaby, and O. A. A. El-Shamy, "Polymers as hydrophobic adsorbent surface for some surfactants," *Journal of Dispersion Science and Technology*, vol. 30, no. 4, pp. 445–450, 2009.

[22] S. A. Elfeky, S. E. Mahmoud, and A. F. Youssef, "Applications of CTAB modified magnetic nanoparticles for removal of chromium (VI) from contaminated water," *Journal of Advanced Research*, vol. 8, no. 4, pp. 435–443, 2017.

[23] Department of Chemical Engineering, Faculty of Engineering, Chulalongkorn University, S. Puttamat, and V. Pavarajarn, "Adsorption study for removal of Mn (II) ion in aqueous solution by hydrated ferric (III) oxides," *International Journal of Chemical Engineering and Applications*, vol. 7, no. 4, pp. 239–243, 2016.

[24] E. M. El-Fawal and O. A. A. El-Shamy, "Photodegradation enhancement of 2-chlorophenol using ZnO-CdS@CS nanocomposite under visible light," *International Journal of Environmental Science and Technology*, pp. 1–12, 2019.

[25] M. R. Lasheen, I. Y. El-Sherif, D. Y. Sabry, S. T. El-Wakeel, and M. F. El-Shahat, "Removal and recovery of Cr (VI) by magnetite nanoparticles," *Desalination and Water Treatment*, vol. 52, pp. 6464–6473, 2014.

Hindawi
Journal of Nanomaterials
Volume 2019, Article ID 7265450, 8 pages
https://doi.org/10.1155/2019/7265450

Research Article

TfR mAb-Cross-Linked Rituximab/MTX-PEG-PLL-PLGA Drug-Loaded Nanoparticles Enhance Anticancer Action in B Lymphocytes

Ran Liu,[1] **Gang Zhao**,[1] **Shujun Wang**,[2] **Yan Gu**,[1] **Qi Han**,[1] **and Baoan Chen**[1]

[1]*Department of Hematology and Oncology, Zhongda Hospital Southeast University, Nanjing, Jiangsu Province 210009, China*
[2]*Department of Blood Transfusion, Nanjing General Hospital of PLA, Nanjing, Jiangsu Province 210009, China*

Correspondence should be addressed to Baoan Chen; cba8888@hotmail.com

Received 1 February 2019; Revised 16 June 2019; Accepted 29 July 2019; Published 11 September 2019

Guest Editor: Biaolin Peng

Nanoparticles could enhance the drug targeted to the cancer cell by the enrichment of the drug levels, which leads to the improvement of the codelivery of both drugs for an antitumor effect. In the current study, we reported an efficient, local drug-loaded delivery strategy with a nanoparticle-loaded system. After the synthesis of Rituximab/MTX-PEG-PLL-PLGA, the transferrin receptor monoantibody (TfR mAb) was subsequently cross-linked to the nanoparticles. Compared to the traditional drug, the nanoparticle-loaded system can precisely and efficiently transport the Rituximab and Methotrexate (MTX) drug into SU-DHL-4 cells, a typical kind of B lymphocytes, which can significantly increase the cell apoptosis in the SU-DHL-4 cells. Thus, the multifunctional drug-loaded nanoparticles displayed the persistent stability and precise targeting properties, which enhanced the efficiency of anticancer efficiency in B lymphocytes.

1. Introduction

Although decades of efforts of research and billions of funding have enhanced our understanding of the underlying mechanisms of tumorigenesis, the death rate from cancer remains running at a high level nowadays [1]. Innovative strategies fighting cancer by inducing antitumor responses from the immune system are urgently needed [2, 3]. Chemotherapeutics from the class of the anthracyclines have been shown to induce the death of cancer cells with immunogenic features and triggering immunogenic antitumor responses [4]. But they also bring big damage to the patient's immune system by the unspecific action of these cytotoxic drugs in systemic chemotherapy [5].

Nanotechnology carries the characteristics of antitumor drugs, and the emergence of nanotechnology has made it possible for drugs to be effectively delivered to tumors [6, 7]. The single drug carrier can monitor the therapeutic effect in real time by combining radiographic imaging technology and antitumor intervention, and then the drug can be directly and efficiently reach the inside of the tumor, to maximize the reversal or overcome the antitumor multidrug resistance. Nanomedicine offers unique advantages in treating human cancers which are reported by several studies previously [8–10].

At present, the mechanism of tumor resistance is relatively complicated, but it also has shown that if a higher blood concentration is to be achieved and maintained, it is necessary to use a targeted site to deliver drugs to effectively control and reverse the starvation resistance of most tumor cells [2, 11]. In order to better increase the accumulation of antitumor drugs in tumor sites, it is necessary to achieve nanocarrier preparation. There are three key points in the progress of nanocarrier preparation. Firstly, passive targeting of high permeability will allow a retention effect by enhancing the permeability [12]. Secondly, active tumor targeting of nanoparticles through the specific molecules on the surface of tumor cells can be an optimal strategy [13]. Thirdly, it should be damage-free or should give low toxicity to the surrounding of the normal cells. For the aim of having a damage-free tissue, it is necessary to apply responsive nanoparticles to achieve targets under the stimulation of

physicochemical factors [14]. Some previous studies have found that the dendritic molecules have unique chemical structure properties, which make them act on tumors for a short period of time, inefficient tumor accumulation, and limited drug loading [15, 16]. The novel nanodrug carrier shows excellent potentials in increasing the antitumor activity of the drug and reducing the side effects [17]. Although nanomedicine carriers are an important part of fighting cancer, cancer treatment drugs are also critical.

Rituximab was the first monoclonal antibody to be approved for the treatment of cancer, and it is estimated that more than 4 million people have been treated with Rituximab worldwide [18, 19]. In the meantime, Methotrexate (MTX) is also still used in the treatment of a variety of tumors, including acute lymphocytic leukemia, breast cancer, osteosarcoma, primary central nervous system lymphoma, and head and neck cancers [20, 21]. Combined MTX and Rituximab with the nanodrug carrier may improve the accumulation of antitumor drugs and enhance permeability and retention effect.

Here, we aimed to investigate the effect of TfR mAb-cross-linked Rituximab/MTX-PEG-PLL-PLGA drug-loaded nanoparticles, which served as a precise and efficient carrier for the Rituximab and Methotrexate (MTX) drug into SU-DHL-4 cells, a typical kind of B lymphocytes, which can significantly increase the cell apoptosis in the SU-DHL-4 cells. The novel multifunctional drug-loaded nanoparticles persistently and precisely targeted SU-DHL-4 cells, which enhanced the efficiency of anticancer efficiency in B lymphocytes.

2. Materials and Methods

2.1. Synthesis of Rituximab/MTX-PEG-PLL-PLGA. The amount of PEG-PLL-PLGA was dissolved in 3 mL of a mixed solvent of dichloromethane-acetone-DMSO as the oil phase, while MTX (80 mg) (Sigma-Aldrich, St. Louis, Mo.) and Rituximab (40 mg) (Selleck Chemicals Houston, TX) were dissolved in 6 mL of 0.9% physiological saline as the aqueous phase. Then, the water phase was divided into 2 equal parts, labeled as aqueous phase 1 and aqueous phase 2, following the next two steps: (1) Aqueous phase 1 was poured into the oil phase, ultrasonically forming an emulsion, (2) and aqueous phase 2 was successively added dropwise to the oil phase, and the ultrasonication continued to form an emulsion. Finally, the above emulsion was added to 3 mL PVA (3 mg/mL) in 0.9% physiological saline. After ultrasonication for 6 min, the solution was evaporated on a vacuum rotary evaporator to remove methylene chloride-acetone in the solution. The solution was centrifuged at 15000 r/min for 10 min twice in 3 mL 0.9% normal saline. The supernatant was collected and freeze-dried to solid. The product was obtained, weighed (427.1 mg), and stored at 2-8°C. In the preparation of PEG-PLL-PLGA nanoparticles, the procedure is the same as above using the 0.9% physiological saline without drugs.

To determine the content of Rituximab/MTX in micelles, a series of known amounts of Rituximab/MTX-loaded nanoparticles were separately dissolved in 3 mL PBS. A UV-Vis spectrophotometer (Cary 300, Agilent Technologies, USA) was used to determine the concentration of Rituximab at 278 nm and MTX at 258 nm to obtain a standard curve. Based on the standard curve, the drug loading content (DLC) and drug loading efficiency (DLE) could be calculated by the following equations:

$$\text{DLC}\,(\%) = \frac{\text{weight of drug in nanoparticles}}{\text{weight of drug-loaded nanoparticle}} \times 100\%, \quad (1)$$

$$\text{DLE}\,(\%) = \frac{\text{weight of drug in nanoparticles}}{\text{weight of feeding drug}} \times 100\%. \quad (2)$$

2.2. Preparation of TfR mAb/Rituximab/MTX-PEG-PLL-PLGA. To prepare the TfR mAb-cross-linked Rituximab/MTX-PEG-PLL-PLGA, 30 mg Rituximab/MTX-PEG-PLL-PLGA was dissolved in 3 mL PBS and ultrasonicated. Then, 300 μg TfR mAb (Invitrogen) and 9 mg Genipin were mixed gently at room temperature for 2 hours and an additional 12 hours at 2-8°C. The solution was centrifuged at 15000 r/min for 10 min twice in 1 mL 0.9% normal saline. The product was obtained after lyophilization and stored at 2-8°C.

To determine the TfR mAb modification rate in Rituximab/MTX-PEG-PLL-PLGA, a series of known amounts of TfR mAb-cross-linked Rituximab/MTX-PEG-PLL-PLGA nanoparticles were separately dissolved in 3 mL PBS. A UV-Vis spectrophotometer was used to determine the concentration of TfR mAb at 279 nm. The modification rate (%) was calculated by the above equation (1).

2.3. Characterization. The morphology of PEG-PLL-PLGA and drug-loaded nanoparticles was analyzed using a transmission electron microscope (TEM; Hitachi S-4800, Japan) with a voltage of 10 kV. The size and size distribution of nanoparticles were determined using a Malvern Zetasizer Nano ZS instrument (Malvern Instruments, Malvern, UK). A UV-Vis spectrophotometer (Cary 300, Agilent Technologies, USA) was used to determine the concentration of Rituximab, MTX, and TfR mAb.

2.4. In Vitro Drug Release. 300 mg of the Rituximab/MTX-loaded PEG-PLL-PLGA nanoparticles was dissolved in 5 mL 0.9% physiological saline. The diluted solutions were transferred into dialysis membrane tubes and immersed in 60 mL PBS (0.01 M) then shaken at 150 rpm at 37°C. At scheduled intervals, 3 mL of solution was withdrawn from the release medium and replaced with the same volume of fresh PBS. The Rituximab/MTX content in the withdrawn solution was analyzed by a UV-Vis spectrophotometer and calculated based on the standard curve.

2.5. Cell Culture. The human SU-DHL-4 cell line was purchased from American Type Culture Collection (ATCC, Manassas, VA). The SU-DHL-4 cells were cultured in RPMI-1640 medium (Hyclone, UT, USA), supplied with 10% FBS (Gibco, CA, USA) and 1% penicillin-streptomycin liquid at 5% CO_2 in a humidified incubator at 37°C.

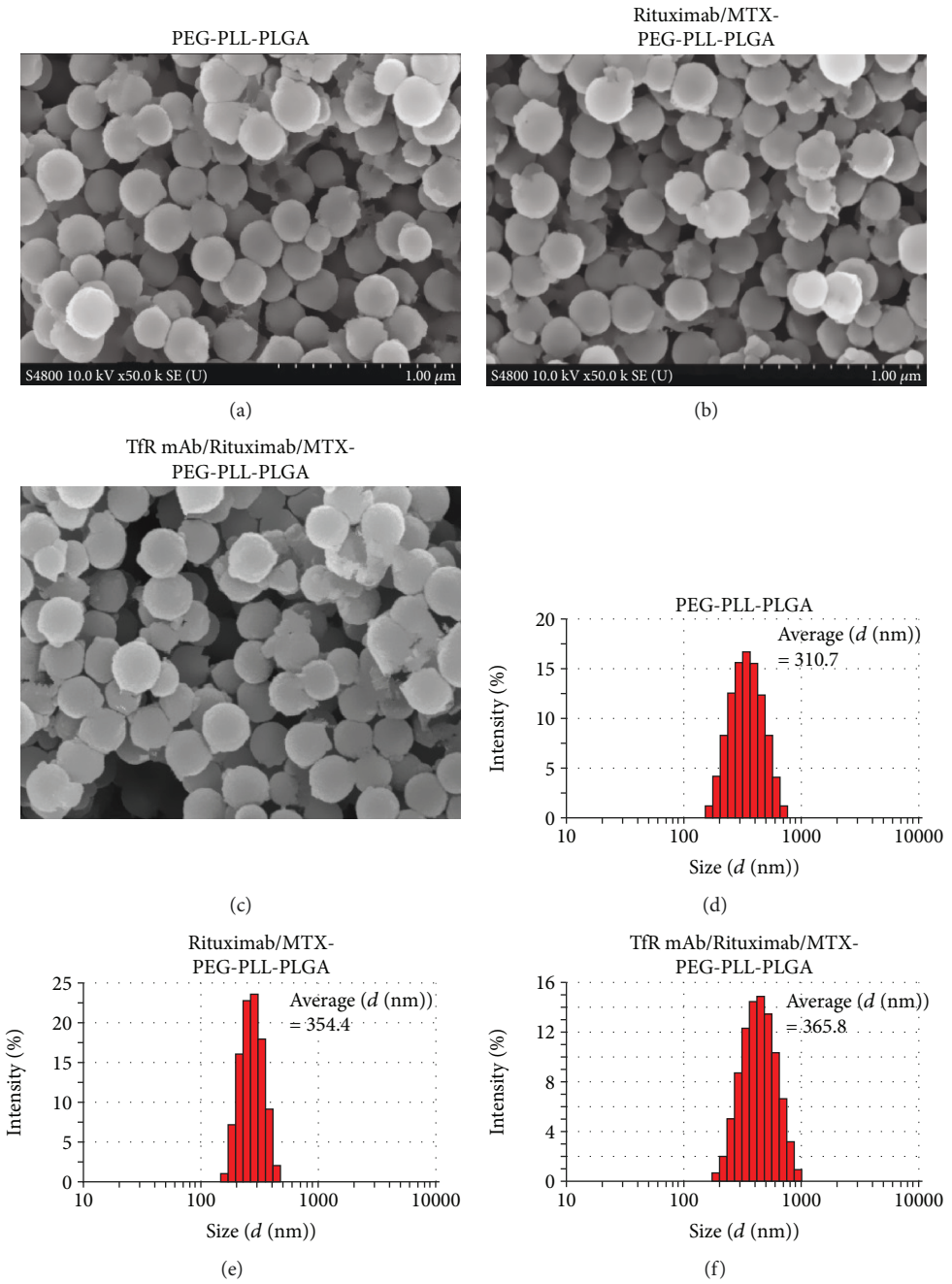

Figure 1: (a–c) The morphology of PEG-PLL-PLGA and drug-loaded nanoparticles was analyzed using TEM. Scale bar = 100 nm. (d–f) Particle size and size distribution of nanoparticles were determined using a Malvern Zetasizer Nano ZS instrument. The average diameters (d (nm)) of particles were calculated by intensity.

2.6. In Vitro Cytotoxicity Evaluation. Cytotoxicity was measured using a CCK8 assay (Dojindo, Japan) according to the manufacturer's suggested procedures. SU-DHL-4 cells were seeded into 96-well plates at a concentration of 2.5×10^4 cells, and different concentrations of nanoparticles were added to be cultured for 48 and 72 hours, respectively. Then, 10 μL of the CCK8 reagent was added to each well and incubated for 2 hours in the incubator. The OD value was measured at 450 nm with a microplate reader.

2.7. Analysis of Cell Cycle and Cell Apoptosis. SU-DHL-4 cells were inoculated into a 6-well plate at a concentration of 2×10^6 cells/well while the drug concentration was 175 μg/L Rituximab, 300 μg/L MTX, 175 μg/L Rituximab plus 300 μg/L MTX, and 2100 μg/L TfR mAb-MTX-PEG-PLL-PLGA nanoparticles, and the medium treatment group was used as a control. After 48 hours of drug treatment, the cells were harvested and resuspended in 1 mL PBS. After centrifugation, the supernatant was discarded and the cells were

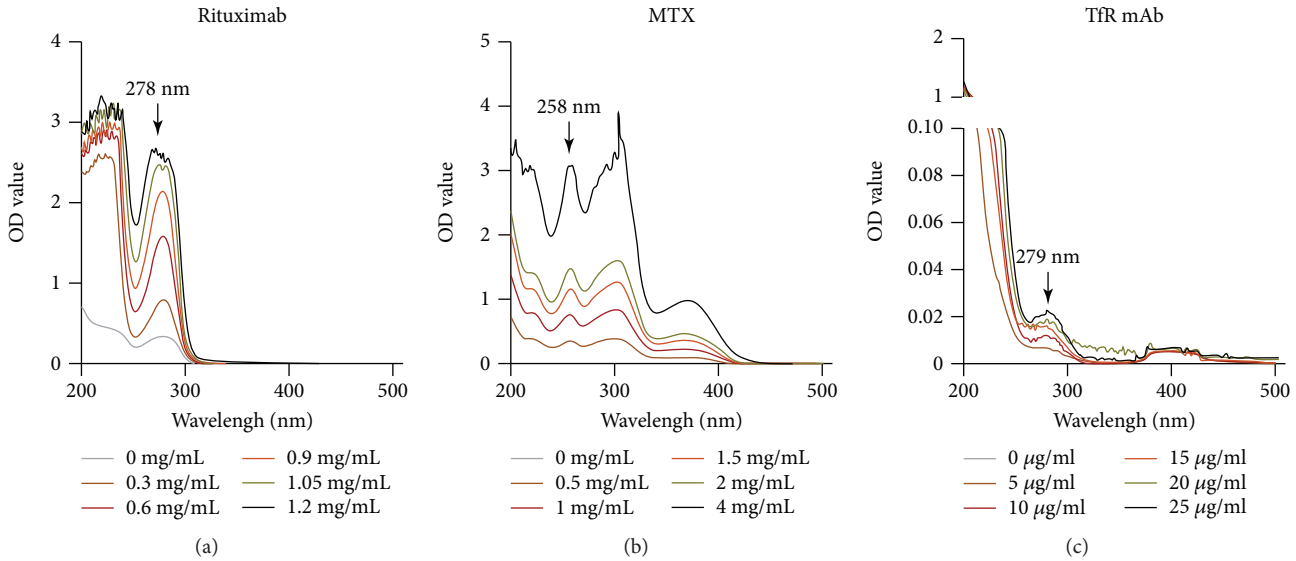

Item	Rituximab	MTX	TfR mAb
DLC (%)	8.17±0.02	14.87±0.01	/
DLE (%)	87.25±0.02	79.41±0.01	/
Modification rate (%)	/	/	70.90±2.33

(d)

Figure 2: UVA sensitivity and stability of Rituximab- (a), MTX- (b), or TfR mAb- (c) loaded nanoparticles. (d) The drug loading content (DLC) and drug loading efficiency (DLE) of Rituximab and MTX and the modification rate of TfR mAb in TfR mAb/Rituximab/MTX-PEG-PLL-PLGA nanoparticles.

resuspended in 0.5 mL PBS and 5 mL of precooled 70% ethanol. After being mixed well, the cells were fixed at 4°C overnight and then washed with PBS. RNase A (50 μg/mL) was added to dissolve for 30 min in a water bath at 37°C, and then 5 μL of PI (50 μg/mL) (Solarbio, China) was added to stain for 15 min at 4°C in the dark. Finally, the samples were detected by flow cytometry (BD Biosciences).

To detect cell apoptosis, cells were resuspended in 400 μL of 1x Binding Buffer and supplied with 5 μL FITC-Annexin V and 5 μL PI (50 μg/mL) (Solarbio, China). The control cells were divided into the nonstained group, single-stained Annexin V group, single-stained PI group, and double-stained Annexin V plus PI group. The samples were gently bounced, mixed, and incubated for 15 min at room temperature in the dark. 400 μL of 1x Binding Buffer was added to each tube and mixed. Finally, the samples were detected by flow cytometry (BD Biosciences) within 1 hour.

2.8. Statistics. Pharmacokinetic data were analyzed using the noncompartmental WinNonlin method. Statistical analysis was performed using the SPSS 22.0 program. P values were obtained using the two-sample t-test. For cellular uptake, bidistribution, and antitumor activity data, statistical analyses were performed by ANOVA, with $P < 0.05$ considered to be statistically significant and $P < 0.01$ considered to be an extremely significant difference. Statistical analysis was performed using the GraphPad Prism 5 (GraphPad Software, San Diego, CA).

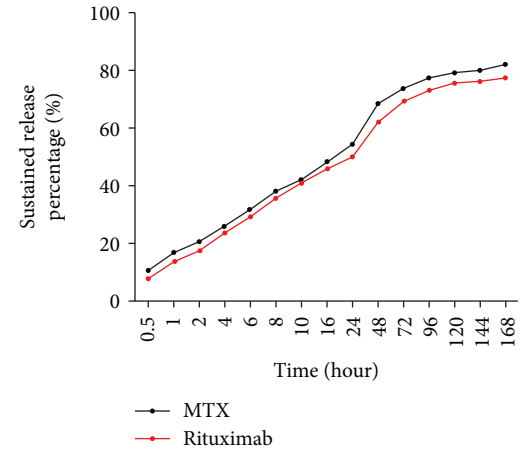

Figure 3: The sustained release percentage of MTX- and Rituximab-loaded nanoparticles *in vitro*.

3. Results and Discussion

Prior to carrying out efficacy studies, the Rituximab and MTX drug-loaded PEG-PLL-PLGA nanoparticles were synthesized, followed by cross-linking by TfR mAb. The particles of the drug-loaded nanoparticles were evaluated by transmission electron microscope (TEM) morphology, which showed uniform particle distribution in three kinds

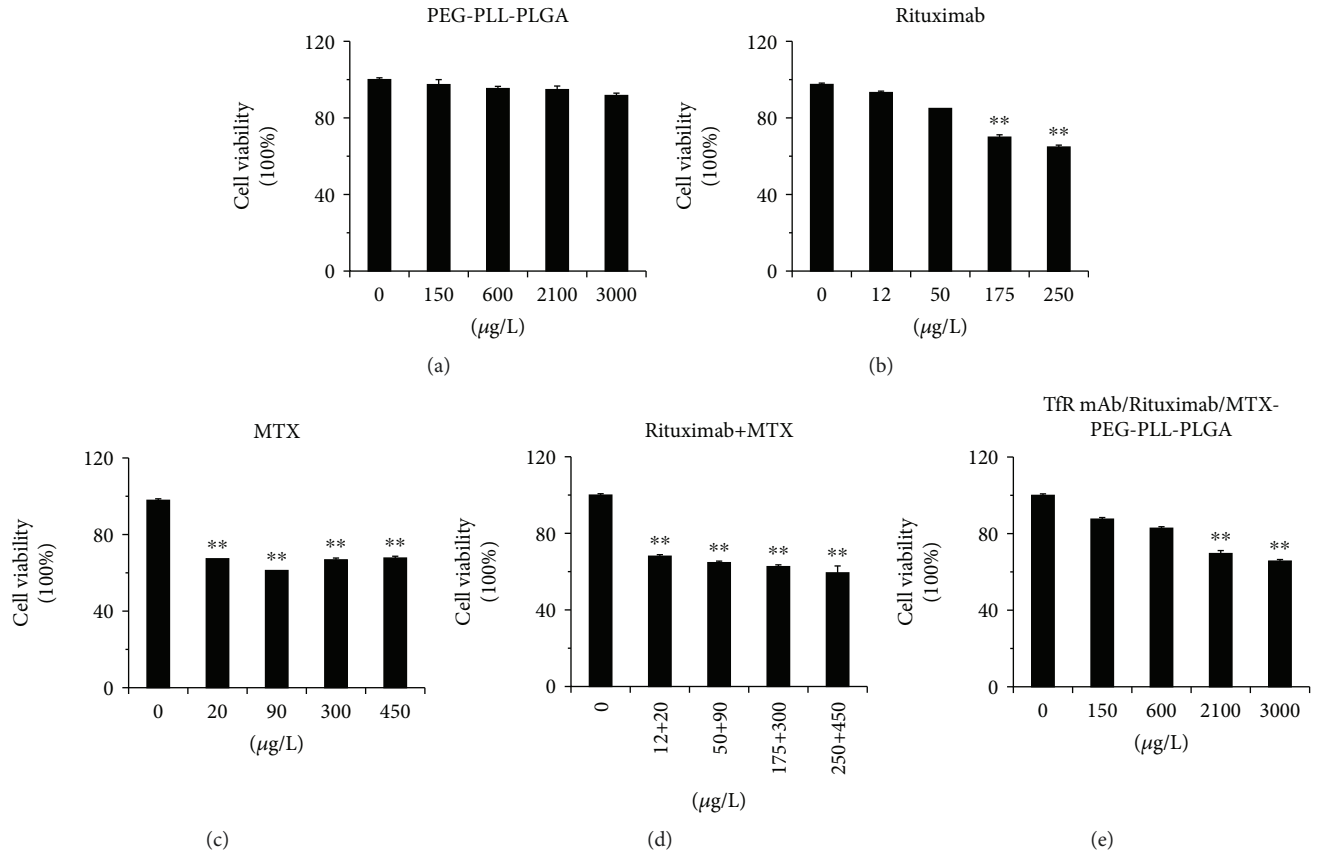

Figure 4: *In vitro* cytotoxicity evaluation of SU-DHL-4 cells using CCK assay. The SU-DHL-4 cells were treated by different drugs for 48 hours. (a) PEG-PLL-PLGA, (b) Rituximab, (c) MTX, (d) Rituximab combined with MTX, and (e) TfR mAb/Rituximab/MTX-PEG-PLL-PLGA nanoparticles. Data are shown as the mean ± SD. $^{*}P < 0.05$; $^{**}P < 0.01$.

of nanoparticles before and after drug loading: PEG-PLL-PLGA (Figure 1(a)), Rituximab/MTX-PEG-PLL-PLGA (Figure 1(b)), and TfR mAb Rituximab/MTX-PEG-PLL-PLGA (Figure 1(c)). The size and size distribution of nanoparticles were also determined. The average diameter of the kinds of particles ranged from 310.7 nm before drug loading (Figure 1(d)) to 354.4 nm after Rituximab/MTX loading (Figure 1(e)) and to 365.8 nm after TfR mAb cross-linking (Figure 1(f)).

Then, a UV-Vis spectrophotometer was used to determine the concentrations of Rituximab at 278 nm (Figure 2(a)), MTX at 258 nm (Figure 2(b)), and TfR mAb at 279 nm (Figure 2(c)) in the drug-loaded nanoparticles. Based on the standard curve, the drug loading content (DLC) and drug loading efficiency (DLE) were calculated. The percentages of DLC of Rituximab and MTX were 8.17% and 14.87% (Figure 2(d)), respectively. The percentages of DLC of Rituximab and MTX were 87.25% and 79.41% (Figure 2(d)), respectively. In addition, the TfR mAb modification rate is up to 70.90% (Figure 2(d)), suggesting that the rates of drug loading and encapsulation were comparable and efficient.

The drug release of the nanoparticles *in vitro* was further evaluated. The sustained release rates of Rituximab and MTX reached 49.9% and 54.12%, respectively (Figure 3). Until 168 hours (7 days), the sustained release efficiency was maintained to 77.6% and 81.81% (Figure 3), indicating that the sustained release of the two drugs in the nanoparticles owned a long effect.

To assess the cytotoxicity of the drugs, we treated the B lymphocytes and SU-DHL-4 cells by different concentrations of drugs (PEG-PLL-PLGA, Rituximab, MTX, Rituximab +MTX, and TfR mAb/Rituximab/MTX-PEG-PLL-PLGA), respectively. The cell viability of SU-DHL-4 cells was not affected treated with PEG-PLL-PLGA for 48 hours (Figure 4(a)), while it was significantly reduced treated with 175 and 250 μg/L Rituximab for 48 hours (Figure 4(b)), MTX (ranged from 20 to 450 μg/L) for 48 hours (Figure 4(c)), and Rituximab combined with MTX for 48 hours (Figure 4(d)), respectively. Moreover, the cell viability of SU-DHL-4 cells treated with a high concentration of TfR mAb/Rituximab/MTX-PEG-PLL-PLGA for 48 hours was significantly reduced, ranging from 0.59 to approximately 0.62 ($P < 0.01$ vs. mock control), which was commensurate with other groups (Figure 4(e)).

We selected drug concentrations in subsequent experiments for further evaluation as follows: 175 μg/L Rituximab, 300 μg/L MTX, 175 μg/L Rituximab+300 μg/L MTX, and 2100 μg/L TfR mAb/Rituximab/MTX-PEG-PLL-PLGA for 48 hours of treatment. The cell cycle was detected by flow cytometry (Figure 5(a)). Compared with the control group, Rituximab, MTX, or coprocessing of Rituximab plus MTX treatment resulted in a decrease in the proportion of S phase

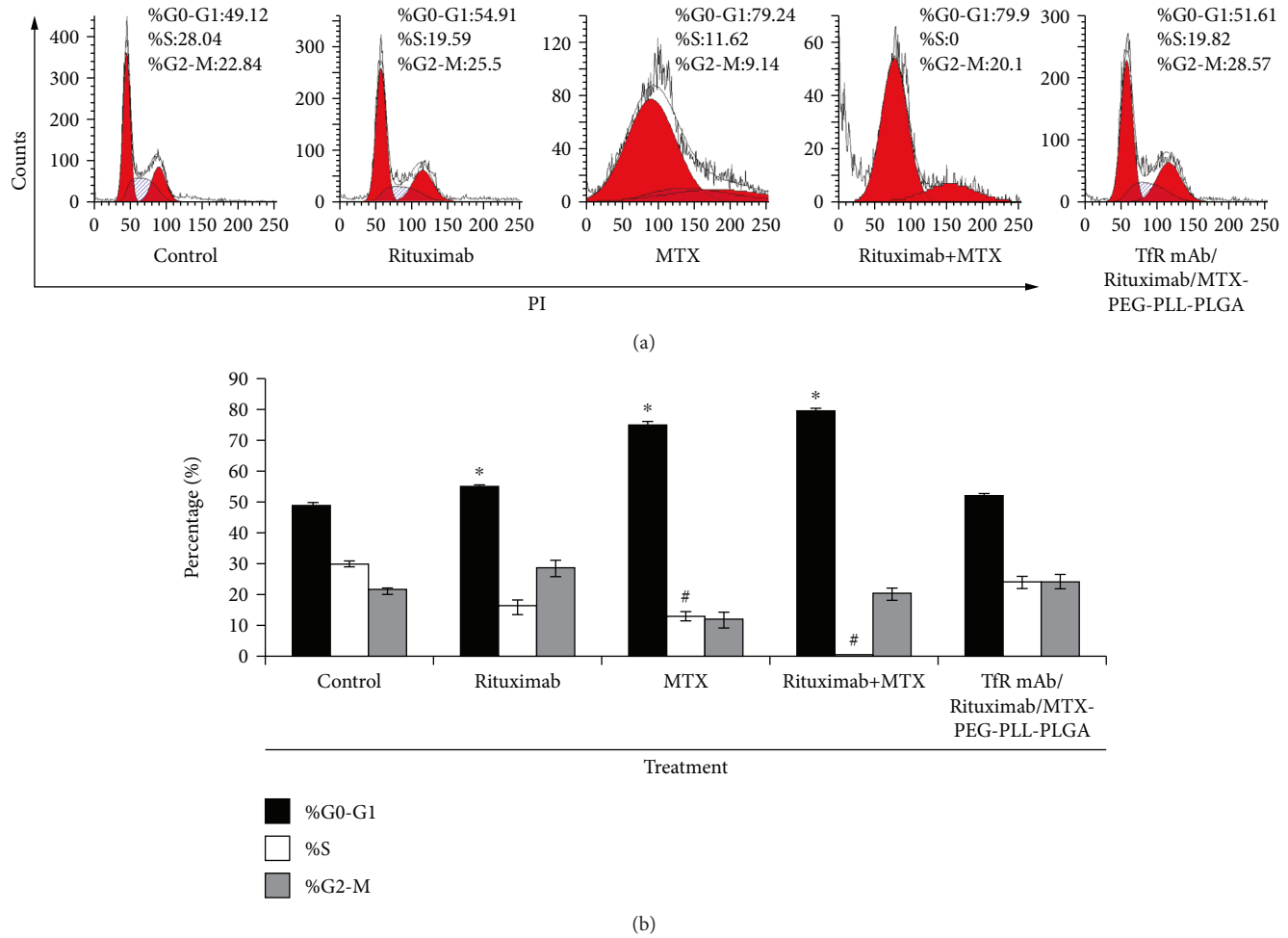

Figure 5: (a) Cell cycle analysis of SU-DHL-4 cells treated by different kinds of drug for 48 hours using flow cytometry. (b) The percentages of phases in the cell cycle are shown as the mean ± SD. $^{*}P < 0.05$; $^{**}P < 0.01$.

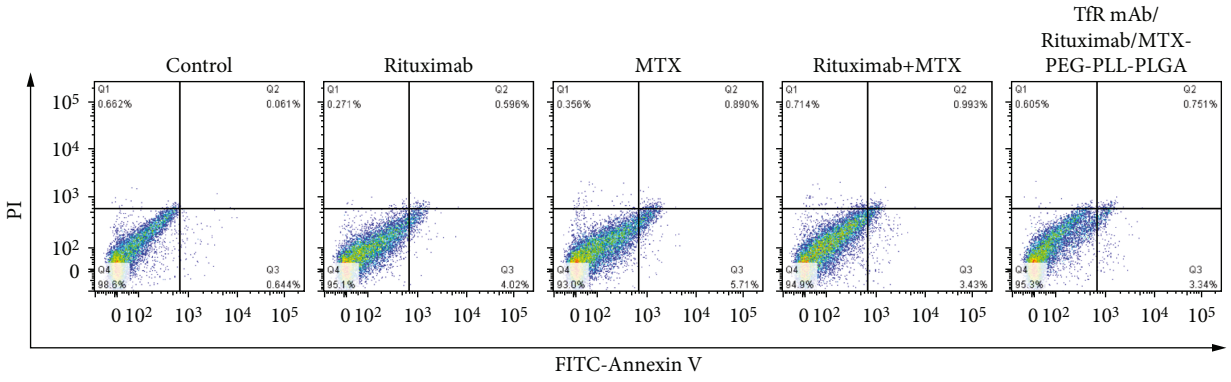

Figure 6: Cell apoptosis analysis of SU-DHL-4 cells treated by different kinds of drug for 48 hours using flow cytometry with PI and FITC-Annexin V staining.

cells while there is an increase in the proportion of G0-G1 (Figure 5(b)). However, TfR mAb/Rituximab/MTX-PEG-PLL-PLGA treatment did not have a significant effect on the cell cycle (Figure 5(b)).

To further identify the cytotoxicity of the drugs, cell apoptosis affected by drugs was determinate by forward scatter (FSC) and side scatter (SSC) in flow cytometry. Being measured for cell size and granularity in cell apoptosis, the cell shrinks and releases apoptotic blebs as reflected by decreasing FSC and increasing SSC compared to normal cells. Exposed phosphatidylserine can be detected in the presence of calcium using FITC-Annexin V. After SU-DHL-4 cells

were treated with Rituximab, MTX, Rituximab+MTX, or TfR mAb/Rituximab/MTX-PEG-PLL-PLGA, the cell apoptosis rates of all treated groups were significantly higher than that of the control group (Figure 6). These results demonstrated the effect of cytotoxicity by TfR mAb/Rituximab/MTX-PEG-PLL-PLGA drug-loaded nanoparticles which relied on cell apoptosis.

4. Conclusions

In summary, we showed novel anticancer effects of TfR mAb cross-linked Rituximab and MTX drug-loaded nanoparticles on B lymphocytes and preliminarily studied the interference mechanism involved in cell cycle and cell apoptosis. The multifunctional single drug-loaded nanoparticles displayed maintained stability and precise targeting, which enhanced the anticancer efficiency of cell death for B lymphocytes. This enhanced cancer treatment provides a potential strategy in clinical anticancer therapy and deeper insights into the physiological and pathophysiological variability among individual patients. These findings also guide the design of precise nanomedicine towards personalized cancer treatments.

Data Availability

The data used to support the findings of this study are included within the article.

Conflicts of Interest

The authors declare that there is no conflict of interest regarding the publication of this article.

Acknowledgments

This work was supported by the National Natural Science Foundation of China Program (81600161).

Supplementary Materials

A precise and efficient carrier for the Rituximab and Methotrexate (MTX) was designed as nanomedicine for anticancer action in B lymphocytes. After the synthesis of Rituximab/MTX-PEG-PLL-PLGA, the TfR mAb was subsequently cross-linked to the nanoparticles. The nanoparticle-loaded system can precisely and efficiently transport the Rituximab and MTX drug with long-term sustained release of into SU-DHL-4 cells. The TfR mAb/Rituximab/MTX-PEG-PLL-PLGA nanoparticle increased the cell apoptosis in the SU-DHL-4 cells, resulting in a notable cytotoxicity in B lymphocytes. *(Supplementary Materials)*

References

[1] N. Oishi and X. W. Wang, "Novel therapeutic strategies for targeting liver cancer stem cells," *International Journal of Biological Sciences*, vol. 7, no. 5, pp. 517–535, 2011.

[2] M. Nikolaou, A. Pavlopoulou, A. G. Georgakilas, and E. Kyrodimos, "The challenge of drug resistance in cancer treatment: a current overview," *Clinical & Experimental Metastasis*, vol. 35, no. 4, pp. 309–318, 2018.

[3] M. Alev, L. Egenberger, L. Muhleisen et al., "Targeting of drug-loaded nanoparticles to tumor sites increases cell death and release of danger signals," *Journal of Controlled Release*, vol. 285, pp. 67–80, 2018.

[4] M. N. Messmer, A. G. Snyder, and A. Oberst, "Comparing the effects of different cell death programs in tumor progression and immunotherapy," *Cell Death and Differentiation*, vol. 26, no. 1, pp. 115–129, 2019.

[5] M. B. Agarwal, "Is cancer chemotherapy dying?," *Asian Journal of Transfusion Science*, vol. 10, no. 3, pp. 1–7, 2016.

[6] N. R. Jabir, S. Tabrez, G. M. Ashraf, S. Shakil, G. A. Damanhouri, and M. A. Kamal, "Nanotechnology-based approaches in anticancer research," *International Journal of Nanomedicine*, vol. 7, pp. 4391–4408, 2012.

[7] S. A. Chew and S. Danti, "Biomaterial-based implantable devices for cancer therapy," *Advanced Healthcare Materials*, vol. 6, no. 2, 2017.

[8] S. Kim, Y. Shi, J. Y. Kim, K. Park, and J. X. Cheng, "Overcoming the barriers in micellar drug delivery: loading efficiency, in vivostability, and micelle-cell interaction," *Expert Opinion on Drug Delivery*, vol. 7, no. 1, pp. 49–62, 2010.

[9] C. von Roemeling, W. Jiang, C. K. Chan, I. L. Weissman, and B. Y. S. Kim, "Breaking down the barriers to precision cancer nanomedicine," *Trends in Biotechnology*, vol. 35, no. 2, pp. 159–171, 2017.

[10] C. D. Walkey, J. B. Olsen, H. Guo, A. Emili, and W. C. Chan, "Nanoparticle size and surface chemistry determine serum protein adsorption and macrophage uptake," *Journal of the American Chemical Society*, vol. 134, no. 4, pp. 2139–2147, 2012.

[11] J. Rueff and A. S. Rodrigues, "Cancer drug resistance: a brief overview from a genetic viewpoint," *Methods in Molecular Biology*, vol. 1395, pp. 1–18, 2016.

[12] B. Tyler, D. Gullotti, A. Mangraviti, T. Utsuki, and H. Brem, "Polylactic acid (PLA) controlled delivery carriers for biomedical applications," *Advanced Drug Delivery Reviews*, vol. 107, pp. 163–175, 2016.

[13] B. Layek, T. Sadhukha, J. Panyam, and S. Prabha, "Nano-engineered mesenchymal stem cells increase therapeutic efficacy of anticancer drug through true active tumor targeting," *Molecular Cancer Therapeutics*, vol. 17, no. 6, pp. 1196–1206, 2018.

[14] D. Rosenblum, N. Joshi, W. Tao, J. M. Karp, and D. Peer, "Progress and challenges towards targeted delivery of cancer therapeutics," *Nature Communications*, vol. 9, no. 1, p. 1410, 2018.

[15] L. Zhang, D. Jing, L. Wang et al., "Unique photochemo-immuno-nanoplatform against orthotopic xenograft oral cancer and metastatic syngeneic breast cancer," *Nano Letters*, vol. 18, no. 11, pp. 7092–7103, 2018.

[16] J. Ma, K. Kang, Y. Zhang, Q. Yi, and Z. Gu, "Detachable polyzwitterion coated ternary nanoparticles based on peptide dendritic carbon dots for efficient drug delivery in cancer therapy," *ACS Applied Materials & Interfaces*, vol. 10, no. 50, pp. 43923–43935, 2018.

[17] Z. Li, S. Tan, S. Li, Q. Shen, and K. Wang, "Cancer drug delivery in the nano era: an overview and perspectives (Review)," *Oncology Reports*, vol. 38, no. 2, pp. 611–624, 2017.

[18] A. Joly-Battaglini, C. Hammarstrom, B. Stankovic et al., "Rituximab efficiently depletes B cells in lung tumors and normal lung tissue," *F1000Res*, vol. 5, p. 38, 2016.

[19] S. H. Lim and R. Levy, "Translational medicine in action: anti-CD20 therapy in lymphoma," *Journal of Immunology*, vol. 193, no. 4, pp. 1519–1524, 2014.

[20] M. G. Cipolleschi, I. Marzi, E. Rovida, M. Olivotto, and P. Dello Sbarba, "Low-dose methotrexate enhances cycling of highly anaplastic cancer cells," *Cell Cycle*, vol. 16, no. 3, pp. 280–285, 2017.

[21] N. Hagner and M. Joerger, "Cancer chemotherapy: targeting folic acid synthesis," *Cancer Management and Research*, vol. 2, pp. 293–301, 2010.

Hindawi
Journal of Nanomaterials
Volume 2019, Article ID 8936095, 9 pages
https://doi.org/10.1155/2019/8936095

Research Article

Highly Sensitive Detection of Dopamine at Ionic Liquid Functionalized RGO/ZIF-8 Nanocomposite-Modified Electrode

Lei Cheng, Youjun Fan, Xingcan Shen, and Hong Liang

State Key Laboratory for Chemistry and Molecular Engineering of Medicinal Resources, School of Chemistry and Pharmaceutical Science, Guangxi Normal University, Guilin 541004, China

Correspondence should be addressed to Lei Cheng; chenglei@mailbox.gxnu.edu.cn, Xingcan Shen; xcshen@mailbox.gxnu.edu.cn, and Hong Liang; hliang@gxnu.edu.cn

Received 28 April 2019; Accepted 11 July 2019; Published 25 August 2019

Guest Editor: Laijun Liu

A hybrid and hierarchical nanocomposite was successfully prepared by the growth of zeolitic imidazolate framework-8 (ZIF-8) on the template of ionic liquid (IL, [Bmim][BF_4]) functionalized reduced graphene oxide (IL-RGO). The structure and morphology of the IL-RGO/ZIF-8 nanocomposite were characterized by X-ray diffraction (XRD), scanning electron microscopy (SEM), Fourier transform infrared spectrometer (FTIR), and Raman spectroscopy. The results showed that RGO sheets were refrained from restacking by IL, and ZIF-8 nanoparticles grew well on the surface of IL-RGO. Owing to the synergistic effect from large surface area and excellent electrocatalytic activity of ZIF-8 and great electrical conductivity of IL-RGO, a highly sensitive sensor for dopamine (DA) can be obtained. IL-RGO/ZIF-8-modified electrode exhibits good electrocatalytic activity and electroconductive properties towards DA which were investigated by cyclic voltammetry (CV), differential pulse voltammetry (DPV), and electrochemical impedance spectroscopy (EIS). Compared with bare or IL-RGO-modified electrodes, the IL-RGO/ZIF-8-modified electrode effectively depressed the oxidation overpotential of DA. The linear response range of DA was from 1.0×10^{-7} to 1.0×10^{-4} mol/L with a low detection of limit 3.5×10^{-8} mol/L. In addition, the sensor was shown to provide satisfactory stability for the determination of DA.

1. Introduction

As a message transmission medium between neurons and the brain, dopamine (DA) plays an important role as a neurotransmitter in mammalian central nervous systems [1, 2]. Several neurological illnesses could be related to an abnormal dopaminergic neuron process [3]. As a result, the clinical analysis needs an accurate, sensitive, and rapid determination of DA. Many methods, such as chemiluminescence [4], liquid chromatography [5, 6], capillary electrophoresis [7], and fluorescence [8], were proposed for detecting DA. Compared with them, the electrochemical method shows lower cost of instrument and operation, faster response, and higher accuracy [9].

Zeolitic imidazolate frameworks (ZIF) have ordered porous structure, constructed from metal ions and organic ligands, and are characterized by micropore size, high porosity, and large surface areas. ZIF-8 is one of the most interesting materials in the ZIF family, which is considered as a promising substrate for constructing electrochemical sensors [10, 11]. Ma et al. prepared an electrochemical biosensor based on ZIF-8 [12]; unfortunately, the conductivity of ZIF-8 is too poor and depresses the performance of the electrodes. Later, many researchers paid more attention to improve the conductivity of MOF-based composites with different conductive materials, such as metal nanoparticles [13, 14], organic polymers [15], and carbon [16, 17]. Based on excellent thermal, chemical, and mechanical stability, especially the exceptional electron transfer rate and superior electronic conductivity, graphene is widely used in sensing and biosensing [18]. Kinds of biomarker including glucose, hydrogen peroxide, dopamine, uric acid, ascorbic acid, and cancer markers have been detected based on graphene [19, 20]. The electrochemical determination performance was enhanced due to ultrafast electron transfer between the nanocomposite and electrode, which was caused by

the introduction of graphene. Kim et al. constructed a graphene/ZIF-8 composite by growing ZIF-8 crystal on graphene [21] to create fast mass transfer and high conductivity. Yu et al. prepared a hierarchical and hybrid nanocomposite of RGO/ZIF-8 which possesses high sensitivity for the determination of DA [22]. However, due to the high specific surface area of graphene, it is easy to form irreversible agglomerates or even restack through *van der Waals* interaction and π-π stacking [23]. As a result, it needs to be added much RGO to obtain good performance for the composite. It is reported that ionic liquid (IL) could prevent aggregation due to its wide solubility and created surface charge [24]. In addition, IL has a large electrochemical window up to 4 V, making it suitable for detecting various redox enzymes as electrochemical sensors and biosensors [25–27]. Therefore, the efficient direct electron transfer could be facilitated with the combination of IL and graphene.

In this work, nanocomposite IL-RGO/ZIF-8 (ionic liquid functionalized reduced graphene oxide/zeolitic imidazolate framework-8) was prepared by the growth of ZIF-8 on a small quantity of IL-RGO template. Crystal structure and morphology of the composite were identified by XRD and SEM, respectively. The prepared composite was coated on a glass carbon electrode (GCE) to fabricate a sensor for detecting DA. The electrochemical performance for DA detection is enhanced owing to the synergistic effect of ZIF-8 with large surface area and order porous structure and IL-RGO with high electronic conductivity.

2. Materials and Methods

2.1. Chemicals and Materials. Ionic liquid functionalized reduced graphene oxide (IL-RGO) was prepared according to Shao's method [28]. $Zn(CH_3COO)_2{\cdot}2H_2O$, 2-methylimidazole (Hmim), and dopamine (DA) were provided from Aladdin Reagent Co. Ltd. (Shanghai, China). H_2SO_4, $NaNO_3$, H_2O_2, hydrazine, 1-butyl-3-methylimidazolium tetrafluoroborate ([Bmim][BF_4]), and ethanol were obtained from Sinopharm Chemical Reagent Co. Ltd. Phosphate buffer solutions (PBS) with different pH values were prepared by mixing 0.02 M NaCl, $NaH_2PO_4{\cdot}2H_2O$, and $Na_2HPO_4{\cdot}12H_2O$. All chemicals were of analytical grade and used without further purification. Doubly distilled water (DDW) was used in these experiments.

2.2. Apparatus. The phase structure of ZIF-8 was identified by X-ray diffraction (XRD) on a Bruker D8-Advance diffractometer (Germany) using Cu $K\alpha$ radiation, $\lambda = 1.5415$ Å. Morphology of ZIF-8 and relative composites was observed by scanning electron microscopy (SEM, Philips-FEI, Netherlands). The bond vibration characterizations were investigated by Fourier transform infrared spectrometer (FTIR) (Perkin Elmer System 2000) and micro Raman spectroscopy (Renishaw-InVia, UK). Nitrogen adsorption-desorption isotherms were carried out using a volumetric adsorption analyzer (Bei Shi De 3H-2000PS4) at liquid nitrogen temperature (77 K). The surface area of the composites was determined by the Brunauer-Emmett-Teller (BET) method. Cyclic voltammetry (CV) and differential pulse voltammetry (DPV) were carried out on an electrochemical workstation (Parstat 3000A, American) with a conventional three-electrode system. An Ag/AgCl electrode [Ag/AgCl, KCl (sat′d)] was used as the reference electrode, a platinum plate as the auxiliary electrode, and glassy carbon electrodes (GCE) as the working electrode.

2.3. Preparation of ZIF-8 and IL-RGO/ZIF-8 Nanocomposite. An aqueous method for preparing ZIF-8 was employed as shown in literature [29]. And the preparation of IL-RGO/-ZIF-8 nanocomposite was as follows: first, 0.134 g of $Zn(CH_3COO)_2{\cdot}2H_2O$ and 5.3333 g of Hmim were dissolved in 15 mL and 25 mL of DDW, respectively. Then, 28 μL, 56 μL, and 84 μL of IL-RGO suspension (corresponding to 0.05 wt%, 0.10 wt%, and 0.15 wt%, respectively, for the production ZIF-8, assigned as IL-RGO(1)/ZIF-8, IL-RGO(2)/ZIF-8, and IL-RGO(3)/ZIF-8) were dropped into the $Zn(CH_3COO)_2$ aqueous solution with vigorous stirring for 3 min. Afterwards, the Hmim solution was added into the $Zn(CH_3COO)_2$ solution with vigorous stirring for 5 min. The mixture kept quietly maturing for 48 h. Then, the product was collected by centrifugal separation at 5000 rpm for 10 min and washed with DDW for three times repeatedly. Finally, the product was dried at 60°C for 48 h under vacuum.

2.4. Preparation of IL-RGO/ZIF-8-Modified Electrode. Bare GCE was polished with 50 nm alumina slurry and rinsed ultrasonically in DDW for 1 min, then dried by N_2. The IL-RGO/ZIF-8 was ultrasonically dispersed in DDW with the concentration of 1.0 mg mL^{-1}. Then, 10 μL of IL-RGO/ZIF-8 nanocomposite dispersion was dropped on the polished GCE surface and dried at room temperature to obtain the IL-RGO/ZIF-8-modified GCE (IL-RGO/ZIF-8/GCE). In addition, only ZIF-8-modified GCE (ZIF-8/GCE) and IL-RGO-modified GCE (IL-RGO/GCE) were prepared in the same way for comparison.

3. Results and Discussion

3.1. Characterization of IL-RGO/ZIF-8 Nanocomposite. The morphology of the nanocomposite was carried out by SEM. Smooth and flat sheets without wrinkles and noticeable pore in the rigid structure are observed in the image of IL-RGO as shown in Figure 1(a). It suggests that the aggregation of the RGO is prevented by ionic liquid due to its wide solubility and created surface charge. Pristine ZIF-8 crystals can be seen in Figure 2(b); it displays tightly distributed and homogeneous nanoparticles with hexagonal morphology. The average particle size is approximately 200 nm. With the increased contents of IL-RGO, the morphology of ZIF-8 crystals in IL-RGO/ZIF-8 nanocomposites is identical with the pristine ZIF-8, while the particle size increases slightly to 320 nm for IL-RGO(1)/ZIF-8 (Figure 1(c)) and then reduces to 120 nm for IL-RGO(2)/ZIF-8 and IL-RGO(3)/-ZIF-8 (Figures 1(d) and 1(e)). The increase of size of ZIF-8 on IL-RGO could associate with the nucleating center of ZIF-8 provided by IL-RGO, while the decrease may be

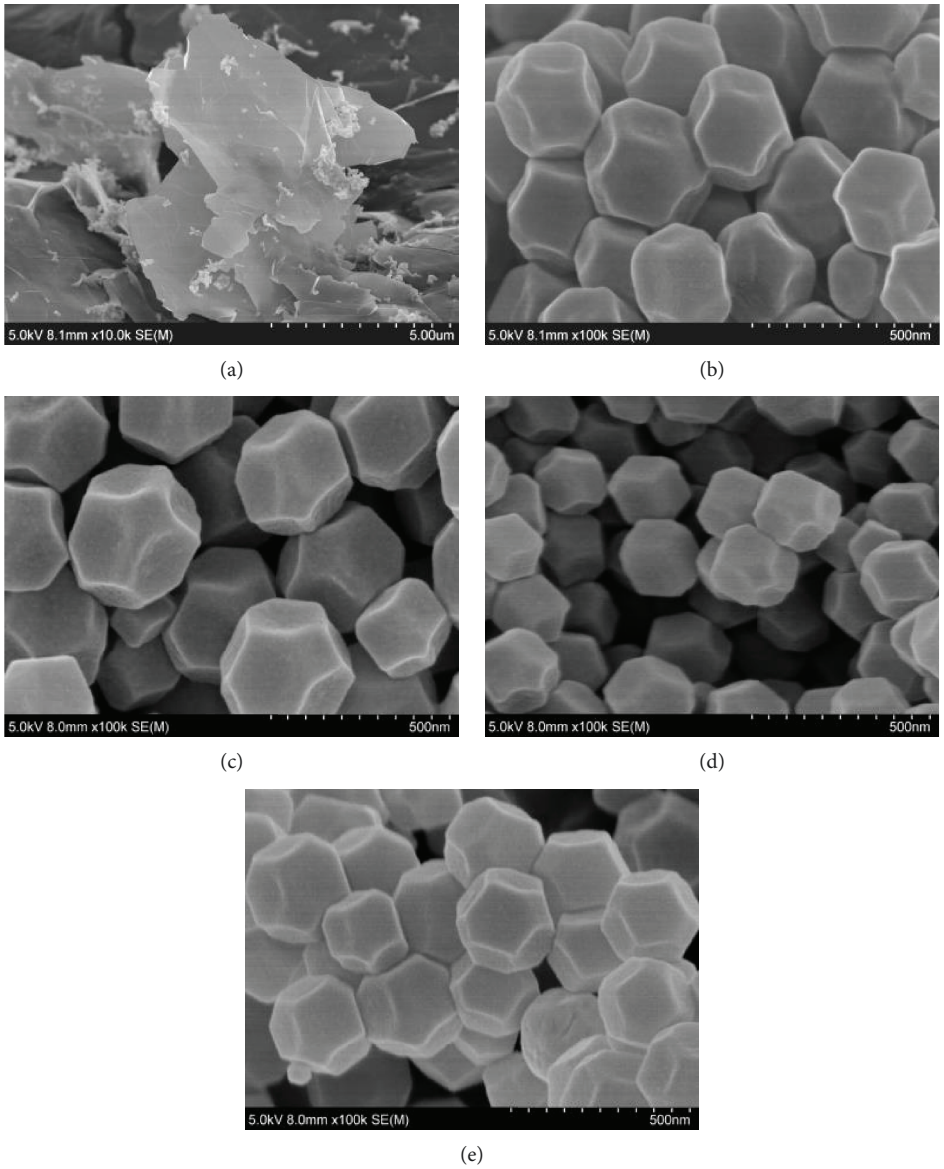

Figure 1: SEM images of (a) IL-RGO, (b) ZIF-8, (c) IL-RGO(1)/ZIF-8, (d) IL-RGO(2)/ZIF-8, and (e) IL-RGO(3)/ZIF-8.

contributed to the fact that (1) the 2D IL-RGO sheet restrains the free growth of ZIF-8 in the 3D direction and (2) the created surface charge on IL-RGO provides more nucleation centers for ZIF-8.

The XRD patterns of IL-RGO, ZIF-8, and IL-RGO/-ZIF-8 nanocomposites are shown in Figure 2(a). The Bragg reflections of ZIF-8 are identified well with the previous report [30–33]. It suggests that the pure ZIF-8 phase is successfully obtained. According to XRD patterns of the ZIF-8 and IL-RGO/ZIF-8 composites, the same Bragg reflections indicate that IL-RGO does not destroy the crystalline structure of ZIF-8. However, no characteristic peak of IL-RGO is presented in the patterns of the nanocomposites because of a low content of IL-RGO. On the other hand, the reflection (420) of ZIF-8 is the same angle (2theta ~23.5°) to the peak (002) of IL-RGO, a reflection crossover could be presented.

Since the content of IL-RGO is very low, the growth of ZIF-8 nanocrystals that occurred on the IL-RGO surfaces cannot be found by SEM and XRD. In order to further study the interaction between IL-RGO and ZIF-8, FTIR and micro Raman spectroscopy were carried out. Raman spectra are shown in Figure 2(b) for which IL-RGO has two feature peaks at 1354 and 1586 cm^{-1} associated with the G and D bands, respectively. The G band contributes to the vibration of graphitic (sp^2 carbon) lattice while the D band is related to the defects and disordered regions of the lattice caused by the oxidation reaction. Raman shifts of ZIF-8 at 686, 1144, 1183, 1459, and 1405 cm^{-1} are assigned to the vibrational modes of the Hmim ligand [34–36]. It is clear that the Raman shifts of both IL-RGO and ZIF-8 are presented in IL-RGO/ZIF-8 nanocomposites; furthermore, the intensity of feature peak 1586 cm^{-1} associated with the G band of RGO becomes stronger with the increase of IL-RGO in

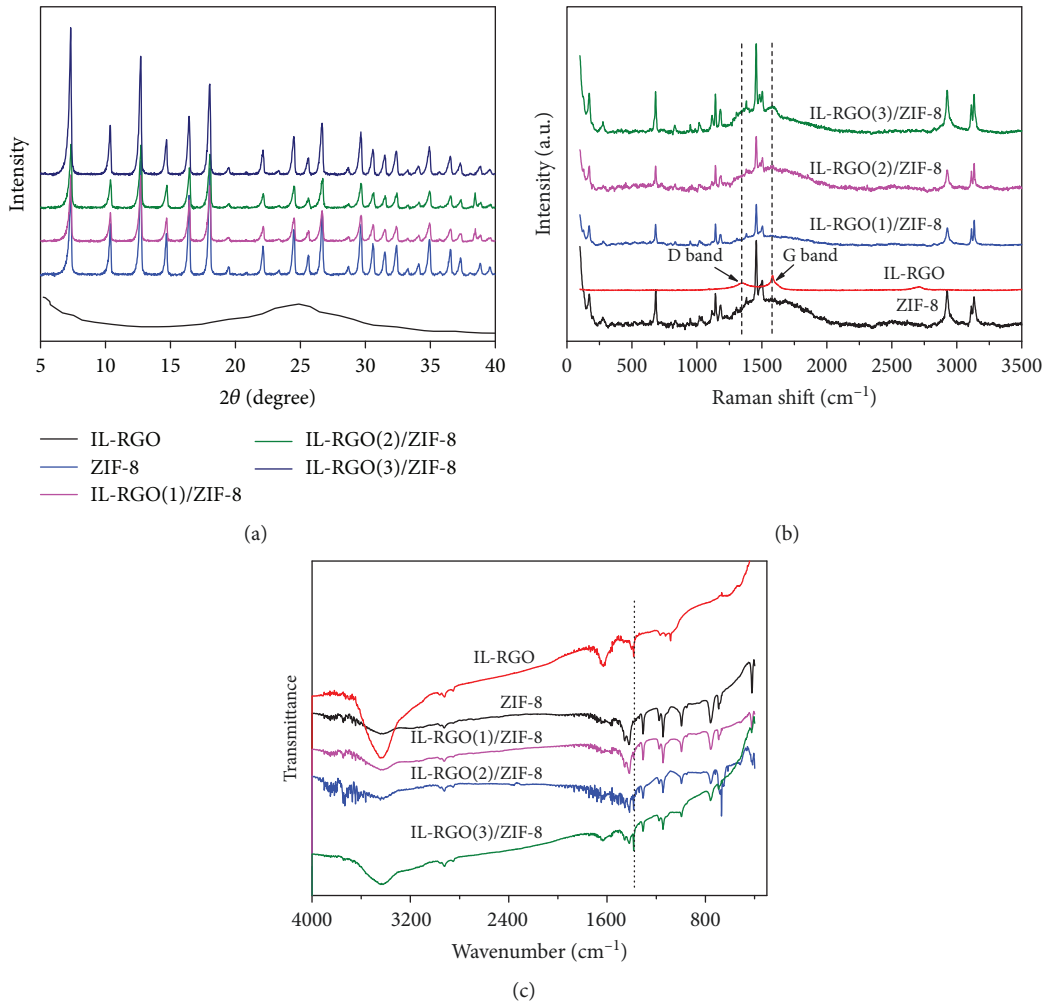

Figure 2: (a) XRD patterns, (b) Raman spectra, and (c) FTIR spectra of ZIF-8, IL-RGO, and IL-RGO/ZIF-8 nanocomposites.

the IL-RGO/ZIF-8 nanocomposites. It suggests that ZIF-8 is anchored on the IL-RGO.

The FTIR spectra of the nanocomposites are shown in Figure 2(c). The major absorption peaks are clear at 3428 cm^{-1} (O–H), at 1760 cm^{-1} (C=O), at 1650 cm^{-1} (skeletal C=C), at 1244 cm^{-1} (C–OH), and at 1080 cm^{-1} (C–O) [37–39]. The FTIR spectrum of ZIF-8 shows the vibrational modes of the Hmim ligand. The peaks at 3135 cm^{-1}, 2929 cm^{-1}, 1558 cm^{-1}, and 421 cm^{-1} are related to the aromatic and the aliphatic C–H, C=N, and Zn–N, respectively [40, 41]. The FTIR spectrum of the nanocomposites displays the same features to XRD as the ZIF-8 spectrum overwhelmed the peaks of IL-RGO due to the low loading content of IL-RGO. However, the absorption peak at 1382 cm^{-1} of IL-RGO is enhanced with the increase of IL-RGO in the IL-RGO/ZIF-8 nanocomposites, which is in agreement with the Raman results.

Nitrogen adsorption-desorption isotherms of pure ZIF-8 and IL-RGO/ZIF-8 composites are shown in Figure 3. The N_2 adsorption of the pure ZIF-8 and IL-RGO/ZIF-8 composites exhibited type I profile, which indicated that both ZIF-8 and IL-RGO/ZIF-8 composites were dominated by microporous structure. The surface area of pure ZIF-8, IL-RGO(1)/ZIF-8, IL-RGO(2)/ZIF-8, and IL-RGO(3)/ZIF-8 is 1067.5 m^2/g, 979.8 m^2/g, 1030.4 m^2/g, and 914.6 m^2/g, respectively. Among the IL-RGO/ZIF-8 nanocomposites, IL-RGO(2)/ZIF-8 owns the largest microporous surface area which is only a little smaller than that of pure ZIF-8. According to the electrochemical response of DA for the nanocomposites as shown in Figure 4, IL-RGO(2)/ZIF-8 has the best detective performance with the strongest current peak. The microporous surface area could play an important role on improving the electrochemical capability. Although pure ZIF-8 has the largest surface area with 1067.5 m^2/g, the electrochemical detection ability of pure ZIF-8 is worse than that of IL-RGO/ZIF-8 composites due to its poor electrical conductivity.

3.2. Electrochemical Response of DA for Different Electrodes. The electrochemical behavior of DA at different electrodes was studied in the PBS (0.1 M, pH 7.0) using the CV method in order to evaluate the electrocatalytic activity of the IL-RGO/ZIF-8 nanocomposites as shown in Figure 4. It can be seen that DA undergoes a good reversible oxidation-reduction reaction at the bare GCE and IL-RGO/GCE. Anodic and cathodic peaks of bare GCE are stronger than

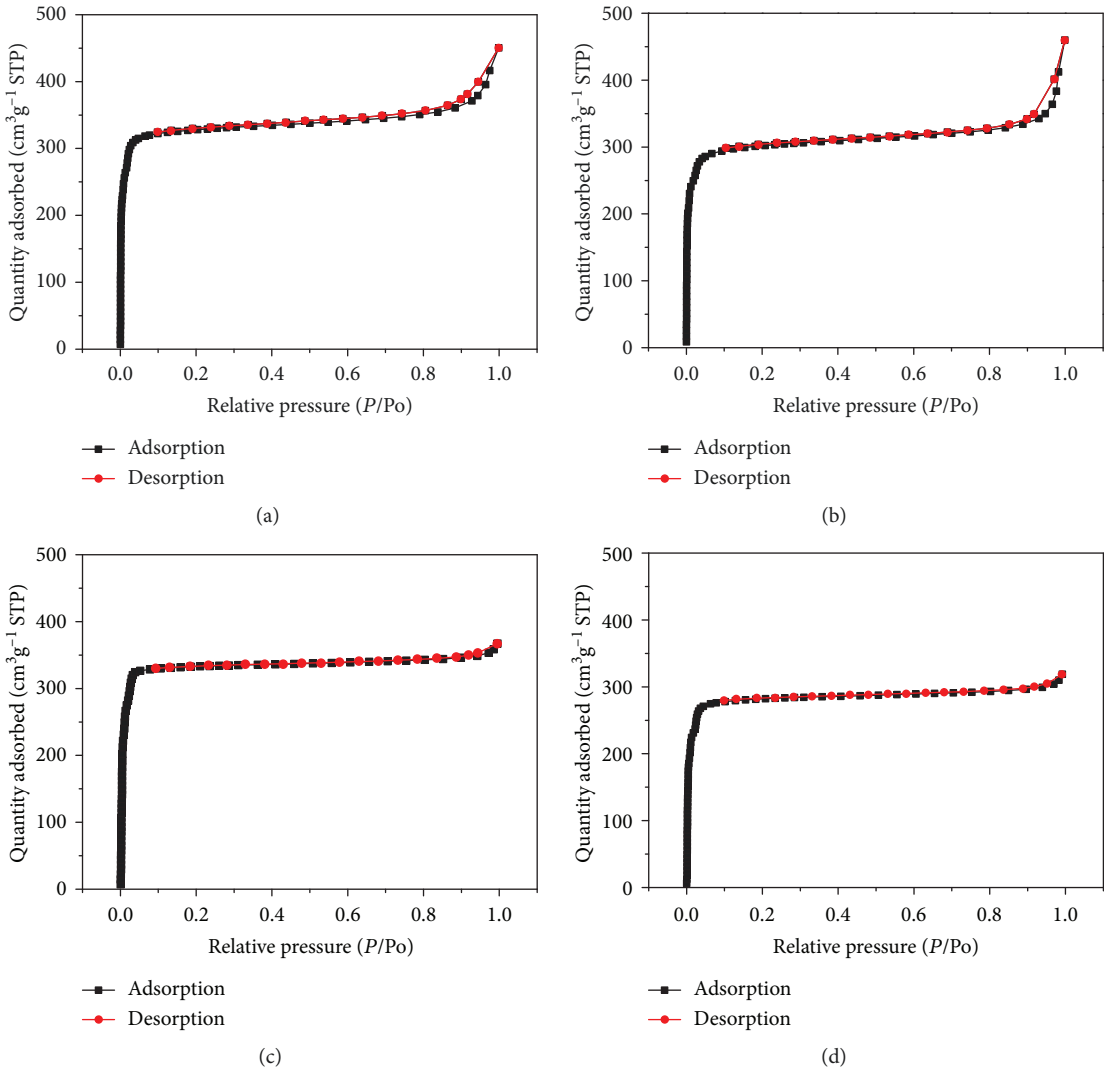

Figure 3: N_2 adsorption-desorption isotherms for (a) ZIF-8, (b) IL-RGO(1)/ZIF-8, (c) IL-RGO(2)/ZIF-8, and (d) IL-RGO(3)/ZIF-8.

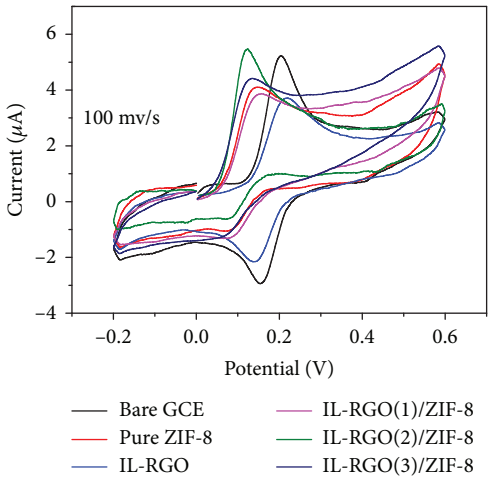

Figure 4: CV curves of bare GCE, ZIF-8/GCE, IL-RGO/GCE, and IL-RGO/ZIF-8/GCE in 0.1 M PBS solution (pH 7.0) containing 1.0×10^{-4} M DA.

those of IL-RGO/GCE, indicating a possible repulsive interaction between DA and IL-RGO. When ZIF-8 is introduced in electrodes, the electrochemical reaction of DA becomes highly irreversible; in addition, the overpotential is significantly decreased. It is very important that IL-RGO/ZIF-8/GCE shows the strongest current peak, which is associated with the synergistic effect from large surface areas of ZIF-8 and good electrical conductivity of IL-RGO. The content of IL-RGO in the composite influenced the electrochemical capability of modified electrode due to the repulsive effect of IL-RGO, and the 0.10 wt% was identified the best proportion of IL-RGO. This kind of composite was employed for the following determination of DA.

3.3. Impedance and Transport Behavior of IL-RGO/ZIF-8 Nanocomposites. Electrochemical impedance spectroscopy (EIS) is an effective tool for probing the interfacial behavior of modified electrodes; furthermore, it is also usually employed for understanding the chemical transformation associated with conductive supports [42]. Figure 5(a) shows EIS results of the bare GCE, ZIF-8/GCE, IL-RGO/GCE, and

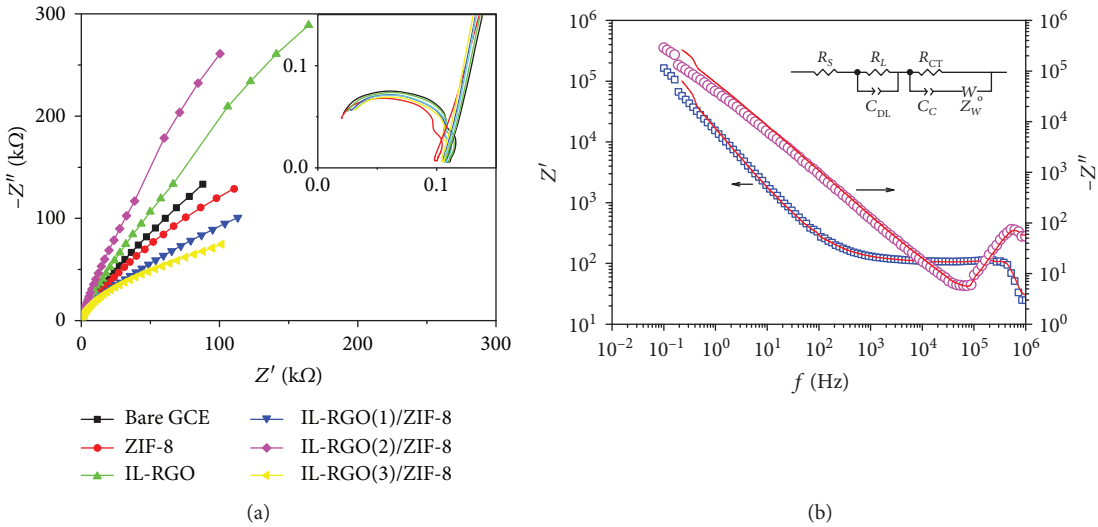

Figure 5: (a) Nyquist plots of the bare GCE, ZIF-8/GCE, IL-RGO/GCE, and IL-RGO/ZIF-8 with different contents of IL-RGO-modified GCEs in the presence of 0.1 M PBS solution (pH 7.0) containing 1.0×10^{-4} M DA; inset: semicircles at high frequency. (b) Frequency as a function of the real part and imaginary part of impedance of IL-RGO(2)/ZIF-8/GCE (the diamond is the real part of the impedance and the pink circle is the imaginary part of the impedance). Inset: the equivalent circuit of the IL-RGO/ZIF-8/GCE electrode in PBS solid solution. The red solid lines were fitted by the inset equivalent circuit.

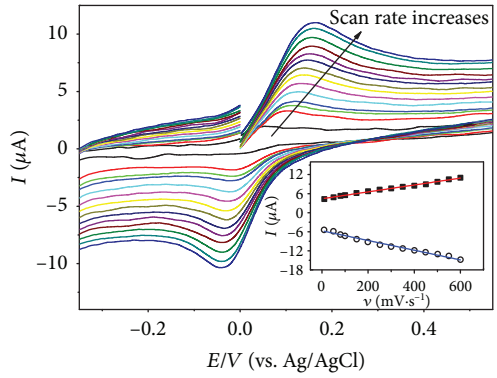

Figure 6: CV curves of IL-RGO(2)/ZIF-8/GCE in 0.1 M PBS solution (pH 7.0) containing 1.0×10^{-4} M DA at different scan rates: 10, 50, 80, 100, 150, 200, 250, 300, 350, 400, 450, 500, 550, and 600 mV·s^{-1}. Inset: plots of the anodic and cathodic peak currents (I_{pa} and I_{pc}) vs. the scan rate.

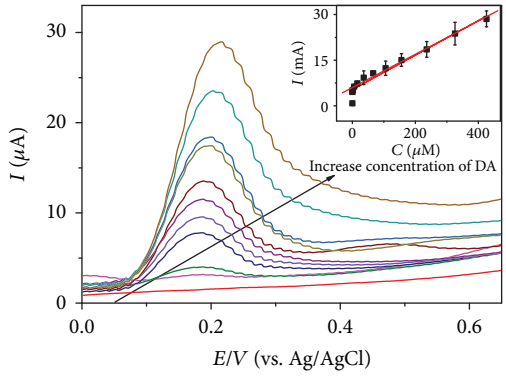

Figure 7: DPV curve for different concentrations of DA (from bottom to top: 0, 0.01, 0.1, 1, 5, 10, 30, 50, 70, 90, and 100 μM) on IL-RGO(2)/ZIF-8/GCE in 0.1 M PBS solution with pH 7.0 (scan rate: 100 mV·s^{-1}). Inset: the linear calibration plots of peak current (I_{pa}) versus the concentration of DA.

different contents of IL-RGO/ZIF-8/GCE in the presence of 0.1 M PBS solution (pH 7.0) containing 1.0×10^{-4} M DA at a frequency range from 0.01 Hz to 1 MHz. The typical Nyquist plot includes a semicircle at higher frequencies related to the electron transfer-limited process and a linear part at lower frequencies corresponding to the diffusion-limited processes. In this system, an addition semicircle can be found in the high frequency, as shown in the inset of Figure 5(a). In order to present the impedance information in the whole probing frequency, the real part and imaginary part of impedance of IL-RGO(2)/ZIF-8/GCE are plotted in Figure 5(b); the corresponding equivalent circuit is shown in the inset of Figure 5(b). The fitting curves (solid lines in Figure 5(b)) based on the equivalent circuit match the measurement results well, indicating that the circuit is reasonable to describe the electrochemical process. For the equivalent circuit, R_S is the bulk solution resistance of the electrolyte, C_{DL} is the electrical double layer capacitor of the system, R_L is the leakage resistance, C_C is the interfacial contact capacitance, R_{CT} is the ionic charge transfer resistance of DA on electrodes, and Z_W is the Warburg impedance. According to the fitting results, R_S and R_L of all plots are the same about 17.5 Ω and 81.5 Ω, respectively, while the magnitude of C_{DL} is about ~10^{-11} F slightly dependent on the modifiers on the electrodes. It suggests that the electrolyte and interface between solution and electrodes remain unchanged with different modifiers (IL-RGO, ZIF-8, and IL-RGO/ZIF-8). R_{CT} plays a key role on the performance of electrodes. It exhibits the electron transfer kinetics of the redox probe at the electrode interface. IL-RGO(2)/ZIF-8/GCE shows a low electron transfer resistance about 141700, which is lower than that of bare GEC and ZIF-8/GEC and IL-RGO(1)/ZIF-8/GCE. The

Table 1: Comparison of analytical performances for DA at different modified electrodes.

Modifier	Method	Linear ranges (μM)	Detection limits (μM)	Reference
GO	DPV	0.15-1	0.27	[45]
Polypyrrole@RGO	DPV	0.06-8	6×10^{-3}	[46]
Fe_3O_4/RGO	DPV	0.04-1.6	0.08	[47]
Fe_3O_4@ZIF-8/RGO	DPV	2×10^{-4}-10	6.67×10^{-4}	[48]
Au NPs@RGO	DPV	0.5-20	0.13	[49]
Cu(tpa)-EGR	DPV	1-50	0.21	[50]
IL-RGO/ZIF-8	DPV	0.1-100	0.035	This work

low resistance of IL-RGO(2)/ZIF-8/GCE is attributed to the synergistic effect of ZIF-8 and IL-RGO that enhanced the rate of electron transfer, which is agreement with the CV results.

The dynamic and transport characteristic of IL-RGO(2)/ZIF-8/GCE was determined by CV curves with different scan rates on the oxidation of 0.1 mM DA. The oxidation and reduction peak currents of DA, as shown in Figure 6, exhibit ideal linear relationship towards the scan rate (v) in the range from 10 to 600 mV·s^{-1}. It suggests that the electrochemical reaction of DA on IL-RGO(2)/ZIF-8/GCE is an adsorption-controlled process. The linear relationship is $I_{pa}\,(\mu A) = 4.3828 + 0.0108\,v$ (mV·s^{-1}) ($R^2 = 0.993$) and $I_{pc}\,(\mu A) = -5.6935 - 0.0153\,v$ (mV·s^{-1}) ($R^2 = 0.992$). The anodic peak shifts towards more positive while the cathodic peak shifts towards more negative with the increase of scan rate, which indicates a reversible electron transfer for DA. The number of electron transfer (n) of the redox process of DA can be estimated [43]:

$$I_p = \frac{n^2 F^2 A \Gamma v}{4RT} = \frac{nFQv}{4RT}, \quad (1)$$

where I_p is the peak current, F is the Faraday constant (96485 C ·mol^{-1}), A is the electrode surface area (m^2), Γ is the surface concentration of the electroactive substance (mol m^{-2}), v is the scanning rate (V s^{-1}), R is the gas molar constant (8.314 J mol^{-1} K^{-1}), T is the absolute temperature (298 K in this process), and $Q = nFA\Gamma$ is the peak area (calculated by the charges) (C). n is evaluated 1.95 from the relation between I_p and v. Further, the value of Γ can be obtained as 8.6×10^{-6} mol m^{-2}, which indicates that IL-RGO(2)/ZIF-8 provides a three-dimensional structure for the effective adsorption of DA. The increased concentration of DA on the electrode surface gives rise to the improvement of the sensitivity. As mentioned above, the redox reaction of DA includes two electrons and two protons process as suggested:

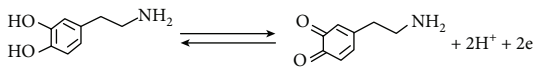

3.4. Determination of DA. DPV was employed to evaluate the electrochemical detection performance of IL-RGO(2)/ZIF-8/GCE towards DA due to its higher analytical signal than that of CV. It can be seen from Figure 7 that the peak current of DA increases linearly with the concentration of DA in the range from 1.0×10^{-7} M to 1.0×10^{-4} M. A linear relationship can be obtained: $I_p\,(\mu A) = 5.3328 + 0.0567\,C\,(\mu M)$ ($R^2 = 0.998$). The limit of detection (LOD) can be calculated 3.5×10^{-8} M ($S/N = 3$), and the sensitivity is 0.0567 μA μM^{-1}. The comparison of the performance of IL-RGO/ZIF-8 nanocomposite with other materials for sensing DA is listed in Table 1. It is clear that IL-RGO/ZIF-8 nanocomposite has a low detection limit and wide linear range. The excellent electrochemical analytical performance could be attributed to the synergistic effect of IL-RGO and ZIF-8. ZIF-8 has order pore structure and large surface area while IL-RGO has good electrical conductivity. Both electron transfer and mass transfer could be enhanced in the composite of IL-RGO and ZIF-8. Furthermore, the growth of ZIF-8 on IL-RGO prevents the aggregation of graphene, which promotes its electroanalysis performance [44].

3.5. Reproducibility and Stability of the Electrochemical Sensor. Six paralleled electrodes were prepared with the same condition for evaluating the reproducibility of IL-RGO(2)/ZIF-8/GCE by detecting current signal in PBS buffer with 1.0×10^{-4} M DA. The relative standard deviation (RSD) of the electrodes is 2.4%. The stability of IL-RGO(2)/-ZIF-8/GCE was verified by intermittently testing current signal of 1.0×10^{-4} M DA every three days with 5 cycles. After each testing, the electrodes were stored in a refrigerator at 4°C. The RSD for the testing is 4.7%. It indicates that good stability and reproducibility can be obtained for electrochemical detection by the prepared electrodes.

4. Conclusions

A novel nanocomposite IL-RGO/ZIF-8 was prepared by the in situ growth of ZIF-8 on a small quantity of IL-RGO template. Both electron transfer and mass transfer were enhanced due to the combination of the great electric conductivity for IL-RGO and the large surface area and order pore structure for ZIF-8. IL-RGO(2)/ZIF-8/GCE shows very good sensitivity for the determination of DA. In addition, the electrochemical sensor displays great reproducibility and stability. As a result, it is considered that the IL-RGO/ZIF-8 nanocomposite has excellent electrochemical performance and potential application as a novel electrochemical detection platform.

Data Availability

The data used to support the findings of this study are included within the article.

Conflicts of Interest

The authors declare that there is no conflict of interest regarding the publication of this paper.

Acknowledgments

Funding from the National Natural Science Foundation of China (21671046, 21502028, and 21601038) and the Guangxi Natural Science Foundation of China (2017GXNSFGA198004 and 2018GXNSFAA281220) is acknowledged. The authors appreciate Dr. Huahong Zou for his useful discussion and kind help.

References

[1] L. Wu, L. Y. Feng, J. S. Ren, and X. G. Qu, "Electrochemical detection of dopamine using porphyrin-functionalized graphene," *Biosensors and Bioelectronics*, vol. 34, no. 1, pp. 57–62, 2012.

[2] W. X. Zhang, J. Z. Zheng, J. G. Shi et al., "Nafion covered core–shell structured Fe_3O_4@graphene nanospheres modified electrode for highly selective detection of dopamine," *Analytica Chimica Acta*, vol. 853, pp. 285–290, 2015.

[3] S. E. Hyman and R. C. Malenka, "Addiction and the brain: the neurobiology of compulsion and its persistence," *Nature Reviews. Neuroscience*, vol. 2, no. 10, pp. 695–703, 2001.

[4] W. Gao, L. Qi, Z. Liu, S. Majeed, S. A. Kitte, and G. Xu, "Efficient lucigenin/thiourea dioxide chemiluminescence system and its application for selective and sensitive dopamine detection," *Sensors and Actuators B: Chemical*, vol. 238, pp. 468–472, 2017.

[5] K. T. Ngo, E. L. Varner, A. C. Michael, and S. G. Weber, "Monitoring dopamine responses to potassium ion and nomifensine by in vivo microdialysis with online liquid chromatography at one-minute resolution," *ACS Chemical Neuroscience*, vol. 8, no. 2, pp. 329–338, 2017.

[6] S. Janku, M. Komendova, and J. Urban, "Development of an online solid-phase extraction with liquid chromatography method based on polymer monoliths for the determination of dopamine," *Journal of Separation Science*, vol. 39, no. 21, pp. 4107–4115, 2016.

[7] H. F. Fang, M. L. Pajski, A. E. Ross, and B. J. Venton, "Quantitation of dopamine, serotonin and adenosine content in a tissue punch from a brain slice using capillary electrophoresis with fast-scan cyclic voltammetry detection," *Analytical Methods*, vol. 5, no. 11, pp. 2704–2711, 2013.

[8] J. J. Zhao, L. M. Zhao, C. Q. Lan, and S. L. Zhao, "Graphene quantum dots as effective probes for label-free fluorescence detection of dopamine," *Sensors and Actuators B: Chemical*, vol. 223, pp. 246–251, 2016.

[9] Q. Y. Zhao, F. F. Zhang, J. F. Xia et al., "Self-assembled ionic liquid-phosphomolybdic acid/reduced graphene oxide composite modified electrode for sensitive determination of dopamine," *ECS Journal of Solid State Science and Technology*, vol. 6, no. 6, pp. M3014–M3018, 2017.

[10] W. Liu and X. B. Yin, "Metal–organic frameworks for electrochemical applications," *TrAC Trends in Analytical Chemistry*, vol. 75, pp. 86–96, 2016.

[11] L. T. Liu, Y. L. Zhou, S. Liu, and M. T. Xu, "The applications of metal–organic frameworks in electrochemical sensors," *ChemElectroChem*, vol. 5, no. 1, pp. 6–19, 2018.

[12] W. J. Ma, Q. Jiang, P. Yu, L. F. Yang, and L. Q. Mao, "Zeolitic imidazolate framework-based electrochemical biosensor for in vivo electrochemical measurements," *Analytical Chemistry*, vol. 85, no. 15, pp. 7550–7557, 2013.

[13] J. Yang, H. L. Ye, F. Q. Zhao, and B. Z. Zeng, "A novel Cu_xO nanoparticles@ZIF-8 composite derived from core–shell metal–organic frameworks for highly selective electrochemical sensing of hydrogen peroxide," *ACS Applied Materials & Interfaces*, vol. 8, no. 31, pp. 20407–20414, 2016.

[14] H. R. Moon, D. W. Lim, and M. P. Suh, "Fabrication of metal nanoparticles in metal-organic frameworks," *Chemical Society Reviews*, vol. 42, no. 4, pp. 1807–1824, 2013.

[15] Z. Zhang, H. T. H. Nguyen, S. A. Miller, and S. M. Cohen, "polyMOFs: a class of interconvertible polymer-metal-organic-framework hybrid materials," *Angewandte Chemie International Edition*, vol. 54, no. 21, pp. 6152–6157, 2015.

[16] Z. H. Xiang, Z. Hu, D. P. Cao et al., "Metal–organic frameworks with incorporated carbon nanotubes: improving carbon dioxide and methane storage capacities by lithium doping," *Angewandte Chemie International Edition*, vol. 50, no. 2, pp. 491–494, 2011.

[17] Y. F. Jin, C. Y. Ge, X. B. Li, M. Zhang, and G. R. Xu, "A sensitive electrochemical sensor based on ZIF-8–acetylene black–chitosan nanocomposites for rutin detection," *RSC Advances*, vol. 8, no. 57, pp. 32740–32746, 2018.

[18] J. F. Xia, X. Y. Cao, Z. H. Wang et al., "Molecularly imprinted electrochemical biosensor based on chitosan/ionic liquid–graphene composites modified electrode for determination of bovine serum albumin," *Sensors and Actuators B: Chemical*, vol. 225, pp. 305–311, 2016.

[19] P. Bollella, G. Fusco, C. Tortolini et al., "Beyond graphene: electrochemical sensors and biosensors for biomarkers detection," *Biosensors and Bioelectronics*, vol. 89, Part 1, pp. 152–166, 2017.

[20] Y. Wang, C. Hou, Y. Zhang, F. He, M. Liu, and X. Li, "Preparation of graphene nano-sheet bonded pda/mof microcapsules with immobilized glucose oxidase as a mimetic multi-enzyme system for electrochemical sensing of glucose," *Journal of Materials Chemistry B*, vol. 4, no. 21, pp. 3695–3702, 2016.

[21] D. Kim, D. W. Kim, W. G. Hong, and A. Coskun, "Graphene/-ZIF-8 composites with tunable hierarchical porosity and electrical conductivity," *Journal of Materials Chemistry A*, vol. 4, no. 20, pp. 7710–7717, 2016.

[22] G. G. Yu, J. F. Xia, F. F. Zhang, and Z. H. Wang, "Hierarchical and hybrid RGO/ZIF-8 nanocomposite as electrochemical sensor for ultrasensitive determination of dopamine," *Journal of Electroanalytical Chemistry*, vol. 801, pp. 496–502, 2017.

[23] D. Li, M. B. Muller, S. Gilje, R. B. Kaner, and G. G. Wallace, "Processable aqueous dispersions of graphene nanosheets," *Nature Nanotechnology*, vol. 3, no. 2, pp. 101–105, 2008.

[24] H. Yang, C. Shan, F. Li, D. Han, Q. Zhang, and L. Niu, "Covalent functionalization of polydisperse chemically-converted graphene sheets with amine-terminated ionic liquid," *Chemical Communications*, vol. 26, no. 26, pp. 3880–3882, 2009.

[25] D. Wei and A. Ivaska, "Applications of ionic liquids in electrochemical sensors," *Analytica Chimica Acta*, vol. 607, no. 2, pp. 126–135, 2008.

[26] C. Shan, H. Yang, D. Han, Q. Zhang, A. Ivaska, and L. Niu, "Electrochemical determination of NADH and ethanol based on ionic liquid-functionalized graphene," *Biosensors and Bioelectronics*, vol. 25, no. 6, pp. 1504–1508, 2010.

[27] J. Peng, C. Hou, and X. Hu, "Determination of metronidazole in pharmaceutical dosage forms based on reduction at graphene and ionic liquid composite film modified electrode," *Sensors and Actuators B: Chemical*, vol. 169, pp. 81–87, 2012.

[28] Q. G. Shao, J. Tang, Y. X. Lin et al., "Ionic liquid modified graphene for supercapacitors with high rate capability," *Electrochimica Acta*, vol. 176, pp. 1441–1446, 2015.

[29] S. Tanaka, K. Kida, M. Okita, Y. Ito, and Y. Miyake, "Size-controlled synthesis of zeolitic imidazolate framework-8 (ZIF-8) crystals in an aqueous system at room temperature," *Chemistry Letters*, vol. 41, no. 10, pp. 1337–1339, 2012.

[30] K. S. Park, Z. Ni, A. P. Cote et al., "Exceptional chemical and thermal stability of zeolitic imidazolate frameworks," *Proceedings of the National Academy of Sciences of the United States of America*, vol. 103, no. 27, pp. 10186–10191, 2006.

[31] J. Cravillon, R. Nayuk, S. Springer, A. Feldhoff, K. Huber, and M. Wiebcke, "Controlling zeolitic imidazolate framework nano- and microcrystal formation: insight into crystal growth by time-resolved in situ static light scattering," *Chemistry of Materials*, vol. 23, no. 8, pp. 2130–2141, 2011.

[32] M. He, J. Yao, Q. Liu, K. Wang, F. Chen, and H. Wang, "Facile synthesis of zeolitic imidazolate framework-8 from a concentrated aqueous solution," *Microporous and Mesoporous Materials*, vol. 184, pp. 55–60, 2014.

[33] H. Chen, L. Wang, J. Yang, and R. T. Yang, "Investigation on hydrogenation of metal–organic frameworks HKUST-1, MIL-53, and ZIF-8 by hydrogen spillover," *Journal of Physical Chemistry C*, vol. 117, no. 15, pp. 7565–7576, 2013.

[34] R. Kumar, K. Jayaramulu, T. K. Maji, and C. N. R. Rao, "Hybrid nanocomposites of ZIF-8 with graphene oxide exhibiting tunable morphology, significant CO_2 uptake and other novel properties," *Chemical Communications*, vol. 49, no. 43, pp. 4947–4949, 2013.

[35] C. Petit and T. J. Bandosz, "Synthesis, characterization, and ammonia adsorption properties of mesoporous metal–organic framework (MIL(Fe))–graphite oxide composites: exploring the limits of materials fabrication," *Advanced Functional Materials*, vol. 21, no. 11, pp. 2108–2117, 2011.

[36] S. Luanwuthia, A. Krittayavathananona, P. Srimuka, and M. Sawangphruk, "*In situ* synthesis of permselective zeolitic imidazolate framework-8/graphene oxide composites: rotating disk electrode and Langmuir adsorption isotherm," *RSC Advances*, vol. 5, no. 58, pp. 46617–46623, 2015.

[37] D. C. Marcano, D. V. Kosynkin, J. M. Berlin et al., "Improved synthesis of graphene oxide," *ACS Nano*, vol. 4, no. 8, pp. 4806–4814, 2010.

[38] Y. Sanguansak, P. Srimuk, A. Krittayavathananon et al., "Permselective properties of graphene oxide and reduced graphene oxide electrodes," *Carbon*, vol. 68, pp. 662–669, 2014.

[39] T. Rattana, S. Chaiyakun, N. Witit-anun et al., "Preparation and characterization of graphene oxide nanosheets," *Procedia Engineering*, vol. 32, pp. 759–764, 2012.

[40] Y. Hu, H. Kazemian, S. Rohani, Y. Huang, and Y. Song, "*In situ* high pressure study of ZIF-8 by FTIR spectroscopy," *Chemical Communications*, vol. 47, no. 47, pp. 12694–12696, 2011.

[41] J. Yao, R. Chen, K. Wang, and H. Wang, "Direct synthesis of zeolitic imidazolate framework-8/chitosan composites in chitosan hydrogels," *Microporous and Mesoporous Materials*, vol. 165, pp. 200–204, 2013.

[42] M. I. Prodromidis, "Impedimetric immunosensors-a review," *Electrochimica Acta*, vol. 55, no. 14, pp. 4227–4233, 2010.

[43] E. Laviron, "General expression of the linear potential sweep voltammogram in the case of diffusionless electrochemical systems," *Journal of Electroanalytical Chemistry and Interfacial Electrochemistry*, vol. 101, no. 1, pp. 19–28, 1979.

[44] J. F. Xia, Z. H. Wang, F. Cai et al., "An electrochemical sensor for the sensitive detection of rutin based on a novel composite of activated silica gel and graphene," *RSC Advances*, vol. 5, no. 49, pp. 39131–39137, 2015.

[45] F. Gao, X. L. Cai, X. Wang et al., "Highly sensitive and selective detection of dopamine in the presence of ascorbic acid at graphene oxide modified electrode," *Sensors and Actuators B: Chemical*, vol. 186, pp. 380–387, 2013.

[46] T. Qian, S. S. Wu, and J. Shen, "Facilely prepared polypyrrole-reduced graphite oxide core–shell microspheres with high dispersibility for electrochemical detection of dopamine," *Chemical Communications*, vol. 49, no. 41, pp. 4610–4612, 2013.

[47] H. Teymourian, A. Salimi, and S. Khezrian, "Fe_3O_4 magnetic nanoparticles/reduced graphene oxide nanosheets as a novel electrochemical and bioeletrochemical sensing platform," *Biosensors & Bioelectronics*, vol. 49, pp. 1–8, 2013.

[48] Y. Wang, Y. Zhang, C. Hou, and M. Z. Liu, "Magnetic Fe_3O_4@MOFs decorated graphene nanocomposites as novel electrochemical sensor for ultrasensitive detection of dopamine," *RSC Advances*, vol. 5, no. 119, pp. 98260–98268, 2015.

[49] T. Chen, L. Tang, F. Yang et al., "Electrochemical determination of dopamine by a reduced graphene oxide-gold nanoparticle-modified glassy carbon electrode," *Analytical Letters*, vol. 49, no. 14, pp. 2223–2233, 2016.

[50] X. Wang, Q. X. Wang, Q. H. Wang et al., "Highly dispersible and stable copper terephthalate metal–organic framework–graphene oxide nanocomposite for an electrochemical sensing application," *ACS Applied Materials & Interfaces*, vol. 6, no. 14, pp. 11573–11580, 2014.

Hindawi
Journal of Nanomaterials
Volume 2019, Article ID 9214186, 8 pages
https://doi.org/10.1155/2019/9214186

Research Article

Triggering WORM/SRAM Memory Conversion by Composite Oxadiazole in Polymer Resistive Switching Device

Enming Zhao, Xiaodan Liu, Guangyu Liu, and Bao Zhou

School of Engineering, Dali University, Dali 671003, China

Correspondence should be addressed to Xiaodan Liu; liuxiaodandali@163.com

Received 14 April 2019; Accepted 1 July 2019; Published 21 August 2019

Guest Editor: Laijun Liu

Electrical characterization indicates that the nonvolatile write once read many (WORM) times/volatile static random access memory (SRAM) conversion was triggered by the composite of the oxadiazole small molecule. FTO/PMMA/Ag device possesses nonvolatile WORM memory behavior, while the FTO/PMMA+oxadiazole/Ag device shows vastly different volatile SRAM feature. The FTO/PMMA/Ag and FTO/PMMA+oxadiazole/Ag memory devices both exhibit high ON/OFF ratio nearly 10^4. The additive oxadiazole small molecule in the polymethyl methacrylate was suggested to form an internal electrode and serve as a channel during the charge transfer process, which is easy to both the charge transfer and back charge transfer, as a consequence, the WORM/SRAM conversion upon oxadiazole small molecule complexation was triggered. The results observed in this work manifest the significance of oxadiazole small molecule to the memory effects and will arouse the research interest about small molecule composite applied in memory devices.

1. Introduction

Resistive random access memory (RRAM) devices has aroused the research scholar's widespread interest on the account of their fast operation speed, simple construction, low power dissipation, and compatibility with conventional CMOS technique [1–4]. RRAM devices are probably a promising solution to traditional memory technologies facing the physical limit. On account of their widespread applications in nonvolatile data memory [5], logic operation [6–8], neuromorphic circuits [9], and programmable analogue circuits [10]. For resistive switching effect, the device could be repeatedly converted between the OFF state and the ON state, once an appropriate voltage is applied. Up till now, resistive switching has been reported in a variety of materials, for instance, perovskites [11], binary oxides [12], organics [13–16], TiO_x [17], $MoSe_2$-doped ultralong Se microwires [18], Fe_2O_3 solid electrolyte [8], and chalcogenide [19]. In particular, resistive switching memory integrated with nanogenerators for self-powered device has been developed recently [20]. During the last several years, organic resistive switching memory device has attracted special attention, such as polyvinyl carbazole [21], epoxy methacrylate resin [22], and poly(vinyl alcohol) [23]. Taking these into account, organic memory shows excellent mechanical flexibility, high ductility, excellent bendability, low cost, and the possibility for molecular design through chemical synthesis [24]. The charge transfer mechanisms in RRAM memory devices could be ascribed to various physical and/or chemical behavior theory and still needs more work [25].

In a variety of organic materials that were applied in the resistive switching memory devices, polymer has drawn a lot of attention on account of easy processing, favourable environmental stability, easiness in the fabrication of thin films, and low cost [26]. The application of the polymer made the flexible RRAM film devices possible. Flexible devices promise a broad application prospect [27, 28]. Integrating polymer with small molecule material has been recently investigated with the purpose of realizing preferable synergetic effects with the two materials [29].

Polymethyl methacrylate (PMMA) has been verified a polymeric matrix in resistive switching application [30, 31], which being a low cost and easily processed organic material, has more and more interest in flexible resistive switching

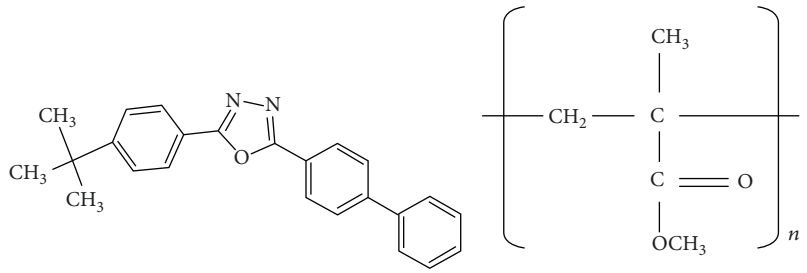

Figure 1: Chemical structure of oxadiazole and PMMA.

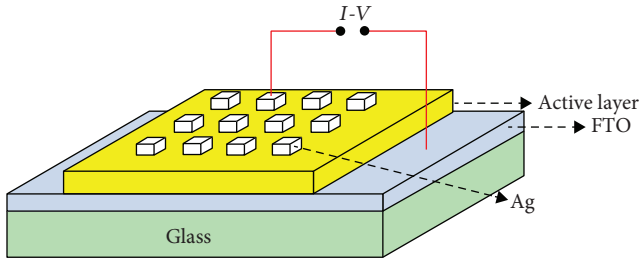

Figure 2: The structure of the memory device.

devices owing to its favourable switching and for its function as a normative resistance material in submicron RRAM lithography [32]. Simultaneously, oxadiazole derivatives were intensively reported as ideal electron acceptor materials in electronic devices [33–39]; 2-(4-tert-butylphenyl)-5-(4-biphenylyl)-1,3,4-oxadiazole was one of the most efficient electron-transporting materials on account of its high electron affinity. In the present work, PMMA is used as the host body for forming a thin film. And it was used to form the nanocomposite with 2-(4-tert-butylphenyl)-5-(4-biphenylyl)-1,3,4-oxadiazole to demonstrate resistive switching characteristics. And 2-(4-tert-butylphenyl)-5-(4-biphenylyl)-1,3,4-oxadiazole functions as the donor.

2. Experimental

The 2-(4-tert-butylphenyl)-5-(4-biphenylyl)-1,3,4-oxadiazole ($M_w = 354$, MDL: MFCD00003101) and PMMA (average $M_w = 150{,}000$, MDL: MFCD00134349) were both purchased from Sigma-Aldrich. The chemical structures of oxadiazole and PMMA are shown in Figure 1. To prepare PMMA+oxadiazole nanocomposites, 1 g of 2-(4-tert-butylphenyl)-5-(4-biphenylyl)-1,3,4-oxadiazole powder was mixed to 20 g of PMMA, then 5 g of the prepared composite was added to 50 ml of chlorobenzene solvent and PMMA in chlorobenzene solvent of 10 mg/ml with subsequent magnetic stirring for 48 h. After that, the PMMA+oxadiazole composite solution (filtered by polytetrafluoroethylene membrane, pore size of 0.22 mm) and PMMA of chlorobenzene solvent were spin-coated on a cleaned SnO_2 doped with fluorine (FTO) glass (purchased from Guluo Co. Ltd. Luoyang, China) at 800 rpm for 15 s, and then 4000 rpm for 60 s. Afterwards, the spin-coated FTO glasses were baked in 40°C for overnight on a hot plate to remove the residual solvent. The top Ag electrode with a thickness of 200 nm was deposited by using thermal evaporation under the pressure of 1×10^{-4} Pa. The fabricated structure of the memory device is schematically exhibited in Figure 2. The morphology of the cross-section properties of the active layer was tested by scanning electron microscopy (SEM; Nova Nano 450). All electrical measurements were performed by using a semiconductor characterization system (Keithley 4200) at room temperature. The bottom FTO electrode was grounded in the process of the resistive switching performance test, and an external voltage was applied to the top Ag electrode.

3. Results and Discussion

The cross-section SEM images of the PMMA and PMMA +oxadiazole composite films before the deposition of the top Ag electrode are shown in Figure 3.

The electrical memory behavior of the two devices was characterized by the current-voltage ($I - V$) curves of the FTO/PMMA/Ag and FTO/PMMA+oxadiazole/Ag sandwich devices. Figure 4(a) shows the $I - V$ curves of the FTO/PMMA/Ag memory device, which indicates a typical nonvolatile WORM performance. As seen in Figure 4(a), the FTO/PMMA/Ag device is initially in the high resistance state (the OFF state). In the process of the first positive voltage sweep, a sudden increase in current happened at the voltage of about 1.25 V, indicating the transition of the FTO/PMMA/Ag device from the high-resistance state to the low-resistance state (ON state) with an ON/OFF ratio up to 10^4 as shown in Figure 4(b). On this transformation, the FTO/PMMA/Ag device retains this ON state in the process of the succeeding positive scan (2nd sweep) and negative scan (3rd sweep) and cannot retrieve to its initial high-resistance state even though power supply shut down (4th sweep), manifesting its nonreversible nonvolatile nature and write once read many (WORM) times memory properties. Broadly speaking, the quantitative evaluation of resistive switching was assessed with the I_{OFF}/I_{ON} ratio at each applied voltage. This would help in providing information about the optimum operation parameters of the threshold resistive switching voltage (V_{th}) and the range of applied voltage for observing the obvious ON and OFF, and the amount of distinctiveness (I_{OFF}/I_{ON}) can result in defining the critical process parameters for the preparation of memory device structures with an efficient bipolar resistive switching behavior. Figure 4(b) describes the evaluated values for I_{OFF}/I_{ON} depending on the applied bias of the representative FTO/PMMA/Ag device structures. In order to assess the stability and reliability of the

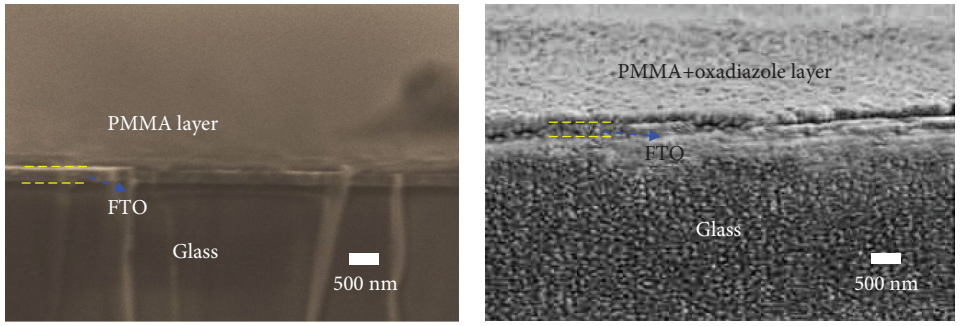

(a) (b)

Figure 3: (a) SEM images of PMMA layer films. (b) SEM images of PMMA+oxadiazole composite films.

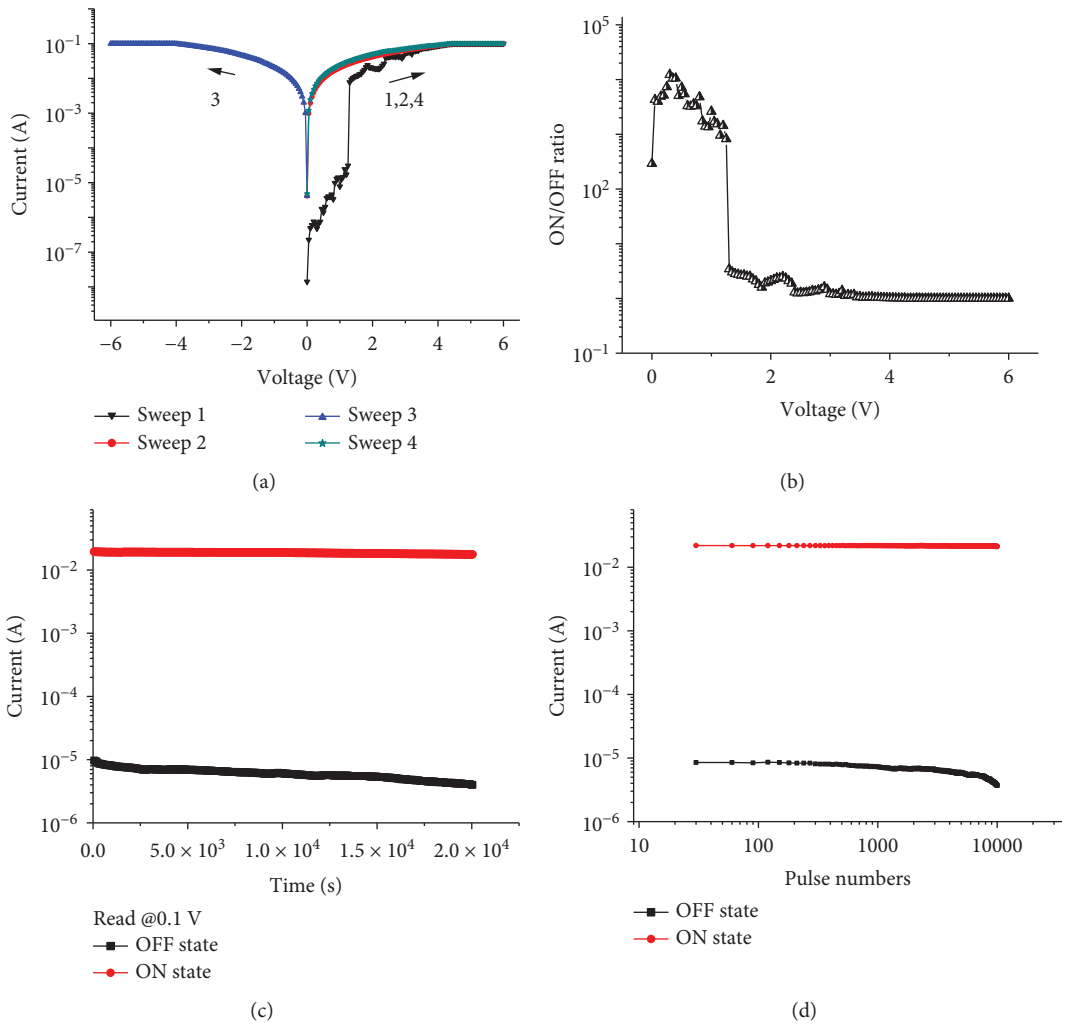

(a) (b) (c) (d)

Figure 4: (a) $I - V$ curves of the FTO/PMMA/Ag device. (b) Switching ratio (I_{ON}/I_{OFF}) versus the applied bias, as estimated from the $I - V$ sweeps recorded for FTO/PMMA/Ag device. (c) Retention performance of the ON and OFF states of the FTO/PMMA/Ag device tested at 0.1 V. (d) Stimulus effect of 0.1 V read pulse under the ON and OFF states of the FTO/PMMA/Ag device.

FTO/PMMA/Ag memory behavior, Figures 4(c) and 4(d) show the performance of retention time and stimulus read pulse under the ON and OFF states of the FTO/PMMA/Ag device. Both ON and OFF states were tested under constant voltage stress and continuous pulse. No significant attenuation in current was observed, and both the ON and OFF current responses were fairly stable which reached up to 2×10^4 s and 10^4 continuous read pulses, manifesting favourable stability and reliability of the FTO/PMMA/Ag device.

Figure 5(a) shows the $I - V$ curves of the FTO/PMMA +oxadiazole/Ag device. Totally different from the FTO/PMMA/Ag memory device, the added 2-(4-tert-butylphenyl)-

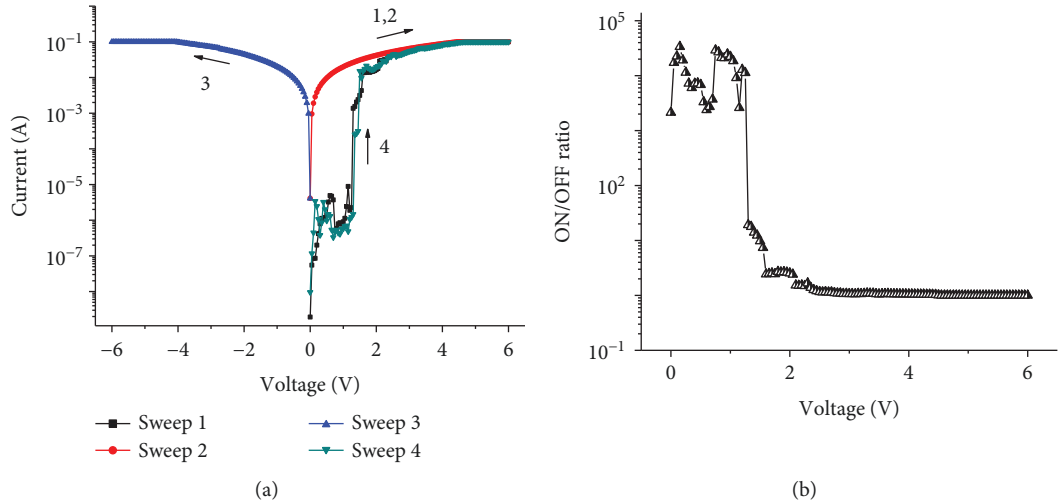

FIGURE 5: (a) $I - V$ curves of FTO/PMMA+oxadiazole/Ag device. (b) Switching ratio (I_{ON}/I_{OFF}) depends on the applied bias, as estimated from the $I - V$ sweeps recorded for FTO/PMMA+oxadiazole/Ag device.

5-(4-biphenylyl)-1,3,4-oxadiazole small molecule indicates a reversible volatile SRAM memory property, manifesting the important role of oxadiazole small molecule in the PMMA composite. As shown in Figure 5(a), in the process of the first positive sweep from 0 to 6 V, the FTO/PMMA+oxadiazole/Ag device maintains its OFF state until a threshold switching voltage of 1.30 V was reached. The current of the FTO/PMMA/Ag device then increased suddenly from 10^{-6} A to 10^{-2} A, converting the FTO/PMMA+oxadiazole/Ag device to the ON state. The FTO/PMMA+oxadiazole/Ag device stablely maintained in the ON state in the process of the continued positive and negative scan (2nd and 3rd sweeps). Nevertheless, the subsequent tests exhibit that the ON state can only be maintained transiently and will relax to the original OFF state spontaneously once cutting off power supply for over 3 min, manifesting its actually "volatile" feature. Then, in the fourth scan, the FTO/PMMA+oxadiazole/Ag device can be converted to the ON state again, manifesting its volatile static random access memory (SRAM) properties. The $I - V$ curves in Figure 5(a) indicate that the FTO/PMMA+oxadiazole/Ag takes on the volatile but reprogrammable electrical bistability, which could be applied in SRAM devices in digital information technology. Figure 5(b) shows the estimated values for comparable I_{OFF}/I_{ON} versus the applied voltage of representative FTO/PMMA+oxadiazole/Ag device structures. To this point, it could be confirmed that it must be the added-(4-tert-butylphenyl)-5-(4-biphenylyl)-1,3,4-oxadiazole small molecule which plays a vital function and has a significant change in the resistive switching process. The function of the oxadiazole small molecule is regarded as it serves as a medium or a charge transport channel, which affords a more convenient path for carrier transport and consequently be convenient for the electron-accepting process.

Comparative analyses of both devices' switching uniformity have been made between FTO/PMMA+oxadiazole/Ag and FTO/PMMA/Ag memory device. The cumulative distributions of resistive switching voltage (V_{th}) and resistance of ON and OFF states (R_{ON} and R_{OFF}) for FTO/PMMA+oxadiazole/Ag and FTO/PMMA/Ag device are shown in Figures 6(a)–6(d). For the sake of comparison and evaluation, the variation coefficients of all switching parameters have been calculated by σ/μ (where σ is the standard deviation and μ is the average value). Figure 6(e) shows the variation coefficients of V_{th}, R_{OFF}, and R_{ON}, respectively.

Figure 7 shows the UV-vis absorption spectra of the PMMA and the composite film of PMMA and oxadiazole small molecule. The PMMA and PMMA+oxadiazole show a distinct absorption peaks near 345.5 nm, respectively, both of which are corresponding to the $\pi - \pi*$ transition of PMMA. Obviously, the $\pi - \pi*$ absorption of the oxadiazole small molecule is blue-shifted, manifesting that the addition of oxadiazole in the PMMA matrix was beneficial to the $\pi - \pi*$ electron transitions of the PMMA, for which one considered reason is the ameliorated molecular coplanarity of the methacrylate methacrylic ring after oxadiazole small molecule composite. Whereas a weak absorption peak appeared at 301.5 nm, the absorption transitions were wholly blue-shifted to a lower wavelength region, manifesting the possible formation of oxadiazole chains aggregation, which will facilitate charge transfer in the PMMA bulk when the external bias was applied.

To better catch on the resistive switching mechanism, the $I - V$ characteristics were redrawn in the double-log coordinate system as exhibited in Figure 8. The ON state of the FTO/PMMA/Ag and FTO/PMMA+oxadiazole/Ag devices shows linearity in the $I - V$ relationship and the slope of the plot is nearly 1 (1.04 and 1.02), manifesting that the ohmic conduction through the conducting filament is dominant. In the OFF state of the FTO/PMMA/Ag and FTO/PMMA+oxadiazole/Ag device, the ohmic conduction was observed in a low voltage region, and the slope increased to over 2 (2.94, 1.19, and 3.78), manifesting that the space-charge-limited conduction (SCLC) among the disconnected portion of the conducting filament governs in a high voltage region. These conduction properties in

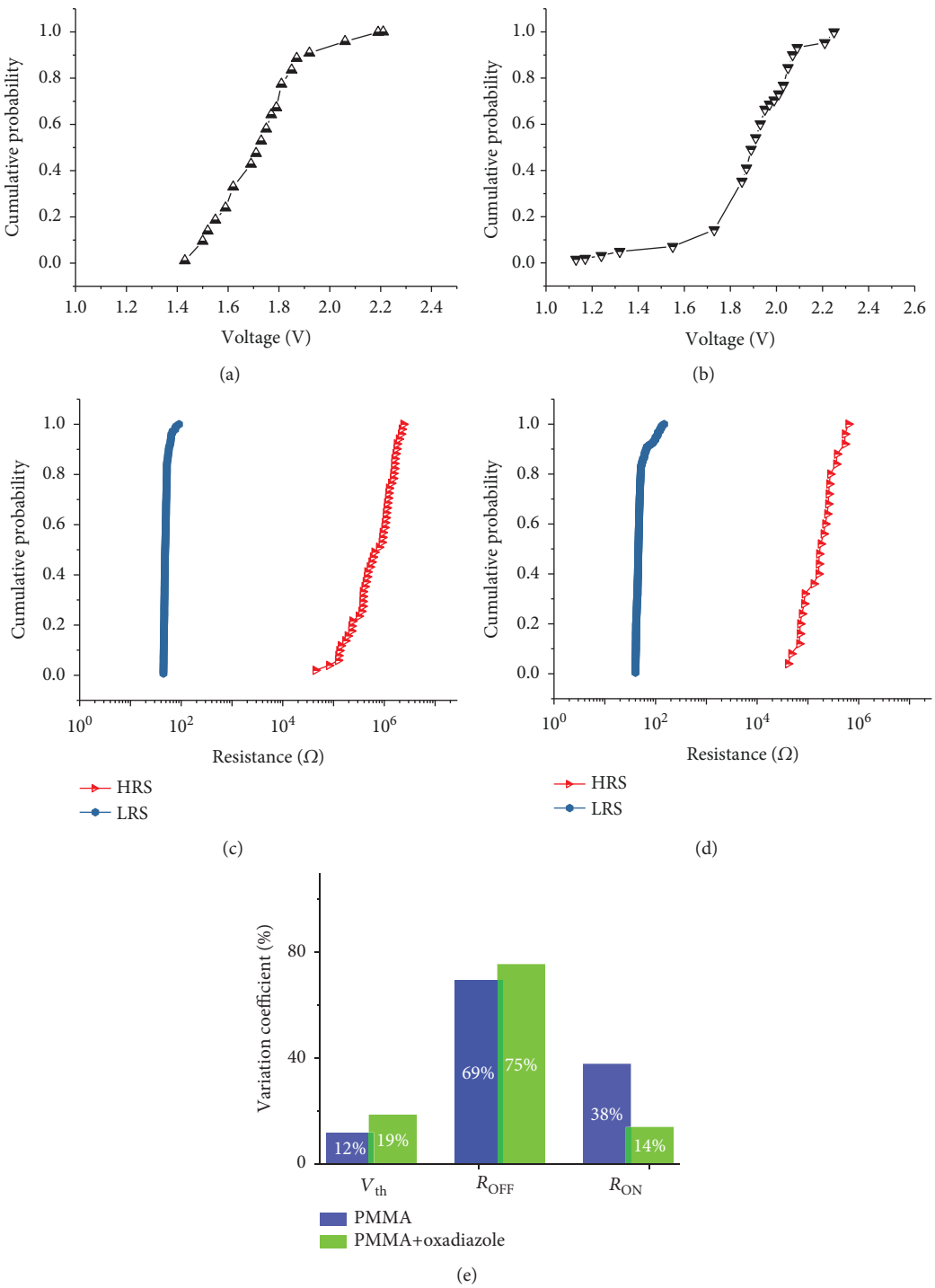

Figure 6: (a) Cumulative distributions of V_{th} for FTO/PMMA/Ag. (b) Cumulative distributions of V_{th} for FTO/PMMA+oxadiazole/Ag device. (c) Cumulative probability of R_{ON} and R_{OFF} for FTO/PMMA/Ag. (d) Cumulative probability of R_{ON} and R_{OFF} for FTO/PMMA +oxadiazole/Ag device. (e) Variation coefficients of V_{th}, R_{OFF}, and R_{ON}.

ON and OFF states are also in keeping with those in the previous report [40–42].

The experimental results indicate that the resistive switching property have a high association of the oxadiazole small molecule additives in polymer host. At initial stage, the charge carriers have no sufficient energy to overcome the charge injection barrier between PMMA molecules; the built-in electric field between the interface was formed [43–45], at the same time, the formation of built-in electric field will further hinder the injection of carriers. Thus, the FTO/PMMA/Ag device is on the high resistance state. Once the voltage scanning is up to the V_{th}, the occurrence of intermolecular charge transfer leads to transition in the FTO/PMMA/Ag device from OFF to ON state. The formed

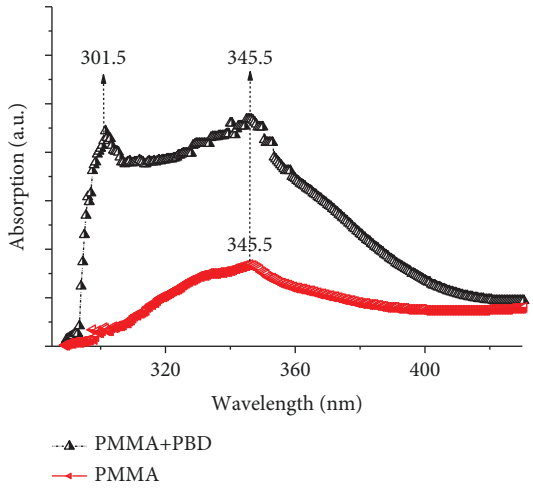

Figure 7: Absorption spectra of PMMA and PMMA+oxadiazole composite thin films.

charge transfer was in favour of the holding of the generated charge carriers, which may be related to the nonvolatility of the resulting data-storage devices. As indicated above, oxadiazole small molecule complexation has facilitated electron accepting in active layer and endows the active layer with a quasireversible *n*-doping feature, suggesting that the oxadiazole moieties in PMMA could act as mediators to facilitate the intramolecular charge transfer. Here, the quasireversible features of the oxadiazole group are supposed to be partially responsible for the reversible volatile SRAM memory behaviors for the FTO/PMMA+oxadiazole/Ag device. Because of the quasireversible and unstable charge transfer, the charge transfer state immediately dissociates via the back charge transfer or a recombination process of the separated charges after taking out the external power supply, which leads to volatile memory characteristic in FTO/PMMA+oxadiazole/Ag device.

4. Conclusions

In summary, small molecule oxadiazole was composited with polymer PMMA, which easily formed a thin film in this work for memory applications, that effectively avoids the defect of crystallization of small molecules during the formation of thin film. The FTO/PMMA/Ag device show irreversible nonvolatile WORM feature. However, after oxadiazole was added, the FTO/PMMA+oxadiazole/Ag device exhibits reversible volatile SRAM memory properties. More importantly, the added oxadiazole forms an internal electrode and serves as a medium in the process of charge transfer, which facilitates the forth and back charge transfers, furthermore triggering the conversion from WORM to SRAM memory. This work indicates the feasibility of oxadiazole in electronic resistive switching memory and demonstrates the consequence of oxadiazole complexation in the resistive switching memory effects, which would probably attract the interest of academic researchers to prepare desirable memory device by

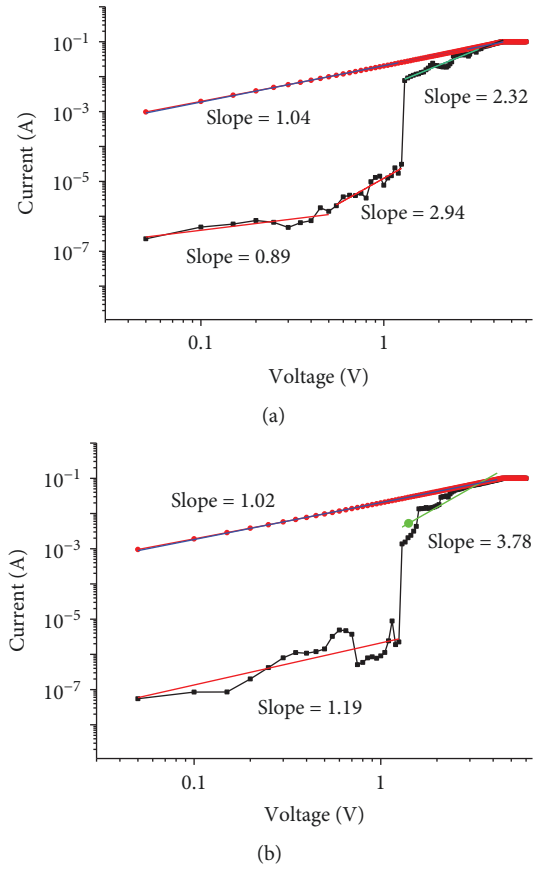

Figure 8: Double logarithm plot of $I - V$ curves.

using small molecule oxadiazole species and the memory effect of WORM to SRAM conversion application.

Data Availability

The data used to support the findings of this study are included within the article.

Conflicts of Interest

The authors declare that they have no conflicts of interest.

Acknowledgments

The authors acknowledge the financial support of the basic research project of the basic research business of the provincial higher school in Heilongjiang Province (RCCX201702).

References

[1] R. Waser, R. Dittmann, G. Staikov, and K. Szot, "Redox-based resistive switching memories—nanoionic mechanisms, prospects, and challenges," *Advanced Materials*, vol. 21, no. 25-26, pp. 2632–2663, 2009.

[2] G. Zhou, Z. Ren, L. Wang, B. Sun, S. Duan, and Q. Song, "Artificial and wearable albumen protein memristor arrays with integrated memory logic gate functionality," *Materials Horizons*, 2019.

[3] W. J. Liu, L. Chen, P. Zhou et al., "Chemical-vapor-deposited graphene as charge storage layer in flash memory device," *Journal of Nanomaterials*, vol. 2016, Article ID 6751497, 6 pages, 2016.

[4] J. R. Rani, S. I. Oh, J. M. Woo, and J. H. Jang, "Low voltage resistive memory devices based on graphene oxide-iron oxide hybrid," *Carbon*, vol. 94, pp. 362–368, 2015.

[5] B. Sun, Y. X. Liu, L. F. Liu et al., "Highly uniform resistive switching characteristics of TiN/ZrO_2/ Pt memory devices," *Journal of Applied Physics*, vol. 105, no. 6, p. 061630, 2009.

[6] E. Linn, R. Rosezin, S. Tappertzhofen, U. Böttger, and R. Waser, "Beyond von Neumann-logic operations in passive crossbar arrays alongside memory operations," *Nanotechnology*, vol. 23, no. 30, p. 305205, 2012.

[7] M. S. Kadhim, F. Yang, B. Sun et al., "Existence of resistive switching memory and negative differential resistance state in self-colored MoS_2/ZnO heterojunction devices," *ACS Applied Electronic Materials*, vol. 1, no. 3, pp. 318–324, 2019.

[8] G. Zhou, X. Yang, L. Xiao, B. Sun, and A. Zhou, "Investigation of a submerging redox behavior in Fe2O3solid electrolyte for resistive switching memory," *Applied Physics Letters*, vol. 114, no. 16, p. 163506, 2019.

[9] T. Shi, X. B. Yin, R. Yang, and X. Guo, "Pt/WO_3/FTO memristive devices with recoverable pseudo-electroforming for time-delay switches in neuromorphic computing," *Physical Chemistry Chemical Physics*, vol. 18, no. 14, pp. 9338–9343, 2016.

[10] J. Zha, H. Huang, and Y. Liu, "A novel window function for memristor model with application in programming analog circuits," *IEEE Transactions on Circuits and Systems*, vol. 63, no. 5, pp. 423–427, 2016.

[11] F. Lv, C. Gao, H.-A. Zhou, P. Zhang, K. Mi, and X. Liu, "Nonvolatile bipolar resistive switching behavior in the perovskite-like $(CH_3NH_3)_2FeCl_4$," *ACS Applied Materials & Interfaces*, vol. 8, no. 29, pp. 18985–18990, 2016.

[12] B. Singh and B. R. Mehta, "Relationship between nature of metal-oxide contacts and resistive switching properties of copper oxide thin film based devices," *Thin Solid Films*, vol. 569, pp. 35–43, 2014.

[13] B. Cho, S. Song, Y. Ji, T.-W. Kim, and T. Lee, "Organic resistive memory devices: performance enhancement, integration, and advanced architectures," *Advanced Functional Materials*, vol. 21, no. 15, pp. 2806–2829, 2011.

[14] B. Sun, X. Zhang, G. Zhou et al., "An organic nonvolatile resistive switching memory device fabricated with natural pectin from fruit peel," *Organic Electronics*, vol. 42, pp. 181–186, 2017.

[15] B. Sun, S. Zhu, S. Mao et al., "From dead leaves to sustainable organic resistive switching memory," *Journal of Colloid and Interface Science*, vol. 513, pp. 774–778, 2018.

[16] Y. Sun, J. Lu, C. Ai, D. Wen, and X. Bai, "Enhancement of memory margins in the polymer composite of [6,6]-phenyl-C61-butyric acid methyl ester and polystyrene," *Physical Chemistry Chemical Physics*, vol. 18, no. 44, pp. 30808–30814, 2016.

[17] G. Zhou, S. Duan, P. Li et al., "Coexistence of negative differential resistance and resistive switching memory at room temperature in TiO_x modulated by moisture," *Advanced Electronic Materials*, vol. 4, no. 4, p. 1700567, 2018.

[18] G. Zhou, B. Sun, Y. Yao et al., "Investigation of the behaviour of electronic resistive switching memory based on $MoSe_2$-doped ultralong Se microwires," *Applied Physics Letters*, vol. 109, no. 14, p. 143904, 2016.

[19] A. Pradel, N. Frolet, M. Ramonda, A. Piarristeguy, and M. Ribes, "Bipolar resistance switching in chalcogenide materials," *Physica Status Solidi*, vol. 208, no. 10, pp. 2303–2308, 2011.

[20] G. Zhou, Z. Ren, L. Wang et al., "Resistive switching memory integrated with amorphous carbon-based nanogenerators for self-powered device," *Nano Energy*, vol. 63, p. 103793, 2019.

[21] Y. Sun, D. Wen, and F. Sun, "Influence of blending ratio on resistive switching effect in donor-acceptor type composite of PCBM and PVK-based memory devices," *Organic Electronics*, vol. 65, pp. 141–149, 2019.

[22] Y. Sun, J. Lu, C. Ai, D. Wen, and X. Bai, "Multilevel resistive switching and nonvolatile memory effects in epoxy methacrylate resin and carbon nanotube composite films," *Organic Electronics*, vol. 32, pp. 7–14, 2016.

[23] Y. Sun, J. Lu, C. Ai, and D. Wen, "Nonvolatile memory devices based on poly(vinyl alcohol)+graphene oxide hybrid composites," *Physical Chemistry Chemical Physics*, vol. 18, no. 16, pp. 11341–11347, 2016.

[24] Y. Sun, F. Miao, and R. Li, "Bistable electrical switching and nonvolatile memory effect based on the thin films of polyurethane-carbon nanotubes blends," *Sensors and Actuators A: Physical*, vol. 234, pp. 282–289, 2015.

[25] D. Chaudhary, S. Munjal, N. Khare, and V. D. Vankar, "Bipolar resistive switching and nonvolatile memory effect in poly (3-hexylthiophene)-carbon nanotube composite films," *Carbon*, vol. 130, pp. 553–558, 2018.

[26] Y. Li and X. Ni, "One-step preparation of graphene oxide–poly(3,4-ethylenedioxythiophene) composite films for nonvolatile rewritable memory devices," *RSC Advances*, vol. 6, no. 20, pp. 16340–16347, 2016.

[27] G. Khurana, P. Misra, and R. S. Katiyar, "Multilevel resistive memory switching in graphene sandwiched organic polymer heterostructure," *Carbon*, vol. 76, pp. 341–347, 2014.

[28] Y. Chen, G. Liu, C. Wang, W. Zhang, R.-W. Li, and L. Wang, "Polymer memristor for information storage and neuromorphic applications," *Materials Horizons*, vol. 1, no. 5, pp. 489–506, 2014.

[29] S. Miao, Y. Zhu, Q. Bao et al., "Solution-processed small molecule donor/acceptor blends for electrical memory devices with fine-tunable storage performance," *Journal of Physical Chemistry C*, vol. 118, no. 4, pp. 2154–2160, 2014.

[30] H. Y. Tsao, Y. W. Wang, and Z. K. Gao, "Resistive switching behavior of Ag/PMMA:Na/Ag devices for memory applications," *Thin Solid Films*, vol. 612, pp. 61–65, 2016.

[31] B. Cheng, J. Zhao, L. Xiao et al., "PMMA interlayer-modulated memory effects by space charge polarization in resistive switching based on CuSCN-nanopyramids/ZnO-nanorods p-n heterojunction," *Scientific Reports*, vol. 5, no. 1, 2015.

[32] J.-W. Lee and W.-J. Cho, "Fabrication of resistive switching memory based on solution processed PMMA-HfO_x blended thin films," *Semiconductor Science and Technology*, vol. 32, no. 2, p. 025009, 2017.

[33] Y. Sun, L. Li, D. Wen, and X. Bai, "Bistable electrical switching characteristics and memory effect by mixing of oxadiazole in polyurethane layer," *Journal of Physical Chemistry C*, vol. 119, no. 33, pp. 19520–19525, 2015.

[34] L. Pan, B. Hu, X. Zhu et al., "Role of oxadiazole moiety in different D-A polyazothines and related resistive switching

properties," *Journal of Materials Chemistry C*, vol. 1, no. 30, pp. 4556–4564, 2013.

[35] C. Weng, Z. Liu, H. Guo, and S. Tan, "The photoelectric properties of polymer acceptors containing oxadiazole and thiadiazole," *Macromolecular Chemistry and Physics*, vol. 218, no. 16, 2017.

[36] Y. Sun, L. Li, D. Wen, and X. bai, "Bistable electrical switching and nonvolatile memory effect in mixed composite of oxadiazole acceptor and carbazole donor," *Organic Electronics*, vol. 25, pp. 283–288, 2015.

[37] Y. Sun, F. Miao, R. Li, and D. Wen, "Resistive switching memory devices based on electrical conductance tuning in poly(4-vinyl phenol)-oxadiazole composites," *Physical Chemistry Chemical Physics*, vol. 17, no. 44, pp. 29978–29984, 2015.

[38] S. Levent, B. Kaya Çavuşoğlu, B. Sağlık et al., "Synthesis of oxadiazole-thiadiazole hybrids and their anticandidal activity," *Molecules*, vol. 22, no. 11, p. 2004, 2017.

[39] K. Kim, Y. K. Fang, W. Kwon, S. Pyo, W. C. Chen, and M. Ree, "Tunable electrical memory characteristics of brush copolymers bearing electron donor and acceptor moieties," *Journal of Materials Chemistry C*, vol. 1, no. 32, pp. 4858–4868, 2013.

[40] Y. Sun, D. Wen, and X. Bai, "Nonvolatile ternary resistive switching memory devices based on the polymer composites containing zinc oxide nanoparticles," *Physical Chemistry Chemical Physics*, vol. 20, no. 8, pp. 5771–5779, 2018.

[41] G. S. Kim, T. H. Park, H. J. Kim et al., "Investigation of the retention performance of an ultra-thin HfO_2 resistance switching layer in an integrated memory device," *Journal of Applied Physics*, vol. 124, no. 2, p. 024102, 2018.

[42] Y. Sun, D. Wen, X. Bai, J. Lu, and C. Ai, "Ternary resistance switching memory behavior based on graphene oxide embedded in a polystyrene polymer layer," *Scientific Reports*, vol. 7, no. 1, p. 3938, 2017.

[43] P. Zheng, B. Sun, Y. Chen et al., "Photo-induced negative differential resistance in a resistive switching memory device based on $BiFeO_3$/ZnO heterojunctions," *Applied Materials Today*, vol. 14, pp. 21–28, 2019.

[44] Y. Sun and D. Wen, "Conductance quantization in nonvolatile resistive switching memory based on the polymer composite of zinc oxide nanoparticles," *Journal of Physical Chemistry C*, vol. 122, no. 19, pp. 10582–10591, 2018.

[45] B. Sun, W. Zhao, Y. Liu, and P. Chen, "Resistive switching effect of Ag/MoS_2/FTO device," *Functional Materials Letters*, vol. 08, no. 01, p. 1550010, 2015.

Hindawi
Journal of Nanomaterials
Volume 2019, Article ID 5761439, 8 pages
https://doi.org/10.1155/2019/5761439

Research Article

Dielectric Properties of Epoxy-Matrix Composites with Tungsten Disulfide Nanotubes

Povilas Bertasius,[1] Mark Shneider,[2] Jan Macutkevic,[3] Vytautas Samulionis,[1] Juras Banys,[2] and Alla Zak[4]

[1]*Physics Faculty, Vilnius University, Vilnius 00122, Lithuania*
[2]*Weizmann Institute of Science, 234 Herzl St., Rehovot 7610001, Israel*
[3]*Center for Physical Sciences and Technology, Vilnius 10257, Lithuania*
[4]*HIT (Holon Institute of Technology), 52 Golomb St., Holon 58102, Israel*

Correspondence should be addressed to Jan Macutkevic; jan.macutkevic@gmail.com

Received 5 March 2019; Accepted 25 June 2019; Published 8 August 2019

Guest Editor: Emad M. Masoud

Addition of conductive nanotubes to an insulating polymer matrix has been proven as an efficient strategy that can improve the electromagnetic shielding performance, due to the high aspect ratio of nanotubes. Herein, a set of epoxy-matrix composites filled with 0.15-1.6 vol% of tungsten disulfide (WS_2) nanotubes being of 30-120 nm in diameter and 5-20 μm in length has been produced. Electromagnetic properties of the prepared composites were probed in the frequency range from 20 Hz to 1 MHz in a temperature range from 250 K to 500 K. Broadband properties of these materials are controlled by the dynamics of epoxy resin molecules, and no electrical percolation was observed up to the highest concentration (1.6 vol%) of WS_2 nanotubes. The value of dielectric permittivity for all composites is not bigger than 6 at room temperature and 1 kHz frequency, and the electrical conductivity of composites is about 10^{-6} S/m at 500 K, which demonstrate that the composites are suitable for antistatic applications at higher temperatures. The relaxation time follows the Vogel-Fulcher law, and the Vogel temperature T_0 has the minimum for the WS_2 nanotube concentration 0.15 vol%. Above 410 K, the electrical conductivity determines the properties of the investigated composites due to nonzero electrical conductivity of epoxy resin. The value of DC electrical conductivity for pure epoxy at $T = 450$ K is 0.3 μS/m, while the DC conductivity of the composites slightly increases with the WS_2 concentration. Therefore, the electrical contacts between WS_2 nanotubes and polymer matrix are rather ohmic. Additionally, the activation energy is almost independent on the concentration of WS_2. However, it is higher in composites than in pure epoxy resin.

1. Introduction

Nanoparticles are very interesting objects for investigations due to the possibility to control properties at the nanoscale and to find new physical phenomena. The nanotubes are a very important type of nanoparticles, due to the high aspect ratio of these structures. The nanotubes are typical for all layered materials, including tungsten disulfide (WS_2). Recently, it was demonstrated that WS_2 nanotubes and composites with these inclusions can be applied in various fields, including lithium ion batteries [1], bone tissue engineering [2], ultrafast photonics [3], and solar cells [4]. A lot of papers was already published on mechanical [5] and tribological [6] applications of WS_2 nanotubes and composites with these inclusions [7–12].

Moreover, due to the needle-like shape of WS_2 nanotubes and the appearance of chemical bonds between WS_2 nanotubes and polymer matrix, preparation of composites with these inclusions should be simpler than the carbon-based polymer composite preparation [13, 14]. Chemical bonds between WS_2 nanotubes and polymer matrix and unique mechanical and thermal properties of WS_2 nanotubes [5] are responsible for improved mechanical behavior and thermal stability of polymer composites [14]. Moreover, the

functionalization of WS_2 for obtaining composites in various polymer matrices is not needed [15]. This is due to unique chemical properties of the WS_2 nanotubes surface.

Despite the fact that the electrical conductivity of WS_2 nanotubes is about 10^3 S/m [16, 17] and these nanotubes can be used in transistors, photodetectors, and other electronic devices [2, 18, 19], the amount of publications on electromagnetic properties of polymer composites with WS_2 nanotubes is still very small [20–22]. Therefore, being of nanosize, having excellent mechanical and electrical properties, and possessing good dispersion and adhesion to polymers, inorganic nanotubes of WS_2 could be a good candidate for broadband electromagnetic composite applications.

In the earlier studies, it was established that the percolation threshold in WS_2/epoxy composites can be close to 25 vol% [20] and in polyurethane/WS_2 composites-larger than 2 wt% [21]. No electrical percolation for polyvinylidene fluoride (PVDF) composites with WS_2 was observed in reference [20]; however, in this work was established that pellets of WS_2 nanotubes are quite conductive. Such high values of electrical percolation, established in the previous works, are quite surprising, because of the WS_2 nanotube shape comparable to one of the carbon nanotubes, where percolation threshold in epoxy resin can be 0.0025 wt% [23]. Namely, WS_2 nanotubes have a high aspect ratio (30-120 nm in diameter and 5-20 μm in length [13]); therefore, the electrical percolation in composites with WS_2 nanoinclusions should be low enough, while electromagnetic properties of these composites are quite high. The comparison with carbon nanotube composites [24], where a wide range of percolation thresholds was observed depending on composite preparation technology, suggests that the composite with WS_2 nanotube preparation technology and WS_2 nanotube dispersion inside the polymer matrix should be important for electrical percolation in WS_2 nanotube composites as well. So, the open question was as following: is it possible to make the percolation threshold value in WS_2 nanotubes as low as in carbon nanotube composites? Other challenging tasks were to study the dielectric properties of composites with WS_2 nanotubes and the properties of conductive polymers modified with WS_2 nanoparticles. For example, to investigate an impact of WS_2 nanotubes on the electromagnetic properties of epoxy-matrix composites in a wide temperature and frequency ranges. These questions are crucial for further development of the WS_2 composite engineering and promising applications. Therefore, this paper is focused on the above questions, answers to which were not given hitherto. In order to address these points, an investigation of the broadband (20 Hz–1 MHz) electromagnetic properties of WS_2/epoxy-matrix composites in the broad temperature range (250 K–500 K) presented.

2. Materials and Methods

WS_2 nanotubes were produced through the chemical reaction of WO_{3-x} nanoparticles with H_2S and H_2 gases at high temperatures. Actually, the process consists of two main parts: formation of suboxide whiskers, by which majority is 5-20 μm in length and 30-120 nm in diameter, and their subsequent sulfidization into WS_2 nanotubes. More details about the WS_2 nanotube preparation mechanism are in [13]; according to the formation mechanism of nanotubes, the sizes of WS_2 nanotubes repeat those of suboxide whiskers, being in average of 20 μm in length and 60 nm in diameter.

As synthesized, these nanotubes at different concentrations (0.15, 0.3, 0.94, and 1.6 vol%, which is corresponding to 0.5, 1, 3, and 5 wt%) were dispersed in epoxy resin diglycidyl ether of bisphenol-A (DGEBA) (D.E.R. 331 product of Dow Chemical, Midland, MI, USA), and further, polyetheramine, used as a curing agent (JEFFAMINE T-403 product of Huntsman), was added, taken in a ratio of 100 : 40 w/w. The mixture of WS_2 nanotubes and DGEBA was sonicated for 1 hr under controlled temperature and constant mechanical stirring. The sonicator was a high-intensity ultrasonic processor with a tip diameter of 19 mm that resonates at 20 kHz ± 50 Hz (VCX 400 (ultrasonic processor) and CV26 (tip), Sonics & Materials Inc., Newtown, CT, USA). The sonication process was performed in a pulsed on/off mode of 6 and 4 sec, respectively. The curing agent was added to the epoxy/WS_2 nanotube mixture and mixed manually. The curing conditions were 100°C for 6 hours; before the curing process took place, all the mixtures were degassed for 20 minutes at 45°C. All composite preparation technology conditions were varied in order to obtain the biggest complex dielectric permittivity value of samples at room temperature; it was determined that the above listed conditions are optimal. These conditions are different from those, which applied for epoxy/WS_2 composite preparation in [21].

To make sure of the morphological and structural quality of the nanotubes, a transmission electron microscope (TEM, Philips CM 120 operated at 120 kV) and scanning electron microscope (E-SEM, model FEI XL-30) were used. The crystallographic phase of the reaction product was confirmed by an X-ray powder diffractometer (XRD, Ultima III, Rigaku, Japan) operated at 40 kV and 40 mA (not shown). TEM, SEM, and XRD analyses were carried out after each synthesis and before impregnation into the polymer matrix. The dispersion of the nanoparticles inside the polymer was characterized by E-SEM analysis of sample's cross section.

The dielectric properties of the samples were investigated using a LCR meter (HP4284 A) in the frequency range 20 Hz-1 MHz. The measurements were done by heating and cooling in the temperature interval of 300 K–500 K at the constant temperature rate of 0.5 K/min. No noticeable hysteresis in experimental results was observed in both temperature change modes. The picture of measurement equipment is presented in Figure 1. The dielectric measurement accuracy was as better as 1%.

3. Results and Discussion

SEM and TEM images of WS_2 nanotubes are presented in Figures 2(a) and 2(b)), respectively. SEM images of epoxy/WS_2 nanotube cross section are presented in Figure 3. The WS_2 nanotubes are very well dispersed in the

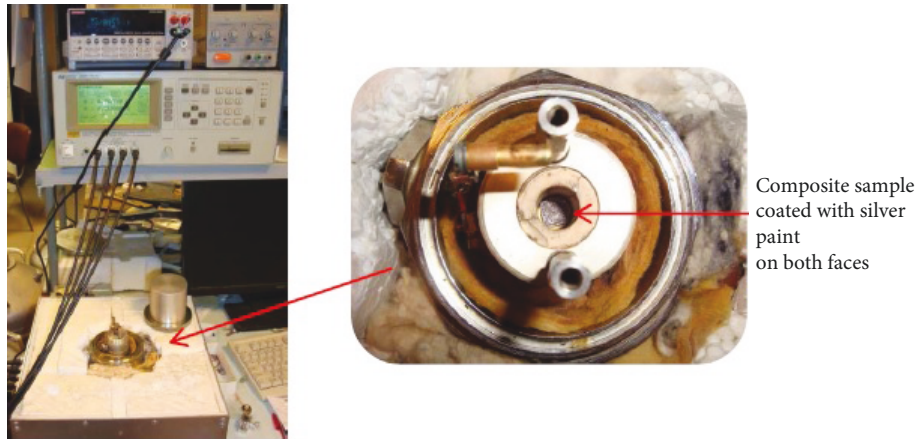

Figure 1: View of the LCR meter and the sample holder for measuring dielectric properties of composites in the 20 Hz–1 MHz frequency range.

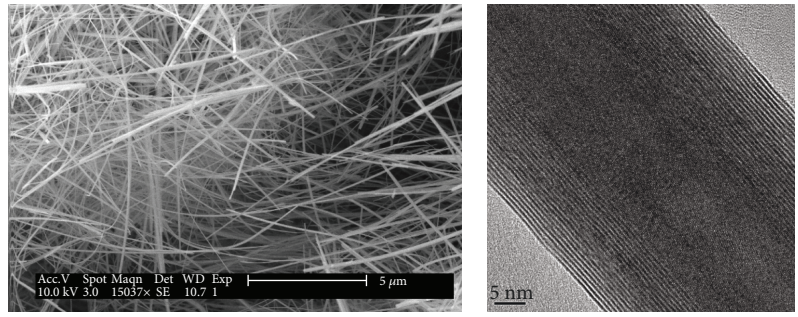

(a) (b)

Figure 2: Scanning electron microscopy (SEM) (a) and transmission electron microscopy (b) images of WS_2 nanotubes.

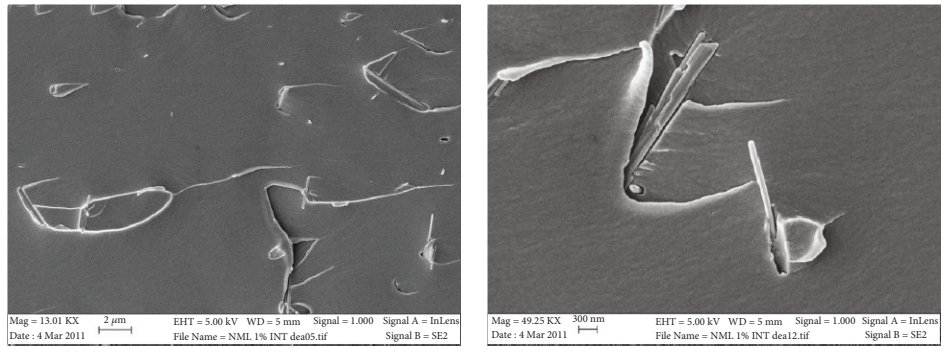

(a) (b)

Figure 3: SEM images of epoxy/WS_2 nanotubes.

polymer matrix and no agglomerates of the WS_2 nanotubes are observed.

Temperature dependencies of complex relative dielectric permittivity for all composites at 1 kHz are presented in Figure 4. The complex relative dielectric permittivity strongly increases with WS_2 concentration; however, its value at room temperature remains very low even for the biggest concentration (1.6 vol%, $\varepsilon' < 6$, $\varepsilon'' < 0.3$). Therefore, all composites are below the percolation threshold.

However, the complex relative dielectric permittivity increases with temperature and has two anomalies: first, below room temperature, which is related to α relaxation

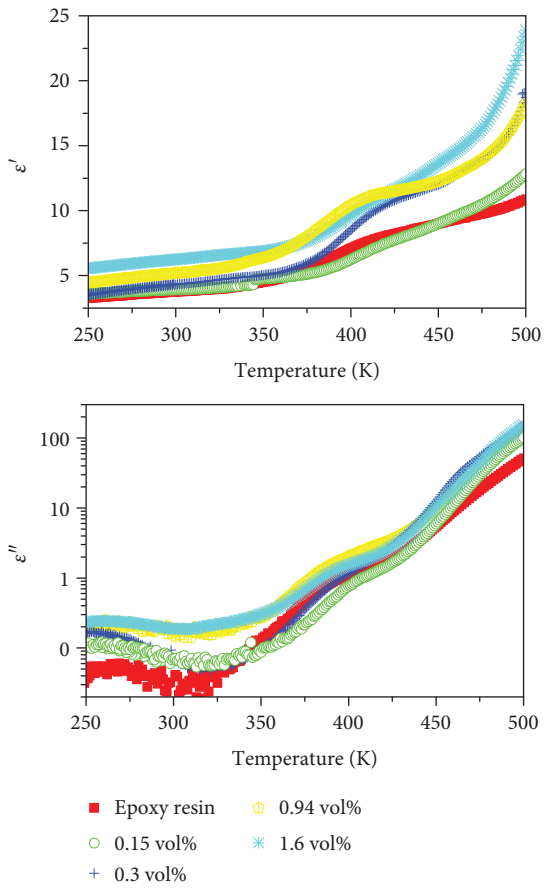

Figure 4: Temperature dependence of complex dielectric permittivity for epoxy/WS_2 composites at 1 kHz frequency.

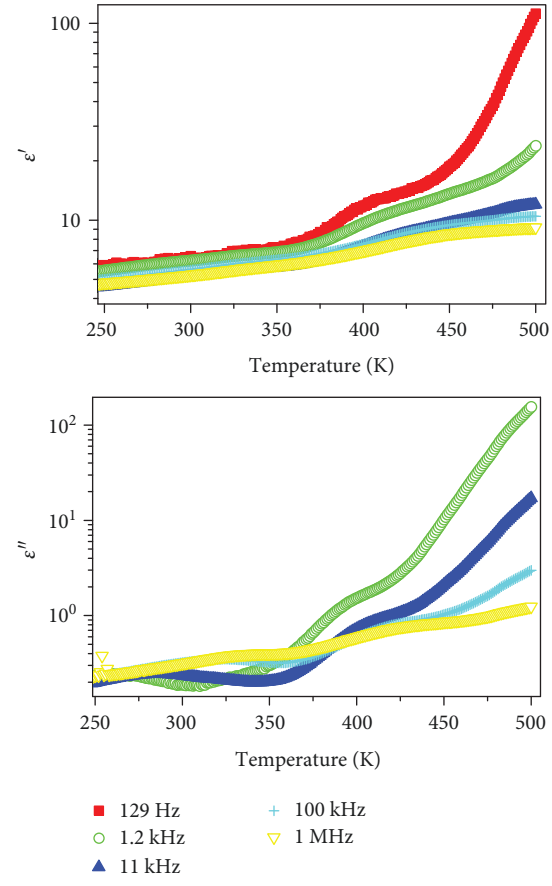

Figure 5: Temperature dependence of complex dielectric permittivity for epoxy with 1.6 vol% WS_2 inclusions at different frequencies.

[25], and second, in the temperature range of 350-400 K, which is related to the Maxwell-Wagner relaxation [26] and the onset of electrical conductivity [27]. Both anomalies are strongly affected by the presence of WS_2 nanotubes. Temperature dependencies of complex relative dielectric permittivity for composites with 1.6 vol% of WS_2 at different frequencies are presented in Figure 5. Below room temperature, the maximum of losses is frequency-dependent and it is related to α relaxation [25]. Above 350 K, the step-like anomaly is related to the Maxwell-Wagner relaxation [26]. At higher temperatures, the electrical conductivity strongly affects results [27]. The temperature of the maximum of the dielectric losses (T_m) is strongly frequency-dependent (Figure 6). The behavior was characterized by the Vogel-Fulcher-Tammann law [28]:

$$\nu = \nu_0 \exp \frac{-E_f}{k(T_m - T_0)}, \quad (1)$$

where k is the Boltzmann constant, ν_0 is the frequency approached with $T_m \to \infty$, E_f is the pseudoactivation energy, and T_0 is the Vogel temperature.

Obtained parameters are listed in Table 1.

The best-fit value of ν_0 was determined as 1 THz for all investigated composites. The value is consistent with phonon spectra of epoxy resin [29]. The Vogel temperature T_0 has the minimum for concentration 0.15 vol%. The decrease of T_0 is related to the intensified polymer molecule dynamics due to the additional free space at the polymer-filler junction. A similar change of the glass transition temperature (which is related to the Vogel temperature [30]) in polymeric composites with nanoinclusions was observed in reference [31]. On the other hand, the increasing of the Vogel temperature can be clarified by the strong interplay between epoxy resin and WS_2 nanotubes. Furthermore, the density of the composite could be higher than the pure polymer density, and consequently, the increasing of the glass transition temperature with the concentration of inclusions could be observed [32].

Frequency dependencies at different temperatures of complex relative dielectric permittivity for composites with 1.6 vol% inclusions are presented in Figure 7.

At low temperatures, the maximum of dielectric losses is observed, which shifts to the higher frequencies with temperature. The mean relaxation time was calculated as $\tau = 1/\nu_{max}$, where ν_{max} is the frequency at which dielectric losses have the maximum. The temperature dependence of the mean relaxation time is presented in Figure 8.

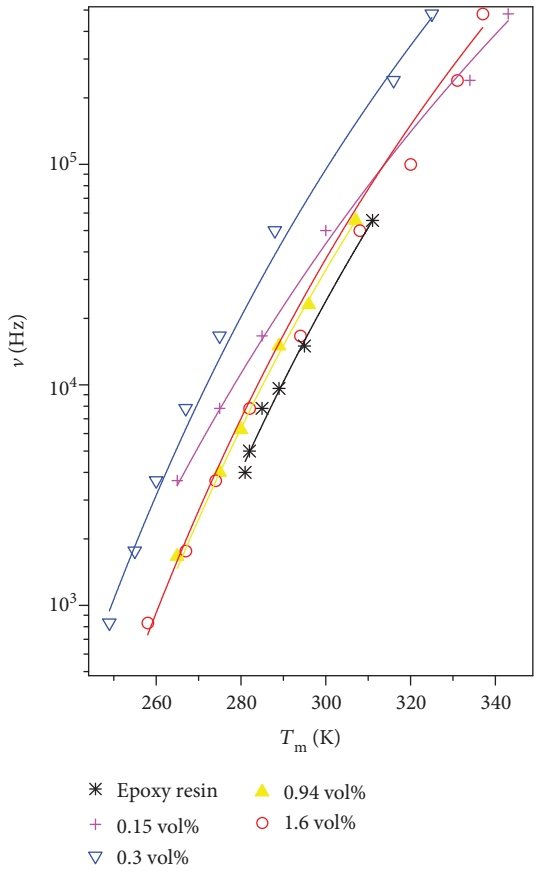

Figure 6: Measured frequencies ν versus T_m of WS_2/epoxy composites.

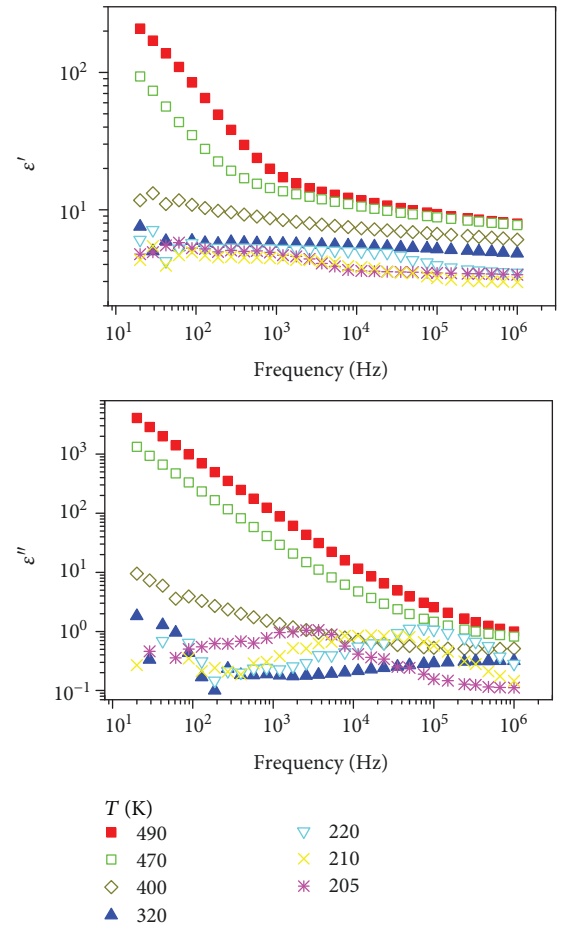

Figure 7: Frequency dependence of complex dielectric permittivity for epoxy with 1.6 vol% WS_2 inclusions at different temperatures.

Table 1: Parameters of the Vogel-Fulcher relationship (equation (1)) for WS_2/epoxy composites.

	E_f/k_B (K(eV))	T_0 (K)
Epoxy	3839 (0.33) ± 209 (0.01)	81 ± 11
0.15 vol%	4651 (0.4) ± 135 (0.01)	25 ± 7
0.3 vol%	3660 (0.31) ± 114 (0.01)	72 ± 6
0.94 vol%	4044 (0.35) ± 77 (0.01)	65 ± 4
1.6 vol%	4047 (0.35) ± 126 (0.01)	65 ± 7

The mean relaxation time increases on cooling according to the Vogel-Fulcher law [28]:

$$\tau = \tau_0 \exp \frac{E_f}{k(T - T_0)}, \quad (2)$$

where τ_0 is the relaxation time at very high temperatures, E_f is the activation energy, and T_0 is the Vogel-Fulcher temperature. Obtained parameters are listed in Table 2. The behavior is more diffused in comparison with the data presented in Table 1.

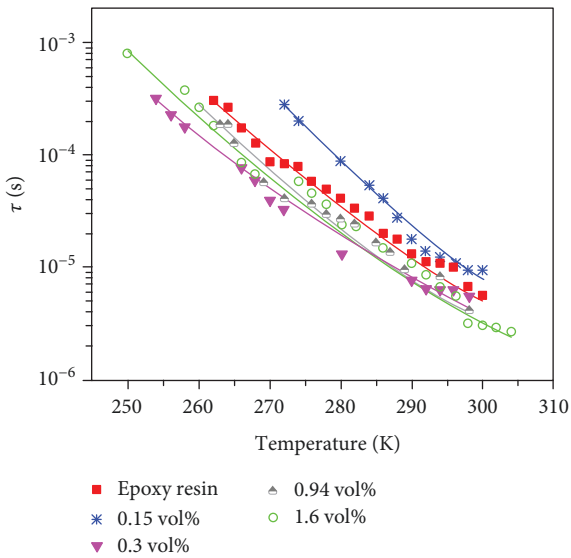

Figure 8: Temperature dependence of the mean relaxation time of WS_2/epoxy composites. The solid lines are calculated according to equation (2).

Table 2: Parameters of the Vogel-Fulcher law (equation (2)) for WS_2/epoxy composites.

	E/k_B (K(eV))	T_0 (K)
Epoxy	2981 (0.26) ± 61 (0.01)	109 ± 3
0.15 vol%	2363 (0.2) ± 88 (0.01)	150 ± 5
0.3 vol%	3167 (0.27) ± 111 (0.01)	90 ± 6
0.94 vol%	2877 (0.25) ± 114 (0.01)	111 ± 6
1.6 vol%	2826 (0.24) ± 75 (0.01)	114 ± 4

Spectra of the electrical conductivity for epoxy-matrix composites with 1.6 vol% (5 wt%) inclusions of the WS_2 nanotubes are presented in Figure 9. Above 420 K, the accidental distribution of the electrons according to energies causes a frequency-independent conductivity (DC conductivity) (Figure 9). The electrical conductivity of composites is caused by the electrical conductivity of the pure epoxy resin matrix. Above some critical frequency, the electrical conductivity strongly increases with frequency. The spectra of σ have been fitted according to the Almond-West type power law [33]:

$$\sigma = \sigma_{DC} + A\omega^s, \tag{3}$$

where σ_{DC} is the DC conductivity and $A\omega^s$ is the AC conductivity. The model fits the electrical conductivity spectra of the investigated composites quite well; only at lower frequencies, the divergence is observed due to the nonohmic contact impact.

In order to separate effects of contacts and volume conductivity materials, we calculated the real part (ρ') and the imaginary part (ρ'') of the complex specific resistance $\rho^* = \rho' - i\rho''$:

$$\rho' = \frac{\varepsilon''}{\varepsilon'^2 + \varepsilon''^2}\frac{1}{\varepsilon_0\omega},$$
$$\rho'' = \frac{\varepsilon'}{\varepsilon'^2 + \varepsilon''^2}\frac{1}{\varepsilon_0\omega}, \tag{4}$$

where $\omega = 2\pi\nu$ and ν is the measurement frequency. In the plot $\rho''(\rho')$, the half circles at higher frequencies are caused by volume conductivity of the composite, and the higher values of ρ^* are already influenced by contacts (Figure 10). The contact influence is playing an important role at higher temperatures and low frequencies.

The temperature dependence of $\ln(\sigma_{DC})$ of epoxy-matrix composites with various WS_2 concentrations is presented in Figure 11. The DC conductivity strongly increases with the WS_2 concentration. Therefore, electrical contacts between epoxy resin and WS_2 are rather ohmic. $\ln(\sigma_{DC})$ $(1/T)$ is the linear temperature dependence. Therefore, from this dependence, the activation energy E_B of the conductivity and the prefactor σ_0 were determined (the

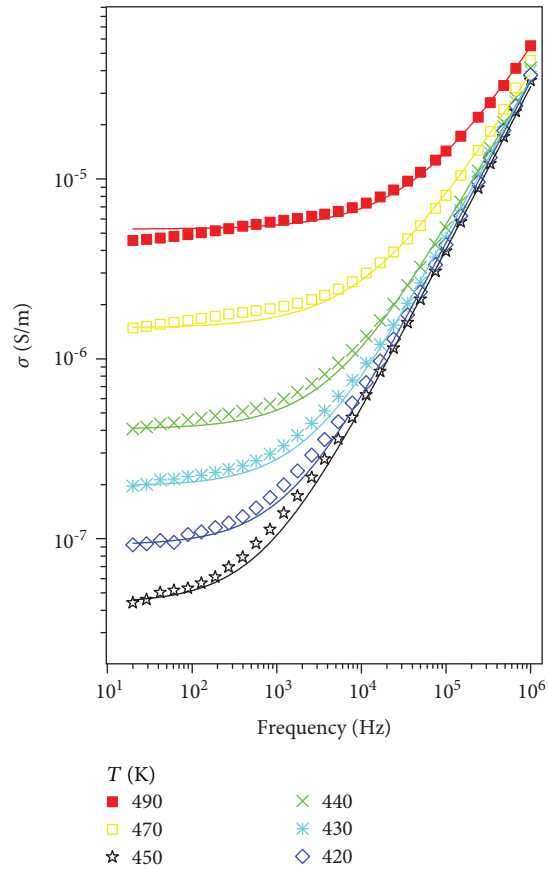

Figure 9: Frequency dependence of the electrical conductivity of WS_2/epoxy composites with 1.6 vol% inclusions at different temperatures.

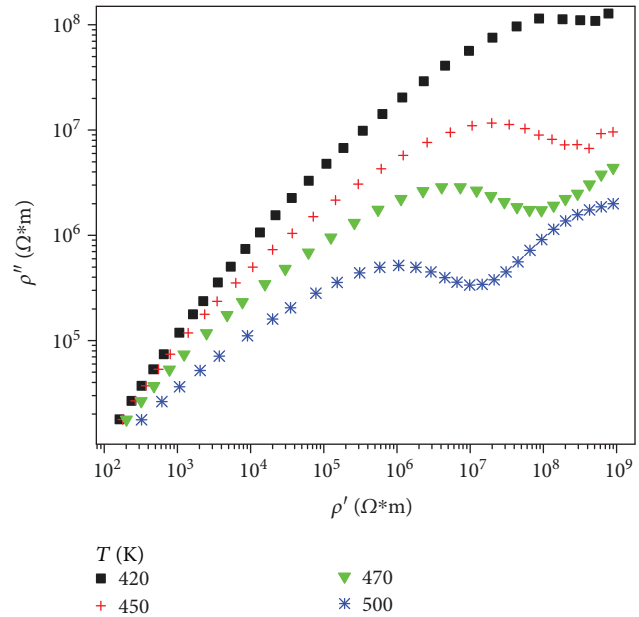

Figure 10: Cole-Cole diagram of $\rho^* = \rho' - i\rho''$ for epoxy with 1.6 vol% WS_2 inclusions at different temperatures.

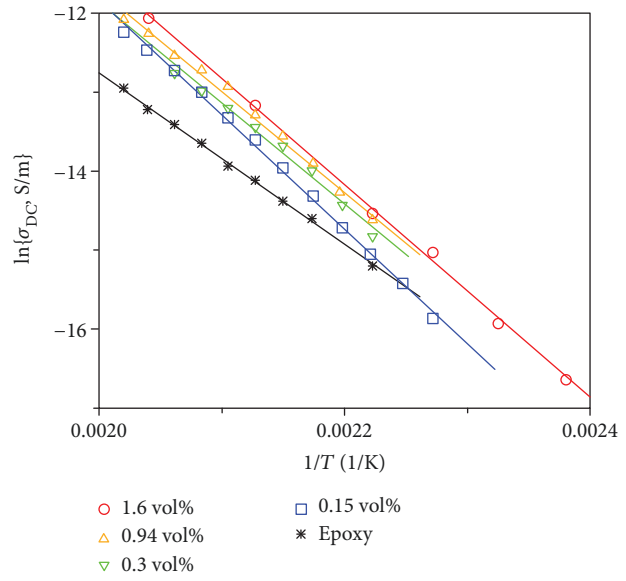

Figure 11: Temperature dependence of the DC electrical conductivity of WS_2/epoxy composites.

conductivity at very high temperatures) according to the Arrhenius law:

$$\sigma_{DC} = \sigma_0 \exp \frac{-E_B}{kT}. \quad (5)$$

The obtained parameters are presented in Table 3. The activation energy E_B and the conductivity σ_0 are practically not impacted by the concentration of nanoinclusions. However, the activation energy in composites is higher than in that in pure epoxy.

4. Conclusions

Broadband dielectric properties of tungsten disulfide (WS_2) nanotube epoxy-matrix composites over a wide temperature range (250 K-500 K) are presented for concentrations up to 1.6 vol% (5 wt%). The electrical percolation was not detected in the investigated composites at room temperature. The relative dielectric permittivity of composites with 1.6 vol% inclusions is almost 3 times higher than the relative dielectric permittivity of the pure polymer, and the DC electrical conductivity of composites is about 10^{-6} S/m at 500 K, which indicates that the composites are appropriate for antistatic applications at higher temperatures [34], similarly to WS_2/polyurethane composites [22]. Broadband electromagnetic spectra of the composites are largely governed by the dynamics of epoxy resin molecules. The Vogel temperature T_0 has the minimum for concentration 0.15 vol%. Above 410 K, the electrical conductivity is typical for WS_2/epoxy composites with the WS_2 inclusions as well. The DC conductivity increases with the WS_2 concentration, while its activation energy is almost uncontrolled by the concentration of nanoinclusions; however, in composites, it is higher than in pure epoxy resin. Therefore, the electrical transport occurs between WS_2 nanotubes and epoxy matrix at higher temperatures (above 410 K).

Table 3: Arrhenius law fit parameters for WS_2/epoxy composites.

	ln $\{\sigma_0$, S/m$\}$	E_A/k_B (K(eV))
Epoxy	8.7 ± 0.1	10727 (0.92) ± 85 (0.01)
0.15 vol%	16.9 ± 0.3	14367 (1.24) ± 132 (0.01)
0.3 vol%	11.4 ± 0.3	11702 (1.01) ± 143 (0.01)
0.94 vol%	13.7 ± 0.1	12681 (1.1) ± 74 (0.01)
1.6 vol%	15.4 ± 0.1	13457 (1.16) ± 74 (0.01)

Data Availability

The underlying data related to this article are available upon request.

Conflicts of Interest

The authors declare that there is no conflict of interest regarding the publication of this paper.

Acknowledgments

A. Zak is grateful for the financial support to the Israel PAZI Foundation and to the Israel "Ministry of Science, Technology and Space" grant (number 3-11839).

References

[1] R. J. Chen, T. Zhao, W. P. Wu et al., "Free-standing hierarchically sandwich-type tungsten disulfide nanotubes/graphene anode for lithium-ion batteries," *Nano Letters*, vol. 14, no. 10, pp. 5899–5904, 2014.

[2] G. Lalwani, A. M. Henslee, B. Farshid et al., "Tungsten disulfide nanotubes reinforced biodegradable polymers for bone tissue engineering," *Acta Biomaterialia*, vol. 9, no. 9, pp. 8365–8373, 2013.

[3] P. G. Yan, A. J. Liu, Y. S. Chen et al., "Microfiber-based WS_2-film saturable absorber for ultra-fast photonics," *Optical Materials Express*, vol. 5, no. 3, pp. 479–489, 2015.

[4] M. Shangmugam, T. Bansal, C. A. Durcan, and B. Yu, "Schotky-barrier solar cell based on layered semiconductor tungsten disulfide nanofilm," *Applied Physics Letters*, vol. 101, no. 26, article 263902, 2012.

[5] I. Kaplan-Ashiri, S. R. Cohen, K. Gartsman, R. Rosentsveig, G. Seifert, and R. Tenne, "Mechanical behavior of individual WS_2 nanotubes," *Journal of Materials Research*, vol. 19, no. 2, pp. 454–459, 2004.

[6] D. Maharaj and B. Bhushan, "Characterization of nanofriction of MoS_2 and WS_2," *Materials Letters*, vol. 142, pp. 207–210, 2015.

[7] C. S. Reddy, A. Zak, and E. Zussman, "WS_2 nanotubes embedded in PMMA nanofibers as energy absorptive material," *Journal of Materials Chemistry*, vol. 21, no. 40, pp. 16086–16093, 2011.

[8] X. F. Zhang, B. Luster, A. Church et al., "Carbon nanotube – MoS_2 composites as solid state lubricants," *ACS Applied Materials & Interfaces*, vol. 1, no. 3, pp. 735–739, 2009.

[9] M. Sahu, L. Narashimhan, O. Prakash, and A. M. Raichur, "Noncovalently functionalized tungsten disulfide nanosheets for enhanced mechanical and thermal properties of epoxy nanocomposites," *ACS Applied Materials and Interfaces*, vol. 9, no. 16, pp. 14347–14357, 2017.

[10] D. Haba, A. J. Brunner, M. Barbezat, D. Spetter, W. Tremel, and G. Pinter, "Correlation of epoxy material properties with the toughening effect of fullerene-like WS2 nanoparticles," *European Polymer Journal*, vol. 84, pp. 125–136, 2016.

[11] Y. Wang, Y. Zhao, X. Han, and M. Liu, "Epoxy nanocomposites with two-dimensional tungsten disulfide additives," in *2015 ICCM International Conferences on Composite Materials*, Copenhagen, July 2015.

[12] M. Naffakh, C. Marco, G. Ellis et al., "Novel poly(3-hydroxybutyrate) nanocomposites containing WS_2 inorganic nanotubes with improved thermal, mechanical and tribological properties," *Materials Chemistry and Physics*, vol. 147, no. 1-2, pp. 273–284, 2014.

[13] A. Zak, L. Sallacan-Ecker, A. Margolin et al., "Scaling up of the WS_2 nanotubes synthesis," *Fullerenes, Nanotubes and Carbon Nanostructures*, vol. 19, no. 1-2, pp. 18–26, 2011.

[14] M. Shneider, H. Dodiuk, S. Kenig, and R. Tenne, "The effect of tungsten sulfide fullerene-like nanoparticles on the toughness of epoxy adhesives," *Journal of Adhesion Science and Technology*, vol. 24, no. 6, pp. 1083–1095, 2010.

[15] M. Naffakh, Z. Martin, N. Fanegas, C. Marco, M. A. Gómez, and I. Jiménez, "Influence of inorganic fullerene-like WS_2 nanoparticles on the thermal behavior of isotactic polypropylene," *Journal of Polymer Science Part B: Polymer Physics*, vol. 45, no. 16, pp. 2309–2321, 2007.

[16] M. Naffakh, C. Marcoa, M. A. Gómeza, and I. Jiménez, "Novel melt-processable nylon-6/inorganic fullerene-like WS_2 nanocomposites for critical applications," *Materials Chemistry and Physics*, vol. 129, no. 1-2, pp. 641–648, 2011.

[17] C. Zhang, Z. Ning, Y. Liu et al., "Electrical transport properties of individual WS_2 nanotubes and their dependence of water and oxygen absorption," *Applied Physics Letters*, vol. 101, no. 11, article 113112, 2012.

[18] R. Levi, O. Bitton, G. Leitus, R. Tenne, and E. Joselevich, "Field-effect transistors based on WS_2 nanotubes with high current-carrying capacity," *Nano Letters*, vol. 13, no. 8, pp. 3736–3741, 2013.

[19] G. Viskadouros, A. Zak, M. Stylianakis, E. Kymakis, R. Tenne, and E. Stratakis, "Enhanced field emission of WS_2 nanotubes," *Small*, vol. 10, no. 12, pp. 2398–2403, 2014.

[20] J. Petzelt, D. Nuzhnyy, V. Bovtun, M. Savinov, M. Kempa, and I. Rychetsky, "Broadband dielectric and conductivity spectroscopy of inhomogeneous and composite conductors," *Physica Status Solidi A: Applications and Materials Science*, vol. 210, no. 11, pp. 2259–2271, 2013.

[21] A. Sedova, S. Khodorov, D. Ehre et al., "Dielectric and electrical properties of WS_2 nanotubes/epoxy composites and their use for stress monitoring of structures," *Journal of Nanomaterials*, vol. 2017, Article ID 4838095, 13 pages, 2017.

[22] J. Macutkevic, J. Belovickis, G. Otorgust et al., "Broadband dielectric and ultrasonic properties of WS_2 nanotubes/polyurethane composites," *Polymer Composites*, vol. 39, no. 12, pp. 4477–4485, 2018.

[23] J. K. W. Sandler, J. E. Kirk, I. A. Kinloch, M. S. P. Shaffer, and A. H. Windle, "Ultra-low electrical percolation threshold in carbon-nanotube-epoxy composites," *Polymer*, vol. 44, no. 19, pp. 5893–5899, 2003.

[24] H. Deng, L. Lin, M. Z. Ji, S. Zhang, M. Yang, and Q. Fu, "Progress on the morphological control of conductive network in conductive polymer composites and the use as electroactive multifunctional materials," *Progress in Polymer Science*, vol. 39, no. 4, pp. 627–655, 2014.

[25] G. A. Pogany, "The α relaxation in epoxy resins," *European Polymer Journal*, vol. 6, no. 2, pp. 343–353, 1970.

[26] H. Neumann and G. Arlt, "Maxwell-wagner relaxation and degradation of $SrTiO_3$ and $BaTiO_3$ ceramics," *Ferroelectrics*, vol. 69, no. 1, pp. 179–186, 1986.

[27] J. Macutkevic, P. P. Kuzhir, A. G. Paddubskaya et al., "Broadband dielectric/electric properties of epoxy thin films filled with multiwalled carbon nanotubes," *Journal of Nanophotonics*, vol. 7, no. 1, article 073593, 2013.

[28] A. K. Tagantsev, "Vogel-Fulcher relationship for the dielectric permittivity of relaxor ferroelectrics," *Physical Review Letters*, vol. 72, no. 7, pp. 1100–1103, 1994.

[29] K. E. Chike, M. L. Myrick, and R. R. Lyon, "Raman and near-infrared studies of an epoxy resin," *Applied Spectroscopy*, vol. 47, no. 10, pp. 1631–1635, 1993.

[30] P. Frübing, H. Krüger, H. Goering, and R. Gerhard-Multhaupt, "Relaxation behaviour of thermoplastic polyurethanes with covalently attached nitroaniline dipoles," *Polymer*, vol. 43, no. 9, pp. 2787–2794, 2002.

[31] L. C. Tang, Y. J. Wan, K. Peng et al., "Fracture toughness and electrical conductivity of epoxy composites filled with carbon nanotubes and spherical particles," *Composites Part A: Applied Science and Manufacturing*, vol. 45, pp. 95–101, 2013.

[32] C. Wei, D. Srivastava, and K. Cho, "Thermal expansion and diffusion coefficients of carbon nanotube-polymer composites," *Nano Letters*, vol. 2, no. 6, pp. 647–650, 2002.

[33] P. G. Bruce, A. R. West, and D. P. Almond, "A new analysis of ac conductivity data in single crystal β-alumina," *Solid State Ionics*, vol. 7, no. 1, pp. 57–60, 1982.

[34] N. A. Aal, F. El-Tantawy, A. Al-Hajry, and M. Bououdina, "New antistatic charge and electromagnetic shielding effectiveness from conductive epoxy resin/plasticized carbon black composites," *Polymer Composites*, vol. 29, no. 2, pp. 125–132, 2008.

Hindawi
Journal of Nanomaterials
Volume 2019, Article ID 5390562, 11 pages
https://doi.org/10.1155/2019/5390562

Research Article

Controlled Gold Nanoparticle Placement into Patterned Polydimethylsiloxane Thin Films via Directed Self-Assembly

Keith R. Berry Jr.[1], **Ricardo L. Romo**,[2] **Megan Mitchell**,[1] **Vinith Bejugam**,[3] **and D. Keith Roper**[4]

[1]*Ralph E. Martin Department of Chemical Engineering, University of Arkansas, Fayetteville, AR 72701, USA*
[2]*Microelectronics-Photonics Graduate Program, University of Arkansas, Fayetteville, AR 72701, USA*
[3]*PacTech, Packaging Technologies, Santa Clara, CA 95050, USA*
[4]*Department of Biological Engineering, Utah State University, Logan, UT 84322, USA*

Correspondence should be addressed to D. Keith Roper; keith.roper@usu.edu

Received 9 April 2019; Accepted 18 July 2019; Published 5 August 2019

Guest Editor: Laijun Liu

An economically scalable and reproducible method to assemble nanoparticles (NPs) into ordered arrays with high fidelity remains a fundamental roadblock. Methods like directed self-assembly have shown the highest promise resulting in >85% density of NP-filled prepatterned polymer cavities. This work refines directed self-assembly by controlling the evaporation rate, substrate velocity (deposition rate), and NP diameter resulting in reproducible fabrication of ordered arrays with areas >2 mm × 2 mm and ~100% density of filled cavities. Measured optical spectra showed a blueshift in the localized surface plasmon resonance (LSPR) and surface lattice resonance (SLR) peaks with increasing NP density for both 100 and 150 nm gold (Au) NPs. Discrete dipole approximation (DDA), coupled dipole approximation (CDA), rapid semi-analytical CDA (rsa-CDA), and Mie theory simulations closely matched extinction per nanoparticle (extinction/NP) calculations for measured extinction spectra. An ordered array containing 150 nm AuNPs was used for comparison with rsa-CDA estimates using both polydimethylsiloxane (PDMS) and glass refractive indices (RI) resulting in peak location estimates within 1.7% and comparable relative increases in peak heights. Both the measured and simulated SLR peak heights were shown to significantly increase when the array was on glass as opposed to within PDMS.

1. Introduction

Gold (Au) nanoparticles (NPs) exhibit localized surface plasmon resonance (LSPR) through conduction-electron oscillations when an external electromagnetic (EM) field is applied [1–3]. When the AuNPs are ordered into a square lattice and exposed to an external EM field, the LSPRs on each individual particle couple with light diffracted from the ordered arrangement resulting in a surface lattice resonance (SLR), i.e., a Fano resonance or coupled lattice resonance (CLR), spectral feature corresponding to the lattice spacing [3–10]. SLR features can be tuned by varying the lattice spacing, NP geometry, incident EM field intensity, and refractive index (RI) [8, 9, 11–16]. Simulations, such as plasmon hybridization, coupled dipole approximation (CDA), rapid semi-analytical CDA (rsa-CDA), finite-difference time-domain (FDTD), and Fano theory, have been used to estimate both the LSPR and SLR peak locations, peak heights, scattering amplitudes, and scattering cross-sections [5, 7, 10, 17–19].

Popular commercial microfabrication techniques, such as electron beam lithography (EBL), nanoimprint lithography (NIL), laser ablation (LA), and focused ion beam (FIB), have been used to produce random and ordered assemblies of AuNPs [12, 20–24]. Recent advances in the fabrication of ordered arrays include thermal evaporation, dip-coating

self-assembly, template-assisted self-assembly, and directed self-assembly [4, 19, 25–35]. In particular, a variety of self-assembly techniques have been developed and employed to cost-effectively fabricate arrays of AuNPs. These techniques range from receding contact line, i.e., meniscus moving, approaches (the solution is between a fixed glass superstrate and a fixed substrate where evaporation controls the deposition of AuNPs) to fixed glass superstrates with moving substrates (the solution between a fixed glass superstrate and a substrate attached to a linear translation stage where evaporation and the rate of substrate motion controls the deposition) [26, 27, 30–32]. These advances offer economically scalable approaches to fabricate ordered arrays of AuNPs, but a reproducible approach that can produce high-density, millimeter-scale areas with single AuNP per cavity is lacking.

This work introduced a refined directed self-assembly process for fabricating ordered arrays of AuNPs yielding >2 mm × 2 mm areas of ~100% density of filled prepatterned polydimethylsiloxane (PDMS) cavities containing one NP per cavity. Extinction spectra and extinction per NP (extinction/NP) values showed blueshifting of the LSPR and SLR peaks as the density of AuNPs increased. Mie theory and DDA closely matched measured values for extinction/NP for LSPR peaks of both 100 and 150 nm AuNPs. CDA and rsa-CDA resulted in greater differences between measured extinction/NP values but closely matched the measured peak locations for both LSPR and SLR for 150 nm AuNPs. Discrepancies between these simulated results for CDA and measured results were likely a function of RI because the measured values were surrounded by air, water, Triton X-100, and PDMS while simulated values assumed only PDMS surrounded the AuNPs. An ordered array containing 150 nm AuNPs was spectroscopically characterized before being transferred onto a glass slide and spectroscopically characterized again. rsa-CDA simulations were performed using PDMS and glass RI and compared to the measured spectra, which showed that peak locations for LSPR, quadrupole, and SLR features matched within 1.7%. Relative increases in peak heights also closely matched for rsa-CDA simulation and measured extinction spectra.

2. Materials and Methods

2.1. Fabrication of 2D Array Stamps. Silicon (Si) master stamps lithographed with a square lattice of posts at a 600 nm pitch (150 nm post height; 195 nm post diameter) were purchased from LightSmyth Technologies (Eugene, OR, S2D-24B2-0808-150-P). Polydimethylsiloxane (PDMS) monomer and curing agent (Sylgard 184 silicone elastomer kit; #240 401 9862) were purchased from Dow Corning Corporation (Midland, MI). Monomer and curing agent were mixed at a 10 : 1 monomer : cross-linker ratio at 3000 rpm for 6 minutes in a speed mixer purchased from FlackTek Inc. (#DAC 150SP/601 0064, Landrum, SC). The mixture was then degassed until observable air bubbles were removed (5-25 minutes) and poured onto a prerinsed (acetone+water) Si stamp and cured for 15 min at 180°C. Cured PDMS templates with 600 nm cavity arrays were peeled away from the Si stamp. PDMS arrayed-cavity stamp thickness averaged 300 μm.

2.2. Solution Preparation. Triton X-100 purchased from Sigma-Aldrich (St. Louis, MO) was diluted to 1 weight (wt) % in DI water and nitrogen capped (nitrogen gas was blown into the vessel for ~1 min) to remove air bubbles. 100 and 150 nm citrate-stabilized AuNPs (stock: 6 and 6.4 mg/mL, respectively) purchased from Nanopartz (Loveland, CO) were diluted to 3 and 3.2 mg/mL, respectively, in 1 wt% Triton X-100. The solution was nitrogen capped to remove air bubbles.

2.3. Stage Preparation. A substrate with a cavity (see Scheme 1) was built using glass slides (VWR, 16004-430) to support and translocate the stamp and slow evaporative AuNP deposition. The substrate consisted of a 2 in × 3 in single glass slide base (Premiere, 6101) supporting four glass slide walls (VWR, 16004-430) forming a 4 mm × 20 mm cavity with a depth of ~1 mm in the center as shown in Schemes 1(a)–1(d). The walls were one glass slide thick (1 mm) and were cut using a diamond knife and then attached to the base using epoxy resin (Loctite, heavy duty). The substrate was attached via carbon tape to a motorized syringe pump (KD Scientific, KDS-100) as shown in Scheme 1(c). A fixed superstrate was built by using superglue (Loctite, Super Glue Gel) to attach a 2 mm × 2 mm glass slide with a thickness of 1 mm (VWR, 16004-430) that was cut with a diamond knife to a second 1 in × 3 in glass slide for high evaporation experiments (Scheme 1(a)) or a 2 in × 3 in single glass slide for low evaporation experiments (Scheme 1(b)). The purpose of this 2 mm × 2 mm glass slide was to facilitate contact line pinning of the NP solution on the PDMS arrayed-cavity stamp as shown in Scheme 1(d). The 2 mm × 2 mm glass slide on the 2 in × 3 in slide for low evaporation experiments was surrounded by a single layer of glass coverslips (Corning, 2845-18, 0.12-0.16 mm thickness) that were spaced ~5 mm from each side of the 2 mm × 2 mm slide as shown in Scheme 1(e). The superstrate was then attached to a 3-axis positioner (Line Tools Company, Model A-LH) so that the 2 mm × 2 mm glass slide could be lowered into the 4 mm × 20 mm cavity containing the stamp.

2.4. Gold Nanoparticle Deposition. The PDMS arrayed-cavity stamp was cut in half using a razorblade so that two experiments could be performed with each stamp. A half-stamp was placed inside the substrate cavity, and a 2.5 μL drop of 1 wt% Triton X-100 in DI water was added to the bottom center of the stamp. The superstrate was then lowered into position so that the drop pinned to the 2 mm × 2 mm glass slide and lowered until it spread and pinned to all four sides of the slide (as shown in Schemes 1(a) and 1(d)). The linear stage was then set to 8.0 μm/s. A cardboard box was placed over the system to minimize evaporation due to ambient light and convection. This process acted as a precoat to increase AuNP deposition. Once the precoat was finished (~15 min), a 2.5 μL drop of 3 (100 nm AuNPs) or 3.2 mg/mL (150 nm AuNPs) in 1 wt% Triton X-100 was placed in the same

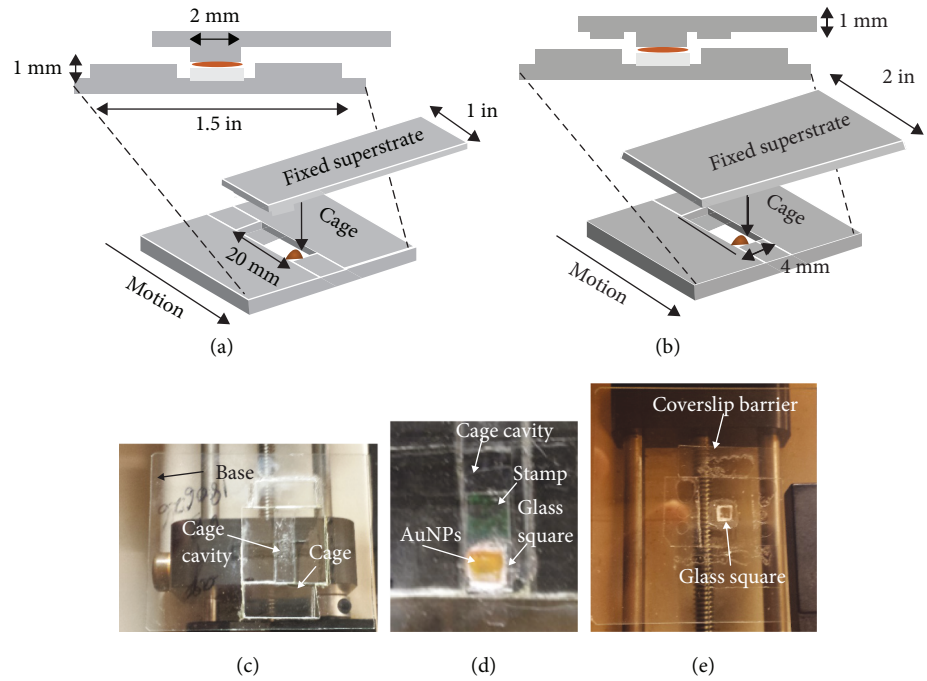

Scheme 1: Schematic of directed self-assembly stage setup used for (a) high evaporation and (b) low evaporation experiments. (c) Shows the location on the syringe pump where the cage is attached. (d) Shows an example of a drop of AuNPs pinned by the fixed superstrate at the beginning of a high evaporation self-assembly experiment. (e) Shows the superstrate used for the low evaporation self-assembly experiments.

position and the superstrate was lowered until the drop pinned on all four sides of the glass slide. The linear stage was set at rates ranging from 2.1 μm/s to 1.2 μm/s.

2.5. Optical Characterization. Transmission spectra of each AuNP ordered array were measured using a light microscope (Eclipse LV100, Nikon Instruments, Melville, New York) integrated with a UV-Vis spectrometer (Shamrock 303, Andor Technology, Belfast, UK). Extinction amplitudes for both LSPR and SLR peaks were taken using a tangent line corresponding to each peak. The extinction was normalized by setting the valley before the SLR peak to 0.01 A.U. for the extinction of each AuNP array. Dark-field microscopic images were captured at 20x and 100x objectives using the same light microscope used for the spectral characterization.

2.6. Rapid Semi-analytical Coupled Dipole Approximation (rsa-CDA) Simulations. Rapid semi-analytical coupled dipole approximation (rsa-CDA) was performed to determine estimated spectral peak locations for arrays of AuNPs with a diameter of 150 nm using a previously developed method [5, 36, 37]. Briefly, this configuration treats each AuNP as a single dipole point with a dipole polarizability of, α. The NPs were arranged in a 2D square lattice with an array dimension of 301 × 301 and a lattice constant, distance from the center of one NP to the adjacent NP, set at 600 nm. The simulation was performed across a wavelength range of 500-950 nm for refractive indices (RI) of PDMS (1.42) and glass (1.52). The simulation outputted extinction efficiencies across the spectral range. The primary observable features were the SLR peak, the LSPR peak, and the quadrupole peak (150 nm only).

2.7. Discrete Dipole Approximation (DDA) and CDA Simulations. Discrete dipole approximation (DDA) simulations were performed in a 12-core supercomputer node with a 64 GB memory for 500 to 950 nm PDMS (1.42) wavelengths and a resolution of 5 nm. Target and parameter files for DDSCAT 7.3 were generated, using a custom-made MATLAB tool available on nanoHUB [38], for 100 and 150 nm diameter AuNPs. The generated spectra for a single AuNP were output into Microsoft Excel for further analysis, and real and imaginary parts of the polarizability were stored for ordered array simulations. The polarizability data was then imported into MATLAB for CDA to generate a 301 × 301 array of AuNPs with a lattice spacing of 600 nm in PDMS (1.42). The generated spectra for both 100 nm and 150 nm diameter AuNP arrays were output into Microsoft Excel for further analysis.

2.8. Extinction per NP Calculations. Estimates of extinction per NP were calculated previously using Mie solutions to Maxwell's equations, DDA, and CDA by Dunklin et al. [2]. Briefly, extinction per NP for a single particle Mie theory was determined via $\sigma(\log_{10}e)/n$, where σ was the Mie theory extinction cross-section in cm^2, $\log_{10}e$ was a conversion factor between log bases, and n was the spectrum-averaged RI of PDMS (1.42). DDA and CDA output extinction efficiency were converted to an extinction cross-section before being converted to extinction per NP. The conversion from extinction efficiency to extinction cross-section was performed by multiplying the extinction efficiency by the NP geometric cross-section, i.e., πr^2, where r was the radius of the sphere (50 or 75 nm). Extinction per NP for the current work was determined by A/cn, where A is the extinction peak height

and c is the density of NPs in a square lattice assuming one particle per cavity with an interparticle spacing of 600 nm.

3. Results and Discussion

3.1. Current Self-Assembly Approaches. Possible options to fabricate ordered arrays of AuNPs using patterned substrates include self-assembly techniques like template-assisted self-assembly, dip-coating self-assembly, and directed self-assembly. Template-assisted self-assembly is a process that uses a patterned substrate (e.g., templated PDMS and templated silicon wafer) as a template to facilitate the NPs in solution to arrange in a regular, periodic structure either within the patterned substrate or on a separate substrate [19]. In dip-coating self-assembly, a hydrophilic or hydrophilized patterned substrate is dipped at controllable rates for various time intervals into a solution of NPs, where the NPs are drawn into the patterned cavities via convective and capillary forces [28, 29]. In directed self-assembly, a patterned substrate is attached to a linear translation stage and a fixed glass slide is used as a superstrate where a droplet of NPs is sandwiched between the fixed superstrate and the patterned substrate that moves at a controllable velocity [26, 27].

Table 1 summarizes the four key features of current self-assembly approaches and the method described in this work: (1) structure and dimensions of the nanostructure, (2) fabrication conditions, (3) substrate on which the nanostructure is fabricated, and (4) fidelity achieved. Matricardi et al. introduced a template-assisted self-assembly method to fabricate ordered arrays of close-packed, mesoscopic clusters of AuNPs onto a hydrophilized glass coverslip by sandwiching a drop of AuNPs between a patterned PDMS substrate and a hydrophilized glass coverslip superstrate [19]. Bejugam introduced an alternative template-assisted self-assembly method that sandwiched a 1-2 μL droplet of AuNPs between a PDMS-PEO copolymer substrate contained within a walled cage and a glass coverslip that sealed the cage and pinned the droplet to three sides of the substrate, after which the droplet was left to evaporate for >6 hours [4]. Kinnear et al. introduced a dip-coating self-assembly method using a silanized patterned PDMS substrate, and Juillerat et al. introduced a dip-coating self-assembly method using a hydrophilic patterned PMMA substrate, in which both substrates were dipped into solutions of NPs at various controlled rates [28, 29]. Cerf and Vieu used a directed self-assembly approach with a suspension of citrate-coated AuNPs containing 1 wt% Triton X-100 surfactant to increase the deposition in a hydrophobic patterned PDMS substrate, while Fan et al. used a much slower substrate velocity (0.6 μm/s), lower controlled temperature (21°C), and a controlled contact angle (25°) rather than surfactant or a hydrophilic patterned substrate to deposit silica-gold nanoshells into ordered arrays in PDMS [26, 27]. Based on the approaches described above, directed self-assembly offers the best approach to achieve high fidelity ordering of single AuNPs per cavity in a PDMS substrate across millimeter scale areas with high reproducibility and scalability.

This work introduces a refined directed self-assembly approach that uses a modified fixed glass superstrate and utilizes contact line pinning that conforms the droplet across a small square glass slide for deposition to occur. In conjunction with the modified fixed glass superstrate, the substrate was contained within a walled cage that reduced the evaporation rate of the droplet rather than controlling the temperature. Controlling the evaporation rate with the walled cage and modified superstrate offers a reproducible and scalable method for fabricating ordered arrays under ambient conditions. Varying the substrate velocity (deposition rate), AuNP diameter, and evaporation rate resulted in densities of filled cavities between 85% and 100% with single AuNPs per cavity in higher density arrays.

3.2. Developing Uniform, Large-Area AuNP Ordered Arrays. The development of a scalable, economic, and reproducible approach to fabricating large-area ordered arrays with high fidelity, density, and accuracy remains important for the advancement of electronic, sensing, and photonic devices. Directed self-assembly, in particular, offers a scalable, economic approach for fabricating ordered arrays with high fidelity and densities ranging from 70 to 85% for single particles per cavity and >85% for multiple particles per cavity [26, 27, 30–32]. This work refines a directed self-assembly approach yielding densities of ~100% for large-area (>2 mm × 2 mm) arrays by manipulating three primary variables: (1) evaporation rate, (2) deposition rate, and (3) NP diameter. The evaporation rate in this work was primarily due to the head-space within the walled cage when the superstrate was in contact with the droplet of AuNPs, the separation distance between the stamp and the superstrate, the separation distance between the cage and the superstrate, and the overall size of the superstrate that affected the airflow potential. It was observed that increasing the size of the superstrate resulted in a lower evaporation rate and higher deposition. Reducing the deposition rate resulted in higher overall densities for both high and low evaporation conditions. Increasing the AuNP diameter resulted in a more viscous solution with relatively similar concentrations of AuNPs, which also improved the densities while reducing evaporation potential due to the increased viscosity of the solution. These variables were adjusted to fabricate the six arrays shown in Figure 1.

Figure 1 shows the results for six arrays fabricated using two different evaporation rates (high and low), two different AuNP diameters (100 and 150 nm), and four different deposition rates (2.1, 1.8, 1.5, and 1.2 μm/s). A deposition rate of 1.2 μm/s (lower evaporation rate and 150 nm AuNP diameter held constant) was performed resulting in a >2 mm × 2 mm area of ~100% filled cavities with high uniformity as shown in the bottom right (red filled triangle) images in Figure 1. The 20x inset shows a uniform color across the entire image while the 100x image shows the high density of filled cavities. Matricardi et al. and Zhang et al. report that the uniform color across the entirety of the array suggests that the nanoparticles are aligned and deposited in a uniform and reproducible manner within each cavity [19, 33]. The results for the bottom right image (red filled triangle) differ from many of the reported processes in that the array appears to consist of a uniform area of single AuNPs per cavity while reports by

Table 1: Characteristics and outcomes of current self-assembly processes compared with the self-assembly process introduced in this work.

Structure and dimensions	Conditions/state	Substrate	Fidelity	Characterization/modeling techniques
Template-assisted self-assembly [4, 19]				
Array dimensions: Diameter: 230, 270, 330, 440, and 960 nm Spacing: 400, 500, 600, 740, and 1600 nm AuNP diameter: ~52 nm	AuNP dispersion between the hydrophilized coverslip and the patterned PDMS at room temperature	Hydrophilized coverslip Templated PDMS-PEO	Large-area arrays with ~17 NPs per cavity, ~100% density of filled cavities, inconsistent size and number of NPs in each cavity	Characterization: UV-Vis, FTIR, SEM, TEM, and SERS Modeling: FDTD
Array dimensions: Diameter: 195 and 260 nm Depth: 150 and 350 nm Spacing: 600 and 700 nm AuNP diameter: 76 and 100 nm	Patterned PDMS-PEO contained within a walled cage and AuNP dispersion between the substrate in cage and the glass coverslip superstrate		Large-area arrays with 1-20 NPs per cavity, 50-90% density, inconsistent number of NPs in each cavity, wave-like deposition	Characterization: UV-Vis and dark-field microscopy Modeling: COMSOL, Mie theory, and CDA
Dip-coating self-assembly [28, 29]				
Array dimensions: Grooves: 40, 50, and 100 nm periods and 50-100 nm depths Holes: 70, 85, 100, and 115 nm periods and 50-100 nm depths AuNP diameter: 15 and 50 nm Silica NP diameter: 50 nm	Hydraulic actuation, antivibratory system, ultrasonic treatment, sodium hydroxide, and nitric acid required Dip velocity: 0.3-10 mm/min pH: 2, 6, or 10	Si substrate coated with a layer of SiO_2/Cr and an additional layer of PMMA Etched PMMA on a hydroxylated silicon wafer	Grooves resulted in 30-90% density with varying NP type and size as well as pH of the solution Holes also resulted in 30-90% density with varying NP type and with/without ultrasonic treatment	Characterization: High-resolution SEM (HRSEM) and photon correlation spectrometer (PCS) Modeling: linear standard approximation (LSA)
Array dimensions: Diameter: 160-180, 200, and 220 nm Depth: 50 nm Spacing: 6 μm NP diameter: 10-100 nm	Polyamine-based silane, piranha, methanol, mercaptoundecanoic acid, and 24 hr incubation period in NP suspension required at room temperature		105×105 arrays with 1-6 NPs per cavity resulting in 40-100% filled cavities depending on spacing and time pattern remained in solution	Characterization: Dark-field microscopy, SEM, % of filled cavities vs. time, and AFM
Directed self-assembly [26, 27]				
Array dimensions: Diameter: 200, 250, 300, and 370 nm Depth: 120 nm Spacing: 1500, 2000, and 3000 nm NP diameter: 40, 100, and 250 nm	Linear translation stage, fixed glass superstrate, 25 μL drop of AuNPs, 27°C set temperature, 1 μm/s substrate velocity, and 1 wt% Triton X-100	Templated PDMS	100 μm^2 array with 1-5 NPs per cavity resulting in ~85% density of filled cavities	Characterization: Dark-field microscopy and SEM
Array dimensions: Diameter: 580 nm Depth: 140 nm Spacing: 1300-2000 nm NP diameter: ~176 nm	Linear translation stage, fixed glass superstrate, silica-gold nanoshells, 21°C set temperature, and 0.6 μm/s substrate velocity	Templated PDMS	1-8 NPs per cavity resulting in ~100% density of filled cavities and ~30% yield of desired heptamers	Characterization: SEM and scattering spectra Modeling: COMSOL

Table 1: Continued.

Structure and dimensions	Conditions/state	Substrate	Fidelity	Characterization/modeling techniques
Modified directed self-assembly (this work)				
Array dimensions: Diameter: 195 nm Depth: 150 nm Spacing: 600 nm NP diameter: 100 and 150 nm	Linear translation stage, modified fixed glass superstrate, 3 μL drop of AuNPs, 1 wt% Triton X-100 precoat of substrate at 8 μm/s velocity, and 1.2-2.1 μm/s substrate velocity for AuNP deposition	Templated PDMS	2 mm × 2 mm array with 1 NP per cavity resulting in ~100% density of filled cavities at optimal conditions and ~85% density at less optimal conditions	Characterization: Dark-field microscopy, UV-Vis spectroscopy, and extinction per NP calculations Modeling: Mie theory, DDA, CDA, and rsa-CDA

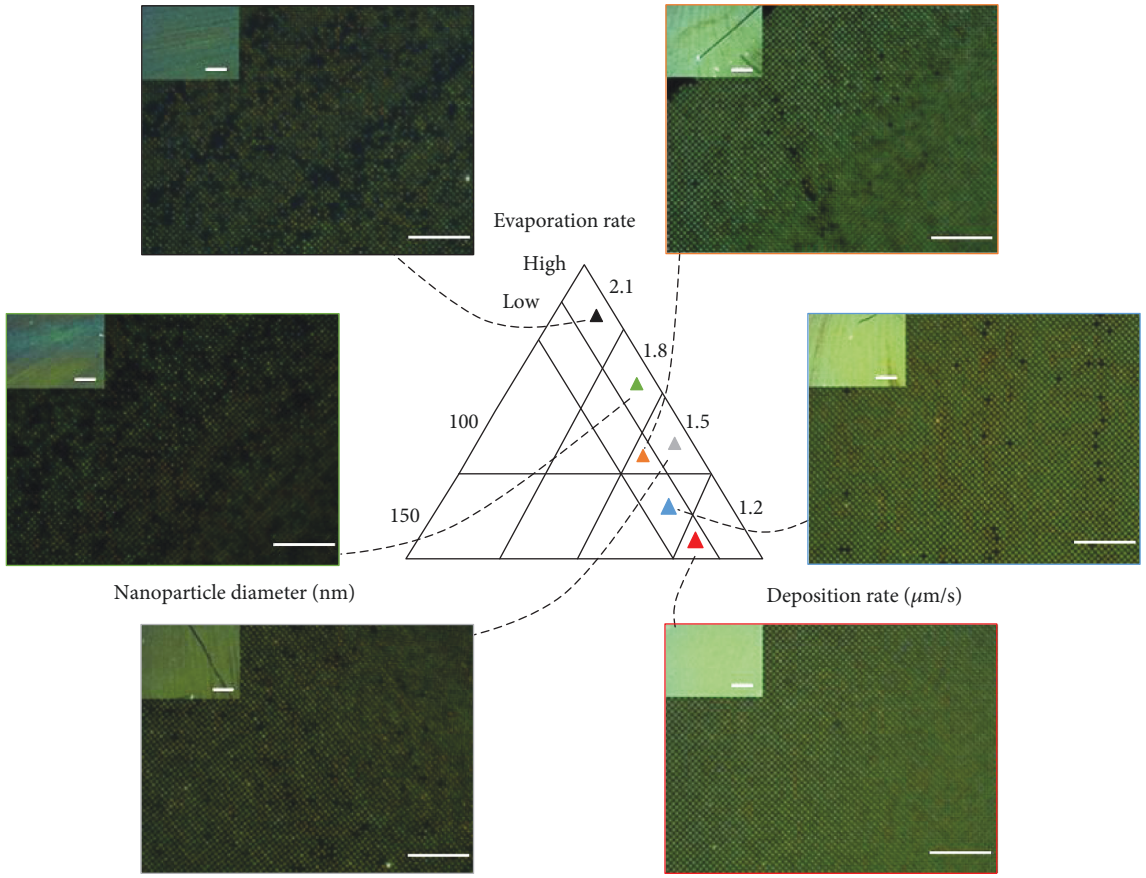

Figure 1: Controlled deposition via NP diameter, deposition rate, and evaporation rate resulted in uniform, large-area (>2 mm × 2 mm) arrays of ~100% ordering. As the evaporation and deposition rates increased and NP diameter decreased, the uniformity, density, and ordering decreased as shown in 100x images (scale bar: 30 μm) and 20x insets (scale bar: 1000 μm).

Cerf and Vieu, Zhang et al., Matricardi et al., Fan et al., and Juillerat et al. show multiple particles per cavity [19, 26–28, 33]. The AuNP diameter of 150 nm and the combination of water and Triton X-100 within a cavity with dimensions of 150 nm × 195 nm (depth × diameter) suggest that only a single AuNP could be within the cavity. Using a slightly faster deposition rate (1.5 μm/s) resulted in slightly lower uniformity and a lower density of filled cavities as shown in the middle right (blue filled triangle) 20x inset and 100x image, respectively. A calculable NP density was determined by counting the number of unfilled cavities and the total number of cavities in the 100x image, which showed that 98% of the cavities were filled.

Decreasing the AuNP diameter resulted in lower densities of filled cavities and a higher likelihood of multiple AuNPs per cavity based on lower uniformity in color across the array. The first array (black filled triangle) was fabricated using a high evaporation rate, a deposition rate of 2.1 μm/s, and 100 nm AuNP diameter, which resulted in the 20x image (inset) with observable nonuniform multicolored deposition and the 100x image that shows ~85% density of filled cavities. When maintaining the high evaporation rate (smaller superstrate) and 100 nm AuNP diameter while simultaneously decreasing the deposition rate to 1.8 and 1.5 μm/s, the uniformity and density increase resulting in the middle left (green filled triangle) and bottom left (gray filled triangle) images, respectively. The 20x images show the improved uniformity at the lower deposition rate (1.5 μm/s), and the 100x images show the improved density of filled cavities (~90%). Decreasing the deposition rate to 1.2 μm/s while leaving the AuNP diameter and evaporation rate constant resulted in little deposition due to the droplet of AuNPs disconnecting from the glass slide on the superstrate as a result of the high evaporation rate. Using a low evaporation rate (larger superstrate) and maintaining the AuNP diameter (100 nm) and deposition rate (1.5 μm/s) result in the top right (orange filled triangle) images, which show a small improvement in the uniformity (20x inset) and density (100x image).

3.3. Optical Properties of AuNP Ordered Arrays. The optical responses of ordered arrays of AuNPs generally determine the sensing efficiencies of ordered AuNPs, where the LSPR and SLR peak locations and peak heights account for a majority of the tunable optical responses for sensing applications [19]. Extinction spectra were performed for the arrays shown in Figure 1 and normalized so that the valley just before the SLR feature was set to 0.01 absorbance units (A.U.) and displayed in Figure 2. The array images from Figure 1 were outlined in the corresponding line color for the extinction spectra and arranged to the right

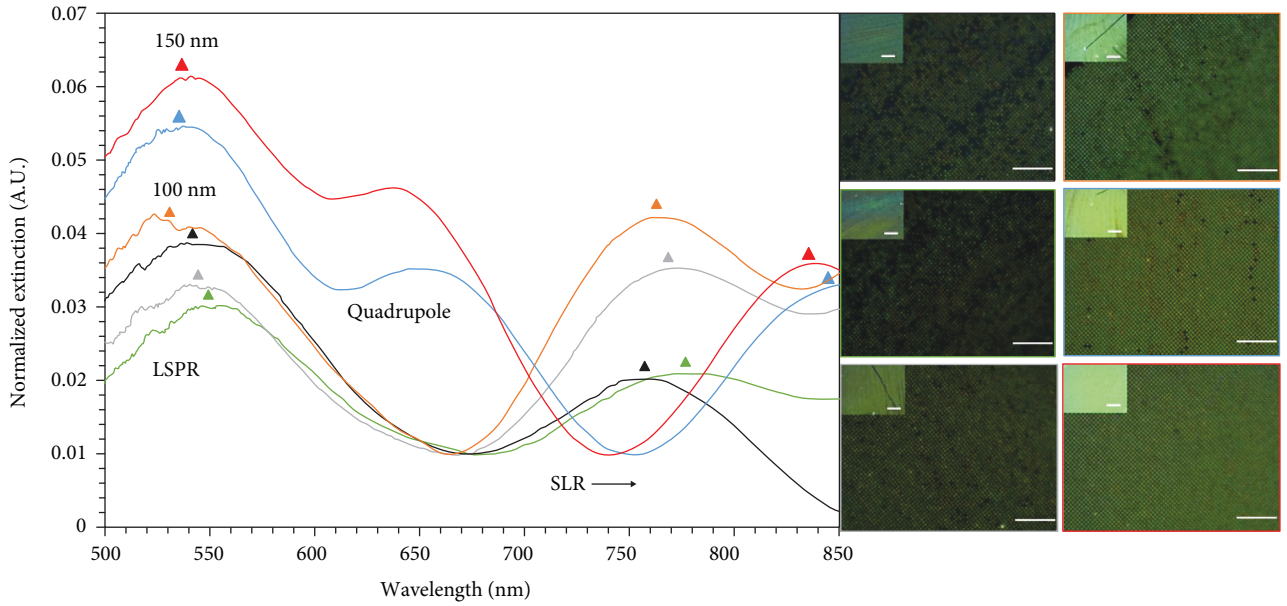

Figure 2: Extinction spectra for the six arrays shown in Figure 1 normalizing the valley before the SLR peak to 0.01 A.U. Colored triangles represent the peak locations for both LSPR and SLR features in spectra.

of the plot in Figure 2. LSPR and SLR peak locations are designated in Figure 2 via a filled triangle matching the line color of the normalized extinction spectra. Extinction spectra for 150 nm AuNPs differ from extinction spectra of 100 nm AuNPs in that the 150 nm AuNPs have a third feature arising from a quadrupole mode at ~650 nm wavelength [39]. High-density ordered arrays like those shown in Figure 1 resulted in observable blueshifts in measured extinction spectra and extinction/NP calculations, which correspond to estimates of DeJarnette et al. previously reported [5, 13]. The LSPR and SLR peak locations blueshift as the density increases (see Figure 2) for the green, gray, and orange lines. For the LSPR feature, the peak locations were ~555, 550, and 535 nm, and the locations for the SLR peaks were ~778, 773, and 765 nm for the green, gray, and orange spectra, respectively. The spectra for the black line (LSPR = 547 nm and SLR = 756 nm) does not follow this trend, which was likely due to multiple layers of particles rather than single layers of particles like the other three spectra. The SLR and quadrupole peaks for the 150 nm AuNP spectra also blueshifts as the density increases, but the LSPR peak has a slight redshift (538 nm for blue line and 541 nm for red line).

Matricardi et al. showed that as the lattice spacing increases, the peak height decreases [19]. This work maintained a lattice spacing of 600 nm and increased the density of filled cavities for 100 nm AuNP arrays resulting in observable increases in peak heights (estimated by subtracting a baseline of 0.01 A.U. from the extinction at the LSPR or SLR peak). The density for the image boxed in gray was significantly higher than the density for the image boxed in green, which resulted in a significant increase in the SLR peak height of 0.011 A.U. (green) to 0.025 A.U. (gray). This 2.3-fold increase in peak height did not hold for the LSPR feature which had an increase from 0.020 A.U. (green) to 0.022 A.U. (gray) or a modest 1.1-fold increase. The difference in density between the gray and orange lines was minor but still resulted in 1.28- and 1.5-fold increases in peak height for the SLR and LSPR features, respectively.

LSPR and SLR peak locations were estimated for Mie theory, DDA, CDA, and rsa-CDA and compared to measured peak locations in Figure 3. Peak locations for Mie theory and DDA estimates (590-595 nm) were redshifted compared to measured values (530-565 nm) due to differences in the RI values. Since an exact material composition surrounding the AuNPs in the PDMS cavity was lacking, Mie theory and DDA assumed that the AuNPs were surrounded by a RI of PDMS (1.42), while the experimental system is surrounded by an unknown composition percentage of components of varying RI including air (1.00), Triton X-100 (1.49), water (1.33), and PDMS (1.42). Each material impacts the overall RI and either blueshifts (decreasing RI) or redshifts (increasing RI) the peak locations depending on which material surrounds the AuNPs at a higher fraction. CDA simulations estimated the LSPR peak location (565 nm) and the SLR peak location (642 nm) for 100 nm AuNPs where the LSPR peak showed a slight redshift and the SLR showed a significant blueshift compared to measured values ranging between 530-560 nm and 755-780 nm, respectively. SLR peak location estimates were closer for 150 nm AuNPs compared to 100 nm AuNPs, which is likely due to the 150 nm AuNP occupying a larger volume of the cavity compared to the 100 nm AuNP. The diameter of 195 nm and a depth of 150 nm cavity dimensions also reduce the possibility of multiple 150 nm AuNPs occupying the same cavity. Peak locations for rsa-CDA simulations were closer to measured values than those of CDA for 150 nm AuNPs. CDA simulations assign an array size of 301×301 like rsa-CDA, but CDA uses a series of dipoles with a resolution of 5 nm to form each 100 and 150 nm AuNP while rsa-CDA assigns each AuNP as a single dipole point for faster computation of the results.

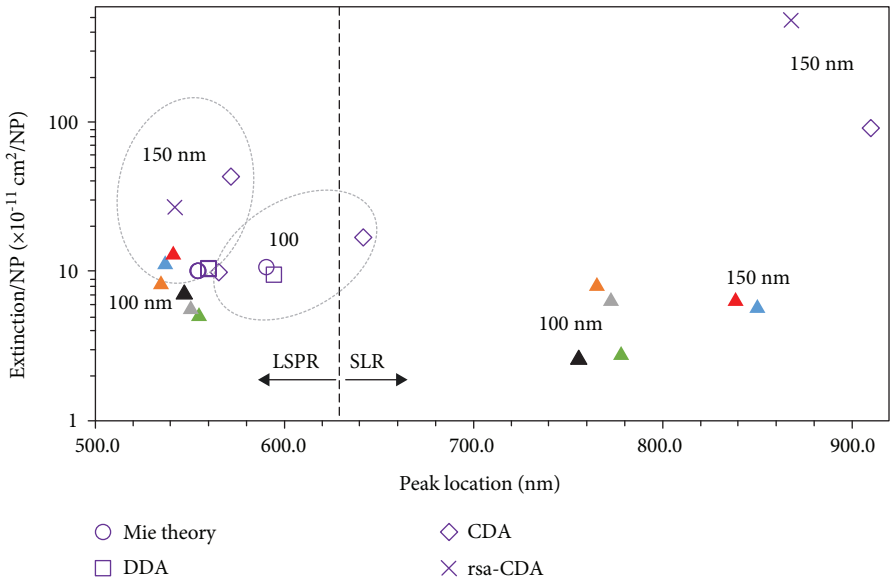

Figure 3: Extinction per NP calculations for measured (filled triangles with colors corresponding to spectra in Figure 2) and simulated (hollow symbols) data of 100 and 150 nm AuNP ordered arrays.

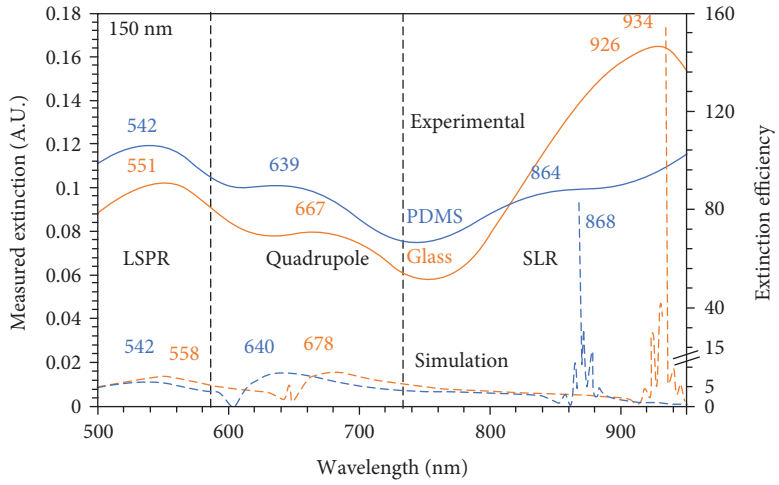

Figure 4: Measured extinction and rsa-CDA simulated extinction efficiency for an ordered array of 150 nm AuNPs in PDMS and transferred to glass.

Measured and estimated extinction/NP values for 150 nm AuNPs were higher than those for 100 nm AuNPs for LSPR peaks while the SLR peaks were redshifted >50 nm for the 150 nm AuNPs compared to 100 nm AuNPs. Extinction/NP estimates for 100 and 150 nm AuNP LSPR peaks using single particle simulations (Mie theory and DDA) and array simulations (CDA and rsa-CDA) were compared to measured extinction/NP values calculated from the spectral peaks in Figure 2 (filled triangles), which is shown in Figure 3. Mie theory and DDA simulations estimated the extinction/NP ($9–10 \times 10^{-11}$) for the 100 nm AuNPs and were compared to measured values ranging from ($5–8 \times 10^{-11}$). The CDA simulations assigned a RI of PDMS (1.42) surrounding the entire AuNP, while the measured values were within 195 nm diameter PDMS cavities and were surrounded by water (1.33), Triton X-100 (1.49), and air (1.00) at varying fractions per cavity.

3.4. Experimental vs. Simulated Optical Properties. As discussed in Optical Properties of AuNP Ordered Arrays, the rsa-CDA simulations resulted in estimated peak locations comparable to measured peak locations for the 150 nm AuNP arrays and to previous estimated values reported by DeJarnette et al. [5, 13]. An ordered array containing 150 nm AuNPs was fabricated using the conditions shown in Figure 1 (red triangle, low evaporation rate, and 1.2 μm/s deposition rate). Optical spectra for this array were measured before the array was transferred to a glass slide via a process developed by Cerf and Vieu [26]. The spectral peak locations for rsa-CDA simulations in PDMS (RI = 1.42) matched

measured values for LSPR (542 vs. 542 nm), quadrupole (640 vs. 639 nm), and SLR (868 vs. 864 nm) values within 0.46% as shown in Figure 4. After performing UV-Vis spectroscopy on the array in PDMS, the array was transferred onto a glass substrate where UV-Vis spectroscopy was again performed to characterize the arrays on glass after the transfer. The spectral peak locations for the simulation versus measured for LSPR (558 vs. 551 nm), quadrupole (678 vs. 667 nm), and SLR (934 vs. 926 nm) on glass (RI = 1.52) matched within 1.7%. The ~3.7-fold increase in the percent difference between the PDMS and glass measured versus simulation data is likely due to the decrease from ~100% density of filled cavities in PDMS to ~85% density on glass.

Not only were the peak locations comparable between experimental and simulation spectra, but the relative increase in peak heights was comparable. The LSPR peak height appeared to slightly increase in the experimental results for glass (~0.09 A.U.) compared to PDMS (~0.04 A.U.). This relative doubling of the measured peak heights was also observed in the simulation results as the LSPR peak height for the simulation of the array on glass appears to be slightly above the simulation spectra for PDMS. This was also observed for the quadrupole peak in which the experimental and simulation results for both glass and PDMS was the same. The experimental peak height for the array on glass (~0.1 A.U.) was nearly double the experimental peak height for the array in PDMS (~0.05 A.U.) while the simulation peak heights were also nearly double for the arrays on glass compared to the arrays in PDMS.

4. Conclusions

In summary, directed self-assembly was used to fabricate square arrays of AuNPs resulting in large-area arrays with observable optical enhancements as the density of filled cavities increased. Controlling the evaporation rate, deposition rate, and AuNP size resulted in >2 mm × 2 mm arrays with ~100% filled cavities containing one AuNP per cavity. Extinction spectra showed that as the density of filled cavities increased, both the LSPR and SLR peak locations blueshifted and the peak heights increased. Extinction/NP calculations for measured 100 and 150 nm AuNPs in square arrays were also blueshifted compared to simulated values for single particles (Mie theory and DDA) and finite arrays (CDA and rsa-CDA). The SLR peak height was shown to significantly increase when transferred from inside PDMS cavities onto a glass substrate. The experimental peak locations for the arrays both in PDMS and on glass were matched within 0.5 and 1.7%, respectively, compared to rsa-CDA simulations.

Data Availability

The data used to support the findings of this study will be archived on the storage drive at Utah State University for at least three years beyond the end of the publication period. The storage drive has over 50 Tb of available disk space for this purpose. This drive is reliably backed up (both daily snapshots and weekly full backups) to prevent data loss. The corresponding author will share project data in accordance with the NSF Data Management Plan requirements.

Conflicts of Interest

The authors declare no competing financial interest.

Authors' Contributions

K. Berry refined the directed self-assembly process that yielded reproducible, large-area, and high-density ordered arrays and drafted text and figures. R. Romo performed the simulations and added text discussing the simulations. M. Mitchell assisted in drafting the table of self-assembly references, added text discussing the table, and fabricated blank stamps used for self-assembly experiments. V. Bejugam built the cage and fabricated blank stamps. D. K. Roper directed the work and refined text and figures.

Acknowledgments

This research work was supported by the Center for Advanced Surface Engineering (CASE), under the National Science Foundation (NSF) Grant No. OIA-1457888 and the Arkansas EPSCoR Program. Dr. Roper also acknowledges support from Utah State University. The authors would like to thank Megan Lanier for fabricating additional blank stamps and Loc Huynh for performing preliminary self-assembly experiments.

References

[1] V. Amendola, R. Pilot, M. Frasconi, O. M. Maragò, and M. A. Iatì, "Surface plasmon resonance in gold nanoparticles: a review," *Journal of Physics: Condensed Matter*, vol. 29, no. 20, article 203002, 2017.

[2] J. R. Dunklin, C. Bodinger, G. T. Forcherio, and D. Keith Roper, "Plasmonic extinction in gold nanoparticle-polymer films as film thickness and nanoparticle separation decrease below resonant wavelength," *Journal of Nanophotonics*, vol. 11, no. 1, article 016002, 2017.

[3] V. G. Kravets, A. V. Kabashin, W. L. Barnes, and A. N. Grigorenko, "Plasmonic surface lattice resonances: a review of properties and applications," *Chemical Reviews*, vol. 118, no. 12, pp. 5912–5951, 2018.

[4] V. Bejugam, "Opto-thermal characterization of plasmon and coupled lattice resonances in 2-D metamaterial arrays," *Theses and Dissertations*, vol. 2868, 2018, https://scholarworks.uark.edu/etd/2868.

[5] D. DeJarnette, J. Norman, and D. K. Roper, "Attribution of Fano resonant features to plasmonic particle size, lattice constant, and dielectric wavenumber in square nanoparticle lattices," *Photonics Research*, vol. 2, no. 1, 2014.

[6] G. T. Forcherio, P. Blake, M. Seeram, D. DeJarnette, and D. K. Roper, "Coupled dipole plasmonics of nanoantennas in discontinuous, complex dielectric environments," *Journal of Quantitative Spectroscopy and Radiative Transfer*, vol. 166, pp. 93–101, 2015.

[7] Y. Francescato, V. Giannini, and S. A. Maier, "Plasmonic systems unveiled by Fano resonances," *ACS Nano*, vol. 6, no. 2, pp. 1830–1838, 2012.

[8] R. Guo, T. K. Hakala, and P. Törmä, "Geometry dependence of surface lattice resonances in plasmonic nanoparticle arrays," *Physical Review B*, vol. 95, no. 15, pp. 1–11, 2017.

[9] A. D. Humphrey and W. L. Barnes, "Plasmonic surface lattice resonances on arrays of different lattice symmetry," *Physical Review B*, vol. 90, no. 7, pp. 1–8, 2014.

[10] A. I. Väkeväinen, R. J. Moerland, H. T. Rekola et al., "Plasmonic surface lattice resonances at the strong coupling regime," *Nano Letters*, vol. 14, no. 4, pp. 1721–1727, 2014.

[11] B. Auguié, X. M. Bendaña, W. L. Barnes, and F. J. García de Abajo, "Diffractive arrays of gold nanoparticles near an interface: critical role of the substrate," *Physical Review B*, vol. 82, no. 15, article 155447, 2010.

[12] P. Blake, S. Kühne, G. T. Forcherio, and D. K. Roper, "Diffraction in nanoparticle lattices increases sensitivity of localized surface plasmon resonance to refractive index changes," *Journal of Nanophotonics*, vol. 8, no. 1, 2014.

[13] D. DeJarnette, G. G. Jang, P. Blake, and D. K. Roper, "Polarization angle affects energy of plasmonic features in Fano resonant regular lattices," *Journal of Optics*, vol. 16, no. 10, article 105006, 2014.

[14] U. Fano, "Effects of configuration interaction on intensities and phase shifts," *Physics Review*, vol. 124, no. 6, pp. 1866–1878, 1961.

[15] N. Flidj, G. Laurent, J. Aubard et al., "Grating-induced plasmon mode in gold nanoparticle arrays," *The Journal of Chemical Physics*, vol. 123, no. 22, article 221103, 2005.

[16] G. T. Forcherio, P. Blake, D. DeJarnette, and D. K. Roper, "Nanoring structure, spacing, and local dielectric sensitivity for plasmonic resonances in Fano resonant square lattices," *Optics Express*, vol. 22, no. 15, pp. 17791–17803, 2014.

[17] S. Baur, S. Sanders, and A. Manjavacas, "Hybridization of lattice resonances," *ACS Nano*, vol. 12, no. 2, pp. 1618–1629, 2018.

[18] D. Khlopin, F. Laux, W. P. Wardley et al., "Lattice modes and plasmonic linewidth engineering in gold and aluminum nanoparticle arrays," *Journal of the Optical Society of America B: Optical Physics*, vol. 34, no. 3, p. 691, 2017.

[19] C. Matricardi, C. Hanske, J. L. Garcia-Pomar, J. Langer, A. Mihi, and L. M. Liz-Marzán, "Gold nanoparticle plasmonic superlattices as surface enhanced Raman spectroscopy substrates," *ACS Nano*, vol. 12, no. 8, pp. 8531–8539, 2018.

[20] P. Blake, J. Obermann, B. Harbin, and D. K. Roper, "Enhanced nanoparticle response from coupled dipole excitation for plasmon sensors," *IEEE Sensors Journal*, vol. 11, no. 12, pp. 3332–3340, 2011.

[21] V. Komanicky, H. Iddir, K. C. Chang et al., "Shape-dependent activity of platinum array catalyst," *Journal of the American Chemical Society*, vol. 131, no. 16, pp. 5732-5733, 2009.

[22] T. Mårtensson, P. Carlberg, M. Borgström, L. Montelius, W. Seifert, and L. Samuelson, "Nanowire arrays defined by nanoimprint lithography," *Nano Letters*, vol. 4, no. 4, pp. 699–702, 2004.

[23] P. Nagpal, N. C. Lindquist, S. H. Oh, and D. J. Norris, "Ultrasmooth patterned metals for plasmonics and metamaterials," *Science*, vol. 325, no. 5940, pp. 594–597, 2009.

[24] M. Tajdidzadeh, A. B. Zakaria, Z. A. Talib, A. S. Gene, and S. Shirzadi, "Optical nonlinear properties of gold nanoparticles synthesized by laser ablation in polymer solution," *Journal of Nanomaterials*, vol. 2017, Article ID 4803843, 9 pages, 2017.

[25] W. Ahn and D. K. Roper, "Periodic nanotemplating by selective deposition of electroless gold island films on particle-lithographed dimethyldichlorosilane layers," *ACS Nano*, vol. 4, no. 7, pp. 4181–4189, 2010.

[26] A. Cerf and C. Vieu, "Transfer printing of sub-100 nm nanoparticles by soft lithography with solvent mediation," *Colloids and Surfaces A: Physicochemical and Engineering Aspects*, vol. 342, no. 1–3, pp. 136–140, 2009.

[27] J. A. Fan, K. Bao, L. Sun et al., "Plasmonic mode engineering with templated self-assembled nanoclusters," *Nano Letters*, vol. 12, no. 10, pp. 5318–5324, 2012.

[28] F. Juillerat, H. H. Solak, P. Bowen, and H. Hofmann, "Fabrication of large-area ordered arrays of nanoparticles on patterned substrates," *Nanotechnology*, vol. 16, no. 8, pp. 1311–1316, 2005.

[29] C. Kinnear, J. Cadusch, H. Zhang et al., "Directed chemical assembly of single and clustered nanoparticles with silanized templates," *Langmuir*, vol. 34, no. 25, pp. 7355–7363, 2018.

[30] D. E. Lee, J. Ryu, D. Hong, S. Park, D. H. Lee, and T. P. Russell, "Directed self-assembly of asymmetric block copolymers in thin films driven by uniaxially aligned topographic patterns," *ACS Nano*, vol. 12, no. 2, pp. 1642–1649, 2018.

[31] L. Malaquin, T. Kraus, H. Schmid, E. Delamarche, and H. Wolf, "Controlled particle placement through convective and capillary assembly," *Langmuir*, vol. 23, no. 23, pp. 11513–11521, 2007.

[32] Y. Yin, Y. Lu, B. Gates, and Y. Xia, "Template-assisted self-assembly: a practical route to complex aggregates of monodispersed colloids with well-defined sizes, shapes, and structures," *Journal of the American Chemical Society*, vol. 123, no. 36, pp. 8718–8729, 2001.

[33] H. Zhang, J. Cadusch, C. Kinnear, T. James, A. Roberts, and P. Mulvaney, "Direct assembly of large area nanoparticle arrays," *ACS Nano*, vol. 12, no. 8, pp. 7529–7537, 2018.

[34] N. A. A. Mohd Arif, C. C. Jiun, and S. Shaari, "Effect of annealing temperature and spin coating speed on Mn-doped ZnS nanocrystals thin film by spin coating," *Journal of Nanomaterials*, vol. 2017, Article ID 2560436, 6 pages, 2017.

[35] E. K. Wujcik, S. R. Aceto, R. Narayanan, and A. Bose, "Lead selenide nanostructures self-assembled across multiple length scales and dimensions," *Journal of Nanomaterials*, vol. 2016, Article ID 9575839, 6 pages, 2016.

[36] D. Dejarnette, P. Blake, G. T. Forcherio, and D. Keith Roper, "Far-field Fano resonance in nanoring lattices modeled from extracted, point dipole polarizability," *Journal of Applied Physics*, vol. 115, no. 2, article 024306, 2014.

[37] D. Dejarnette and D. K. Roper, "Electron energy loss spectroscopy of gold nanoparticles on graphene," *Journal of Applied Physics*, vol. 116, no. 5, article 054313, 2014.

[38] M. Seeram, G. T. Forcherio, and D. K. Roper, *Shape Generator for the DDSCAT Software*, nanoHUB, 2016.

[39] C. P. Burrows and W. L. Barnes, "Large spectral extinction due to overlap of dipolar and quadrupolar plasmonic modes of metallic nanoparticles in arrays," *Optics Express*, vol. 18, no. 3, pp. 3187–3198, 2010.

Hindawi
Journal of Nanomaterials
Volume 2019, Article ID 4304532, 9 pages
https://doi.org/10.1155/2019/4304532

Research Article

Swelling Resistance and Water-Induced Shape Memory Performances of Sisal Cellulose Nanofibers/Polyethylene Glycol/Citric Acid Nanocellulose Papers

Zuocai Zhang,[1] **Yuqi Li**,[1] **Laifu Song**,[1] **Li Ren**,[1] **Xu Xu**,[1,2] **and Shaorong Lu**[1]

[1]*Key Laboratory of New Processing Technology for Nonferrous Metals and Materials, Ministry of Education, School of Material Science and Engineering, Guilin University of Technology, Guilin 541004, China*
[2]*Department of Mechanical, Automotive & Materials Engineering, University of Windsor, 401 Sunset Ave, Windsor, ON, Canada N9B 3P4*

Correspondence should be addressed to Yuqi Li; liyuqi@glut.edu.cn and Shaorong Lu; lushaor@163.com

Received 4 March 2019; Revised 4 May 2019; Accepted 23 May 2019; Published 22 July 2019

Guest Editor: Biaolin Peng

In this work, a kind of nanocomposite paper was obtained by evaporation-induced self-assembly of a mixture of sisal cellulose nanofibers (CNF) and polyethylene glycol (PEG) as the matrix and citric acid (CA) as a cross-linking agent. The CNF/PEG/CA paper exhibited good water swelling resistance which could be controlled by changing the concentration of CA. In addition, this nanocomposite paper exhibited good mechanical properties and water-induced shape memory performance. In particular, when the dosage of CA was 30 wt.%, the tensile strength and the tensile modulus of the CNF/PEG/CA paper after swelling were 25.2 MPa and 813.0 MPa, respectively. Further, this nanocomposite showed great potential for water-induced shape memory materials with fast response speed. The shape recovery rate (Rr) of the CNF/PEG/CA paper reached 90.2% with 30 wt.% CA after being immersed in water for 11 s. It is anticipated that our current work can be used to exploit more efficient methods to overcome the poor water swelling resistance of the cellulose-based shape memory materials.

1. Introduction

Shape memory polymer is a new type of intelligent material, as well as the most important part of intelligent materials. Shape memory polymer can reflect the shape memory performance mainly due to its internal molecular structure. Its molecular structure is a kind of network usually composed of reversible phase and stationary phase. The stationary phase can be a cross-linked node by chemical reaction or physical reaction, and it plays an important role in building a cross-linking network [1, 2]. The reversible phase is usually glassy-amorphous transformation, crystallization-melting transformation, etc., and the phase transition is also varied. Shape memory polymer composites are widely used in many fields, such as drug release material, smart textiles, structural materials, sensors, and fiber optic solar cells [3–5]. With the rapid development of science and technology, most of the shape memory polymers are thermotropic memory materials, such as polycaprolactone (PCL), polyurethane (PU), polylactic acid (PLA), and epoxy resin (EP) [6–10]. Usually, these polymers are network structure formed by covalent cross-linking, and their shape recovery temperature is higher when compared with other common polymers, which leads to limitations in biomedicine or some cryogenic applications [11]. In medicine fields, a key challenge is that an excess of heat usually causes damage to biological tissue. Nevertheless, water-induced shape memory polymers can effectively compensate for this deficiency [12]. Based on the reported water-induced shape memory polymer, most of them are made from petroleum chemical raw materials, which are not renewable, biodegradable, and biocompatible [13, 14].

Cellulose is a kind of natural polymer with green environmental protection, abundant source, and unique layered structure [15]. In recent years, the extraction of nanofiber from biomass raw materials is used as a research hotspot for the enhancement of nanocomposite [16–18]. Due to the

nanometer size effect and high specific surface area of nanocellulose, the mechanical properties of nanocomposite are much higher than those of conventional composites [19, 20]. In addition, the nanocellulose with high mechanical strength, high length-diameter ratio, and low price and degradable is environmentally friendly, which is harmless to humans and animals [21]. Nanocellulose contains a lot of hydroxyl. Using the function of hydrogen bonds, it can be used to synthesize the shape memory polymer with water response effect [18, 22], biodegradability [23, 24], and biocompatibility [25]. However, the nanocomposite material simply combined by the Van der Waals force has a larger volume of swelling and a higher rate of water absorption after soaking in water [16]. Nevertheless, in the wet state, its mechanical properties greatly reduce, limiting its application in certain areas.

Polyethylene glycol (PEG) is a kind of thermoplastic polymer material with high crystallinity and good water solubility, is nontoxic, and is nonirritating, and it has great toughness and good biocompatibility [12, 26], making it a good choice to be used as another kind of flexible chain segment of the interpenetrating network structure [27]. Therefore, based on the advantage of the cellulose nanofibers (CNF) with PEG, the CNF and PEG were cross-linked to form a new network shape memory nanocomposite (CNF/PEG/CA) paper, through citric acid (CA) as a cross-linking agent [28].

The CNF/PEG/CA paper was prepared by the method of evaporation-induced self-assembly (EISA) [29]. The preparation is easy to operate, fast, green environmental, and has high extraction rate. The formation mechanism of the CNF/PEG/CA interpenetrating network structure shape memory nanocomposite paper is shown in Figure 1. The mechanical strength is poor, and the swelling resistance is low when the nanocellulose materials simply are combined by the Van der Waals force under the wetting state. CA can combine cellulose molecules and PEG molecules through covalent bond connection to form an interpenetrating network structure, which improves the performance of the shape memory nanocomposite paper [30, 31]. The flow chart shows the process to prepare the CNF/PEG/CA interpenetrating network shape memory nanocomposite paper by EISA. In addition, the shape and the size of the CNF/PEG/CA paper can be adjusted by the forming mold. And the CNF/PEG/CA paper has good flexibility; as a result, it can be folded into various shapes. The CNF/PEG/CA paper has good hydrophilicity, biocompatibility, and biodegradability and keeps good mechanical properties after swelling by absorbing water, which leads to the CNF/PEG/CA paper having wide application prospection in the biomedical field.

2. Experimental

Sisal fibers were bought from Guangxi Sisal Company, China. NaOH, CH_3COOH, citric acid (CA), and $NaClO_2$ were purchased from Aladdin Chemistry Co. Ltd. Polyethylene glycol 1000 (PEG) and $Na_2SO_4{\cdot}10H_2O$ were supplied by Sinopharm Chemical Reagent. The other chemicals used were all analytical pure reagents without further purification.

2.1. Preparation of Microcrystalline Sisal Fibers (MSF). Firstly, sisal fibers were cut into an approximate length of 5 cm and the lignin and the pectin particles on the surface of sisal fibers were washed away by deionized water. Then, the sisal fibers were dried in an oven at 60°C for later use. The 50 g dry fibers were boiled in aqueous solution of 14.0 g NaOH, 14.0 g $Na_2SO_4{\cdot}10H_2O$, and 400 ml deionized water in 500 ml autoclaves at 170°C for 2 h. After the reaction, the sisal fibers were filtered and washed several times with deionized water until the solution remains the same color, then dried in an oven at 60°C. Later, the 20 g dry fibers were transferred to a 1000 ml three-necked flask, adding 6.7 g $NaClO_2$, 5 ml CH_3COOH, and 650 ml deionized water, and the mixture kept reacting at 75-80°C for 2-3 h to bleach. The product was filtered and washed with water after the reaction. Finally, the MSF were dried in an oven at 60°C until constant weight [16].

2.2. Preparation of Sisal Cellulose Nanofibers (CNF). Firstly, the 12.0 g dried MSF were soaked wet in 40 ml preconfigured aqueous solution of NaOH (10 wt.%) and transferred to the 500 ml three-necked round bottomed flask. Then, 350 ml absolute ethyl alcohol was added into the flask under mechanical agitation for 30 min to make it evenly dispersed and alkalified. After that, 6 g chloroacetic acid ($CH_2ClCOOH$) was added to the mixture, and the reaction was at the temperature of 70°C for 3 h under mechanical stirring. At the end of the reaction, the crude product was collected after filtering the mixture, repeated centrifugal washing with distilled water to remove unreacted chloroacetic acid until the pH value was neutral, and drying. The crude product was mixed with a certain amount of deionized water to make its solid content at about 0.5 wt.%, then the mixture was sheared by a high-shear dispersion homogenizer at 28000 r/min high speed for 30 min to get the transparent jelly product. After using a 400-mesh filter cloth to extrude the product to preliminary filtrate the unsegregated crude fiber, adjusting proportional to about 0.1 wt.% with deionized water and centrifuging for 10 min at 12000 r/min, the CNF with pale blue were obtained from the centrifugal barrel upper 80% solution, at last rotating enrichment and measuring its solid content to set aside.

2.3. Preparation of Shape Memory Nanocomposite (CNF/PEG/CA) Paper. The detailed fabrication procedure of the CNF/PEG/CA paper was as follows. The CNF were configured to 5 mg/ml aqueous dispersion with deionized water, and a certain amount of PEG was weighed to dissolve in 5 ml deionized water at the same time. Then, the abovementioned two kinds of solutions were mixed with continuous stirring and ultrasonic dispersion for 30 min to make it even. After adding a certain amount of CA as a cross-linking agent, stirring for 10 min to mix evenly, the mixture was poured into the tetrafluoroethylene mold and transferred to the drum wind drying oven at 60°C for 24 h. By evaporating the moisture slowly, CNF and PEG molecules were cross-linked by CA molecules to be assembled into a CNF/PEG/CA paper with interpenetrating network structures. The thickness and size of the CNF/PEG/CA paper interpenetrating

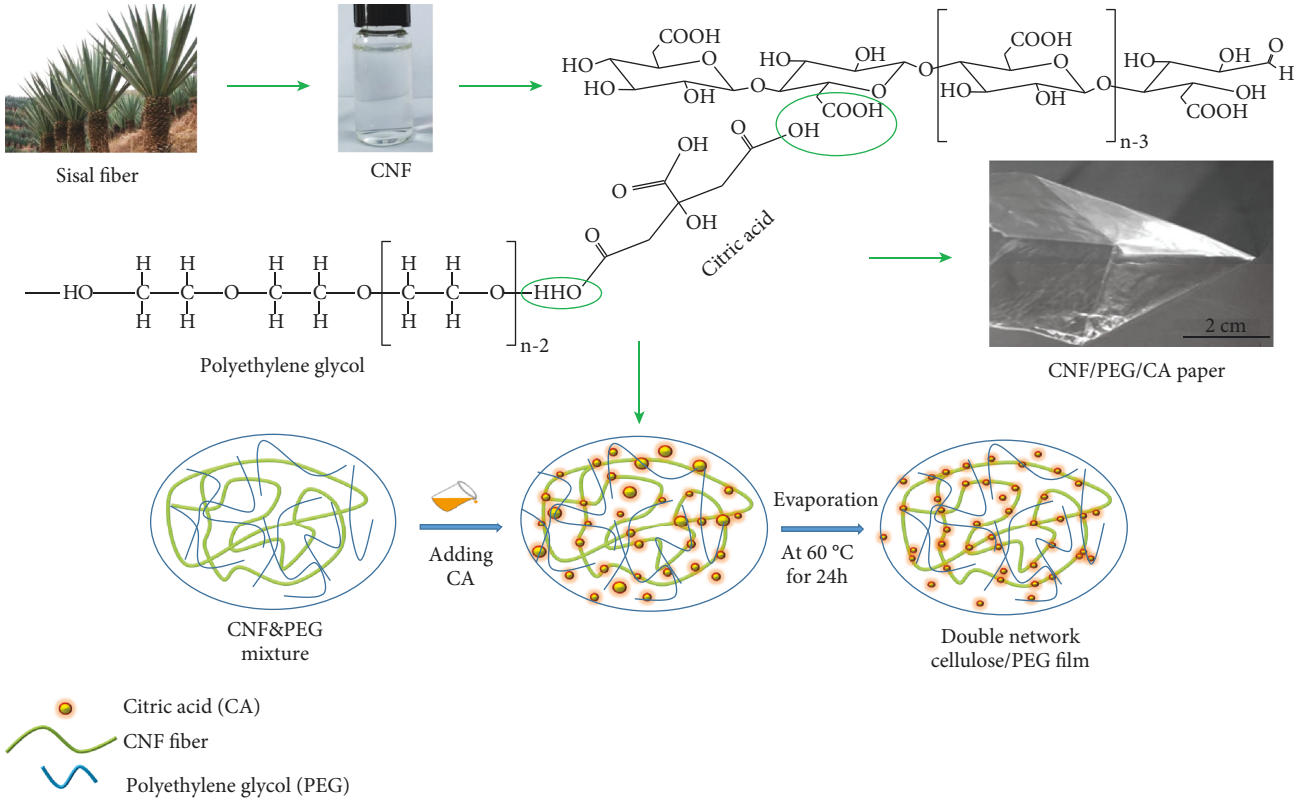

Figure 1: Preparation process of the CNF/PEG/CA paper.

network composite structure can be controlled by the amount of mixed solution and the size of the mold. To study the influence of different contents of the CA cross-linking agent on the interpenetrating network CNF/PEG/CA paper, we prepared different cross-linking degrees of interpenetrating network CNF/PEG/CA paper according to the formula design of Table 1.

2.4. Characterization. The infrared spectrum of the sample prepared by KBr tableting was analyzed by the American Nicolet Nexus 470 type Fourier transformation infrared spectrometer (spectra range: 4000~500 cm^{-1}). The water swelling resistance of the shape memory nanocomposite paper was characterized by the change of the volume and the weight before and after immersion in deionized water at 25°C for 5 min. According to the water absorption (%) = $(M_1 - M_0)/M_0 \times 100$, swelling rate = $(V_1 - V_0)/V_0 \times 100\%$, where M_0 and V_0 are the quantity and the volume of the sample, respectively, before absorbing water, and M_1 and V_1 are the quantity and the volume of the sample, respectively, after absorbing water. All of the samples were cut into the size of 30 mm × 3 mm × 0.05 mm, and the text results were averaged after each group of samples was measured three times. The tensile strength was examined on a Q800 dynamic mechanical analyzer (TA Instruments, USA) by stretching control at the temperature of 25°C and a rate of 3 N min^{-1}. The sample size was 30 mm × 3 mm × 0.05 mm, and the arithmetic average of the tensile strength test of 5 samples was recorded for the tensile properties of the sample. The sample cross section was sputter-coated with gold in case of electronic accumulation and then tested by scanning electron microscopy (JSM-6480LV, Japan JEOL) at an accelerating voltage of 3.0 kV. The gel content of the sample (G) was measured by the mass (miso) of the sample before extraction in methylene chloride as extracting agent for 24 h of Soxhlet extraction and the mass of the dried sample (m_d). According to the following formula, $G = m_d/\text{miso}$ to calculate the gel content of the material. The water-induced shape memory effect was investigated as follows. The specimen was folded to a temporary shape at 60°C and cooled down to 0°C with the external force to fix the temporary shape. The specimen was immersed in water at 25°C to determine the recovery of shape, and the above two processes were recorded by a video camera. The recovery ratio was defined as $\text{Rr} = [(\theta_f - \theta_0)/(180 - \theta_0)] \times 100\%$, where Rr represents

Table 1: The blend design of compounding materials for respective composites.

Nanocomposite	CNF (wt.%)	PEG (wt.%)	CA (wt.%)
CNF/PEG/CA	70	30	0
CNF/PEG/CA-1	70	30	10
CNF/PEG/CA-2	70	30	20
CNF/PEG/CA-3	70	30	30
CNF/PEG/CA-4	70	30	40

the response rate, θ_f represents the recovery angle of sample at a different time, and θ_0 represents the angle of the sample before recovering. All the presented results were an average of three specimens with the size of 30 mm × 3 mm × 0.05 mm (length × width × thickness) [16]. The light transmittance of shape memory nanocomposite paper mainly adopted the double beam spectrophotometer (UV-3600-NIR, Shimadzu) with wavelength range 200-800 nm, scan rate 300 nm/min, sampling interval 1 nm, test temperature 25°C, and 100% sensitivity. Each sample was tested three times to ensure the accuracy of the test data.

3. Results and Discussion

3.1. FT-IR Spectra of CNF, PEG, CA, and CNF/PEG/CA Paper. As shown in Figure 2(a), there are two vibration absorption peaks at 3413 cm^{-1} and 2919 cm^{-1}, respectively, belonging to the stretching vibration of -OH and -CH- on the CNF molecular chains. Additionally, the two vibration absorption peaks at 1599 cm^{-1} and 1382 cm^{-1} can be found, which refer to the symmetric stretching vibration and the antisymmetric stretching vibration of carboxylic acid sodium salt groups on cellulose, respectively [16]. It illustrates that the CNF are mainly in the form of carboxylic acid sodium after being treated with chloroacetic acid. In the FT-IR curve of PEG, the absorption peaks at 3430 cm^{-1}, 2872 cm^{-1}, and 1105 cm^{-1} refer to the stretching vibration of -OH and -CH- and C-O-C, respectively. From the infrared spectrum of CA [30], it can be seen that there are two strong absorption peaks at 1688 cm^{-1} and 1757 cm^{-1}, which belong to the C=O stretching vibration on CA. From Figure 2(b), the -OH vibration absorption of the CNF/PEG/CA paper at 3410 cm^{-1} decreases obviously with the increase of CA adding amount. According to the changes in the FT-IR spectra, it can be found that the PEG and CNF can be effectively cross-linked together by CA.

3.2. Water Resistance of the CNF/PEG and CNF/PEG/CA Papers. To study the water swelling resistance of the CNF/PEG and CNF/PEG/CA paper, the water absorption and swelling rate change with the adding of CA was investigated. As shown in Figure 3, the water absorption and swelling rate of CNF/PEG paper are quite high. The water absorption is up to 1038% and the swelling rate is up to 2100%. This is mainly due to the fact that the surface of CNF contains a lot of -OH and -COOH- hydrophilic groups, leading to high hydrophilicity. By contrast, the water absorption and the volume swelling rate of the CNF/PEG/CA paper are decreased greatly with the increase of CA adding amount. At CA 30 wt.%, the water absorption and swelling rate of the CNF/PEG/CA paper are decreased 46 times and 15 times, respectively, compared to those of the CNF/PEG paper. The reason for this is that the CNF and PEG are cross-linked by CA, leading to the increase of hard segment area in the CNF/PEG/CA paper. In addition, hydrophilic groups such as hydroxyl on the CNF and PEG can react with CA. Therefore, the water absorption and the swelling rate of CNF/PEG/CA paper reduced.

Gel content (G) is used to study the cross-linking degree of the CNF/PEG/CA paper. From Figure 4, the G value of the CNF/PEG paper without CA cross-linking is lower, which is about 74%. When adding CA, the G value of the CNF/PEG/CA paper gradually increases with the addition of CA. When adding 30 wt.% CA, the G value of the CNF/PEG/CA paper tends to be stable, reaching 90%, and the G value of the CNF/PEG paper increases by 21.6% compared with the CNF/PEG paper without CA cross-linking. It indicates that the addition of CA is effective to cross-link PEG and CNF, to form a stable network structure.

3.3. Mechanical Properties of the CNF/PEG and CNF/PEG/CA Papers. Water-induced shape memory materials are mainly limited by the decrease in mechanical properties after swelling. Figure 5 shows the mechanical properties of the CNF/PEG/CA paper with different CA contents before being soaked in water. As shown in Figure 5(a), the elongation at break of the CNF/PEG/CA paper decreases with the content of CA increasing, because of the increasing of the cross-linking degree. As shown in Figure 5(b), with the increase of CA contents, the tensile strength of the CNF/PEG/CA paper shows a downward trend, while the tensile modulus increases. When adding 30 wt.% CA, the tensile modulus of the CNF/PEG/CA paper increases from 853 MPa to 1401 MPa. It can be attributed to the formation of strong covalent bonds, formed by the esterification reaction of carboxyl on CA and hydroxyl groups on PEG and CNF cellulose, which improves the stability of the molecular chain. In addition, the hydroxyl groups on CNF and PEG decrease, so the effect of hydrogen bonding between molecules greatly reduces, which makes it difficult for the movement of chain segments. Therefore, reducing the CNF/PEG/CA paper plastic deformation, the tensile strength and the elongation at break all decrease, and the tensile modulus greatly improves.

Figure 6(a) shows the mechanical properties of the CNF/PEG/CA paper with different CA contents after being soaked in water. It can be seen that the CNF/PEG paper without CA cross-linking exhibits quite poor mechanical properties after being soaked in water. It can be attributed to the combination of the internal molecules of the CNF/PEG paper, which is mainly formed by hydrogen bonding and the molecular chain entanglement between molecular chains without CA cross-linking. When water immerse into the interior of the material, the hydrogen bonding force between the CNF and PEG molecules is damaged, which decreases the mechanical properties. In contrast, as shown in Figure 6(b), the tensile strength and the tensile modulus of the wet CNF/PEG/CA paper increase greatly with the increasing of CA contents. When the addition amount of CA is 30 wt.%, the tensile strength and tensile modulus of the CNF/PEG/CA paper after swelling are 25.2 MPa and 813.0 MPa, respectively. It is the result that demonstrates that the chemical cross-linking network structure among PEG, CNF, and CA leads to good mechanical properties of the CNF/PEG/CA paper after soaking. Therefore, the CNF/PEG/CA paper is more suitable for underwater applications than other shape memory polymers.

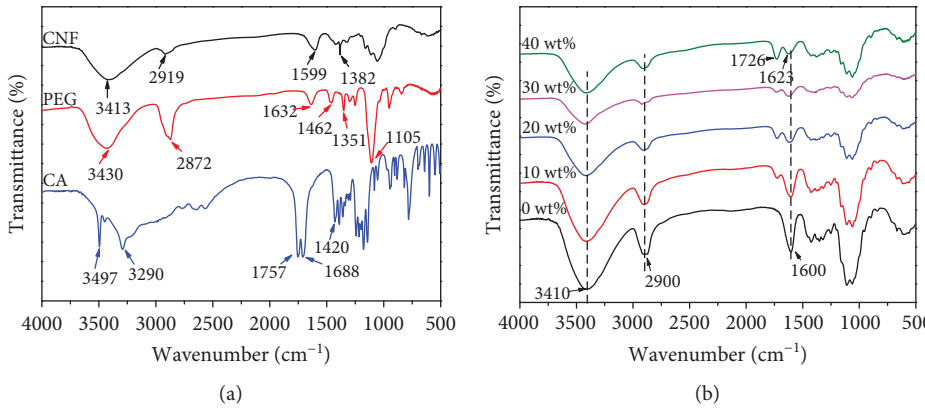

Figure 2: (a) The FT-IR spectra of CNF, PEG, CA, and (b) CNF/PEG/CA paper with different contents of CA.

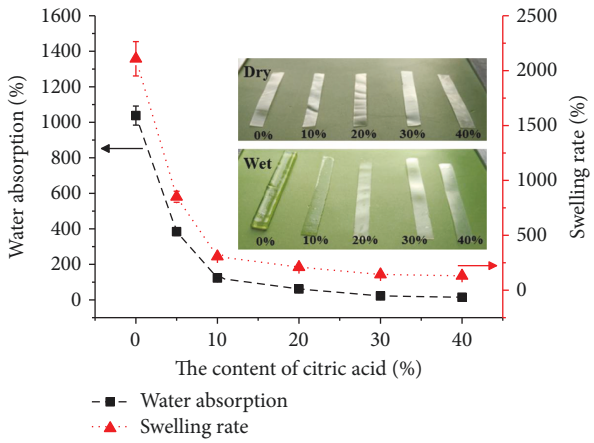

Figure 3: Water absorption and swelling rate of the CNF/PEG/CA paper; inset: the morphology of the CNF/PEG/CA paper before and after soaking.

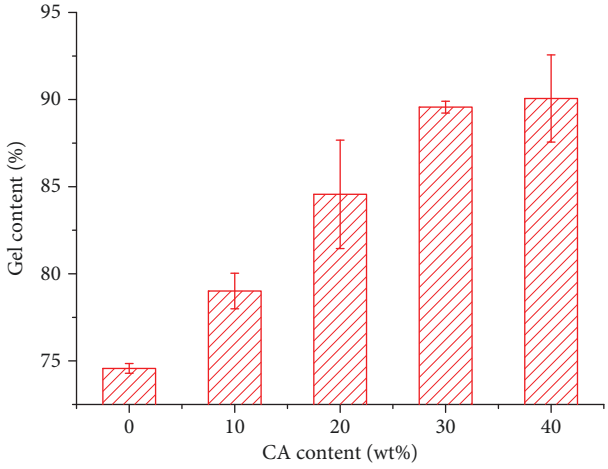

Figure 4: The gel content of the CNF/PEG and CNF/PEG/CA papers.

To microscopically analyze the mechanical performance, the scanning electron microscope (SEM) images of the fracture surfaces of the CNF/PEG/CA paper are used to investigate the interaction between CA and the CNF/PEG paper. As shown in Figure 7(a), it can be seen that the section of the CNF/PEG paper without CA cross-linking is level and close and exhibits orientation arrangement in the vertical direction without obvious holes. It is attributed to the good compatibility between nanocellulose and PEG, due to the hydrogen bonding and mutual physical tangles. Therefore, the direction of fracture is consistent with the direction of force. As shown in Figures 7(b) and 7(c), the sections of the CNF/PEG/CA paper become rough after adding the cross-linking agent CA. In addition, there are many fold structures and interpenetrating holes, which are mainly due to the cross-linking between the carboxyl on CA and the hydroxyl on CNF cellulose and PEG that forms the permanent area of hard segments.

3.4. Water-Induced Shape Memory of the CNF/PEG and CNF/PEG/CA Papers. Figure 8 shows the shape recovery processes of the CNF/PEG/CA paper with different CA amounts. It can be seen that the water response of the CNF/PEG paper without CA in 25°C water is fast, and the response rate is high. It illustrates that the CNF/PEG/CA paper has good water response performance. As shown in Figure 9, the water-induced shape performance of the CNF/PEG/CA paper with CA exhibits good water-induced shape memory performance as well. When the CA addition amount is up to 20 wt.%, the shape recovery rate (Rr) immersed in water for 10 s can reach over 99%. At CA 30 wt.%, Rr of the CNF/PEG/CA paper is about 90.2%. The reason why the response rate reduces mainly is that the CNF/PEG/CA paper is based on hydrogen bonding water response to form memory switch. Additionally, the CNF and PEG molecular chain is fixed by CA, which may form the cross-linked structure. And with the increase of CA amount, the cross-linking degree increases. Thus, the amount of the hydrogen bonds between the molecules greatly reduces, greatly reducing the intermolecular hydrogen bond binding force, and the memory effect performance decreases. The main reason for this phenomenon is that the response

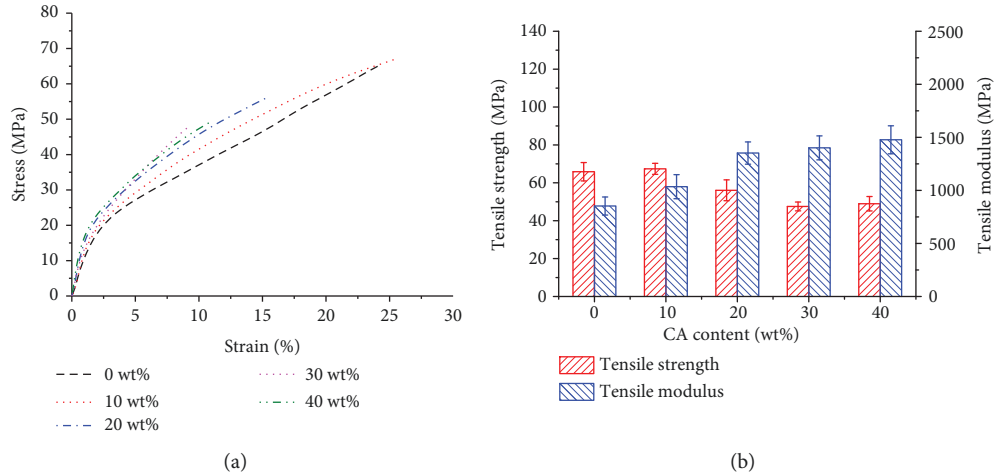

Figure 5: (a) Typical stress-strain curves of the CNF/PEG/CA paper. (b) Tensile strength and modulus of the CNF/PEG/CA paper (before soaking).

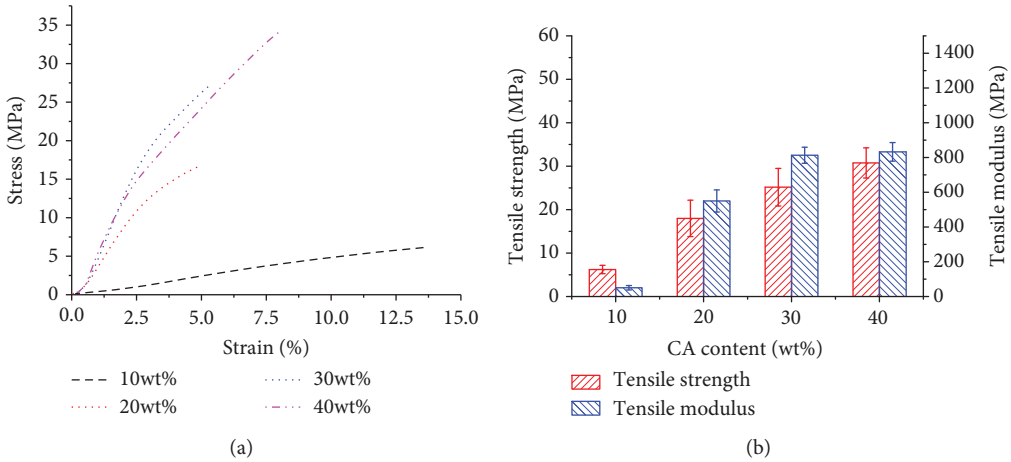

Figure 6: (a) Typical stress-strain curves of the CNF/PEG/CA paper. (b) Tensile strength and modulus of the CNF/PEG/CA paper (after soaking).

mechanism of soluble-induced shape memory materials is different from the thermal-induced shape memory materials [32–34]. The driving force of soluble-induced recovery is the plasticization of solvent molecule. As the solvent molecule enters the polymer network gradually, the transition temperature of the reversible phase gradually decreases, resulting in the phase transition at room temperature and driving the shape recovery of the material. Therefore, the soluble-induced recovery rate depends on the diffusion rate of the solvent molecule into the polymer network, and the diffusion rate of solvent molecules is related to the free volume of the polymer. For the CNF/PEG/CA interpenetrating network polymer, the larger the cross-linking degree is, the smaller the free volume will be, resulting in a lower diffusion rate of the solvent molecule and a slower recovery rate.

A water response mechanism of the CNF/PEG/CA paper was proposed in Figure 10. It can be seen that the CNF/PEG paper is formed by the intermolecular hydrogen bond self-assembly and has a certain interpenetrating network structure. After adding CA, it embeds in the CNF/PEG paper substrate, and the carboxyl on CA and the hydroxyl on the CNF/PEG paper can be combined by esterification, which can form the interpenetrating network structure with a certain of rigidity. The deformation of the CNF/PEG/CA paper is temporary fixed by a strong hydrogen bond force between polymer molecules. When the CNF/PEG/CA paper is in water environment, water molecules enter in the interior of the CNF/PEG/CA interpenetrating network structure. The strong hydrogen bonds between molecules are broken, replaced by the weaker hydrogen bonds formed by water and polymer molecules. Thus, a force is released which fixes the temporary deformation, and the CNF/PEG/CA paper begins to recover from the temporary shape to the initial shape.

4. Conclusions

Shape memory nanocomposite (CNF/PEG/CA) paper was successfully prepared by the evaporation-induced self-

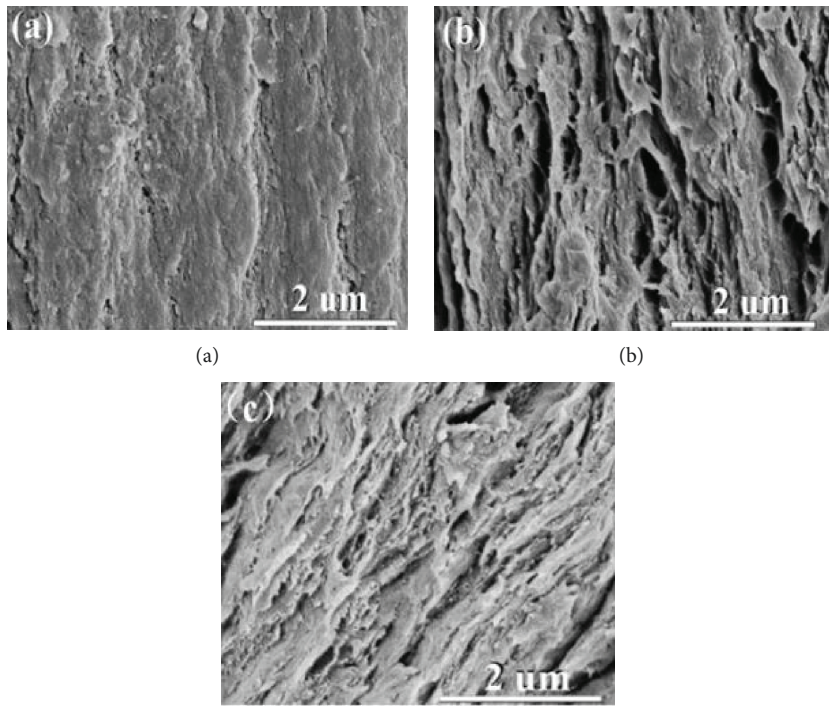

FIGURE 7: SEM images of the fractured surface of the neat CNF/PEG paper (a). CNF/PEG/CA paper with the CA content of 20 wt.% (b) and 30 wt.% (c).

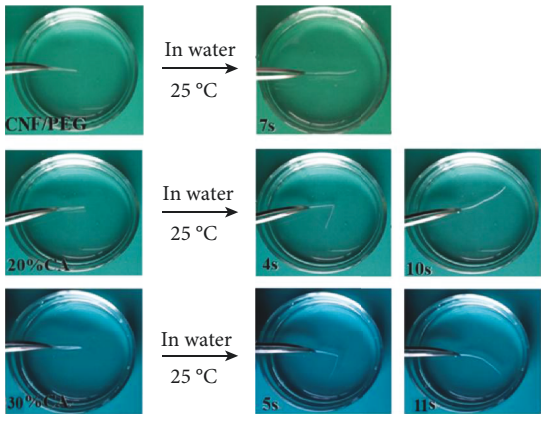

FIGURE 8: The shape recovery process of the CNF/PEG/CA paper.

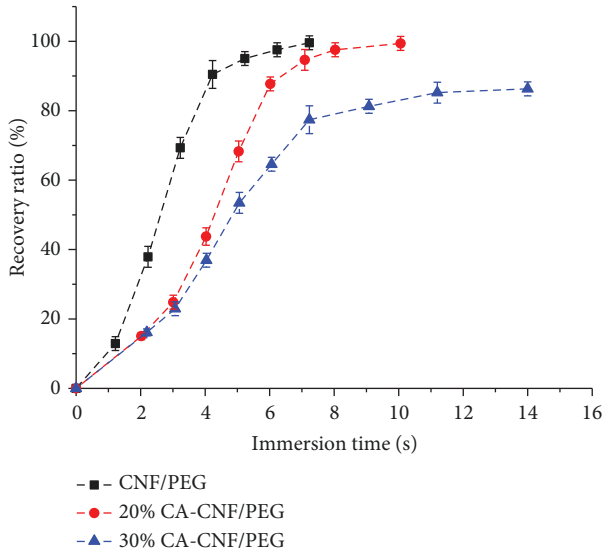

FIGURE 9: The shape memory behavior of the CNF/PEG/CA paper immersed in water.

assembly method, using sisal cellulose nanofibers (CNF) and polyethylene glycol (PEG) as the matrix and citric acid (CA) as a cross-linking agent. The results show that the CNF/PEG/CA paper exhibits good mechanical properties and water-induced shape memory performance. In particular, at CA 30 wt.%, the tensile strength and the tensile modulus of the CNF/PEG/CA paper after swelling are 25.2 MPa and 813.0 MPa, respectively. Further, this nanocomposite has great potential for water-induced shape memory materials with fast response speed. Only for 11 s, the shape recovery rate (Rr) of the CNF/PEG/CA paper with 30 wt.% of CA is 90.2% after being immersed in water. In addition, the CNF/PEG/CA paper has excellent water swelling resistance which could be controlled by changing the concentration of CA. After wet swelling, the highest tensile strength and tensile modulus are up to 30 MPa and 832 MPa, respectively. It is hoped that this work can be used to exploit more efficient methods to overcome the poor water swelling resistance of the cellulose-based shape memory materials.

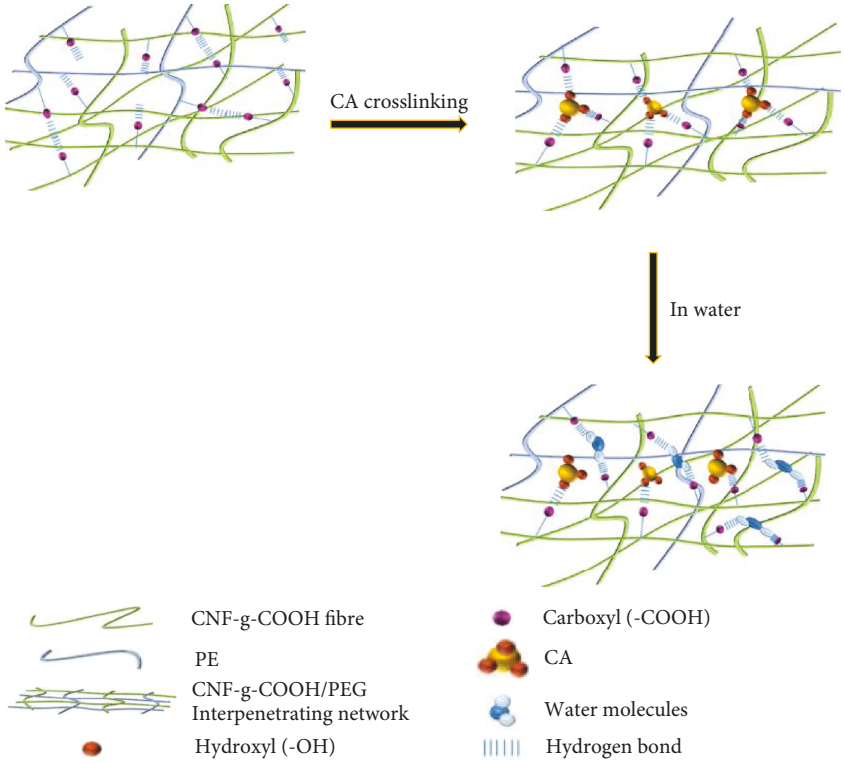

Figure 10: Schematic of the water-induced shape memory effect mechanism of the CNF/PEG/CA paper.

Data Availability

The data used to support the findings of this study are available from the corresponding authors upon request.

Conflicts of Interest

The authors declare no conflict of interest.

Authors' Contributions

Zuocai Zhang, Yuqi Li, and Shaorong Lu contributed equally to this work.

Acknowledgments

The authors gratefully acknowledge the financial support of the National Natural Science Foundation of China (51463007, 51605109, and 51763009), the Natural Science Foundation of Guangxi Province, China (2014GXNSFDA 118006 and 2016GXNSFBA380004), the Project of the Department of Science and Technology of Guilin (No. 2016012005), and the Young Teachers-Based Capacity Building Project of Guangxi (2018KY0243).

Supplementary Materials

Fig 1s: optical images of the contact angle of the CNF/PEG/CA paper TG curves of the CNF/PEG and CNF/PEG/CA paper. *(Supplementary Materials)*

References

[1] Z. C. Jiang, Y. Y. Xiao, Y. Kang, B. J. Li, and S. Zhang, "Semi-IPNs with moisture-triggered shape memory and self-healing properties," *Macromolecular Rapid Communications*, vol. 38, no. 14, article 1700149, 2017.

[2] N. Li, G. Chen, W. Chen et al., "Multivalent cations-triggered rapid shape memory sodium carboxymethyl cellulose/polyacrylamide hydrogels with tunable mechanical strength," *Carbohydrate Polymers*, vol. 178, pp. 159–165, 2017.

[3] Y. Fang, Y. Ni, B. Choi et al., "Chromogenic photonic crystals enabled by novel vapor-responsive shape-memory polymers," *Advanced Materials*, vol. 27, no. 24, pp. 3696–3704, 2015.

[4] Y. Fang, Y. Ni, S. Y. Leo et al., "Direct writing of three-dimensional macroporous photonic crystals on pressure-responsive shape memory polymers," *ACS Applied Materials & Interfaces*, vol. 7, no. 42, pp. 23650–23659, 2015.

[5] C. H. Lu, W. Guo, Y. Hu, X. J. Qi, and I. Willner, "Multitriggered shape-memory acrylamide–DNA hydrogels," *Journal of the American Chemical Society*, vol. 137, no. 50, pp. 15723–15731, 2015.

[6] A. Kausar, "Nanodiamond tethered epoxy/polyurethane interpenetrating network nanocomposite: physical properties and thermoresponsive shape-memory behavior," *International Journal of Polymer Analysis and Characterization*, vol. 21, no. 4, pp. 348–358, 2016.

[7] X. Li, T. Liu, Y. Wang et al., "Shape memory behavior and mechanism of poly(methyl methacrylate) polymer networks in the presence of star poly(ethylene glycol)," *RSC Advances*, vol. 4, no. 37, pp. 19273–19282, 2014.

[8] D. Ratna and J. Karger-Kocsis, "Shape memory polymer system of semi-interpenetrating network structure composed of crosslinked poly (methyl methacrylate) and poly (ethylene oxide)," *Polymer*, vol. 52, no. 4, pp. 1063–1070, 2011.

[9] L. N. Woodard, V. M. Page, K. T. Kmetz, and M. A. Grunlan, "PCL-PLLA semi-IPN shape memory polymers (SMPs): degradation and mechanical properties," *Macromolecular Rapid Communications*, vol. 37, no. 23, pp. 1972–1977, 2016.

[10] L. Zhang, H. Jiao, H. Jiu, J. Chang, S. Zhang, and Y. Zhao, "Thermal mechanical and electrical properties of polyurethane/(3-aminopropyl) triethoxysilane functionalized graphene/epoxy resin interpenetrating shape memory polymer composites," *Composites: Part A*, vol. 90, no. 1, pp. 286–295, 2016.

[11] R. Zarnetta, R. Takahashi, M. L. Young et al., "Identification of quaternary shape memory alloys with near-zero thermal hysteresis and unprecedented functional stability," *Advanced Functional Materials*, vol. 20, no. 12, pp. 1917–1923, 2010.

[12] Y. Li, H. Chen, D. Liu, W. Wang, Y. Liu, and S. Zhou, "pH-responsive shape memory poly(ethylene glycol)–poly(ε-caprolactone)-based polyurethane/cellulose nanocrystals nanocomposite," *ACS Applied Materials & Interfaces*, vol. 7, no. 23, pp. 12988–12999, 2015.

[13] I. Dueramae, M. Nishida, T. Nakaji-Hirabayashi, K. Matsumura, and H. Kitano, "Biodegradable shape memory polymers functionalized with anti-biofouling interpenetrating polymer networks," *Journal of Materials Chemistry B*, vol. 4, no. 32, pp. 5394–5404, 2016.

[14] Y. Feng, H. Zhao, L. Jiao, J. Lu, H. Wang, and J. Guo, "Synthesis and characterization of biodegradable, amorphous, soft IPNs with shape-memory effect," *Polymers for Advanced Technologies*, vol. 23, no. 3, pp. 382–388, 2012.

[15] R. E. Abou-Zeid, E. A. Hassan, F. Bettaieb, R. Khiari, and M. L. Hassan, "Use of cellulose and oxidized cellulose nanocrystals from olive stones in chitosan bionanocomposites," *Journal of Nanomaterials*, vol. 2015, Article ID 687490, 11 pages, 2015.

[16] L. Song, Y. Li, Z. Xiong et al., "Water-induced shape memory effect of nanocellulose papers from sisal cellulose nanofibers with graphene oxide," *Carbohydrate Polymers*, vol. 179, no. 1, pp. 110–117, 2018.

[17] J. S. Yeo and S. H. Hwang, "The effect of dense polymer brush on the microfibrillated cellulose for the mechanical properties of poly(ε-caprolactone) biocomposites," *International Journal of Adhesion and Adhesives*, vol. 78, pp. 89–94, 2017.

[18] E. A. Hassan, S. M. Fadel, and M. L. Hassan, "Influence of TEMPO-oxidized NFC on the mechanical, barrier properties and nisin release of hydroxypropyl methylcellulose bioactive films," *International Journal of Biological Macromolecules*, vol. 113, no. 1, pp. 616–622, 2018.

[19] S. Fujisawa, T. Saito, S. Kimura, T. Iwata, and A. Isogai, "Surface engineering of ultrafine cellulose nanofibrils toward polymer nanocomposite materials," *Biomacromolecules*, vol. 14, no. 5, pp. 1541–1546, 2013.

[20] P. Yu, H. He, and A. Dufresne, "A novel interpenetrating polymer network of natural rubber/regenerated cellulose made by simple co-precipitation," *Materials Letters*, vol. 205, no. 1, pp. 202–205, 2017.

[21] W. S. Abo-Elseoud, M. L. Hassan, M. W. Sabaa, M. Basha, E. A. Hassan, and S. M. Fadel, "Chitosan nanoparticles /cellulose nanocrystals nanocomposites as a carrier system for the controlled release of repaglinide," *International Journal of Biological Macromolecules*, vol. 111, no. 20, pp. 604–613, 2018.

[22] M. Kaushik, K. Basu, C. Benoit, C. M. Cirtiu, H. Vali, and A. Moores, "Cellulose nanocrystals as chiral inducers: enantioselective catalysis and transmission electron microscopy 3D characterization," *Journal of the American Chemical Society*, vol. 137, no. 19, pp. 6124–6127, 2015.

[23] M. Morits, J. R. McKee, J. Majoinen et al., "Polymer brushes on cellulose nanofibers: modification, SI-ATRP, and unexpected degradation processes," *ACS Sustainable Chemistry & Engineering*, vol. 5, no. 9, pp. 7642–7650, 2017.

[24] M. L. Hassan, J. Bras, E. A. Hassan, S. M. Fadel, and A. Dufresne, "Polycaprolactone/modified bagasse whisker nanocomposites with improved moisture-barrier and biodegradability properties," *Journal of Applied Polymer Science*, vol. 125, Supplement 2, pp. E10–E19, 2012.

[25] L. Dai and C. L. Si, "Cellulose-*graft*-poly(methyl methacrylate) nanoparticles with high biocompatibility for hydrophobic anti-cancer drug delivery," *Materials Letters*, vol. 207, pp. 213–216, 2017.

[26] F. Zhuo, X. Liu, Q. Gao, Y. Wang, K. Hu, and Q. Cai, "Injectable hyaluronan-methylcellulose composite hydrogel cross-linked by polyethylene glycol for central nervous system tissue engineering," *Materials Science & Engineering. C, Materials for Biological Applications*, vol. 81, no. 21, pp. 1–7, 2017.

[27] D. Cheng, Y. Wen, L. Wang, X. An, X. Zhu, and Y. Ni, "Adsorption of polyethylene glycol (PEG) onto cellulose nano-crystals to improve its dispersity," *Carbohydrate Polymers*, vol. 123, no. 1, pp. 157–163, 2015.

[28] P. de Cuadro, T. Belt, K. S. Kontturi et al., "Cross-linking of cellulose and poly(ethylene glycol) with citric acid," *Reactive & Functional Polymers*, vol. 90, no. 3, pp. 21–24, 2015.

[29] L. Dong, C. Hu, L. Song, X. Huang, N. Chen, and L. Qu, "A large-area, flexible, and flame-retardant graphene paper," *Advanced Functional Materials*, vol. 26, no. 9, pp. 1470–1476, 2016.

[30] J. J. M. Halls, C. A. Walsh, N. C. Greenham et al., "Efficient photodiodes from interpenetrating polymer networks," *Nature*, vol. 376, no. 6540, pp. 498–500, 1995.

[31] Y. Liu, Y. Li, G. Yang, X. Zheng, and S. Zhou, "Multi-stimulus-responsive shape-memory polymer nanocomposite network cross-linked by cellulose nanocrystals," *ACS Applied Materials & Interfaces*, vol. 7, no. 7, pp. 4118–4126, 2015.

[32] H. Du and J. Zhang, "Solvent induced shape recovery of shape memory polymer based on chemically cross-linked poly(vinyl alcohol)," *Soft Matter*, vol. 6, no. 14, pp. 3370–3376, 2010.

[33] Y. Liu, Y. Li, H. Chen, G. Yang, X. Zheng, and S. Zhou, "Water-induced shape-memory poly(d, l-lactide)/microcrystalline cellulose composites," *Carbohydrate Polymers*, vol. 104, no. 1, pp. 101–108, 2014.

[34] W. Wang, H. Lu, Y. Liu, and J. Leng, "Sodium dodecyl sulfate/epoxy composite: water-induced shape memory effect and its mechanism," *Journal of Materials Chemistry A*, vol. 2, no. 15, pp. 5441–5449, 2014.

Hindawi
Journal of Nanomaterials
Volume 2019, Article ID 5947948, 9 pages
https://doi.org/10.1155/2019/5947948

Research Article

Investigation on the Electrothermal Properties of Nanocomposite HDPE

Ramkumar R[1] **and Pugazhendhi Sugumaran C**[2]

[1]*Division of High Voltage Engineering, College of Engineering Guindy, Anna University, Chennai, 600 025 Tamil Nadu, India*
[2]*Department of Electrical and Electronics Engineering, College of Engineering Guindy, Anna University, Chennai, 600 025 Tamil Nadu, India*

Correspondence should be addressed to Ramkumar R; kumarram077@gmail.com

Received 31 January 2019; Revised 17 March 2019; Accepted 27 March 2019; Published 28 April 2019

Guest Editor: Laijun Liu

Currently, several deep-rooted researches have focused on the significance and application of polymers in electrical and mechanical fields. This is because of the benefits of polymers in its availability, recyclability, and flexibility in processing; economical and most importantly improvement in material property have been achieved by incorporating nanosized metal oxide (inorganic) additives in the polymer matrix. In this study, HDPE (High Density Polyethylene) is considered as base polymer and alumina as nanoadditive. Alumina (Al_2O_3) nanofillers are incorporated in HDPE as 1 wt.%, 3 wt.%, 5 wt.%, and 7 wt.% filler compositions. From the dielectric analysis, it has been inferred that HDPE with 3 wt.% nanoalumina achieved higher permittivity compared with other samples. Also, 5 wt.% composite samples has gained 18.46% improvement in inception voltage, 16.3% increase in the breakdown strength, and 94.47% enhanced thermal conductivity compared with pure HDPE.

1. Introduction

Polymer dielectrics are nowadays widely used in electrical applications. The main objective of the experiments conducted was focused on creating new low cost polymeric composite material with better performance for electrical applications. Polymer dielectrics are mostly preferred based on its better electrical, thermal, and mechanical properties and for its flexibility while processing. Recently, most researches have acknowledged the necessity of incorporating the nanofillers in the polymer matrix to enhance the properties of dielectrics. The enhancement of the properties in dielectrics when nanofillers were incorporated in the polymer matrix has already been proved with many effective illustrations. Literature shows that the nanosized fillers have some unique properties like homogeneity in dispersion and distribution; it can establish better surface area of contact in the polymer matrix and has more interaction with host at a low level of loading. This feature is the major factor for the increased interaction zone, i.e., there is an increase in area between the filler and the polymer matrix, which has considerable impact on electrical insulation properties such as higher resistance towards partial discharge, treeing, and improvement in breakdown strength [1–3].

The interaction zones are made of three layers, bounded layer, bound layer, and loose layer. The bounded layer is the first layer, which has the tight bonding with the inorganic nanofillers and the organic polymer matrix of few nm thickness. The second layer is the bound layer of several nanometer thickness, which interrelates the bounded layer and the nanoparticles. The third layer is the loose layer of several tens of nm thickness, which interacts with the second layer. There is another layer encompassing the third, an electronic double bond layer in which the columbic interaction of charges takes place. In this layer, charges are injected from the higher permittivity nanofillers into the polymer matrix (Gouy-Chapman diffusion layer), which induces the electronic polarizability and orientation of permanent dipoles. Many other factors have influenced on reduction

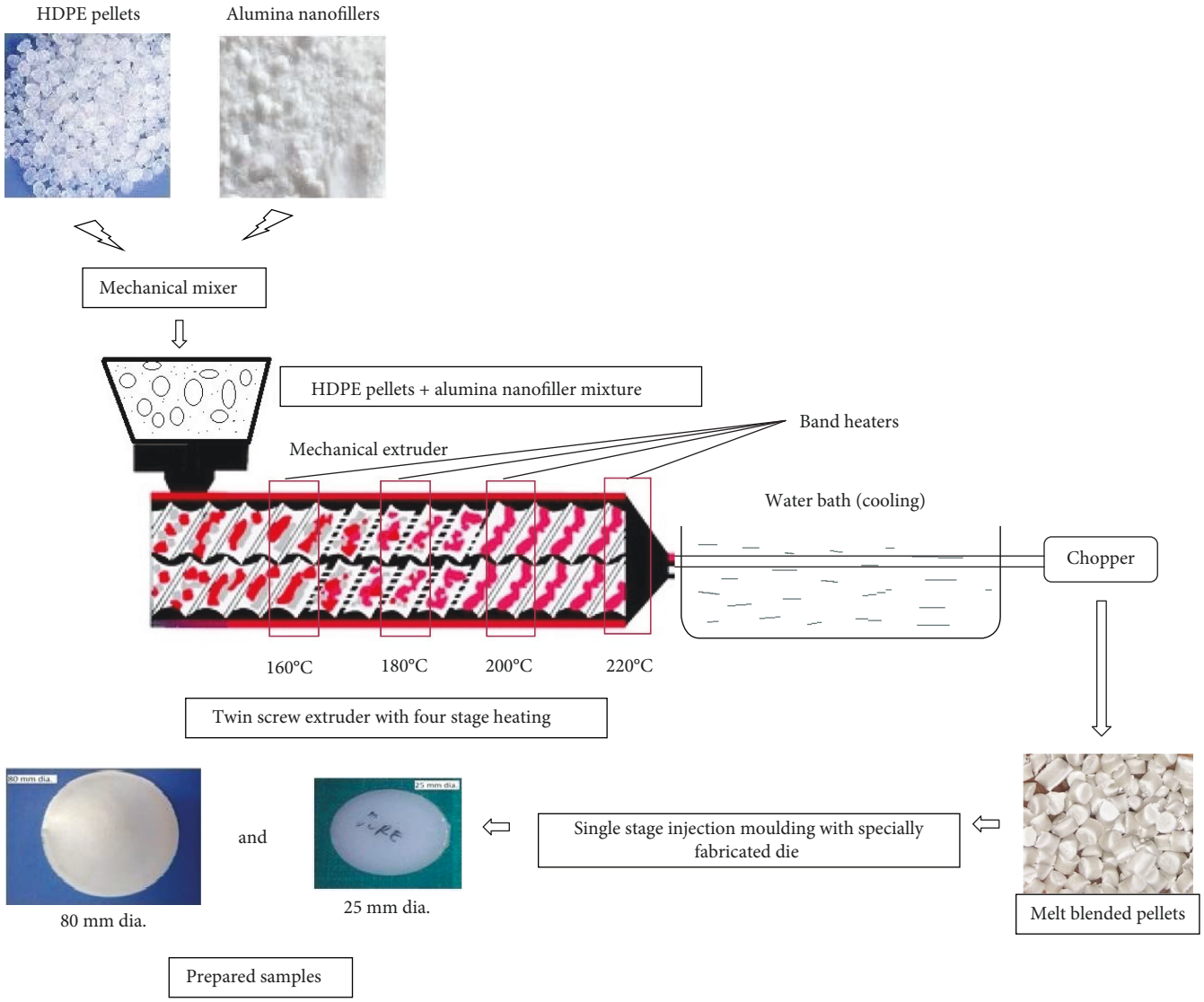

Figure 1: Flow illustration for the melt blending process of HDPE-alumina nanocomposite.

in permittivity due to free volume and the higher energy surface contact of nanomaterial over the polymer matrix [4].

This work consists of various processes such as selection of materials, methodology of sample preparation, and experiments conducted on exploring the electrical and thermal performance of the prepared samples. Based on polymer segmental motion, permittivity and thermal stability of HDPE (High Density Polyethylene) have been chosen as base polymer and alumina (Al_2O_3) as nanofillers. It had been evidently proven that nanosized alumina fillers offered high resistance for partial discharges and better dielectric and mechanical properties, while microsized alumina had been considered upright filler for enhancement of thermal conductivity [5].

2. Experimental Work

In this work, composition of FF00851 grade HDPE with MFI 9 g/10 min from Haldia Corporation and nanosized alumina filler of size < 100 nm from SRL Chemicals were considered for sample preparation. The dielectric parameters such as permittivity, tan δ, and parallel resistance R_p have been measured using Electrochemical Impedance Spectroscopy WAYNE KERR 6500B. The value of AC breakdown strength was determined in AC breakdown setup as per standard IEC 60243-1. TGA (Thermogravimetric analysis) had been carried out in NETZSCH STA 449 F3 Jupiter, thermal analyzer (TA). The partial discharges (PD) for the prepared samples were examined using the PD setup as per standard IEC 60270, 2003.

2.1. Sample Preparation. The various processes involved in the sample preparation are illustrated in Figure 1. The handmade mechanical extrusion technology is opted for sample preparation, which is of environment friendly nature. The temperatures of heaters in the screw mixture barrel are maintained at 160°C, 180°C, 200°C, and 220°C [6]. The extruded materials are molded into a die with injection molding machine.

Table 1 shows the composition of HDPE and nanoalumina for a 100 g samples at different wt.%. Samples of 25 mm diameter and 3 mm thickness are prepared for dielectric measurements, and another sample of 80 mm diameter with 1.5 mm thickness is prepared for AC breakdown (IEC 60243-1) and PD measurement.

2.2. Scanning Electron Microscopy. The morphology of HDPE/alumina nanocomposites for different weight composition was analyzed. The homogeneous dispersion and distribution of alumina nanoparticles in HDPE at 1 wt.%, 3 wt.%, 5 wt.%, and 7 wt.%, respectively, are presented by SEM image from Figures 2(a)–2(d), the alumina nanoparticles are uniformly distributed in the HDPE matrix. The particle sizes are at most around 100 nm. Few agglomerates can be also observed at 7 wt.% samples [7].

2.3. Partial Discharge. The PD resistance measurement setup as shown in Figure 3 was created as per IEC 60270 with a background noise of 4 pC inside the shielding chamber. The measured value of PD inception and extinction voltages was recorded with the help of DSO Agilent 54621A and was tabulated in Table 2.

It has been observed that the addition of nanofiller in the base polymer increases the PD resistance of the samples. There is likely to be strong bonding between the homogeneously dispersed alumina nanoparticles and the HDPE polymer which offers higher resistance to the stress on applying electric field, as a result the PD resistance of the composite increases. It has been noticed that for higher wt.% of nanoalumina added samples, the space in the interfacial zone increases thus reducing the PD resistance of the samples [3, 8–10]. The maximum inception and extinction voltages observed for 5 wt.% samples with a rise of 18.46% and 35.79%, respectively, in comparison with pure HDPE samples.

2.4. AC Breakdown Strength. AC breakdown strength was determined for the prepared samples of HDPE along with 1, 3, 5, and 7 wt.% nanoalumina at power frequencies (50-60) Hz with reference to IEC 60243-1. An average of 10 samples from each composition was tested, and the mean value had been considered for the analysis. The test specimen was immersed in the insulating liquid medium with higher dielectric strength in order to avoid the surface flashover and gliding discharges at the edges [11].

The values of the breakdown strength for different samples obtained were listed in Table 3. It was observed that 5 wt.% composition of alumina with HDPE has attained 16.3% increased breakdown strength compared with pure HDPE.

The characteristics on the enhancement of breakdown strength of the samples based on the effect of alumina nanofillers and the diminution at higher wt.% concentrations of nanofillers are illustrated as follows: (a) nanoparticles act as a scattering electron source, which avoid the formation of a spheroid mass of crystals and macroscopic boundaries. Nanoparticles are high resistance towards PD. (b) There will be a large amount of charge traps at the interfacial region, which decreases the carrier charge mobility. (c) At higher wt.%, agglomeration of nanoparticles takes place which leads to creation of large void defects around it in the polymer matrix. (d) The higher permittivity agglomerated nanoparticles alter an electric field and reduce the space between nanoparticles, which create a conductive path by enhancing the tunneling current between nanofillers. Figure 4 represents the mean and error bar of breakdown voltage (BDV) and Partial Discharge Inception Voltage (PDIV). It can be clearly observed on the BDV that the error bars for each samples does not overlap on each other; thus, the error bars are not different for each samples, but for PDIV, the error bars for the 3 wt.% sample show minimal value. These results also indicate that the BD occurs after the occurrence of PD. Further, error bars for AC breakdown strength clearly show that HDPE with 5 wt.% alumina has the highest mean with good breakdown strength.

Table 1: Weight composition of different samples.

wt.% composition of alumina with HDPE	HDPE in grams	Nanoalumina in grams
0	100	0
1	99.009	0.9900
3	97.0873	0.9708
5	95.2380	4.7619
7	93.4579	6.5420

2.5. Dielectric Constant and Loss Factor. The dielectric parameters had been recorded for all composition of samples at 30°C, 60°C, 90°C, and 120°C temperatures and as a function of frequency from 20 Hz – 1 MHz by using the Impedance Analyzer. The real part of dielectric constant (ε) had been calculated from the recorded value of capacitance, from

$$\varepsilon = \frac{t * C_p}{A * \varepsilon_0}, \tag{1}$$

where C_p is the capacitance in farads, t is the thickness of the sample in meters (m), A is the surface area of samples in sq. meters, and ε_0 is the absolute permittivity.

Figures 5(a)–5(d) represent the variation of dielectric constant (ε) with respect to frequency for the prepared nanocomposite samples at 30, 60, 90, and 120°C temperatures. It is observed that

(a) permittivity usually increases, as a result of incorporating higher permittivity inorganic fillers in the polymer matrix, which initiates the interfacial polarization of the Maxwell-Wagner type. In addition, it was confirmed with the Lichtenecker-Rother logarithmic law of mixing

(b) as the frequency of AC supply varied, initially the ε is invariable, but at a certain critical frequency, the polarization of ions gets saturated or failed to settle; thus, the ε value dropped at lower to higher frequencies

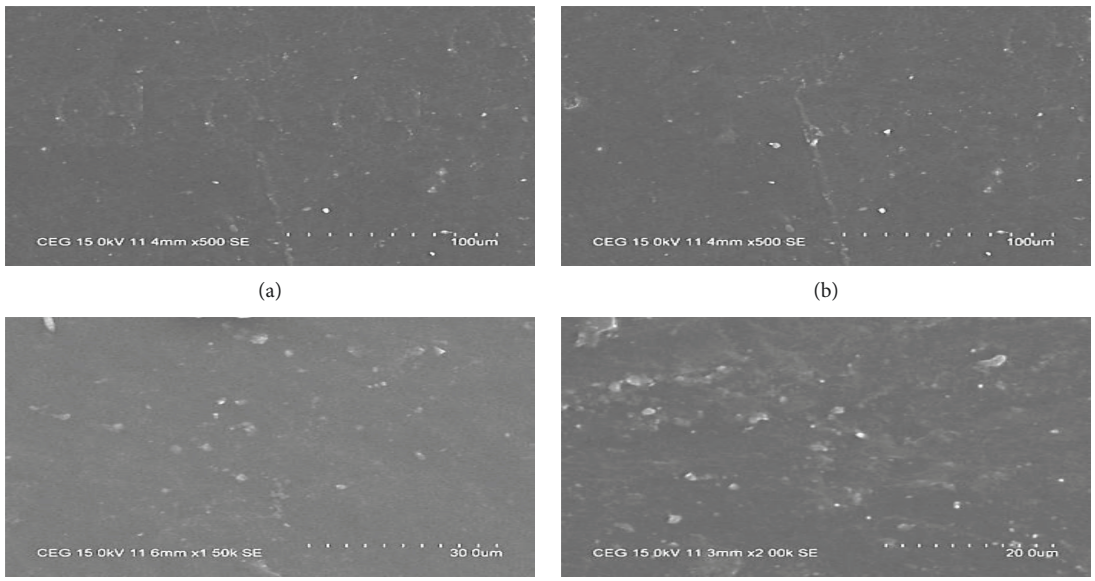

Figure 2: (a)–(d) SEM image of HDPE-alumina nanocomposite: (a) @ 1 wt.%, (b) @ 3 wt.%, (c) @ 5 wt.%, and (d) @ 7 wt.%.

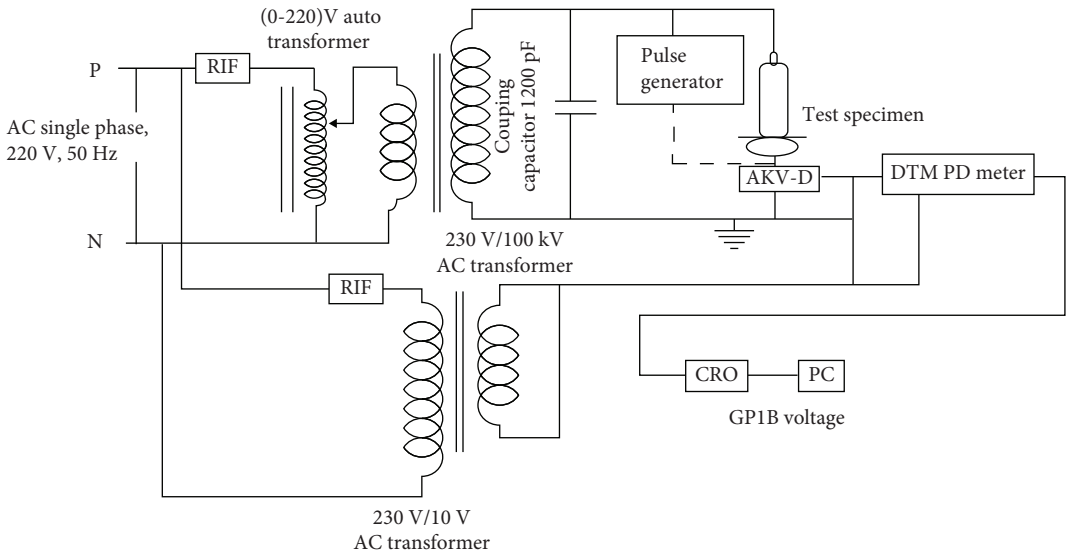

Figure 3: Partial discharge setup.

Table 2: Partial discharge characteristics.

Sample	Inception voltage (kV/mm)	Extinction voltage (kV/mm)
Pure HDPE	18.97	13.52
HDPE with 1 wt.% alumina	19.34	13.84
HDPE with 3 wt.% alumina	20.32	14.074
HDPE with 5 wt.% alumina	22.473	18.36
HDPE with 7 wt.% alumina	21.542	17.615

Table 3: AC breakdown strength (BDV).

Sample	AC BDV (kV/mm)	% increase
Pure HDPE	28.18	—
HDPE with 1 wt.% alumina	28.56	1.34
HDPE with 3 wt.% alumina	29.32	4.04
HDPE with 5 wt.% alumina	32.79	16.3
HDPE with 7 wt.% alumina	30.44	8.01

(c) there was no significant variation in the permittivity at lower temperatures; it was due to high density of the polyethylene matrix, which disturbed the charge mobility at lower temperatures. The increase in temperature on the samples from 30°C to 120°C was noticed; there was an increase in its free volume

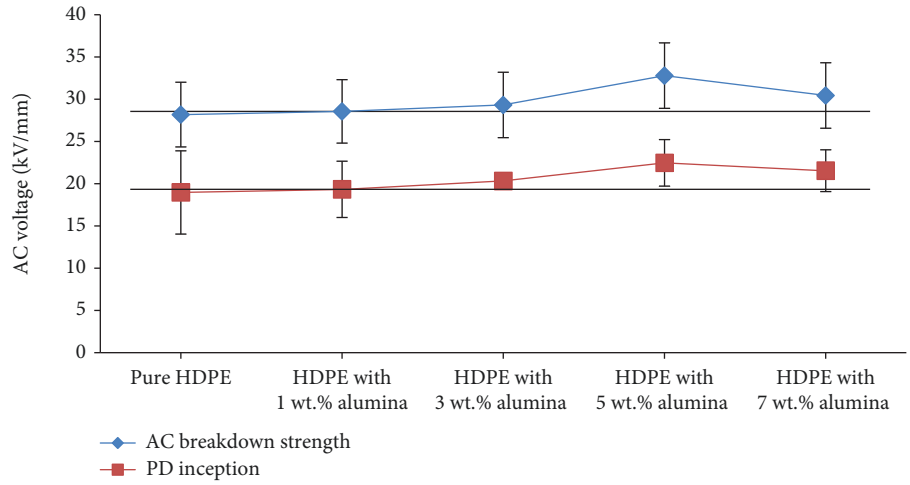

Figure 4: Error bar representing breakdown voltage (BDV) and Partial Discharge Inception Voltage (PDIV).

and thereby increasing the permittivity of the samples. The permittivity is inconsistent beyond 120°C. The collapsing state of the polymer matrix during initiation of melting process (the melting point of the HDPE used in the work was 130°C) causes the inconsistency in ε [12]

(d) it was observed that the 3 wt.% composite sample attained higher permittivity with more filler content, which increased the ionic and electronic polarization in addition to the free dipoles of HDPE. Further increase in the filler content (i.e., at 7 wt.%) led to more agglomeration of nanofillers forming clusters/microstructures, thus reduction in free volume and therefore will be few dipoles and ionic carriers available in the outer layer not free to move; thus, there is reduction in permittivity

Figures 6(a)–6(d) represent the dielectric loss (tan δ) vs. the frequency plot for different weight compositions of nanoalumina on HDPE at different temperatures. It was resolved that

(a) dissipation factor was influenced by the filler loadings and permittivity. In polymer nanocomposites, due to polarization effect, the dipoles in interfacial zones create clusters. There was a setback in orientation of dipoles, which reverses in each cycle on the application of alternating field. At higher frequencies, the dielectric loss might be increased with an effect of speedy reversal of field and orientation of dipoles would lag the field. The less time to orient dipoles among themselves led to a rise of dielectric loss in the higher frequency

(b) at higher frequencies beyond 1 kHz, the tan δ had been observed to be less than unity. The tan δ increased with an increase in temperature and decreased at high frequencies

(c) addition of alumina nanofillers had an influence over the dielectric loss of the composite. The higher wt.% of filler content increased the charge carrier which led to more amount of dielectric loss by charge transport mechanism. The 5 wt.% composition substantiated the tan δ loss at lower frequencies for its better performance [13, 14]

(d) at higher temperatures and frequencies between 50 and 1000 Hz, there was a considerable increase of tan δ loss in the 5 wt.% composition. At high temperatures, the permittivity increase in free volume enhanced the ionic polarization, which caused more loss. Above than 1 kHz, there was no considerable difference in the tan δ loss even at different temperatures

(e) the tan δ losses at 50 Hz frequency varied from 0.67 to 0.77 for 5 wt.% samples with temperatures between 50 and 110°C and reaches the maximum around 150 to 170 Hz for 30°C, 60°C, 90°C, and 120°C

2.6. Volume Resistivity. The volume resistivity (ρ) of pure HDPE and 1, 3, 5, and 7 wt.% nanoalumina samples was obtained from the measured value of parallel resistance (R_p).

The calculated values are plotted against frequencies in Figure 7. It was observed that at lower frequencies the 5 wt.% sample attains higher volume resistivity and was also noticed that the resistivity of all the samples linearly decreases up to 100 Hz. Further, 100 Hz -10 kHz the resistivity showed a constant value. The addition of alumina nanofillers reduced the volume resistivity, which averted the movement of charge carriers. On the application of AC fields, at lower frequencies, there was a considerable time for the charged particles, which had created weak links between nanofillers and HDPE segments. It resulted with a linear drop in volume resistivity when the conduction current at lower frequencies was increased. At higher

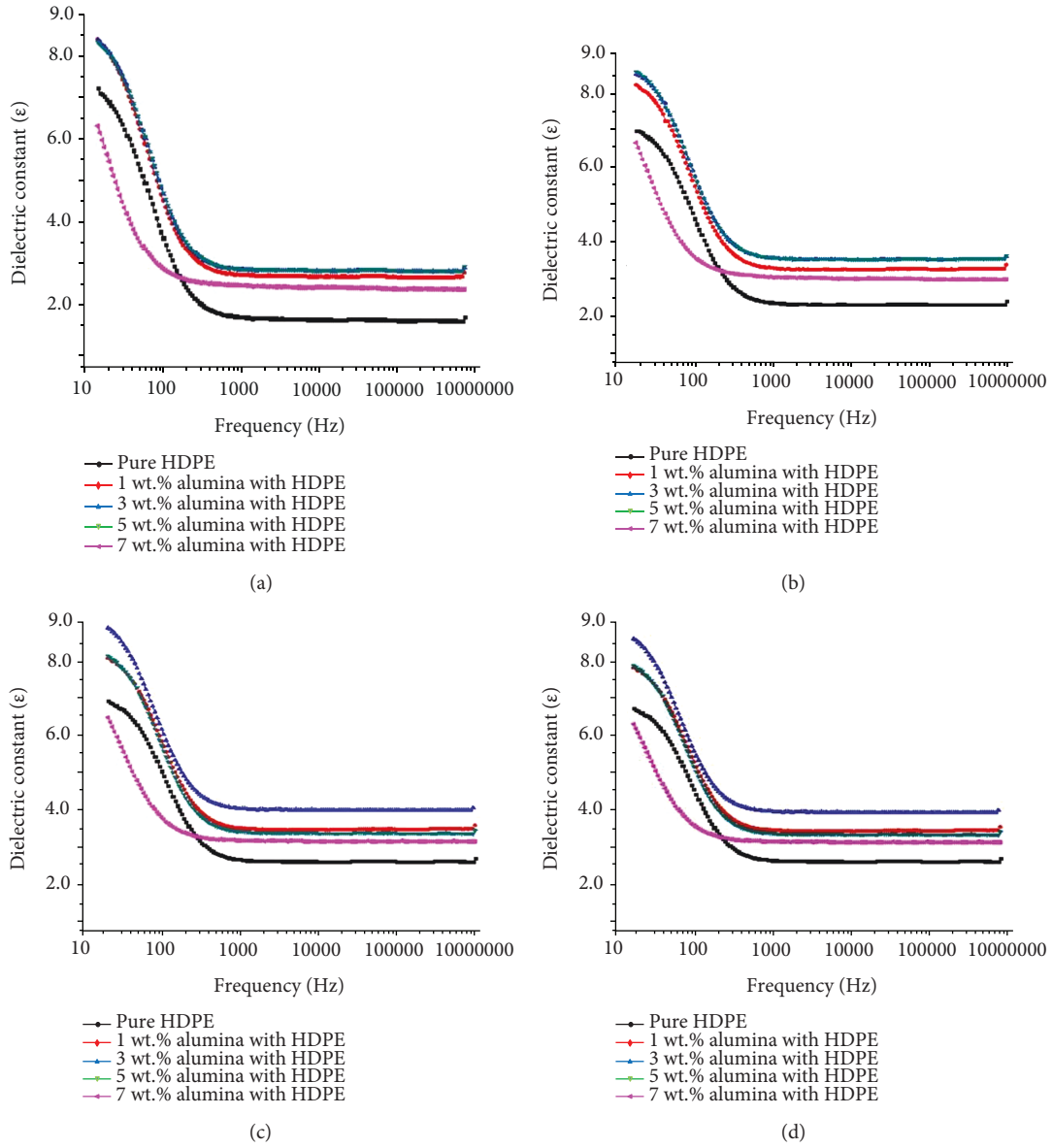

Figure 5: (a)–(d) Dielectric constant dependence on frequency: (a) @ 30°C, (b) @ 60°C, (c) @ 90°C, and (d) @ 120°C.

frequencies, the movement of the charged particle is restricted, which in turn reduces the conduction current without any significant change in the volume resistivity [15].

2.7. Thermal Conductivity. The thermal conductivity was measured using UNITHERM (model 2022) with reference to ASTM E1530. The sample was placed between two polished surfaces, the upper electrode was maintained at higher temperature and the lower electrode was calibrated with heat flow transducer at lower temperature. The heat flowed from the upper surface, establishing an axial temperature gradient in the stack for attaining thermal equilibrium state. The difference of temperature had been measured through the heat flow transducer.

The thermal conductivity was calculated for the samples by considering the transducer output and sample size. The calculated thermal conductivity values for different samples are listed in Table 4.

Equation (2) represents the heat dissipated by the solid dielectrics on the application of AC fields,

$$\mathrm{HD} = C_v \frac{dT}{dt} + \Lambda.(K \ \mathrm{grad} \ T), \tag{2}$$

where HD is the heat dissipated, C_v is the specific heat of the sample, T is the temperature of the sample, K is the thermal conductivity of the sample, and t is the time for heat dissipation. The higher thermal conductivity indicated the more heat dissipation. From Figure 6(d), it was ascertained that 3 wt.% and 5 wt.% samples accomplished the higher dissipation factor by having higher mobility of ions. From Table 4, it was seen that the higher thermal conductivity helps to

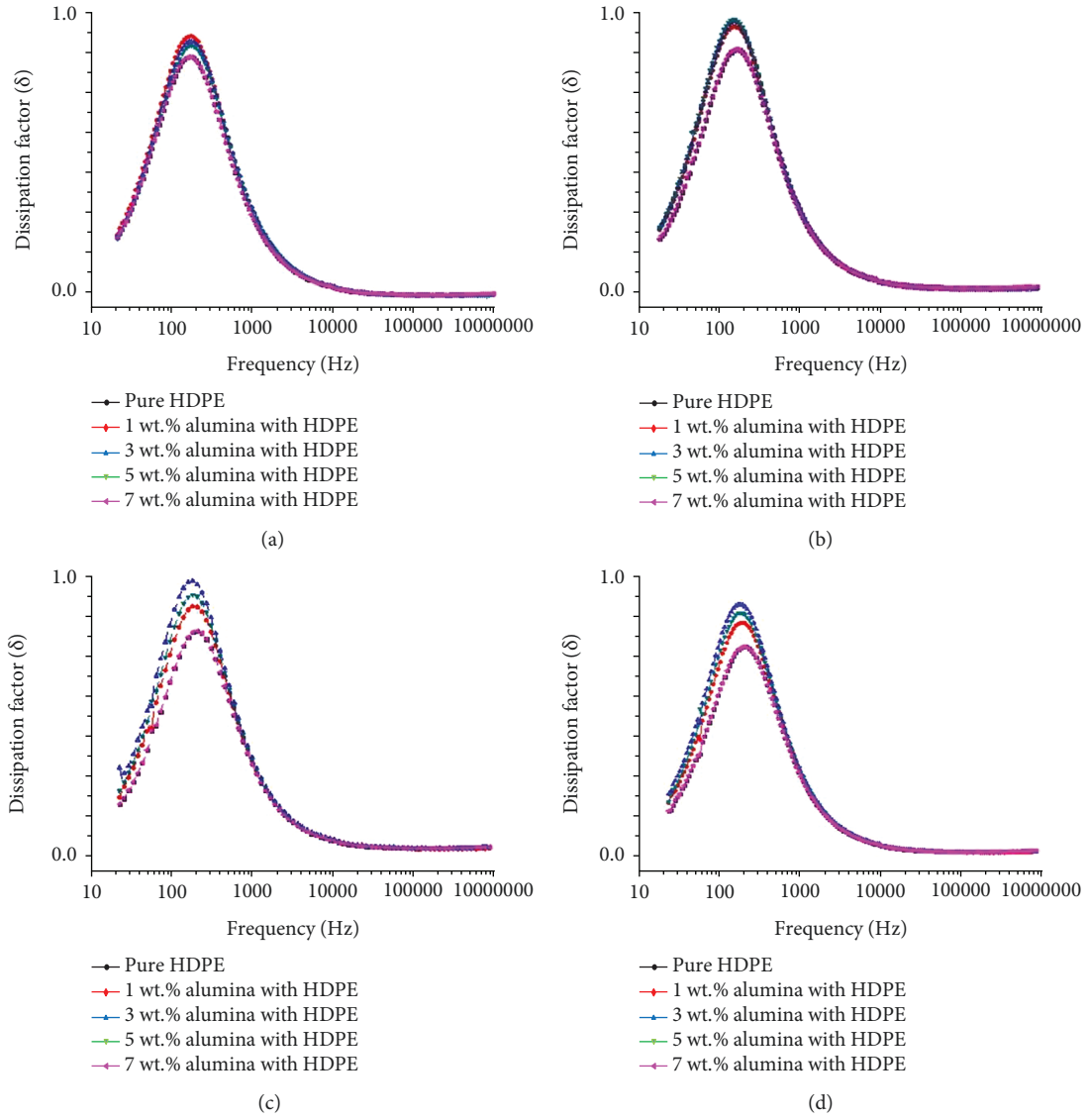

Figure 6: (a)–(d) Dissipation factor (tan δ) dependence on frequency (Hz): (a) @ 30°C, (b) @ 60°C, (c) @ 90°C, and (d) @ 120°C.

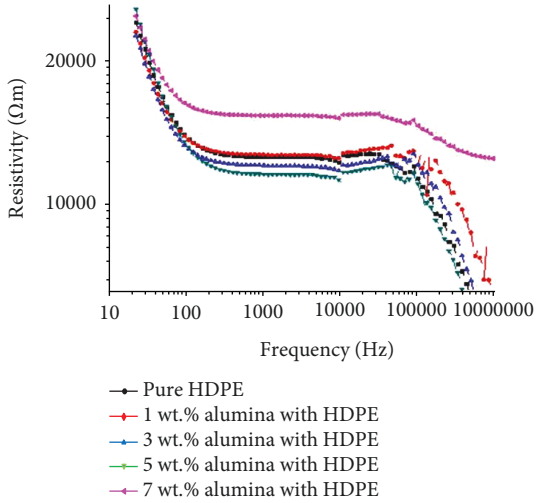

Figure 7: Resistivity (Ω·m) dependence on frequency (Hz).

Table 4: Thermal conductivity.

Sample	Thermal conductivity (W/m·K)	% increase
Pure HDPE	0.471	—
HDPE with 1 wt.% alumina	0.525	11.46
HDPE with 3 wt.% alumina	0.712	51.16
HDPE with 5 wt.% alumina	0.916	94.47
HDPE with 7 wt.% alumina	0.919	95.11

attain the thermal equilibrium of sample, which supports to enhance the dielectric strength as shown in Table 3 with respect to the 5 wt.% sample (thermal BD).

2.8. Thermogravimetric Analysis. The TA Instrument TGA Q50 V20.13 Build 39 was used to record the change in weight of the samples with respect to temperature at the rate of rise

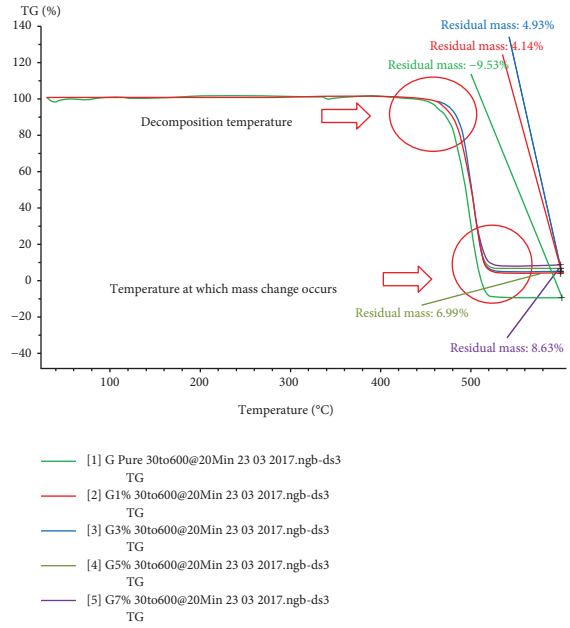

Figure 8: TGA comparison of pure HDPE: 1 wt.%, 3 wt.%, 5 wt.%, and 7 wt.% samples.

of 20°C/minute in the nitrogen atmosphere (dynamic TGA). The thermogram was recorded from 40°C to 600°C. The results were analyzed for validating the purity, rate of reaction, activation energy, heat reaction, and identification of different composition of the samples [16].

From the thermogram shown in Figure 8, it was observed that the pure HDPE sample starts to decompose at 460°C. It was ascertained from the TGA that the pure sample exhausted at 520°C. The 1, 3, 5, and 7 samples had 4.14%, 4.93%, 6.99%, and 8.63% residues, respectively, recorded at 600°C. The 7 wt.% sample had higher amount of residue at 600°C due to higher thermal conductivity.

3. Conclusion

This paper exhibits the detailed study on the electrical and thermal behaviour of the HDPE by the addition of alumina nanofillers. Summary of the observations made is listed as follows: the 5 wt.% HDPE/alumina composite had obtained 16% higher AC breakdown strength in comparison with pure HDPE sample. The 3 wt.% composition gained higher permittivity for 20 – 400 Hz at 30°,60°, 90°, and 120°C.

From PD results, it has been proven that the addition of inorganic alumina nanofillers to HDPE significantly improved the PD characteristic. This has happened as a result of strong bonding between nanoparticles and the HDPE at the interfacial region.

With the increased filler loading content, there was a weak link formation resulted in a decline in volume resistivity. The glass transition temperature of the 5 wt.% composition was observed as 121°C which was 23.4% higher than pure HDPE. Higher thermal conductivity of the specimen helped to attain the thermal equilibrium, which further enhanced the breakdown voltage.

For insulation applications, the HDPE with 5 wt.% alumina was considered as it had improved the breakdown strength and thermal stability.

Data Availability

The data used to support the findings of this study are available from the corresponding author upon request.

Conflicts of Interest

The authors declare that there is no conflict of interest regarding the publication of this paper.

References

[1] V. A. Zakrevskii, N. T. Sudar, A. Zaopo, and Y. A. Dubitsky, "Mechanism of electrical degradation and breakdown of insulating polymers," *Journal of Applied Physics*, vol. 93, no. 4, pp. 2135–2139, 2003.

[2] J. K. Nelson and Y. Hu, "Nanocomposite dielectrics—properties and implications," *Journal of Physics D: Applied Physics*, vol. 38, no. 2, pp. 213–222, 2005.

[3] W. A. Izzati, Y. Z. Arief, Z. Adzis, and M. Shafanizam, "Partial discharge characteristics of polymer nanocomposite materials in electrical insulation: a review of sample preparation techniques, analysis methods, potential applications, and future trends," *The Scientific World Journal*, vol. 2014, Article ID 735070, 14 pages, 2014.

[4] T. Tanaka, M. Kozako, N. Fuse, and Y. Ohki, "Proposal of a multi-core model for polymer nanocomposite dielectrics," *IEEE Transactions on Dielectrics and Electrical Insulation*, vol. 12, no. 4, pp. 669–681, 2005.

[5] Y. Okazaki, M. Kozako, M. Hikita, and T. Tanaka, "Effects of addition of nano-scale alumina and silica fillers on thermal conductivity and dielectric strength of epoxy/alumina microcomposites," in *IEEE International Conference on Solid Dielectrics*, pp. 1–4, Potsdam, Germany, July 4–9, 2010.

[6] R. Ramkumar and C. P. Sugumaran, "Investigation on dielectric properties of HDPE with alumina nano fillers," in *IEEE sponsored Power India conference (PIICON)*, pp. 1–4, Bikaner, India, November 25–27, 2016.

[7] M. Hajian, G. A. Koohmareh, and A. Mostaghasi, "Investigation of the effects of titanate as coupling agent and some inorganic nanoparticles as fillers on mechanical properties and morphology of soft PVC," *International Journal of Polymer Science*, vol. 2011, Article ID 238619, 9 pages, 2011.

[8] T. Imai, F. Sawa, T. Ozaki et al., "Influence of temperature on mechanical and insulation properties of epoxy-layered silicate nanocomposite," *IEEE Transactions on Dielectrics and Electrical Insulation*, vol. 13, no. 2, pp. 445–452, 2006.

[9] G. Zhang, G. Wu, L. Tong, and E. He, "Study of nano TiO_2 filler in the corona-resistant magnetic wire insulation performance of inverter-fed motor," in *Proceedings of 2005 International Symposium on Electrical Insulating Materials*, pp. 180–183, Kitakyushu, Japan, June 2005.

[10] C. P. Sugumaran, "Experimental investigation on dielectric and thermal characteristics of nanosized alumina filler added polyimide enamel," *Journal of Electrical Engineering and Technology*, vol. 9, no. 3, pp. 978–983, 2014.

[11] L. Liu, L. Weng, Y. Song, L. Gao, and Q. Lei, "The effects of coupling agents on the properties of polyimide/nano-Al_2O_3 three-layer hybrid films," *Journal of Nano Materials*, vol. 2010, Article ID 354364, 5 pages, 2010.

[12] B. Tareev, *Physics of Dielectric Materials*, Mir Publishers, Moscow, 2nd edition, 1979.

[13] C. Sugumaran, M. Mohan, and K. Udayakumar, "Investigation of dielectric and thermal properties of nano-filler (ZrO_2) mixed enamel," *IEEE Transactions on Dielectrics and Electrical Insulation*, vol. 17, no. 6, pp. 1682–1686, 2010.

[14] F. Madidi, G. Momen, and M. Farzaneh, "Dielectric properties of TiO_2/silicone rubber micro- and nanocomposites," *Advances in Materials Science and Engineering*, vol. 2018, Article ID 4682076, 7 pages, 2018.

[15] Y. Mobarak, M. Bassyouni, and M. Almutawa, "Materials selection, synthesis, and dielectrical properties of PVC nanocomposites," *Advances in Materials Science and Engineering*, vol. 2013, Article ID 149672, 6 pages, 2013.

[16] P. C. Irwin, Y. Cao, A. Bansal, and L. Schadler, "Thermal and mechanical properties of polyimide nanocomposites," in *2003 Annual Report Conference on Electrical Insulation and Dielectric Phenomena*, pp. 120–123, Albuquerque, NM, USA, 2003.